Effect of Chaos and Complex Wave Pattern Formation in Multiple Physical Systems: Relativistic Quantum Tunneling, Optical Meta-materials, and Co-evolutionary Game Theory

by

Xuan Ni

A Dissertation Presented in Partial Fulfillment
of the Requirements for the Degree
Doctor of Philosophy

Approved August 2012 by the
Graduate Supervisory Committee:

Ying-Cheng Lai, Chair
Richard Akis
Hongbin Yu
Liang Huang

ARIZONA STATE UNIVERSITY

December 2012

ABSTRACT

What can classical chaos do to quantum systems is a fundamental issue highly relevant to a number of branches in physics. The field of quantum chaos has been active for three decades, where the focus was on non-relativistic quantum systems described by the Schrödinger equation. By developing an efficient method to solve the Dirac equation in the setting where relativistic particles can tunnel between two symmetric cavities through a potential barrier, chaotic cavities are found to suppress the spread in the tunneling rate. Tunneling rate for any given energy assumes a wide range that increases with the energy for integrable classical dynamics. However, for chaotic underlying dynamics, the spread is greatly reduced. A remarkable feature, which is a consequence of Klein tunneling, arise only in relativistc quantum systems that substantial tunneling exists even for particle energy approaching zero. Similar results are found in graphene tunneling devices, implying high relevance of relativistic quantum chaos to the development of such devices.

Wave propagation through random media occurs in many physical systems, where interesting phenomena such as branched, fracal-like wave patterns can arise. The generic origin of these wave structures is currently a matter of active debate. It is of fundamental interest to develop a minimal, paradigmatic model that can generate robust branched wave structures. In so doing, a general observation in all situations where branched structures emerge is non-Gaussian statistics of wave intensity with an algebraic tail in the probability density function. Thus, a universal algebraic wave-intensity distribution becomes the criterion for the validity of any minimal model of branched wave patterns.

Coexistence of competing species in spatially extended ecosystems is key to biodiversity in nature. Understanding the dynamical mechanisms of coexistence is a fundamental problem of continuous interest not only in evolutionary biology but also in nonlinear science. A continuous model is proposed for cyclically competing species and the effect of the interplay between the interaction range and mobility on coexistence is investigated. A transition from coexistence to extinction is uncovered with a non-monotonic behavior in the coexistence probability and switches between spiral and plane-wave patterns arise. Strong mobility can either promote or hamper coexistence, while absent in lattice-based models, can be explained in terms of nonlinear partial differential equations.

To my mother and my wife

ACKNOWLEDGMENTS

I would like to express my deepest gratitude to my advisor, Dr. Ying-Cheng Lai, for his guidance, mentoring, and continuous support over the past few years, which I couldn't have achieved so much without. His great personality, diligence and conscientious attitude toward research, and captivating ideas have educated and helped me throughout my PhD studies.

I also want to take this opportunity to thank Dr. Wenxu Wang and Dr. Liang Huang, the former postdocs as well as my sincere friends, who have helped me in so many aspects. Dr. Wang, an old friend ever since my undergraduate thesis, helped me a lot in my first few publications. His sense of humor and generosity always make discussion with him enjoyable. I learned a lot from Dr. Huang, who taught me and inspired me with his solid physics background, broad interest and knowledge, and deep understanding of physical problems. I couldn't appreciate more for his traveling half of the world for my defense.

I always value the excellent research atmosphere built by our Chaos group members, Dr. Qingfei Chen, Dr. Rui Yang, Dr. Luoluo Jiang, Riqi Su, Lei Ying, Yuzhong Chen, Lianren Wu, and Yingli Wu. The fruitful discussions and collaborations with them made me feel so supportive and encouraged all these years, and the friendship will take a lifetime to cherish.

I want to thank Dr. Celso Grebogi for providing helpful suggestions and constructive critiques on many of my projects. Also, I want to thank Dr. Louis M. Pecora for his inspiration and collaboration which made a great topic possible.

My special thanks to the committee members, Dr. Richard Akis and Dr. Hongbin Yu, for their precious time as well as invaluable comments and advices, which helped me improve this dissertation.

"To steal ideas from one person is plagiarism. To steal from many is research." That said, I owe a lot of thanks to many others from whom I have "stolen" ideas. I want thank them, some of whom I may even not know the names of, for their great spirit of sharing knowledge, which made this dissertation possible.

TABLE OF CONTENTS

Page

Page

Page

LIST OF FIGURES

Figure Page

1 . INTRODUCTION

1.1. Dirac equation and relativistic quantum tunneling

Dirac equation, the fundamental equation of relativistic quantum mechanics, has recently attracted a tremendous amount of attention from a much broader community than that in high-energy and elementary-particle physics, due to its high relevance to graphene systems [1–8] and topological insulators [9, 10]. In the fields where the Dirac equation has traditionally been studied, the solutions are usually obtained by some perturbative approach. However, to the best of our knowledge, a general method for completely solving the Dirac equation in a closed system of *arbitrary* geometry does not exist at the present. The development of such a method is thus of fundamental interest.

A number of areas in physics can benefit enormously from an efficient method for solving the Dirac equation. The most relevant area is graphene physics. Graphene ribbons exhibit a linear energy-momentum relation near any of the Dirac points in the energy-band diagram, which is a characteristic of relativistic quantum motion of massless fermions. In the presence of short-range potentials, two Dirac points are coupled together. It is thus of basic interest to investigate the behavior of pure Dirac fermions to distinguish them from those due to the coupling of two relativistic particles. In a recent work [11], a method was developed to study the effect of Dirac fermions in graphene employing the transfer-matrix technique, which addresses the transport properties of a graphene ribbon with periodic boundary conditions in the transverse direction. However, most existing works on quantum transport properties of graphene systems were carried out in, for example, the tight-binding Hamiltonian framework derived from the non-relativistic Schrödinger equation [8].

Another area in physics, where complete solutions of the Dirac equation is of paramount importance, is relativistic quantum nonlinear dynamics and chaos [12–15]. In particular, in the last three decades, quantum chaos, an interdisciplinary field focusing on the quantum manifestations of classical chaos, has received a great deal of attention in the physics community [16–20]. Indeed, the quantization of chaotic Hamiltonian systems and the signatures of classical chaos in quantum regimes are fundamental to physics and have direct applications in condensed matter physics, atomic

physics, nuclear physics, optics, acoustics, and quantum computing. Issues that have been pursued include energy-level statistics, statistical properties of wave functions, quantum chaotic scattering, electronic transport in quantum dots, localization, and the effect of magnetic field. However, existing works on quantum chaos are concerned almost exclusively with non-relativistic quantum mechanical systems described by the Schrödinger equation, where the dependence of the particle energy on the momentum is quadratic. A natural question is whether phenomena in non-relativistic quantum chaos can occur in *relativistic* quantum systems described by the Dirac equation, where the energy-momentum relation is linear. To address this question requires complete solutions of the Dirac equation in systems of arbitrary geometrical domains, especially those that allow for chaos in the classical limit.

Interest in graphene physics and devices calls for an efficient method to solve the Dirac equation in arbitrarily shaped domains. In chapter 2, I develop a numerical framework for obtaining complete eigen-solutions of massless fermions in general two-dimensional confining geometries. The key ingredients of our method are a proper handling of the boundary conditions and an efficient discretization scheme that casts the original equation in a matrix representation. The method is validated by (1) comparing the numerical solutions to analytic results for a geometrically simple confinement, and (2) verifying that the calculated energy level-spacing statistics of integrable and chaotic geometries agree with the known results. An application example, the calculation of the relativistic quantum tunneling rate of massless Dirac fermions between a pair of symmetric cavities, is presented. The method can be reduced to one and extended to three dimensions straightforwardly.

To understand the effect of chaos in the classical limit on quantum behaviors has been a field of interest and active pursuit [40]. This field, named quantum chaos, finds applications in many fields in physics such as condensed matter physics, atomic physics, nuclear physics, optics, and acoustics. Previous works on quantum chaos focused almost exclusively on non-relativistic quantum systems. A fundamental question is whether phenomena in non-relativistic quantum chaos can occur in *relativistic* quantum systems described by the Dirac equation. This field of relativistic quantum

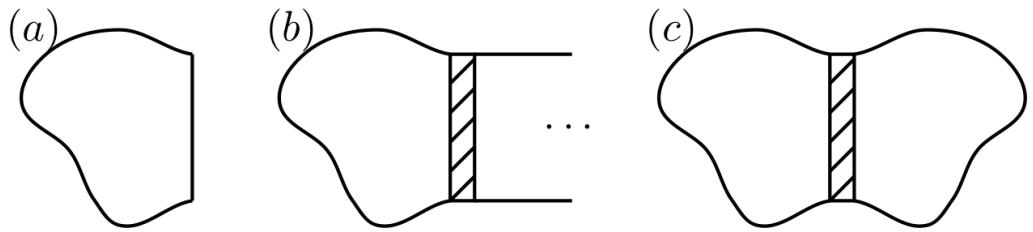

Fig. 1. (a) A closed quantum system of arbitrary shape in two dimensions, (b) the corresponding opened system, and (c) symmetric double-well used in resonant tunneling computations.

chaos [41] is of particular importance because of the relevance of the Dirac equation to graphene systems [42].

Recently, the remarkable phenomenon of chaos-regularized quantum tunneling has been uncovered [39], where classical chaos can suppress, significantly, the spread in the tunneling rate commonly seen in systems whose classical dynamics are regular. For example, consider the system in Fig.1, which consists of two symmetrical cavities connected by a one-dimensional potential barrier along the line of symmetry. When the classical dynamics in each cavity is integrable, for sufficiently large energy the tunneling rate can assume many values in a wide interval. Choosing the geometry of the cavity such that the classical dynamics become chaotic can greatly enhance and regularize quantum tunneling. Heuristically, this can be understood, as follows. When the potential barrier is infinite, each cavity is a closed system with an infinite set of eigenenergies and eigenstates. Many eigenstates are concentrated on classical periodic orbits, forming quantum scars [19]. For classically integrable cavity, some stable or marginally stable periodic orbits can persist when the potential barrier becomes finite so that each cavity system is effectively an open quantum system. Many surviving eigenstates correspond to classical periodic orbits whose trajectories do not encounter the potential barrier, generating extremely low tunneling rate even when the energy is comparable with or larger than the height of the potential barrier. The eigenstates corresponding to classical orbits that interact with the potential barrier, however, can lead to relatively strong tunneling. In a small energy

interval the quantum tunneling rate can thus spared over a wide range. However, when the classical dynamics is chaotic, isolated orbits that do not interact with the potential barrier are far less likely and, consequently, the states associated with low tunneling rates disappear, effectively suppressing the spread in the tunneling rate.

In chapter 3, I solve the Dirac equation in two spatial dimensions in the setting of resonant tunneling, where the system consists of two symmetric cavities connected by a finite potential barrier. The shape of the cavities can be chosen to yield both regular and chaotic dynamics in the classical limit. We find that certain pointer states about classical periodic orbits can exist, which suppress quantum tunneling, and the effect becomes less severe as the underlying classical dynamics in the cavity is chaotic, leading to regularization of tunneling dynamics even in the relativistic quantum regime. Similar phenomena have been observed in graphene. A physical theory is developed to explain the phenomenon based on the spectrum of complex eigenenergies of the non-Hermitian Hamiltonian describing the effectively open cavity system.

1.2. Chaotic scattering and complex branched wave structure in optical media

Metamaterials are artificially designed, engineered and fabricated structures possessing special (unconventional) properties that may not be readily available from natural materials. The last decade has witnessed an explosive growth of research on metamaterials in terms of both fundamental physics and potential applications. A primary research interest in metamaterials lies in their electromagnetic and optical properties. In this regard, negative refractive-index materials [48–53], also referred to as left-handed media, are one of the most extensively investigated types of metamaterials. First conceived theoretically by Veselago [54] in 1968, this extraordinary material with both negative effective permittivity and permeability exhibited a remarkable potential for a variety of applications. For example, superlens [55] made of this doubly negative metamaterials [56] can overcome the diffraction limit for conventional lenses and make subwavelength imaging possible. Another important application is invisible materials, where special cloak was realized in recent experiments for electromagnetic wave at optical frequencies [57, 58].

Quite recently, a link between optics in metamaterial and celestial mechanics was proposed [59], making it possible to investigate an array of gravitational phenomena predicted by Einstein's general relativity using optical analogies in the laboratory. For example, in general relativity, light can be trapped in some specific region in the space where a massive gravitational body exists, but such a trapping can be realized using metamaterials, generating an artificial "black hole" in the laboratory [59]. From this analogy, insights into the design of novel optical cavities and photon traps can be gained, with applications in areas such as micro-cavity lasers.

We first study the light-ray dynamics in a class of inhomogeneous, isotropic optical metamaterials in the presence of a periodic, external electromagnetic perturbation. The driving, analogous to, e.g., a third-body perturbation in classical mechanics, provides a way to break the stable periodic orbits of light ray in the corresponding static material, making complex dynamics possible. Indeed, Ref. [59] predicted the appearance of chaotic dynamics in this class of systems. We then study a class of time-independent metamaterial systems with overlapping or non-overlapping refractive-index distributions. For both time-dependent and time-independent systems, we find that transient chaotic dynamics (or chaotic scattering dynamics) [60–64] of light rays are common. This means that, two incident light rays differing only slightly in initial conditions can exit the metamaterial system in drastically different states [65]. Besides providing direct evidence for transient chaos, we shall establish through computations the dynamical nature of the process, hyperbolic or nonhyperbolic (to be explained below). Due to the analogy between metamaterial optics and gravitational physics, our results suggest that transient chaos can be quite common in gravitational systems obeying Einstein's general relativity. In addition, since ray dynamics can be experimentally observed and investigated in optical metamaterials, our results reinforce the idea that chaotic dynamics in relativistic gravitational systems can be visualized and studied in laboratory experiments [66].

In chapter 4, I investigate the dynamics of light rays in two classes of optical metamaterial systems: (1) time-dependent system with a volcano-shaped, inhomogeneous and isotropic refractive-index distribution, subject to external electromagnetic perturbations, and (2) time-independent sys-

tem that consists of three overlapping or non-overlapping refractive-index distributions. Utilizing a mechanical-optical analogy and coordinate transformation, the wave-propagation problem governed by the Maxwell's equations can be modeled by a set of ordinary differential equations for light rays. We find that transient chaotic dynamics, hyperbolic or nonhyperbolic, are common in optical metamaterial systems. Due to the analogy between light-ray dynamics in metamaterials and the motion of light and matter as described by general relativity, our results reinforce the recent idea that chaos in gravitational systems can be observed and studied in laboratory experiments.

When waves propagate through random media, extreme events and complex structures such as rogue waves and branched, fractal-like wave patterns can form. There has been a substantial amount of interest in complex wave phenomena due to their occurrences in a host of physical systems. For example, in oceanography, rogue waves are an issue of great concern. In the past fifteen years or so there had been experimental and theoretical studies of rogue waves arising from long-range acoustic wave propagation through ocean's sound channel [77, 78], as well as large-scale experiments on directional ocean waves to probe the physical and dynamical origin of these extreme waves [79]. Extreme events and complex wave patterns have also been identified in many other physical situations such as light propagation in doped fibers [80, 81], acoustic turbulence in superfluid helium [82], resonances in nonlinear optical cavities [83], linear light-wave propagation in multi-mode glass fiber [84], and electronic transport in semiconductor two-dimensional electron gas (2DEG) systems [85]. Despite previous efforts, an accepted, relatively complete understanding of complex extreme waves at the level of fundamental physics is still lacking.

To illustrate the extent to which complex branched wave patterns are presently understood, we choose electronic transport in 2DEG systems as an example. In Ref. [85], electron flows from a quantum point contact were reported to exhibit a striking, branched or fractal-like behavior with highly non-uniform amplitude distribution in the physical space. The observed separate, narrow strands of greatly enhanced electron wave intensities were argued to be caused by random background potentials and quantum coherent phase interference among the electron wave functions.

Subsequently a theory was proposed [86] to predict the statistical distribution of the intensities of branched electron flows in the presence of weak, correlated Gaussian random potentials.

The generic origin of wave branching behavior is a matter of active debate [87]. A tacit assumption in most previous investigations is nonlinearity in the underlying medium. In particular, it had been believed that the existence of many uncorrelated, spatially randomly distributed wave elements is key to the occurrence of these exotic wave patterns. These elements can be, for example, solitons in nonlinear systems. However, quite recently, it was demonstrated experimentally in a microwave system [88] and in a multi-mode optical fiber [84] that branched wave patterns can occur even in the absence of nonlinearity. In fact, in the latter case, granularity of light speckles at the fiber exit and inhomogeneity in the spatial clustering of the speckle patterns are speculated to be the two ingredients that trigger complex wave patterns. These recent works thus demonstrate that nonlinearity is not absolutely essential for the emergence of these extreme waves. *A question of significant theoretical and experimental interest concerns thus about a minimal, physical model that can generate robust branched wave patterns*, so that their generic and physical origin may be elucidated. The main task of chapter 5 is to answer this question. A related issue concerns the statistical properties of these waves. In this regard, a general observation in all contexts where branched wave structures arise is the non-Gaussian statistics of the wave amplitude. Typically there is a long tail in the probability density function, which characterizes the extreme intensity of the waves. An essential requirement for a valid minimal model of branched wave patterns is thus that is should generate the universally observed long-tail distribution in the wave intensity.

1.3. Complex pattern formation in cyclic competition games

The coexistence of competing species in spatially extended ecosystems is key to biodiversity in nature. Understanding the dynamical mechanisms of and identifying factors promoting coexistence are a fundamental problem of continuous interest not only in evolutionary biology but also in nonlinear science [113–117]. Species coexistence has been investigated in a variety of systems, such as in microbes, [118–121], ant colonies [122, 123], parasites and hosts [124, 125], predator-prey

dynamics [126] and interference competition [127] etc. Existing models are mostly *macroscopic* in the sense that they focus on the dynamical evolutions of species populations [113, 114]. For any given species, its population is merely a coarse-grained average quantity that is not capable of reflecting the possibly complicated interactions among its own individuals and with those from other competing species. To gain a deeper and more comprehensive understanding of the dynamics of coexistence, *microscopic* models that describe the competitions among species at the level of individual interactions of the stochastic nature are necessary [115, 128–136]. In this regard, a class of microscopic models is proposed in chapter 6 based on cyclic, non-hierarchical competitions [e.g., as described by the classical "rock-paper-scissor" (RPS) game] on spatial lattices. Such competitions have been observed in several real ecosystems [120, 137–139]. The fundamental importance of RPS-like competition in sustaining biodiversity for limited resources in nature has been emphasized through experimental investigations [118, 119]. Theoretical and computational studies of the RPS model have revealed that, due to the presence of stochasticity, local interaction and dispersal can ensure the coexistence of species. More recently, individual mobility as a common feature in ecosystems has been incorporated into spatial games to better model competition dynamics of species and the organization of spatial patterns [130, 132–134].

In chapter 6, I propose a model for cyclically competing species on continuous space and investigate the effect of the interplay between the interaction range and mobility on coexistence. A transition from coexistence to extinction is uncovered with a strikingly non-monotonic behavior in the coexistence probability. About the minimum in the probability, switches between spiral and plane-wave patterns arise. A strong mobility can either promote or hamper coexistence, depending on the radius of the interaction range. These phenomena are absent in any lattice-based model, and we demonstrate that they can be explained in terms of nonlinear partial differential equations. Our continuous-space model is more physical and we expect the findings to generate experimental interest.

Species coexistence is essential to biodiversity, and it is a fundamental issue in ecological sci-

ence. Ecosystems consisting of three species subject to cyclic competitions have become a paradigm to address the coexistence problem. Early works based on population models provided useful insights into the dynamics of coexistence at a macroscopic level, but these models often tended to predict that coexistence is structurally unstable. To resolve this dilemma, microscopic models based on stochastic interactions at the individual level have been introduced. In this regard, the classical game of rock-paper-scissors (RPS) has been used to mimic cyclic competitions at the microscopic level of interactions. In fact, the past several years have witnessed a growing interest in this direction, addressing the role of factors in coexistence such as species mobility, virus spreading, and intraspecific competitions, etc. Inspired by these works, here we address the species coexistence problem in the framework of RPS competitions on spatially extended ecosystems from a global standpoint, i.e., we are interested in how the basins of coexistence and extinction depend on factors such as species mobility, interaction range, and rate of intraspecific competition. An obstacle that needs to be overcome is to find a suitable representation of the phase space to compute the basin structure in a meaningful way, as the underlying dynamical system is spatiotemporal and extremely high dimensional. We find the simplex representation S_2 in the three-dimensional space of population densities effective. We then use two characterizing methods, namely, final state and the inverse of the convergence time toward the final state, to map out the structures of the coexistence and extinction basins by using direct simulations of the microscopic interaction model. In particular, basins calculated according to the final states can identify boundaries among coexistence and extinction basins, whereas the points within a basin are indistinguishable. The basins depicted by the convergence time to reach the final state provide additional information about the intrinsic difference inside each extinction basin. The coexistence basin can emerge at the central area of S_2 surrounded by three rotationally entangled extinction basins. The convergence time within each extinction basin increases universally along the spiral toward the center point. The area of coexistence basin in the phase space measures the robustness of species coexistence and the convergence time within extinction basins quantifies the degree of extinction. To provide credence for the validity of the basin structures, we derive theoret-

ical models based on partial differential equations, which yields results that agree well with those from microscopic models. Our results provide insights into the species coexistence problem at a global level.

Microscopic models based on evolutionary games on spatially extended scales have recently been developed to address the fundamental issue of species coexistence. In this pursuit almost all existing works focus on the relevant dynamical behaviors originated from a single but physically reasonable initial condition. To gain comprehensive and global insights into the dynamics of coexistence, In chapter 7, I explore the basins of coexistence and extinction and investigate how they evolve as a basic parameter of the system is varied. My model is cyclic competitions among three species as described by the classical rock-paper-scissors games, and I consider both discrete lattice and continuous space, incorporating species mobility and intraspecific competitions. The results reveal that, for all cases considered, a basin of coexistence always emerges and persists in a substantial part of the parameter space, indicating that coexistence is a robust phenomenon. Factors such as intraspecific competition can in fact promote coexistence by facilitating the emergence of the coexistence basin. In addition, I find that the extinction basins can exhibit quite complex structures in terms of the convergence time toward the final state for different initial conditions. I have also developed models based on partial differential equations, which yield basin structures that are in good agreement with those from microscopic stochastic simulations. To understand the origin and emergence of the observed complicated basin structures is challenging at the present, due to the extremely high dimensional nature of the underlying dynamical system.

In chapter 8, we investigate intra- and inter-patch migrations in stochastic games of cyclic competition and find that, in contrast to the understanding in the current literature, the interplay between the migrations at the local and global scales can lead to robust species coexistence in the remarkable form of target-wave patterns in the absence of any external control. Even in a single-species system, target waves can arise from rare mutations, leading to an outbreak of biodiversity. A surprising phenomenon is that the target waves in different patches can exhibit synchronization and time-delayed

synchronization, the latter potentially enabling prediction of future evolutionary dynamics. A physical theory is derived to explain these phenomena.

Formation of self-organized pattern is a fundamental aspect of physical and biological systems out of equilibrium. Spiral waves are quite common in a variety of excitable systems and population dynamics, such as Belousov-Zhabotinsky reaction [142, 143], the cardiac tissue [144], inset population dynamics [145] and cyclically competing populations with mobility [189]. Spiral waves play significant roles in the dynamics of excitable systems, e.g., in heart disease, such as arrhythmia and fibrillation, which lead to death [144, 190, 191]. Spiral waves are important in population dynamics as well. In particular, biodiversity in cyclically competing populations with stochastic interactions can be maintained and stabilized by entangled moving spiral waves [189, 192]. The coexistence of two or more spirals may form multi-armed spiral and antispiral waves. These interesting joint spirals have been extensively studied in excitable systems theoretically and experimentally [193–198]. However, in the population dynamics in the presence stochastic processes, multi-armed spirals and multi-pairs antispirals among entangled spirals is rarely studied and far from being well understood. There are two important open questions associated with these waves: Are they able to be generated through stochastic interactions and how is their stability? One of the purpose of this thesis is to address these questions in the framework of cyclic competing games with mobile individuals.

In chapter 9, we study the formation of multi-armed spirals and multi-pairs antispirals in spatial rock-paper-scissors game with mobile individuals. We discover a set of seed distributions of species, which is able to produce multi-armed spirals and multi-pairs antispirals with arbitrary numbers of arms and pairs based on stochastic processes. The joint spiral waves are also predicted by a theoretical model based on partial differential equations associated with specific initial conditions. The spatial entropy of patterns is introduced to differentiate the multi-armed spirals and multi-pairs antispirals. For the given mobility, the spatial entropy of multi-armed spirals is higher than that of single armed spirals. The stability of the waves are explored with respect to individual mobility. Particularly, we find that both two armed spirals and one pair antispirals transform to the single armed

spirals. Both multi-armed spirals and multi-pairs antispirals are relatively stable for intermediate mobility. The joint spirals with lower numbers of arms and pairs are relatively more stable than those with higher numbers of arms and pairs. Our work provides quantitative insight into pattern formation through stochastic interactions in the absence of excitable media.

2 . COMPLETE SOLUTION OF DIRAC EQUATIONS FOR MASSLESS FERMIONS IN CONFINED GEOMETRIES

2.1. Previous work

In this chapter, we develop a general and efficient method to solve the Dirac equation for massless fermions in a two-dimensional closed system. An obstacle to obtaining a complete solution of the Dirac equation, which includes both eigenvalues and eigenfunctions, is the proper handling of the boundary conditions. We shall develop an efficient discretization scheme and a physically meaningful approach to treating the boundary conditions, based on converting the Dirac equation into a set of matrix equations. In our method, the physical symmetries of the system are well preserved. To validate our method, we consider three types of representative geometric confinements, which include domains that generate both integrable and chaotic motions in the classical limit, and calculate the complete spectrum of eigenvalues and the associated eigenvector set. In particular, in the case of integrable geometries for which analytic predictions of the eigenvalues and eigenvectors are available, we obtain excellent agreement between the numerical and analytic results. For more general geometries including classically chaotic systems, the properties of our calculated eigenvalue spectrum, such as the energy level-spacing statistics, agree well with the known results for different symmetry classes [21]. In fact, our method is capable of finding eigenstates of Dirac fermions under arbitrarily electrical potential profiles. Our matrix formulation can be applied directly to one-dimensional systems and, by a straightforward extension of the Dirac spinor to four components and by a proper revision in the discretization and boundary constraints, the method can be extended to solving the Dirac equation in three dimensions as well. To demonstrate our method in applications, we investigate the relativistic quantum tunneling dynamics of a Dirac fermion between two symmetric cavities connected by a potential barrier, and observe the phenomenon of chaos-regularized tunneling that has been identified recently in non-relativistic quantum tunneling systems.

We remark that in the earlier work of Berry and Mondragon on neutrino billiards [21], eigenvalues were computed using the boundary-integral method. However, the Green's function utilized in

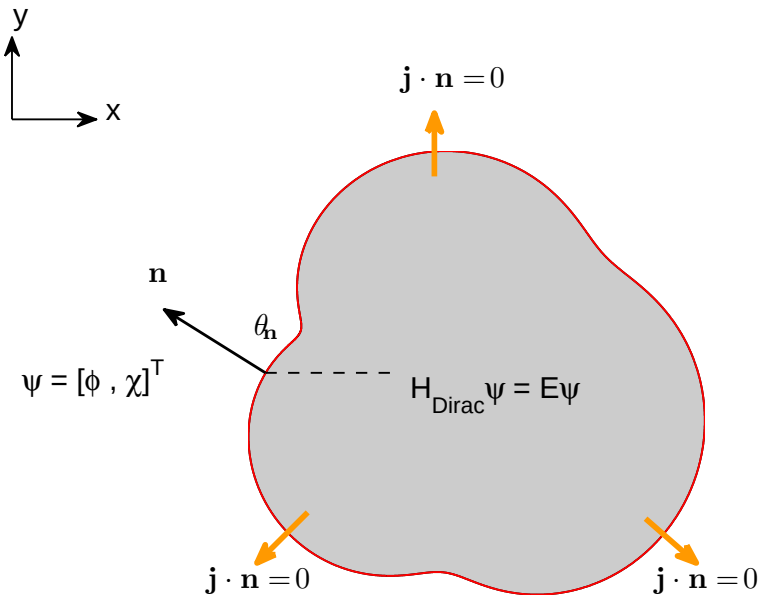

Fig. 2. Schematic picture of closed Dirac system with arbitrary geometry and zero outgoing flux boundary condition $\mathbf{j}\cdot\mathbf{n}=0$. This boundary condition is equivalent to $\chi/\phi = i\exp(i\theta_{\mathbf{n}})$ with $\theta_{\mathbf{n}}$ being the argument of the surface normal $\mathbf{n}$.

the boundary integral is the one associated with open systems. They showed that the higher-order correction terms of Green's function due to boundaries do not contribute to the energy spectrum. However, for a complete solution set, where not only eigenvalues but also eigenfunctions are of interest, it is necessary to obtain the Green's function for the closed system, which is not feasible for arbitrary shaped domains and not necessarily smooth boundaries under the framework of boundary integrals. Consequently, one still needs an appropriate discretization scheme to solve the closed-system Dirac equation, either by numerically evaluating the Green's function or by solving the eigenvalue problem directly.

In Sec. 2.2, we detail our method for obtaining complete solutions of the Dirac equation in two-dimensional closed systems, focusing on proper handling of boundary conditions and on the articulation of discretization scheme. In Sec. 2.3, we test our algorithm using an idealized domain for which analytic solutions of the Dirac equation can be written down, and obtain further validation by calculating the energy level-spacing statistics for three different types of closed geometries. In Sec. 2.4, we briefly demonstrate the power of our method in addressing the problem of chaos regularized relativistic quantum tunneling. In Sec. 2.6, we present conclusions and a discussion.

2.2. Method

2.2.1. Background

A subtle and challenging issue in solving the Dirac equation is the proper treatment of the boundary conditions [22]. Due to the finite domain and the first-order nature of the Dirac equation, a naive treatment of the boundary conditions will lead to trivial or even non-physical solutions. One example is the relativistic particle in a one-dimensional box. By simply letting the whole spinor go to zero at the walls of the box, only a trivial (all-zero) solution of the eigenfunctions are obtained. To overcome this difficulty, many self-adjoint extensions of the boundary conditions in both Dirac and Weyl representations have been proposed [23]. For example, in $(1+1)$ dimensions, one family of boundary conditions is to force either the large or the small component of the spinor to be zero at the walls of the box. Some variances of these boundary conditions also exist [24, 25], e.g., by as-

suming that the large component vanishes at one boundary and the small component vanishes at the other, or by assuming that both components differ by factors $\pm i$. Some of these boundary conditions also preserve the physical symmetries, such as P and CPT symmetries. However, these types of conditions are not all appropriate in $(2+1)$ dimensions, because the walls of the box are impenetrable. Physically, this means that the relativistic current $\mathbf{j} = c\psi^\dagger \boldsymbol{\sigma}\psi$ normal to the boundaries must vanish. The vanishing current condition has been used in the bag model [26–28] of quark confinement, which solves the Dirac equation with a Lorentz scalar potential. It was assumed that the rest mass of the particle $m(\mathbf{r})$ is a position-dependent parameter. One could then solve this infinite-well problem for the particle of varying mass, letting the mass go to infinity outside the box in order to take into account the Klein paradox. A similar method was adopted by Berry et al. [21] for studying random-matrix theory and energy level-spacing statistics for relativistic neutrino billiards.

We consider a two-dimensional closed system within which a relativistic, massless fermion is confined, as shown schematically in Fig. 2. The system is governed by the Dirac equation in $(2+1)$ dimensions:

$$i\hbar\partial_t\psi(t) = \hat{H}\psi(t), \tag{2.1}$$

where the general form of the Hamiltonian is given by

$$\hat{H} = c(\boldsymbol{\alpha}\cdot\mathbf{p}) + \beta mc^2, \tag{2.2}$$

and ψ is a two-component Dirac spinor. Assuming stationary solution $\psi(t) = \psi\exp(-iEt/\hbar)$, we obtain the steady-state Dirac equation

$$\hat{H}\psi = E\psi. \tag{2.3}$$

In two dimensions, $\boldsymbol{\alpha} = \boldsymbol{\sigma} = (\sigma_x, \sigma_y)$ and $\beta = \sigma_z$ are choices satisfying all anticommutation/commutation relations of Dirac/Lorentz algebra [29].

To obtain the proper boundary conditions, two methods can be employed: we either replace the $mc^2\sigma_z$ term with a potential $U(\mathbf{r})\sigma_z$ in the Hamiltonian and let $U(\mathbf{r})$ go to infinity outside the domain, or use the vanishing current condition $\mathbf{j}\cdot\mathbf{n} = 0$, where $\mathbf{n}$ is the boundary surface normal,

as shown in Fig. 2. The latter method yields

$$\mathrm{Re}(e^{i\theta_{\mathbf{n}}}\phi/\chi) = 0,$$

where ϕ and χ are the components of the Dirac spinor, $\psi = (\phi, \chi)^T$, and $\theta_{\mathbf{n}}$ is the argument of the surface normal $\boldsymbol{n}$. The boundary condition can then be written as [21]

$$\chi/\phi = i\exp(i\theta_{\mathbf{n}}). \tag{2.4}$$

When an external electric potential energy V is present, E is replaced by $E - V$. For massless fermion, we can then write the Dirac equation as

$$\left[v(\boldsymbol{\sigma}\cdot\mathbf{p}) + V\right]\psi = E\psi, \tag{2.5}$$

where we replace c by v for more generalized cases or, for instance, in graphene, by the Fermi velocity $v_F \sim 10^6$m/s.

2.2.2. Discretization scheme and elimination of fermion doubling effect

To numerically solve the Dirac equation, it is necessary to develop an efficient and physically meaningful discretization scheme. Unlike the standard discretization of second order differential equations such as the Schrödinger equation, discretization for the massless Dirac equation is a much harder problem. An important issue is that the usual finite difference methods fail because they introduce the so-called *fermion-doubling* effect, even for open or periodic boundaries. Fermion doubling is also a problem for lattice QCD computations [26–28].

To explain the fermion-doubling phenomenon, we take the one-dimensional Dirac equation

$$i\hbar\partial_t\psi = i\hbar v\sigma_x\partial_x\psi, \tag{2.6}$$

as an example. Using the usual lattice grid $x = n\Delta$ and the central difference approximation

$$\partial_x\psi(n) = (\psi(n+1) - \psi(n-1))/(2\Delta),$$

the Fourier transformed equation is

$$i\hbar\partial_t\tilde{\psi} = [\hbar v\sigma_x \sin(p_x\Delta)/\Delta]\tilde{\psi} = \tilde{H}\tilde{\psi}. \tag{2.7}$$

We see that the energy is given by

$$|E| = |\hbar v \sigma_x \sin(p_x \Delta)/\Delta|. \tag{2.8}$$

In the first Brillouin zone (BZ) where $p \in [-\pi/\Delta, \pi/\Delta]$, the energy expression means that there are more than one point satisfying the linear energy-momentum relation, implying fermion doubling. Previous works [30, 31] provided a solution to eliminate this effect.

Figure 3 shows our proposed discretization method, which consists of two steps. Firstly, we discretize the whole domain using a two-dimensional lattice. The Dirac spinors are evaluated at lattice points (m, n). Secondly, we evaluate the Dirac equation at the center of each unit cell, $(m + \frac{1}{2}, n + \frac{1}{2})$. In the Hamiltonian, the derivatives of the Dirac spinor are approximated by

$$\begin{aligned} \partial_x \psi_{m+\frac{1}{2},n+\frac{1}{2}} &= \frac{\psi_{m+1,n+1} + \psi_{m+1,n} - \psi_{m,n+1} - \psi_{m,n}}{2\Delta}, \\ \partial_y \psi_{m+\frac{1}{2},n+\frac{1}{2}} &= \frac{\psi_{m+1,n+1} + \psi_{m,n+1} - \psi_{m+1,n} - \psi_{m,n}}{2\Delta}. \end{aligned}$$

The spinors at the unit cell centers are approximated as the average of the four spinor values from the neighboring lattice points, i.e.,

$$\psi_{m+\frac{1}{2},n+\frac{1}{2}} = \frac{1}{4}(\psi_{m+1,n+1} + \psi_{m,n+1} + \psi_{m+1,n} + \psi_{m,n}). \tag{2.9}$$

Using this numerical scheme, the phenomenon of fermion doubling can be eliminated.

2.2.3. Incorporation of boundary conditions and matrix representation of Dirac equation

It is worth noting that in closed systems, such as rectangles and billiards, the number of Dirac equations at unit cell centers (denoted as M) is less than the number of total spinors at lattice points (denoted as N), i.e., $M < N$. The difference needs to be accounted for by the boundary conditions. To explain how boundary conditions are incorporated in our solution procedure, we write the Dirac equation in matrix form. In particular, we let $\Psi = (\psi_1, \psi_2, \ldots, \psi_N)^T$ be the column vector containing all spinor values on the lattice, where Ψ actually has $2N$ components. Let $D_x/(2\Delta)$, $D_y/(2\Delta)$ and $A/4$ be the matrix form of the operators ∂_x, ∂_y, and the averaging operator in Eq. (2.9), respectively. These matrices are all of dimension $M \times N$. In matrix form, Eq. (2.5) becomes

$$\left[-\frac{2i\hbar v}{\Delta} \left(D_x \otimes \sigma_x + D_y \otimes \sigma_y \right) + VA \otimes \mathbf{1}_2 \right] \Psi = EA \otimes \mathbf{1}_2 \Psi. \tag{2.10}$$

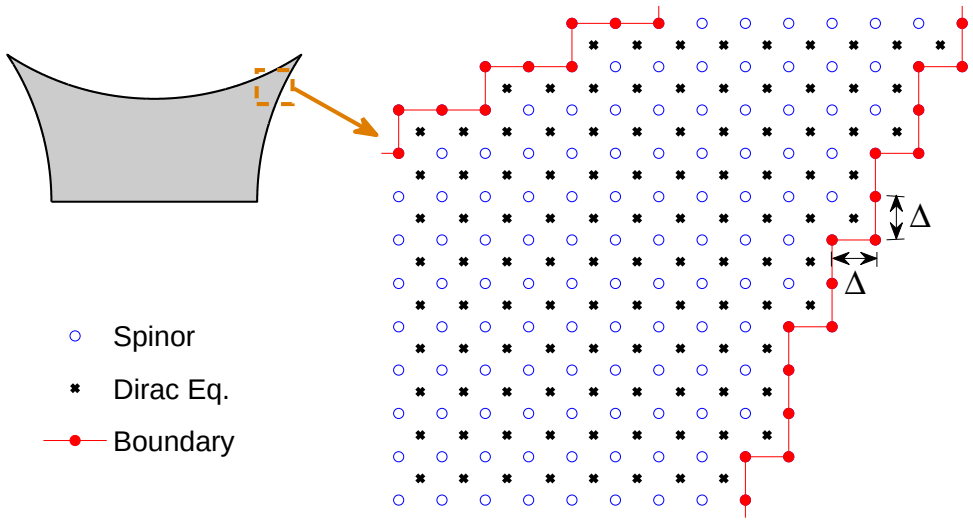

Fig. 3. Proposed discretization scheme to eliminate any fermion-doubling effect. A two-dimensional domain, which exhibits chaos in the classical limit, is illustrated to show the discretized lattice. Red filled circles and blue open circles spaced by Δ represent the boundary and inner lattice points, respectively, where the Dirac spinor values are sampled. The actual Dirac equations are evaluated at black cross points, the centers of unit cells.

Since we have $2M$ equations, we need $2N - 2M$ boundary conditions that can be written as

$$B\Psi = 0, \tag{2.11}$$

where B is a $(2N - 2M) \times 2N$ matrix. Realizing that not all spinors are independent, we permute the spinor vector by

$$\Psi' = P\Psi = \begin{bmatrix} \Psi_D \\ \\ \Psi_B \end{bmatrix}, \tag{2.12}$$

where Ψ_D are independent Dirac spinors and Ψ_B are spinors at the boundary that can be expressed by other components in Ψ_D, and P is an orthogonal permutation matrix. Defining

$$H' = \left[-\frac{2i\hbar v}{\Delta} \left(D_x \otimes \sigma_x + D_y \otimes \sigma_y \right) + VA \otimes \mathbf{1}_2 \right] P^T,$$

$A' = A \otimes \mathbf{1}_2 P^T$, and $B' = BP^T$, we obtain

$$H'\Psi' = EA'\Psi', \qquad B'\Psi' = 0. \tag{2.13}$$

Utilizing the boundary conditions, Ψ_B can be explicitly expressed by Ψ_D. Let $B' = [B_1, B_2]$, where B_2 is a square matrix. We write

$$\Psi_B = -B_2^{-1} B_1 \Psi_D.$$

Letting $H' = [H_1, H_2]$ and $A' = [A_1, A_2]$, where H_2 and A_2 are square matrices, and substituting Ψ_B into $H'\Psi' = EA'\Psi'$, we finally obtain

$$H_D \Psi_D = E\Psi_D, \tag{2.14}$$

where

$$H_D = (A_1 - A_2 B_2^{-1} B_1)^{-1} (H_1 - H_2 B_2^{-1} B_1).$$

One issue with the newly defined Hamiltonian H_D is that it is not Hermitian in general. This non-hermitian characteristic is caused by the finite domain and lattice approximation of the original smooth boundaries. However, the eigenvalues of H_D are all real. To overcome this difficulty, we introduce

$$H = (H_D + H_D^\dagger)/2, \tag{2.15}$$

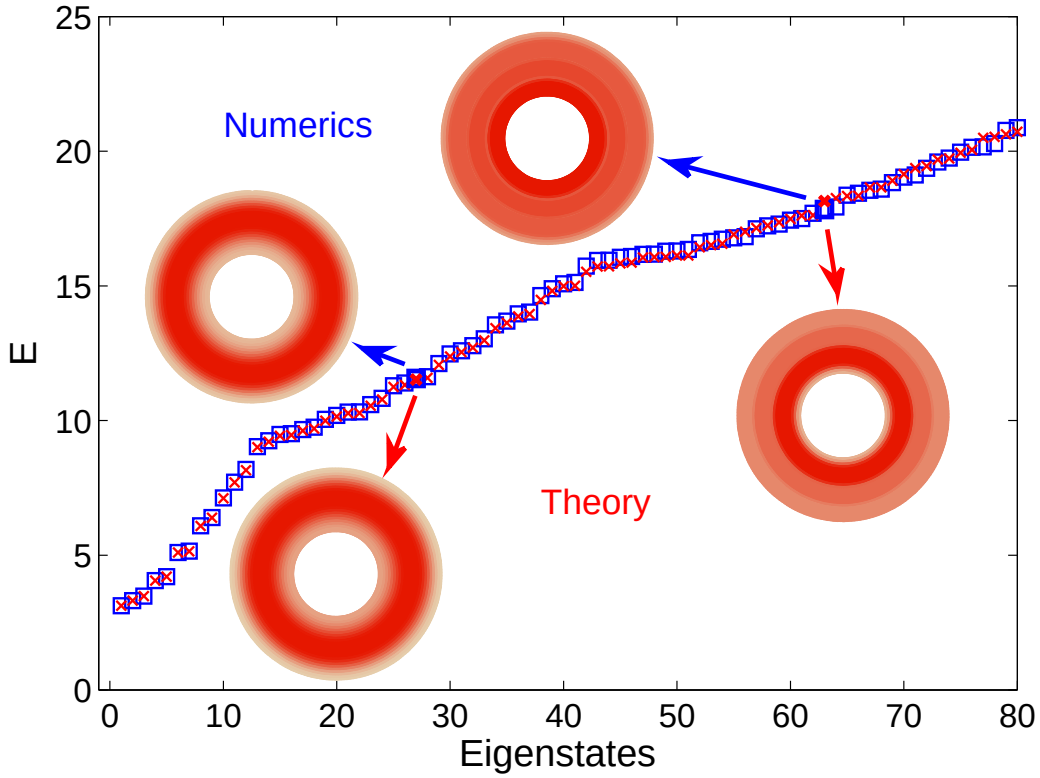

Fig. 4. Comparison of numerical and analytical results of eigenenergies and eigenstates for the ring cavity. The lowest 80 positive eigenenergy levels and two examples of the eigenstates from numerics (blue square, or above the energy spectrum) and theory (red cross, or below the energy spectrum) are compared. The convenient unit convention $\hbar = v = 1$ was used in the numerical computation.

the Hamiltonian for a new physical system, where the difficulties associated with non-smooth boundaries due to lattice discretization are overcome. For small values of Δ, the energy spectra of the two systems are identical, and the eigenstates of the two systems are very close to each other especially at low energies, where the discretized system mimics the Dirac equation perfectly.

2.3. Results

2.3.1. Solutions in analyzable geometry

To validate our method, we first choose a simple geometry, for which the eigenvalues and eigenstates of the Dirac equation can be calculated analytically, and compare directly the numerical results

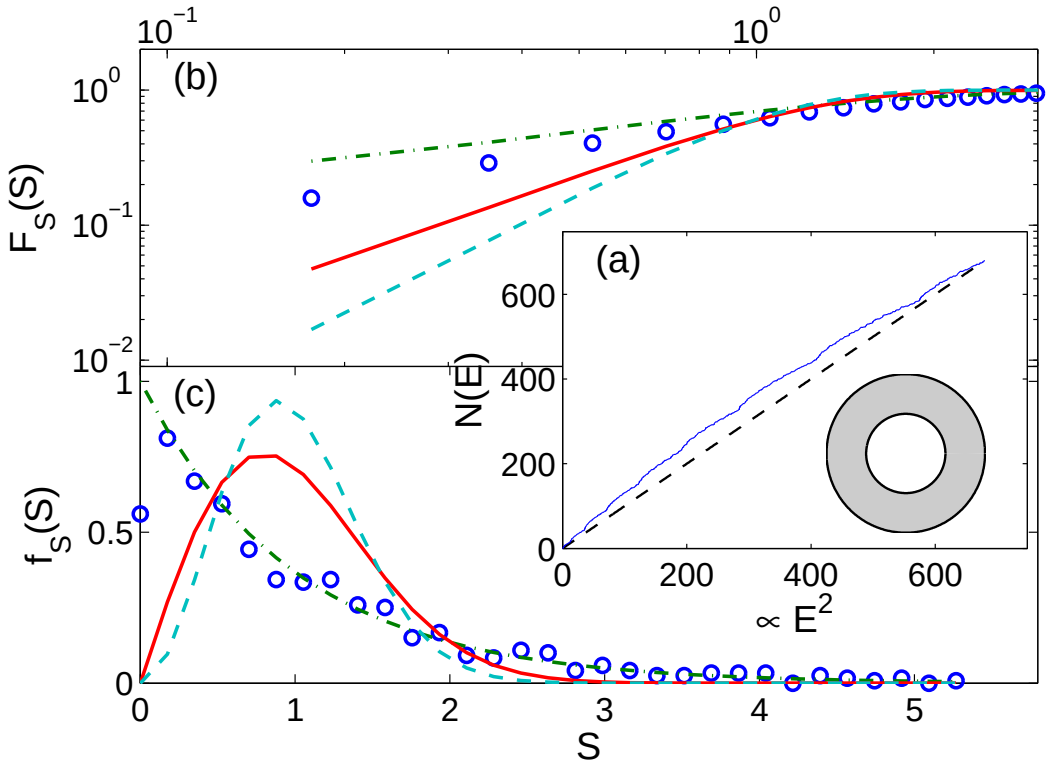

Fig. 5. Level-spacing statistics for eigenenergies of the ring domain.Inset (a) shows spectral staircase $N(E)$ as a function of E^2. The dashed lines represent the linear relationship between $N(E)$ and E^2. Horizontal axes are linear mappings of E^2 to the range $[0, N]$, where N is the total number of eigenstates. Panel (b) is the cumulative distribution of thenearest-neighbor spacing$F_S(S)$as a function of spectral spacings $S_n = E_{n+1}^2 - E_n^2$. Panel (c) represents the density distribution $f_S(S)$ of $F_S(S)$ in (b). In both middle and bottom row, green dash-dotted, red solid, and cyan dashed lines denote theoretical distribution curves for Poisson, GOE, and GUE statistics, respectively. The results of the ring are obtained through a polar coordinate version of our numerical method to preserve the perfect circular symmetry.

with the analytic ones. Even for very simple geometry, due to the entanglement of the two Cartesian coordinates in the Dirac equation, the problem is not analytically solvable except for certain special types of boundary conditions for which the variables can be separated. One particular class of solvable systems are those with circular boundaries, whose general solutions are

$$\psi_n = N_n e^{in\theta} \begin{bmatrix} Z_n(kr) \\ \text{sgn}(E-V) i e^{i\theta} Z_{n+1}(kr) \end{bmatrix}, \; n = 0, \pm 1, \ldots \tag{2.16}$$

where $k = |E - V| / (\hbar v)$, and N_n is a normalization constant. For rings, $Z_n(x)$, the radial function of the spinor components, is a linear combination of the first- and second-kind Bessel functions, $J_n(x)$ and $Y_n(x)$. However, for circles, $Z_n(x) = J_n(x)$ because of the divergence of $Y_n(x)$ at the origin. For our analytical calculation, we considere a ring with inner and outer radii of $R_1 = 0.5$ and $R_2 = 1$, respectively. The electrical potential is set to zero, $V = 0$, for simplicity. Analytically, one can arrive at the above general solution with potential having a staircase-like profile in the radial direction but constant in the angular direction. However, one can solve the case with arbitrary potential numerically, even when the ring is not full. Setting the potential to be zero, we can find the energy levels for each angular mode through the inner and outer boundary conditions, $E_m^{(n)} = \hbar v k_m^{(n)}$, where $k_m^{(n)}$ is obtained by solving

$$\frac{\left[J_{n+1}(kR_1) + J_n(kR_1)\right]\left[Y_{n+1}(kR_2) - Y_n(kR_2)\right]}{\left[J_{n+1}(kR_2) - J_n(kR_2)\right]\left[Y_{n+1}(kR_1) + Y_n(kR_1)\right]} = 1. \tag{2.17}$$

The eigenstates can be calculated after the normalization constants $N_m^{(n)}$ are computed. Results of these analytical calculations as compared with those from numerics are shown in Fig. 4. Almost no discrepancy can be observed. As indirect evidence, the analytical energy spectrum gives statistical results (to be discussed below) identical to numerical results, as shown in Figs. 5-7 (first column) and in Fig. 8.

2.3.2. Relativistic quantum energy-level statistics and eigenstates in two-dimensional geometries

We validate our proposed numerical method by calculating the energy level-spacing statistics [13, 14, 18, 32–38] for relativistic quantum billiards. Figures 5-7 show results of level-spacing statis-

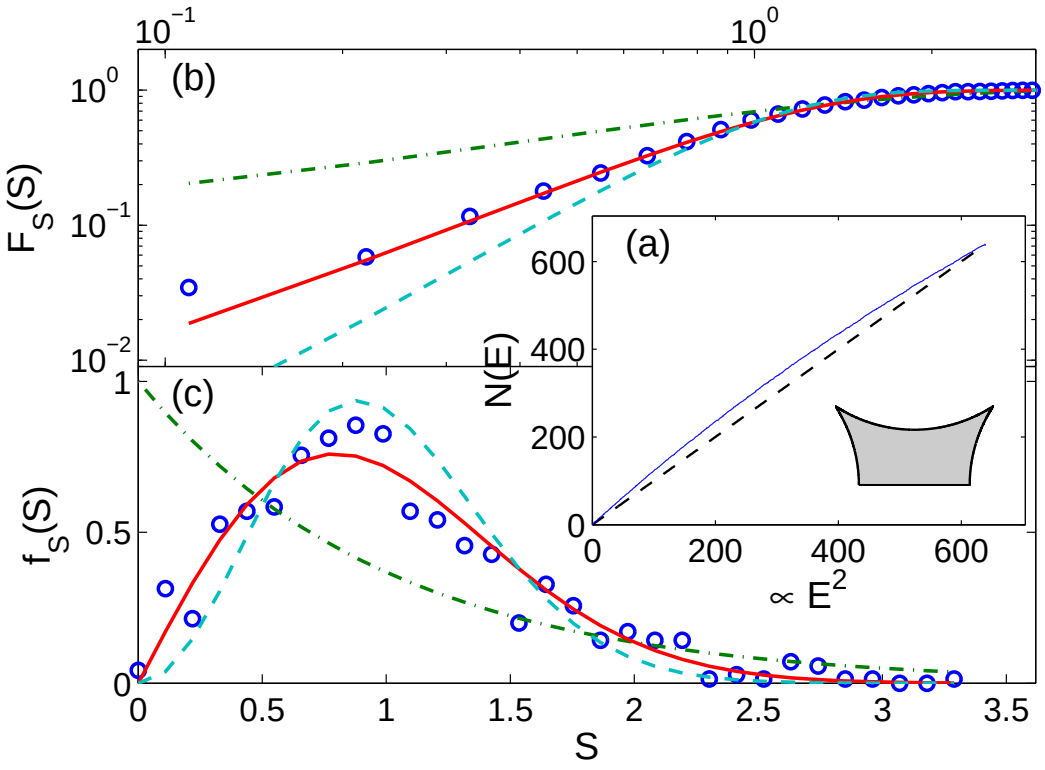

Fig. 6. Level-spacing statistics for eigenenergies of the chaotic bow-tie domain. Figure legends are the same as in Fig. 5.

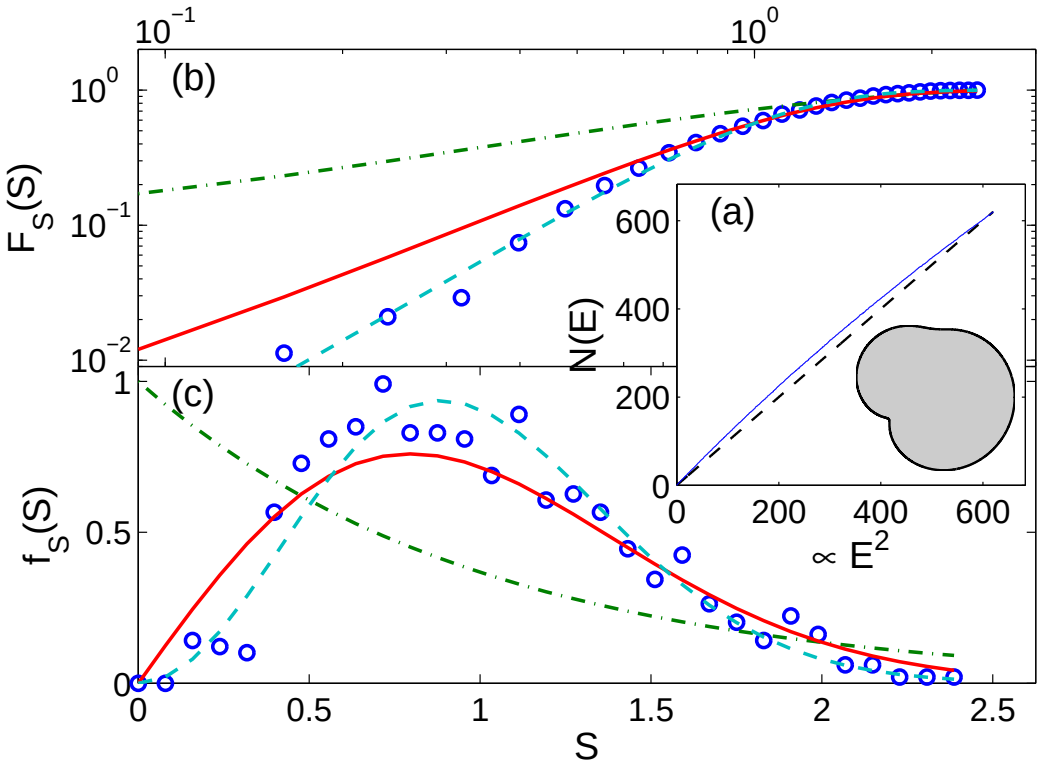

Fig. 7. Level-spacing statistics for eigenenergies of the chaotic Africa domain. Figure legends are the same as in Fig. 5.

tics for three representative geometric domains: a relativistically integrable ring, a chaotic billiard with one geometric symmetry about the central vertical line, and the so-called *Africa* shaped billiard [21] without any geometrical symmetry, respectively. In relativistic quantum systems, we have a linear relation between energy level and the square root of spectral staircase $N(E)$, $E \propto \sqrt{N(E)}$, where $N(E)$ denotes the number of eigenstates between zero and energy E. To confirm that the numerical results preserve the physical properties of the system, we investigate the nearest-neighbor fluctuations of the energy spectra. For relativistically integrable quantum systems, for example, circles or rings governed by the Dirac equation, the level spacing statistics should be Poisson. For non-integrable systems, if the system preserves geometric symmetry of some kind (such as a stadium billiard), the nearest energy-level spacing statistics fall between those of Poisson and GOE (Gaussian orthogonal ensemble). In the fully chaotic case, e.g., the chaotic billiard in Figs. 6 and 7, the GOE statistics apply. However, if no geometric symmetry is present in the system, e.g., the African billiard, the level-spacing statistics should be those given by GUE (Gaussian unitary ensemble) according to the result of Berry and Mondragon [21].

Besides the linear statistics, we also consider an informative least-squares statistic of the energy spectra, the spectral rigidity of the third type, Δ_3 [13, 14, 32–38], as a function of energy range L, where $[0, L]$ denotes the range of energy levels under consideration. Figure 8 shows the Δ_3 statistics for the three domains we considered, as well as theoretical expectation curves for Poisson, GOE, and GUE statistics, where an excellent agreement is obtained for all cases.

Representative eigenstates for non-integrable billiards are shown in Fig. 9 for the bow-tie chaotic billiard and in Fig. 10 for the chaotic "Africa" billiard. These are in fact examples of relativistic quantum scars from the Dirac equation. We note that quantum scars have been observed in graphene systems [12] in the regime where the energy-momentum relation is linear, but they are still solutions of the Schrödinger equation obtained by the tight-binding method. The scars shown in Figs. 9 and 10 are obtained by solving the Dirac equation which, to our knowledge, have not been reported previously.

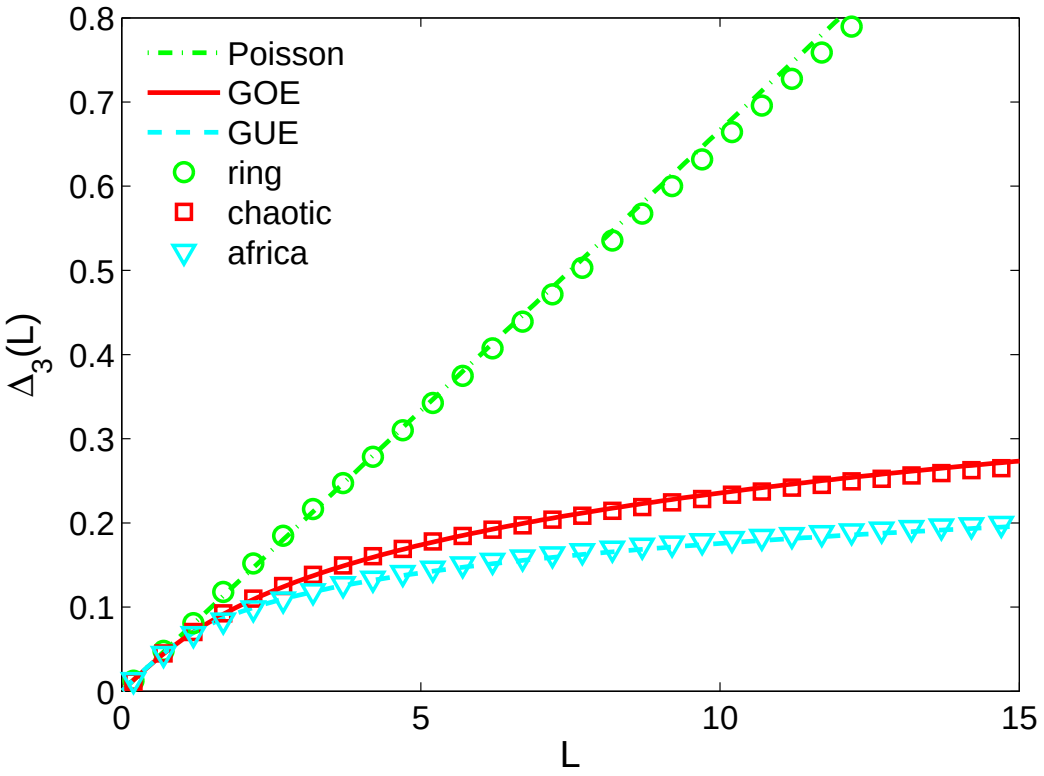

Fig. 8. Spectral rigidity $\Delta_3(L)$ for the three domains in Figs. 5 - 7. Lines with different styles denote theoretical expectations of spectral rigidity for the respective statistics.

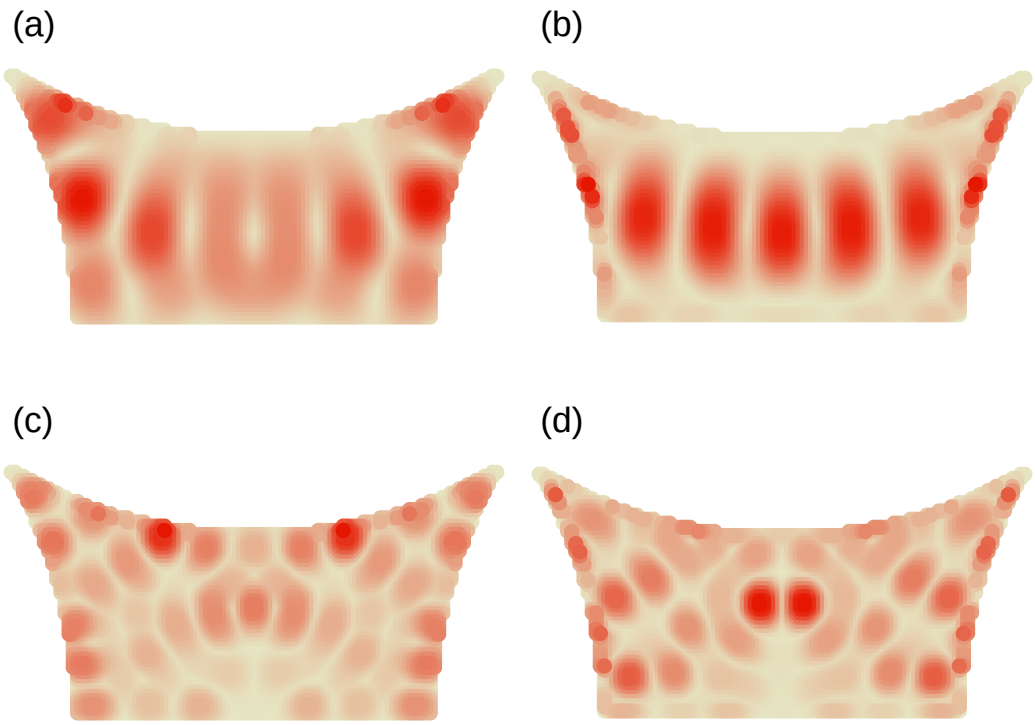

Fig. 9. Examples of eigenstates of the Dirac equation for a bow-tie chaotic billiard. The maximum height (vertical distance from tip to base) is set to 1, and the distance between two tips is 2. Panels (a) and (b) are for $E = 12.6756$, and (c) and (d) are for $E = 23.1622$. Panels (a) and (c) show the ϕ components, while (b) and (d) show the χ components.

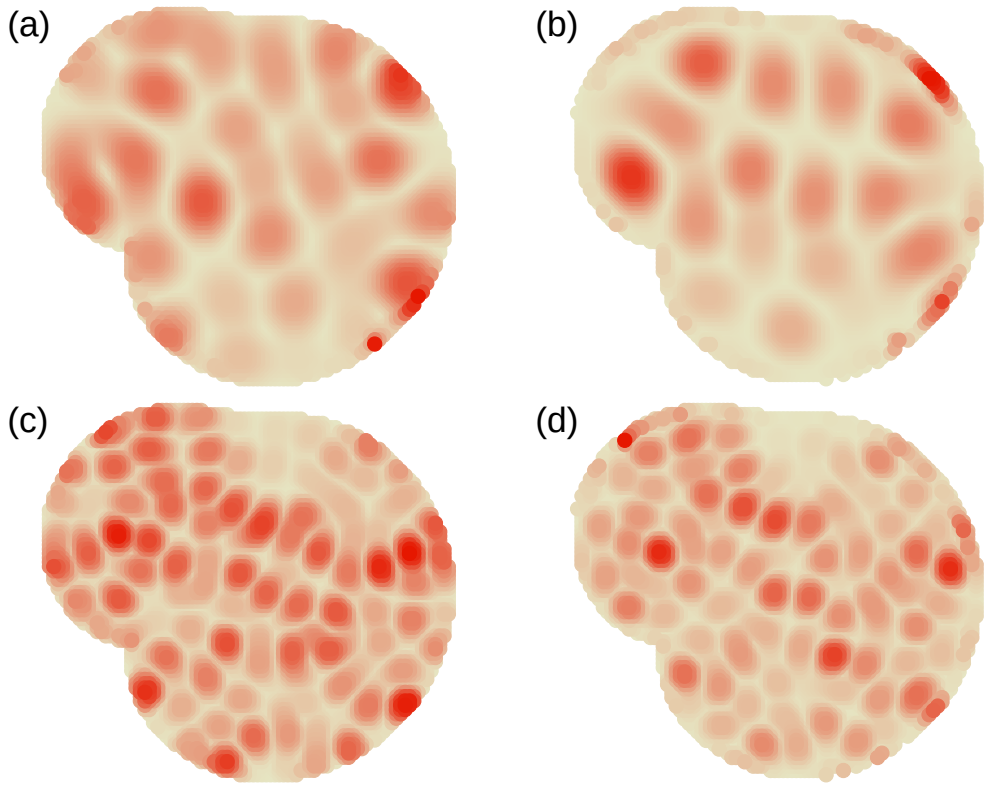

Fig. 10. Examples of eigenstates of the Dirac equation for the chaotic “Africa” billiard. The domain is confined within a rectangular box $x \in [-0.99, 1.35]$ and $y \in [-1.22, 0.92]$. Panels (a) and (b) are for $E = 9.8060$, and (c) and (d) are for $E = 19.4444$. Panels (a) and (c) show the ϕ components, while (b) and (d) show the χ components.

2.4. Application: relativistic quantum tunneling

To demonstrate the power of our method for solving the Dirac equation in arbitrary two-dimensional closed systems, we address the problem of relativistic quantum tunneling in classically chaotic systems. A recent work considered the setting of two symmetric cavities (potential wells) connected by a finite potential barrier in the plane, through which a particle can tunnel [39]. It was showed that for non-relativistic quantum systems governed by the Schrödinger equation, classical chaos can regularize quantum tunneling rate. In particular, for integrable systems, when the particle energy is sufficiently large, the quantum tunneling rate can have values spread in a range that increases with the energy. However, when the system is classically chaotic, the spread in the tunneling rate can be reduced significantly. Equipped with our method for solving the Dirac equation, we set out to test whether the same phenomenon can occur in the relativistic quantum regime.

For non-relativistic quantum tunneling, due to the geometric symmetry in the double-well systems, the eigenstates are either symmetric or antisymmetric about the central barrier. A symmetric/antisymmetric pair means that, on one side of the double well, the eigenfunctions completely overlap, while on the other side, the eigenfunctions differ by the factor of -1. In non-relativistic quantum mechanics, tunneling rate is thus defined as the energy splitting ΔE between the symmetric and antisymmetric eigenstate pairs. This can be understood as follows. Suppose we have symmetric and antisymmetric eigenstate pairs ψ_S and ψ_A. Define a new state $\psi(t) = \psi_S e^{-iE_S t/\hbar} + \psi_A e^{-iE_A t/\hbar}$. At time $t = 0$, $\psi(0) = \psi_S + \psi_A$ describes a state in which the particle can be found only on one side of the double-well. We let this state evolve and find that at time $t_0 = \pi\hbar/\Delta E$, where $\Delta E = |E_S - E_A|$, $\psi(t_0) \propto \psi_S - \psi_A$, meaning that the particle has tunneled to the other side of the well. However, for Dirac fermion systems, there is no clear criterion to separate symmetric/antisymmetric pairs from other mixed states. Paraphrasing it, a symmetric state cannot necessarily be paired with a corresponding antisymmetric state. Moreover, for massless Dirac fermions, because of the violation of the time-reversal symmetry [21], the reflection symmetry is also broken. As a result, the eigenstate itself does not have to be symmetric or antisymmetric.

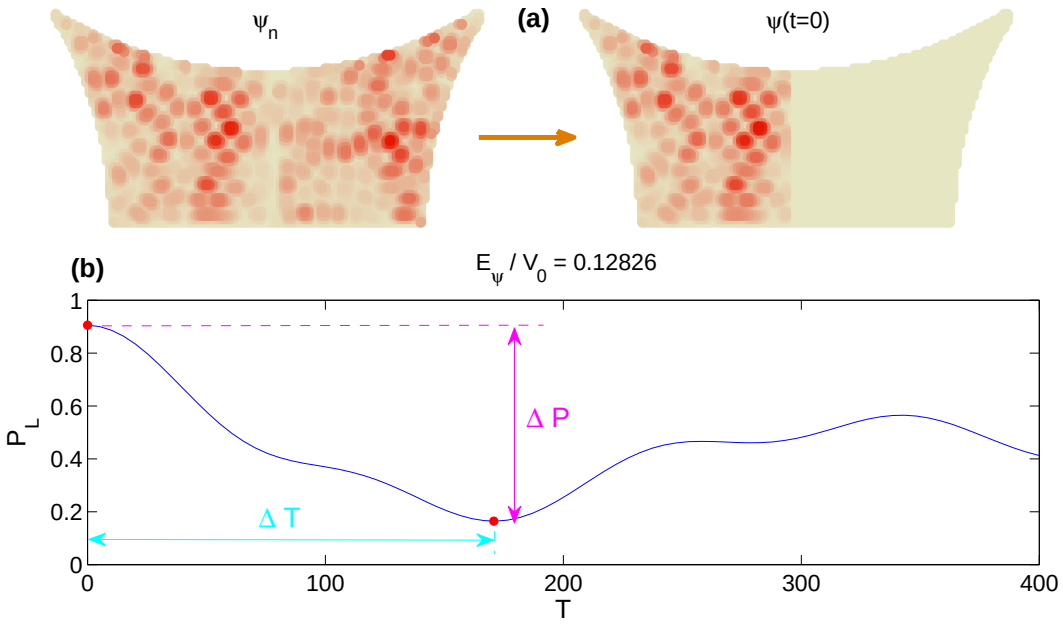

Fig. 11. Generalized method for obtaining the tunneling rate. (a) Pick any eigenstate ψ_n. Renormalizing the wave function localized to the left of the potential barrier yields a new wave function $\psi(t=0)$. (b) Time evolution of probability for particle to be observed in the left part of the billiard, $P_L(t)$. Tunneling rate is defined as $R \equiv \pi \Delta P / \Delta T$.

In such situations, a new and more general definition of the tunneling rate in relativistic quantum systems is needed.

Our idea is the following. For arbitrary symmetric double-well system, we pick a random linear combination of eigenstates denoted as $\psi = \sum_n a_n \psi_n(\boldsymbol{r})$, where it is not necessary to run n over all eigenstates. This is feasible because our method allows the eigenstates to be solved for any closed geometry. Figure 11(a) shows an example where only one eigenstate is selected. We then keep only the left side of ψ, and set the right side and the barrier part of ψ to zero. We re-normalize this state and denote it as $\bar{\psi} = \sum_n \bar{a}_n \psi_n^L(\boldsymbol{r})$, where $\bar{a}_n$'s are the renormalized coefficients, and $\psi_n^L(\boldsymbol{r}) = \psi_n(\boldsymbol{r})$ for $\boldsymbol{r}$ at the left well, and $\psi_n^L(\boldsymbol{r}) = 0$ otherwise. Next, we let this state $\bar{\psi}$ evolve with time. It is necessary to express it in terms of linear combination of all eigenstates, $\bar{\psi} = \sum_m b_m \psi_m(\boldsymbol{r})$,

where the summing index m runs through all eigenstates. The coefficients b_m can then be calculated as

$$\begin{aligned} b_m &= \int_D \psi_m^* \bar{\psi} d\boldsymbol{r} = \int_L \psi_m^* \sum_n \bar{a}_n \psi_n^L d\boldsymbol{r} \\ &= \sum_n \bar{a}_n \int_L \psi_m^* \psi_n d\boldsymbol{r}, \end{aligned} \tag{2.18}$$

where D and L are the integration domains of the whole double well and of the left well, respectively. The time evolution of the state $\bar{\psi}$ is then given by $\bar{\psi}(t) = \sum_m b_m \psi_m e^{-iE_m t/\hbar}$. Because the particle state is initially confined within the left well, to characterize the tunneling process of this state, we calculate the probability that the particle is found in the left well with respect to time, $P_L(t) = \int_L |\bar{\psi}(t)|^2 d\boldsymbol{r}$. An example of the probability evolution is plotted in Fig. 11(b). The tunneling rate R is found at the time when $P_L(t)$ reaches minimum for the first time, i.e., $R \equiv \pi \Delta P / \Delta T$, as shown in Fig. 11(b). This definition is more general because, for non-relativistic quantum tunneling, where symmetric/antisymmetric eigenstate pairs exist, it reduces to ΔE.

Using our definition of the tunneling rate and employing the method for efficiently solving the Dirac equation developed in this chapter, we have verified that classical chaos can indeed regularize tunneling even for relativistic quantum systems.

2.5. Boundary conditions in graphene systems

Because of the high relevance of our method for solving the Dirac equation to experimental graphene systems, it is insightful to examine such systems with the kind of boundary conditions treated in Ref. [22]. As explored there, graphene lattice terminated in an arbitrary orientation usually possesses complicated boundary conditions, as can be seen from Eqs. (3.8) and (3.9) in Ref. [22]. In the summation form in Eq. (3.10), only the terms with $|\lambda_\pm| = 1$ form the four-component spinor in the Dirac equation, and the rest of them describe how the boundary modes decay from the edge. By such an analysis, the authors of Ref. [22] found that, for most orientations, the boundary condition should be zigzag-like. The staggered boundary potential in graphene mimics the infinite-mass confinement for Dirac particles, leading to a boundary condition that sits on an extreme point

opposite from the zigzag one. Consequently, the boundary conditions for confined Dirac particles and for the terminated graphene lattice are somewhat different.

From the point of view of symmetry, graphene system in the absence of magnetic field preserves the time-reversal symmetry, which is the starting point of Ref. [22]. The staggered lattice potential breaks the pseudo-spin symmetry of the sublattice, which resembles the symplectic symmetry of a spin system but preserves the true time-reversal symmetry. A unique characteristic of graphene systems is the occurrence of pseudo-spins. However, the Dirac equation describes the behavior of a single relativistic quantum particle, for which the phenomenon of pseudo-spins does not exist. As a result, for relativistic quantum systems described by the Dirac equation, the mass term (not necessarily infinite) breaks the true time reversal symmetry. This difference can be revealed, for example, by the statistics of the energy-level spacing in the corresponding classes of classically chaotic billiards, where the graphene billiard exhibits GOE (Gaussian Orthogonal Ensemble) statistics, while the Dirac billiard has the GUE (Gaussian Unitary Ensemble) statistics.

Reference [22] studies the boundary conditions of a continuous Dirac-like equation for the pseudo-particles of graphene systems, as imposed by the discrete-lattice structure of graphene. A complete description of graphene incorporating boundaries needs four-component spinors due to the presence of a pseudo-spin for A and B atoms in a unit cell, and also a pseudo-spin for the two non-degenerate valleys. The method we have developed to solve the 2D Dirac equation with two-component spinors thus describes the relativistic quantum motion of the graphene pseudo-particles in the absence of inter-valley scatterings. Since the boundaries of graphene flakes will in general mix quantum dynamics associated with the two valleys, the two-component Dirac equation cannot provide a complete description of such situations. Our point is that, for the first time in the literature we have developed an efficient method to solve the Dirac equation in an arbitrary shaped billiard, and the method can be used to provide deep understanding of phenomena such as scars and pointer states in quantum dots made of materials with linear energy-momentum dispersion relation such as graphene. While in general systems described by the Dirac equation are not identical to

experimentally widely investigated quantum-dot systems, locally the dispersion relation is the same. Our method can thus be used to probe such quantum-dot systems and gain deeper insights through investigation of the Dirac billiards for the low energy states, despite the differences in the boundary conditions between the Dirac and experimental graphene systems.

2.6. Conclusion

To obtain solutions of the Dirac equation in arbitrary two-dimensional geometries, which include complete sets of both eigenvalues and eigenfunctions, is essential for studying and exploring relativistic quantum behaviors and phenomena in graphene systems. To our knowledge, prior to the present work, no such methods existed in the literature. We have developed a general method to address this outstanding issue. The innovative aspects of our method are a proper incorporation of the boundary conditions and an efficient discretization scheme to represent the Dirac equation in matrix form. For a classically integrable system in a circular domain for which analytic solutions of the Dirac equation are available, our method yields results that are in excellent agreement with the analytic ones. For general geometries, including those whose dynamics are chaotic in the classical limit, our method yields the correct statistics of the solutions, such as the energy level-spacing distributions.

We anticipate that our method or its variants will become a basic tool to address a host of problems arising in the study of relativistic quantum mechanics in condensed matter devices. As a concrete example, we have outlined how the method can be applied in the context of resonant tunneling to calculate the relativistic quantum tunneling rate of massless Dirac fermions between a pair of symmetric but in an arbitrary domain.

We have focused our effort on planar system mainly because graphene is two-dimensional. However, our method can be reduced straightforwardly to one-dimensional systems. Extension to three-dimensional systems is also feasible. Particularly, in three dimensions the Dirac spinor consists of at least four components and the Dirac tensors $\boldsymbol{\alpha}$ and β should be modified accordingly. One can still use the zero outgoing current flux and a similar lattice discretization, where now the Dirac equation

needs to be evaluated at the centers of unit lattice cubes.

3 . EFFECT OF CHAOS ON RELATIVISTIC QUANTUM TUNNELING

In this chapter, we address the question of whether chaos can regularize tunneling in relativistic quantum systems. To be concrete, we study the motion of massless Dirac fermions in the setting of resonant tunneling to facilitate comparison with the non-relativistic quantum case. To solve the Dirac equation in a confined geometry is extremely challenging, particularly due to the difficulty to incorporate zero-flux boundary conditions. We overcome this difficulty by developing a numerical scheme based on constructing a physically meaningful, Hermitian Hamiltonian. Our extensive computations reveal unequivocally the existence of surviving eigenstates that lead to extremely low tunneling rates. As for the non-relativistic quantum case, making the cavities classically chaotic can greatly regularize the quantum tunneling dynamics. To explore the practical implications, we consider resonant tunneling devices made entirely of graphene [42], and calculate the tunneling rate for different energy values. We obtain qualitatively similar results as for massless Dirac fermions. One unique feature for both the Dirac and graphene systems, which finds no counterpart in non-relativistic quantum tunneling devices, is the high tunneling rate in the regime where the particle energy is smaller than the height of the potential barrier. This is a manifestation of the Klein-tunneling phenomenon [5, 43, 44]. To explain the numerical findings, we develop a theory based on the concept of self energies and the complex energy spectrum of the non-Hermitian Hamiltonian for the "open" cavity.

3.1. Generalizing tunneling rates for the relativistic particles

Consider the situation where a relativistic Dirac fermion is confined within a two-dimensional double-well system in which two symmetric cavities are weakly coupled by an electrical-potential barrier placed in between. The system is governed by the Dirac equation $i\hbar\partial_t\psi(t) = \hat{H}\psi(t)$, where the general form of Hamiltonian is given by $\hat{H} = c(\boldsymbol{\alpha}\cdot\boldsymbol{p}) + \beta mc^2$, and ψ is a two-component Dirac spinor. Assuming stationary solution $\psi(t) = \psi\exp(-iEt/\hbar)$, we obtain the steady-state Dirac equation $\hat{H}\psi = E\psi$. In two dimensions, $\boldsymbol{\alpha} = \boldsymbol{\sigma} = (\sigma_x, \sigma_y)$ and $\beta = \sigma_z$ are choices satisfying all anticommutation/commutation relations in Dirac/Lorentz algebra [29]. There are two

major challenges in numerically solving the Dirac equation: (i) a proper treatment of boundary conditions and (ii) a efficient and physically meaningful discretization scheme. Firstly, for boundary conditions, we can either replace the $mc^2\sigma_z$ term by a potential $U(\boldsymbol{r})\sigma_z$ in the Hamiltonian and let $U(\boldsymbol{r})$ go to infinity outside the domain, or use the vanishing current condition $\boldsymbol{j}\cdot\boldsymbol{n}=0$, where $\boldsymbol{n}$ is the boundary surface normal. We obtain $\mathrm{Re}(e^{i\theta}\phi/\chi)=0$, where ϕ and χ are the components of Dirac spinor, $\psi=(\phi,\chi)^T$, and θ is the argument of the surface normal $\boldsymbol{n}$. It was demonstrated [21] that the condition is $\chi/\phi=i\exp(i\theta)$. When an external potential V is present, such as the barrier in our tunneling problem, E is replaced by $E-V$. Secondly, for a massless fermion, we can write the Dirac equation as

$$\left[v(\boldsymbol{\sigma}\cdot\boldsymbol{p})+V\right]\psi=E\psi, \tag{3.1}$$

where we have replaced c by v for more generalize cases (e.g., in graphene, the Fermi velocity is $v_F\sim 10^6$m/s). Regarding discretization, the difficulty issue is fermion doubling [30, 31]. We have developed and validated an efficient discretization scheme, incorporating proper boundary conditions, for solving the Dirac equation in arbitrary geometrical confinements in $(2+1)$ dimensions. Different from the k-p models (with different flavors of 6-band or 8-band Luttinger-Kohn model), a simple lattice grid is used to discretize the two-dimensional closed space. However, in solving massless Dirac fermion systems, a necessary ingredient designed to eliminate the fermion doubling problem is to evaluate the Dirac equations and the Dirac spinors at two different sets of square lattice points. Specifically, if one evaluates the Dirac spinors at locations (i,j), the Dirac equations have to be evaluated at $(i+1/2,j+1/2)$, otherwise one ends up with two fermions in the first Brillouin zone, which conflicts with the original single fermion Dirac equation.

For non-relativistic quantum tunneling, due to geometric symmetry in the double-well systems, the eigenstates are either symmetric or antisymmetric about the central barrier. In this case, the tunneling rate is simply proportional to the energy splitting ΔE between the pairing symmetric and antisymmetric eigenstates [39]. However, for relativistic quantum tunneling, only in one spatial dimension can the symmetric and antisymmetric eigenstate pairs be defined. In fact, for both Dirac

fermion in $(2+1)$ dimensions and graphene systems, the symmetric and antisymmetric eigenstates are not necessarily in pair. A more general, physically meaningful definition of the tunneling rate is thus needed. Our approach is the following. For an arbitrary symmetric double-well system, first we choose a random linear combination of eigenstates, denoted as $\psi = \sum_n a_n \psi_n(\boldsymbol{r})$. We then set values of ψ on the right side and barrier region to be zero and renormalize it. The new state is denoted as $\bar{\psi} = \sum_n \bar{a}_n \psi_n^L(\boldsymbol{r})$, where $\bar{a}_n$'s are the renormalized coefficients, $\psi_n^L(\boldsymbol{r}) = \psi_n(\boldsymbol{r})$ for $\boldsymbol{r}$ in the left well, and $\psi_n^L(\boldsymbol{r}) = 0$ otherwise. Next, we let this state $\bar{\psi}$ evolve with time and express it in terms of the linear combination of all eigenstates: $\bar{\psi} = \sum_m b_m \psi_m(\boldsymbol{r})$, where the index m runs through all eigenstates. The coefficient b_m can be calculated as $b_m = \int_D \psi_m^* \bar{\psi} d\boldsymbol{r} = \int_L \psi_m^* \sum_n \bar{a}_n \psi_n^L d\boldsymbol{r} = \sum_n \bar{a}_n \int_L \psi_m^* \psi_n d\boldsymbol{r}$, where D and L denote the integration domains of the whole double well and the left well, respectively. The time evolution of the state $\bar{\psi}$ is then given by $\bar{\psi}(t) = \sum_m b_m \psi_m e^{-iE_m t/\hbar}$. Because the particle state is initially confined within the left well, to characterize the tunneling process of this state, we calculate the probability that the particle may be found in the left well with respect to time, $P_L(t) = \int_L |\bar{\psi}(t)|^2 d\boldsymbol{r}$. The tunneling rate R can be determined when $P_L(t)$ reaches minimum for the first time, i.e., $R \equiv \pi \Delta P / \Delta T$, where ΔP is the probability difference between the initial value and the first minimum of $P_L(t)$, and ΔT is the time it takes to reach the minimum. This definition is general because for non-relativistic quantum tunneling where symmetric/antisymmetric eigenstate pairs do exist, it reduces to ΔE.

3.2. Numerical evidence

We now present numerical evidence for the effect of chaos on relativistic quantum tunneling. Figure 12 shows the generalized tunneling rate R versus the normalized energy E/V_0 for massless Dirac fermion in the double-well barrier system for two types of geometry: one classically integrable and another chaotic. For the integrable geometry, we observe the existence of states with extremely low tunneling rates, as indicated by the arrow in Fig. 12(a). These correspond to states localized nearly entirely in the left or right side of the potential barrier, which "survive" the tunneling process between the two sides, as indicated by the accompanying pattern of local density of states (LDS). We

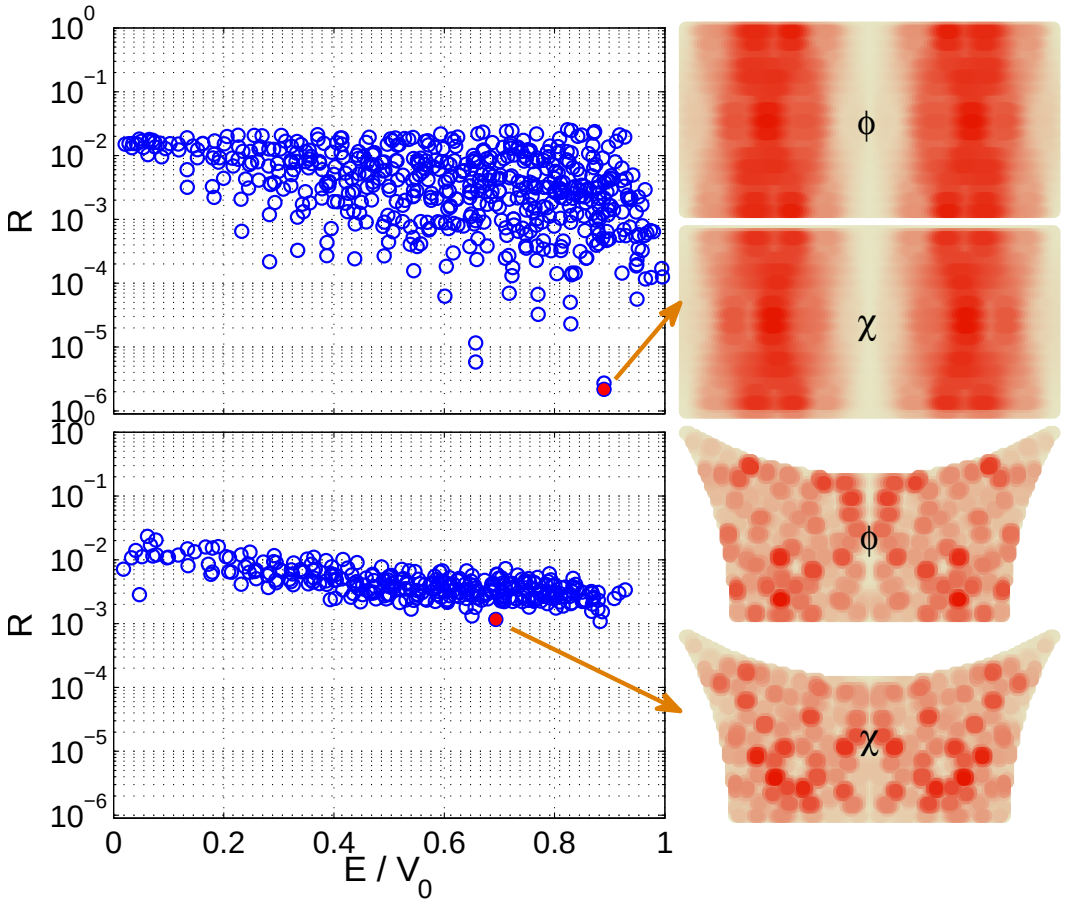

Fig. 12. Tunneling rates and LDS patterns for massless Dirac fermion in integrable and chaotic double-well systems, where ϕ and χ are two components of the Dirac spinor. A unit system $\hbar = c = 1$ has been used in our calculations. The barrier height V_0 is about 60 under such unit system. For the rectangle double-well, the width and the height are set to 2 and 1, respectively. The bow-tie chaotic shape is obtained by cutting the rectangle with three arcs such that the cut parts are all 0.3 measured on both sides of the baseline and central vertical line of the rectangle. The theoretical ratio of the left well width to the barrier width should be 24:1 for the rectangle, however, this ratio may vary after discretization.

note that, in non-relativistic quantum transport, these are effectively quantum pointer states [45, 46]. In relativistic quantum systems, we observe that both components of the underlying Dirac spinor exhibit a heavy concentration of the probability in orbits along which particles travel vertically back and forth on either side, parallel to the barrier. For the chaotic geometry, while signatures of pointer states can still be found, they are weak as compared with those in the integrable counterpart, as shown in Fig. 12(b) and the accompanying LDS pattern. Analogous behaviors occur when the entire cavity is made of graphene, as shown in Fig. 13. Thus, in both Dirac fermion and graphene systems, we observe that classical chaos can greatly suppress the spread in the quantum tunneling rate, as in non-relativistic quantum systems [39].

A common phenomenon between Dirac-fermion and graphene tunneling systems is that, for small energies, pointer states are far less likely than in non-relativistic quantum systems. Consequently, in both systems, the tunneling rate can be quite large even in the small energy regime, as shown in Figs. 12 and 13. This is the direct consequence of Klein tunneling [5, 43, 44], which finds no counterpart in non-relativistic quantum mechanics where the tunneling rate tends to zero as the energy is decreased to zero [39]. Although both systems show almost identical relativistic behaviors at low energies, and both prove chaos regularization to be universal phenomenon across quantum systems, one should not confuse one system with the other. The difference between the two systems lies in the number of massless (quasi-)particles. It is clear that the system described by Eq.(3.1) contain a single massless Dirac fermion. On the other hand, for a graphene system in the low energy limit, the two electron states at different atoms (commonly called A and B) in a unit cell can be think of as the two states of a massless quasi-particle's pseudo-spin. However, there are actually two of these massless particles close to the two distinct Dirac points. In presence of a spatially short-range potential, the coupling between the two Dirac points becomes apparent.

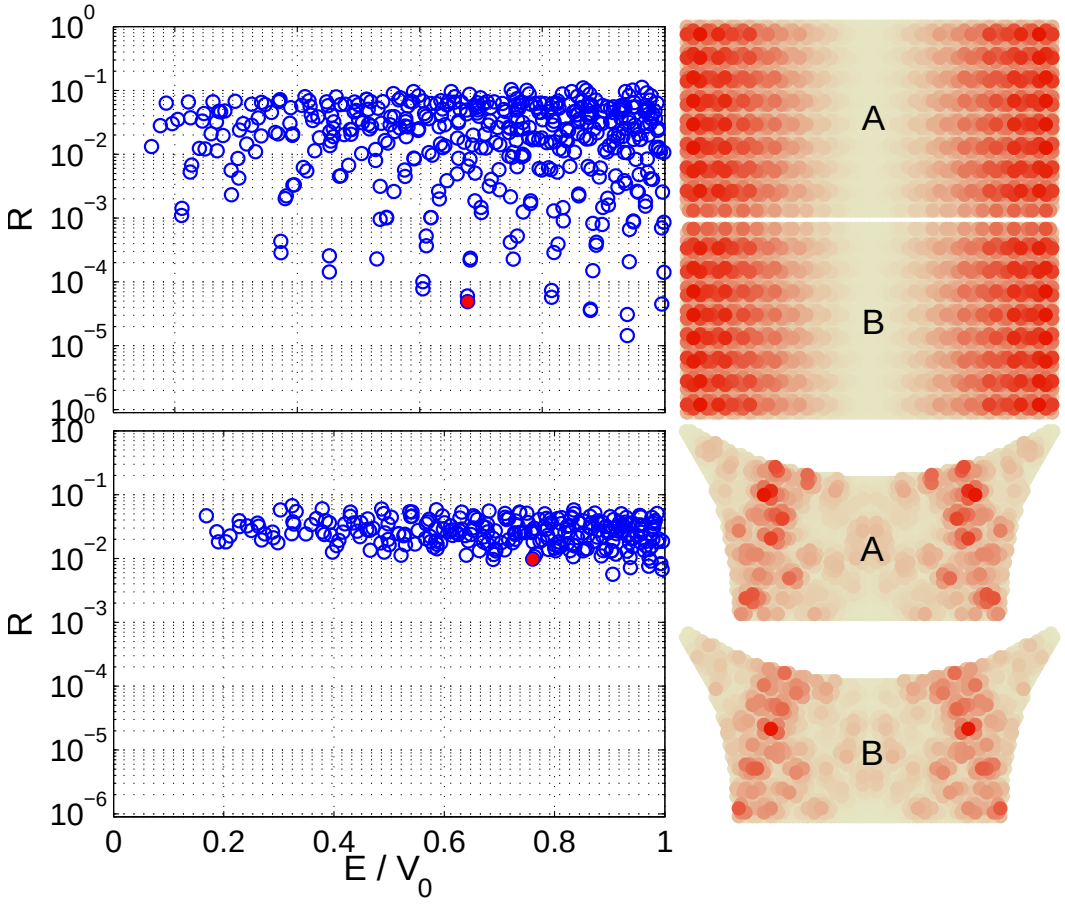

Fig. 13. Tunneling rates and LDS patterns in integrable and chaotic graphene double-well systems, where A and B denote the two distinct types of atoms a graphene unit cell. Tight-binding model is used in calculation for graphene systems. The barrier height is fixed at $V_0 \sim 0.67t$ (with t denoting the nearest-neighbor hopping integral). After converting to the $\hbar = c = 1$ unit system, the geometric measures and the barrier potential are the same as the single Dirac fermion system.

3.3. Analytical theory

3.3.1. The self-energy approach

To understand the effect of chaos on relativistic quantum tunneling, we develop a theory based on the self-energy concept widely employed in the study of quantum transport [15, 47]. The basic observation is that pointer states generally result in low tunneling rate. Thus, when pointer states are present, the coupling between the two wells is weak. The tunneling rate can thus be approximated as the escaping rate of Dirac fermions between two nearly closed, weakly coupled wells. Let the left well be denoted by superscript (1), and the barrier together with the right well denoted by superscript (2). The Dirac equations for the whole double-well system can be written in terms of the Hamiltonians H_1 and H_2 for the separated closed wells as

$$\begin{bmatrix} H_1 & V_{12} \\ V_{21} & H_2 \end{bmatrix} \begin{bmatrix} \psi^{(1)} \\ \psi^{(2)} \end{bmatrix} = E \begin{bmatrix} \psi^{(1)} \\ \psi^{(2)} \end{bmatrix}, \tag{3.2}$$

where V_{ij} are the coupling matrices. Note that, if the left well were itself closed, the corresponding equation is $H_1\psi^{(1)} = E_1\psi^{(1)}$, which becomes $(H_1 + \Sigma^R)\psi^{(1)} = E\psi^{(1)}$ when weak coupling to the right well is taken into account, where $\Sigma^R = V_{12}G^R V_{21}$ is the self energy due to the barrier and the right well, and $G^R = (E + i\eta - H_2)^{-1}$ is the retarded Green's function. For each eigenstate in the left well, the energy shift can be obtained through first-order perturbation theory as $\langle\Sigma^R\rangle = \langle\psi^{(1)}|\Sigma^R|\psi^{(1)}\rangle$, which is typically complex. The real part of this shift changes the oscillating frequency of the corresponding eigenstate, while the imaginary part, denoted by $-\gamma$, introduces a decay factor $\exp(-c_0\gamma t/\hbar)$ in the time evolution of the probability, which describes the escaping rate of the Dirac fermions from the left to the right well. Note that, since the whole system is closed, γ only describes the transient behavior associated with particle's tunneling from left to right, with any recurring behavior neglected. If we let the right well extend to infinity so that there is no reflection, the system is equivalent to a single left well coupled with an semi-infinite lead through a potential barrier, and γ will be the tunneling rate for the single left-well system.

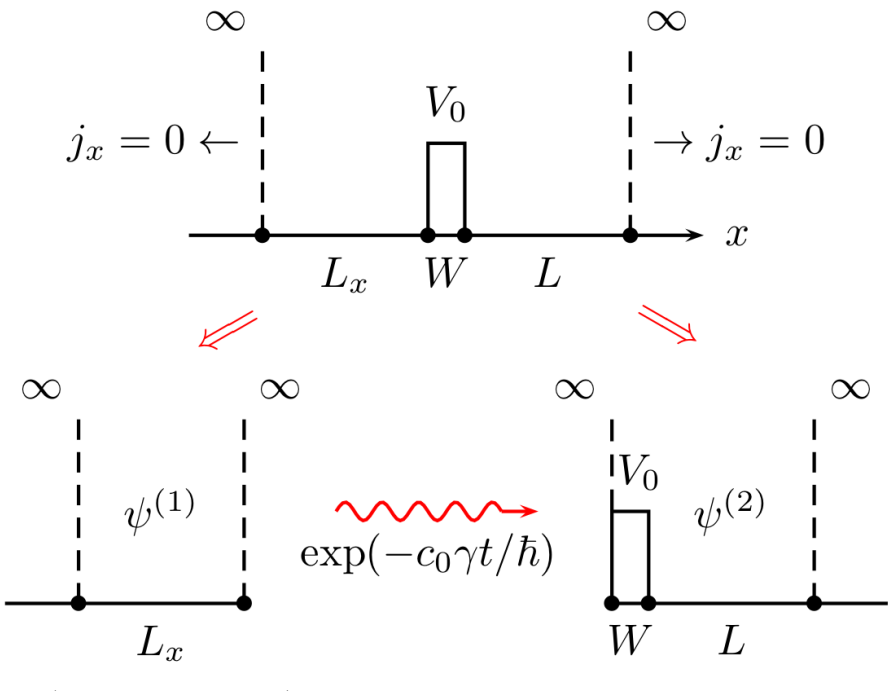

Fig. 14. Schematic diagram for one-dimension tunneling.

3.3.2. One dimensional model

To gain insights and also to validate that our proposed quantity γ is indeed proportional to the tunneling rate, we consider a one-dimensional system for which the Dirac equation can be solved and the self-energy and consequently γ can then be calculated analytically through the Green's function, as shown in Fig. 14. Specifically, the one-dimensional Dirac equation is $(-i\hbar v\sigma_x\partial_x)\psi = (E-V)\psi$. Since the potential is zero in the left well (of width L_x), the solution is

$$\psi_n^{(1)}(x) = \frac{1}{\sqrt{L_x}}\exp(i\frac{\pi}{4})\begin{bmatrix}\cos(k_n x - \frac{\pi}{4}) \\ i\sin(k_n x - \frac{\pi}{4})\end{bmatrix},$$

where $k_n = (n+1/2)\pi/L_x$. For the right part, the barrier has width W and $V = V_0$, and the right well has width L and $V = 0$. We obtain the solution

$$\psi_n^{(2)}(x) = \begin{cases} A_1 e^{i\kappa_n x}u_+ & + & A_2 e^{-i\kappa_n x}u_-, & \text{barrier,} \\ A_3 e^{ik_n x}u_+ & + & A_4 e^{-ik_n x}u_-, & \text{right-well,} \end{cases}$$

where $k_n = E/(\hbar v) = [V_0 W/(\hbar v) + (m+1/2)\pi]/(L+W)$, $\kappa_n = k_n - V_0/(\hbar v)$, $u_+ = (1,1)^T$ and $u_- = (1,-1)^T$ are bases for the spinor, and the coefficients A_i are determined by the boundary conditions. Note that this is a combined solution for both $E < V_0$ and $E > V_0$. To calculate the self energy $\langle\Sigma^R\rangle$, we discretize the space and introduce the Green's function $G^R(x_i, x_j)$. The self energy can be expressed as [47]

$$\langle\Sigma^R\rangle = \psi_n^{(1)\dagger}(L_x - a)V_{12}G^R(L_x + a, L_x + a)V_{21}\psi_n^{(1)}(L_x - a),$$

where $x = L_x$ is the junction between the left well and the barrier, and the coupling components are $V_{12} = V_{21}^\dagger = -i\hbar v\sigma_x$. The Green's function can be calculated explicitly in the limit $L \to \infty$. After a substantial amount of algebra we obtain the following expression for the tunneling rate:

$$\gamma = -\frac{(\hbar v)^2}{2\pi L_x}\left[\cos(2ka)\mathrm{Im}(C) - \sin(2ka)\mathrm{Im}(S)\right] - \frac{\hbar v\eta}{2\pi L_x E},$$

where the quantities S and C are given by

$$\begin{aligned} S &= \int_0^\infty dk \frac{\sin(2\kappa a)}{E + i\eta - \hbar v k}, \\ C &= \int_0^\infty dk \frac{\cos(2\kappa a)}{E + i\eta - \hbar v k}. \end{aligned}$$

The integrals can be evaluated explicitly and we finally obtain $\gamma \approx \hbar v/(2L_x)$. In one spatial dimension the standard tunneling rate ΔE can also be analytically calculated through symmetry considerations. We obtain $\Delta E \approx \hbar v\pi/(2L_x)$ and consequently, $\gamma \approx \Delta E/\pi$. These analytic predictions have been verified numerically.

3.3.3. Two dimensional tunneling

For tunneling systems in two spatial dimensions, even when the geometry is regular it is not possible to calculate the tunneling rate analytically, due to the entanglement of the two Cartesian coordinates in the Dirac equation. The problem is solvable only for certain special types of boundary conditions for which the variables can be separated. One particular class of such systems is tunneling between two concentric ring regions, where the first cavity is given by $R_1 < r < R_2$, the potential barrier is located in the region $R_2 < r < R_3$, and the second cavity is in the region $R_3 < r < R_4$. When all four radii are large, this ring-shaped double-well tunneling system is topologically equivalent to a rectangular double-well with periodic boundary condition in one direction. We have solved the Dirac equation, calculated the Green's function and the self energy, and finally obtained a close-form expression for the tunneling rate γ, which involves various eigenstates that can be evaluated numerically. A representative behavior of γ as a function of the energy is shown in Fig. 15, which is qualitatively similar to that in the rectangular double-well system. Of particular importance to the aim of this chapter are pointer states with extraordinarily low tunneling rates, which are the causes of the tunneling spread.

3.4. Summary

In summary, we have established the phenomenon of chaos-regularized tunneling in the relativistic quantum regime for both Dirac fermion and graphene tunneling systems. While tunneling in non-relativistic quantum mechanics has been well studied, there are two major challenges in investigating the phenomenon in relativistic quantum systems: solution of the Dirac equation in general two-dimensional spatial geometry and physically meaningful definition of the tunneling rate. We have overcome these difficulties and developed numerical methods and analytic theory to reveal

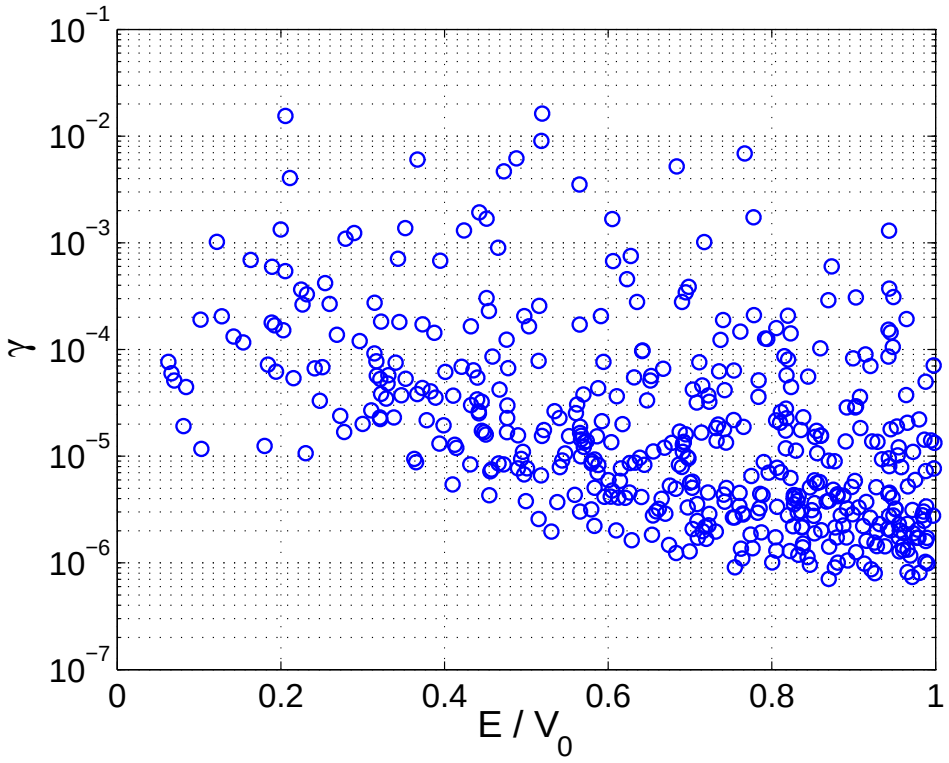

Fig. 15. Theoretical tunneling rate γ for Dirac fermion in the two-dimensional ring system as described in the text. The eigenstates associated with the inner and outer ring regions are calculated numerically by solving the Dirac equation with proper boundary conditions. The parameters are $R_1 = 5$, $R_2 = 10$, and $V_0 = 5$. The dimensions for the outer part are $R_3 = 10.2$, and $R_4 - R_3 = 3(R_2 - R_1)$.

the generic features of relativistic quantum tunneling. While we focus on resonant tunneling, the methodology developed here can be extended to other relativistic quantum transport systems, such as various electronic transport devices made of graphene.

4 . TRANSIENT CHAOS IN OPTICAL METAMATERIALS

4.1. Background

Optical metamaterials, also referred to as negative refractive-index materials, are artificially designed materials with unconventional properties that natural materials do not typically possess. Although the concept of metamaterials was proposed theoretically in 1968, explosive growth in research occurred only about a decade ago, where now the area has become one of the most active, interdisciplinary fields. Significant applications include superlens overcoming the optical diffraction limit and electromagnetically invisible materials. Quite recently, a correspondence of light-ray dynamics in optical metamaterials to general gravitational systems was suggested and signatures of chaos were revealed, opening the avenue to explore fundamental phenomena in gravitational physics that otherwise would not have been possible to be tested in laboratory experiments. In this chapter, we further probe chaos in metamaterial systems. In particular, through systematic computations of light-ray trajectories in two classes of systems, one time-dependent and another time-independent, we establish the existence of transient chaotic dynamics, both hyperbolic and nonhyperbolic, in these systems. In light of the analogy between metamaterial optics and gravitational physics, our results suggest that transient chaos can be quite common in gravitational systems obeying Einstein's general relativity.

In Sec. 4.2, we describe the equations of motion governing the dynamical behavior of light rays in optical metamaterials. In Sec. 4.3, we demonstrate transient chaos in metamaterial systems with time-dependent refractive index. In Sec. 4.4, we present evidence of transient chaos in time-independent systems. A brief conclusion is offered in Sec. 4.5

4.2. Equations of motion

In general relativity, the geometry of the space is described by the four-dimensional space-time metric $g_{\mu\nu}(\mathbf{x}, t)$. The propagation of light rays in this empty but curved spacetime, which follows the natural geodesic lines, is governed by the Lagrangian

$$\mathcal{L} = \frac{1}{2}[g_{00}(\mathbf{x}, t)\dot{t}^2 - g_{ij}(\mathbf{x}, t)\dot{x}^i\dot{x}^j]. \tag{4.1}$$

Here, the Einstein summation convention is used for spatial coordinate indices i and j, and $c = 1$ is used. To relate the light propagation in curved space to that in the composite material, one needs to perform coordinate transformations [67] to Maxwell's equations. For isotropic media, an effective refraction index can be defined as $n = \sqrt{g/g_{00}}$, where $g = g_{ii}$ ($i = 1, 2, 3$). Here we consider media with centro-symmetric effective refractive index n, and light-ray trajectory in the system can be further confined to the plane $\mathbf{r} = (x, y)$ due to the nature of planar motions of light rays in a centrally symmetric potential, as an orthogonal transformation always exists which brings the z-axis to be perpendicular to the plane of motion.

We now demonstrate that, after an appropriate coordinate transformation, the Lagrangian becomes

$$\mathcal{L} = \frac{1}{2}[\dot{t}^2 - n^2(\rho, t)(\dot{\rho}^2 + \rho^2\dot{\phi}^2)], \tag{4.2}$$

where $\rho = |\mathbf{r}|$, ϕ denotes the azimuthal angle, and the derivatives are with respect to the proper time τ. In particular, the key to the optical-mechanical analogy is the invariance of the Maxwell's equations under coordinate transformations. It was demonstrated [67] that the general covariant form of the free-space Maxwell's equations

$$\begin{aligned} F_{\mu\nu,\lambda} + F_{\lambda\mu,\nu} + F_{\nu\lambda,\mu} &= 0, \\ F^{\mu\nu}{}_{,\nu} &= \mu_0 J^\mu \end{aligned}$$

is equivalent to the constitutive equations

$$\begin{aligned} \mathbf{D} &= \varepsilon_0\varepsilon\mathbf{E} + c^{-1}\mathbf{w} \times \mathbf{H} \\ \mathbf{B} &= \mu_0\mu\mathbf{H} - c^{-1}\mathbf{w} \times \mathbf{E}. \end{aligned}$$

Here, the optical medium has the permittivity and permeability tensors $\varepsilon = \mu = \sqrt{-g}g^{ij}/g_{00}$, where $g = \det(g_{\mu\nu})$ and $w_i = g_{0i}/g_{00}$. Consider now light-ray motion in a special curved space-time metric $g_{\mu\nu}$ with the line element

$$ds^2 = g_{00}dt^2 - g_{ii}dx^i dx^i. \tag{4.3}$$

We can perform the coordinate transformation $x'^i = h_i x^i$ (no summation) that relates it to the Minkowski space, where $h_i = \sqrt{g_{ii}}$ denote the Lamé coefficients of the transformation. To take into account the effect of the time-dilation factor $\sqrt{g_{00}}$, we use the normalized field quantities $E'^i = \sqrt{g_{00}}E^i$ and $H'^i = \sqrt{g_{00}}H^i$, which are observable in experiments. The material properties in this case can be written as

$$\varepsilon_{ij} = \mu_{ij} = h_1 h_2 h_3 \delta_{ij}/(h_i\sqrt{g_{00}}). \tag{4.4}$$

For centrally symmetric space-time metric the line element can be expressed using the spherical coordinates as

$$ds^2 = g_{00}dt^2 - g_{\rho\rho}(d\rho^2 + \rho^2 d\Omega^2). \tag{4.5}$$

By defining an effective refractive index $n = \sqrt{g_{\rho\rho}/g_{00}}$, we arrive at the transformed Lagrangian (4.2). This particular refractive index could be realized experimentally using pure dielectric materials that are non-dissipative and non-dispersive.

By reversing such coordinate transformation, the light-ray motion in the material in flat space-time (as the case in a laboratory) is equivalent to that in empty but curved space-time, which can be studied by using the Euler-Lagrangian equations. We obtain

$$\begin{aligned} \rho' &= v, \\ v' &= [v^2 + \gamma(\rho,t)(\rho^2 + v^2)]/\rho, \\ t' &= n(\rho,t)(\rho^2 + v^2)^{1/2}, \end{aligned} \tag{4.6}$$

where $\gamma(\rho,t) = 1 + \rho\partial_\rho \ln n(\rho,t)$, and all derivatives marked by prime are with respect to the azimuthal angle ϕ, e.g., $\rho' \equiv d\rho/d\phi$. For static media [i.e., $\partial_t n(\rho,t) = 0$], a recent stability analysis [59] provided a sufficient condition for having stable orbits inside the potential: $d\gamma(\rho)/d\rho \leq 0$, leading to a well-behaved refractive-index function

$$n(\rho) \sim \exp\,[\int d\rho\gamma(\rho)/\rho]/\rho. \tag{4.7}$$

A convenient case is given by the condition

$$n(\rho) = n_0(\rho/a)\exp\,(-2\rho/a),$$

where a is the radius of the circular orbit, and n_0 is a constant characterizing the maximum refractive index $n_{max} = n_0/(2e)$. Figure 16 presents a schematic illustration of the static effective refraction index with an outer boundary ρ_{max}, outside which the refractive index $n_s(\rho)$ is truncated to unity. There are many periodic light-ray orbits [Figs. 16(b) and 16(c)] within the interaction region $\rho < \rho_{max}$ in this static system, making it a high quality optical cavity. However, in the presence of a time-dependent, external electromagnetic source, light-ray trajectories inside the cavity become more complicated. The time-dependent refractive index can be denoted as $n(\rho, t) = n(\rho) + \Delta n(t)$, where $\Delta n(t) = \xi n_{max} \sin(\omega t)$, ξ and ω are the intensity and the angular frequency of the perturbation, respectively. A possible experimental realization of this perturbation could be adding a small time-varying magnetic field perpendicular to the plane of the thin material plate. For linearly polarized light with magnetic component perpendicular to the material plane, this arrangement causes a small varying term in the effective permeability, and thus perturbs the refractive index in the desired way.

4.3. Transient chaos in systems with time-dependent refractive index

Two parameters characterizing the initial conditions of the ray dynamics are the impact parameter b and the time t_{enter} at which the light ray enters the interaction region defined as $\rho < \rho_{max}$. The parameter t_{enter} is necessary to completely determine the trajectories of light rays because the refractive index is time-dependent. The initial time t_{enter} can affect the light-ray trajectories inside the interaction region even though two beams of light are launched toward the interaction region with the same impact parameter. The two initial conditions can be conveniently defined as follows. The center of the potential is set at the origin in the plane. The light rays are sent from far field ($\rho > \rho_{max}$) in the x direction toward the center of the interaction region. The impact parameter is then $b \equiv |y|$. The time t_{enter} then marks the instant when the light ray reaches the circular outer boundary. Since the external perturbation $\Delta n(t)$ has the period $T = 2\pi/\omega$, it is convenient to use t_{enter}[mod(T)] as the entering time. Figures 17(a) and 17(b) show two parallel but closely separated incoming light-ray trajectories entering the interaction region at the same time, where the resulting trajectories inside the interaction region are also close. However, for another pair of nearby incident

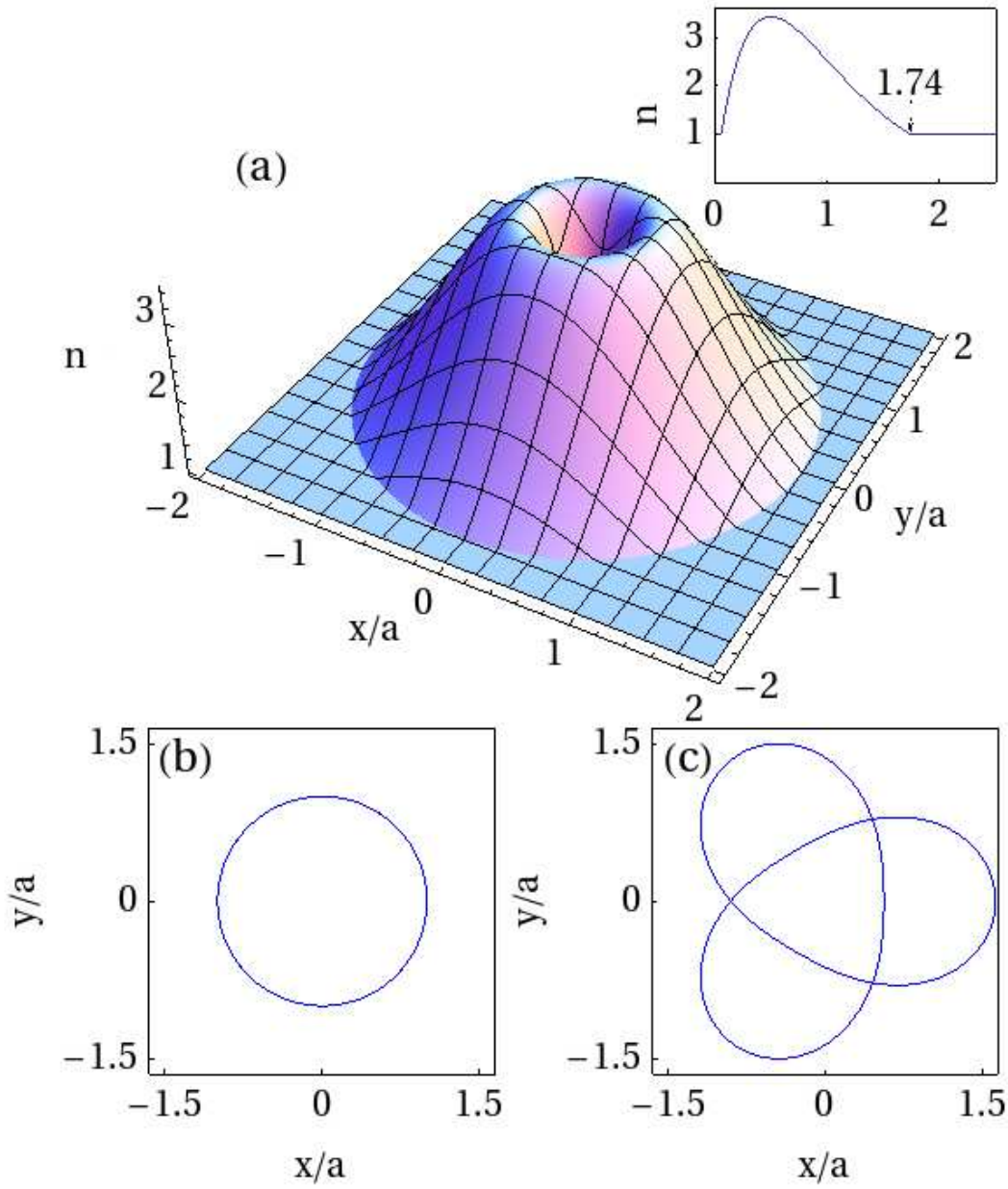

Fig. 16. (a) Static effective refractive index and (b,c) stable periodic light ray orbits. In (a), the refractive index is truncated to unity for $\rho > \rho_{max} = 1.74a$, and the parameters are $n_0 = 18.65$ and $a = 15\mu m$. In (b), the periodic orbit has the period 2π and radius a. In (c), the periodic orbit has the period 4π. The labels x,y and the subsequent occurrences are position parameters.

beams entering simultaneously, the trajectories are completely different, as shown in Figs. 17(c) and 17(d). The light-ray trajectories can thus be highly sensitive to the initial conditions, suggesting the emergence of transient chaos.

We now explore the dynamics of light rays in terms of the scattering functions, which are some quantities characterizing the rays after the interaction versus the impact parameter. In this regard, it is necessary to compensate the influence of the entering time t_{enter} on the light trajectory, which can be quite significant if incident light rays are launched, e.g., from a line segment perpendicular to the incident direction. To achieve this, we send the light rays from an arc of radius ρ_{max} such that the wave front of the incident light beam coincides with the outer boundary of the refractive index potential if the time-dependent term $\Delta n(t)$ were not present. In such an arrangement, the incident light rays with different impact parameters enter the interaction region at the same time, and so the scattering function can be obtained with respect to a single input variable, i.e., the impact parameter. The light rays stay in the region for a certain amount of time t_{delay} and then leave the interaction region. The output variables, the angle $\theta(b)[\text{mod}(2\pi)]$ and delay time $t_{delay}(b)[\text{mod}(T)]$, are then plotted as functions of impact parameter b, as shown in Figure 18. These plots are characteristic of transient chaos in open Hamiltonian systems [60].

There are two types of transient chaos in open Hamiltonian systems: hyperbolic [68] and non-hyperbolic [69, 70]. Of particular relevance to our work are the rigorous results on nonhyperbolic chaotic dynamics in soft-wall billiards [71–73]. In hyperbolic systems, all periodic orbits are unstable and the decay of particles from the interaction region is exponential [68]. In contrast, in non-hyperbolic dynamics, there are Kolmogorov-Arnold-Moser (KAM) tori and nonattracting chaotic sets coexisting in the phase space, and the particle decay is algebraic [69, 70]. To determine the nature of transient chaos of optical rays in metamaterials, we compute and analyze the phase-space structure. In particular, without the time-dependent perturbation, there are two stable periodic orbits in the phase space, as shown in Figs. 16(b) and 16(c). In fact, if the refractive index $n(\rho) = n_0(\rho/a)e^{-2\rho/a}$ were not truncated for $\rho > \rho_{max}$, it can be less than unity. In that case,

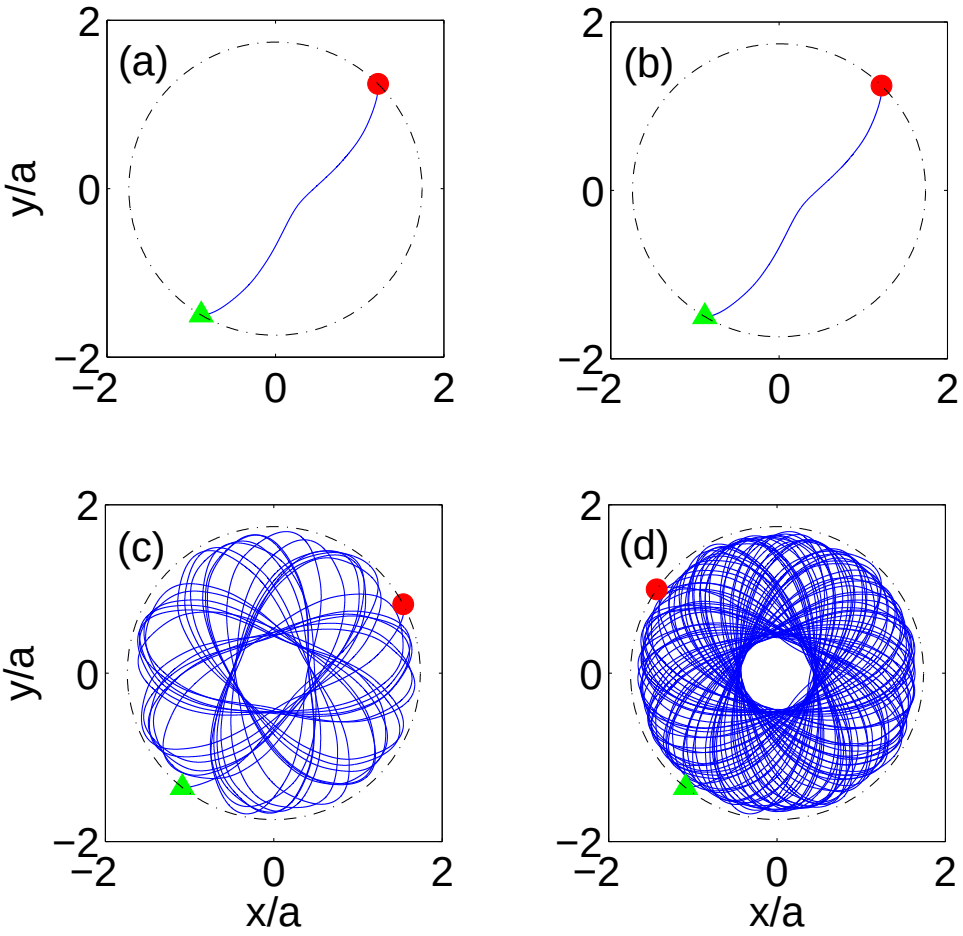

Fig. 17. Scattering trajectories from two pairs of nearby initial conditions. The dash-dotted circles mark the outer boundary of the static refractive index potential, and the (green) triangles and (red) circles mark the incoming and outgoing positions of light ray at the boundary, respectively. All incident photons are sent from the $-x$ to $+x$ direction and the impact parameter is $b \equiv |y|$. The upper two panels (a: $b = 1.50002a, t_{enter} = 0.774T$) and (b: $b = 1.50003a, t_{enter} = 0.774T$) show two nearby incident positions with similar outgoing photon trajectories, while the bottom two panels (c: $b = 1.35995a, t_{enter} = 0.854T$) and (d: $b = 1.35996a, t_{enter} = 0.854T$) show two nearby incident rays with drastically different outgoing trajectories, indicating a sensitive dependence on initial conditions. The parameters are $a = 15\mu m$, $\omega = 6c/a$, and $\xi = 0.2$.

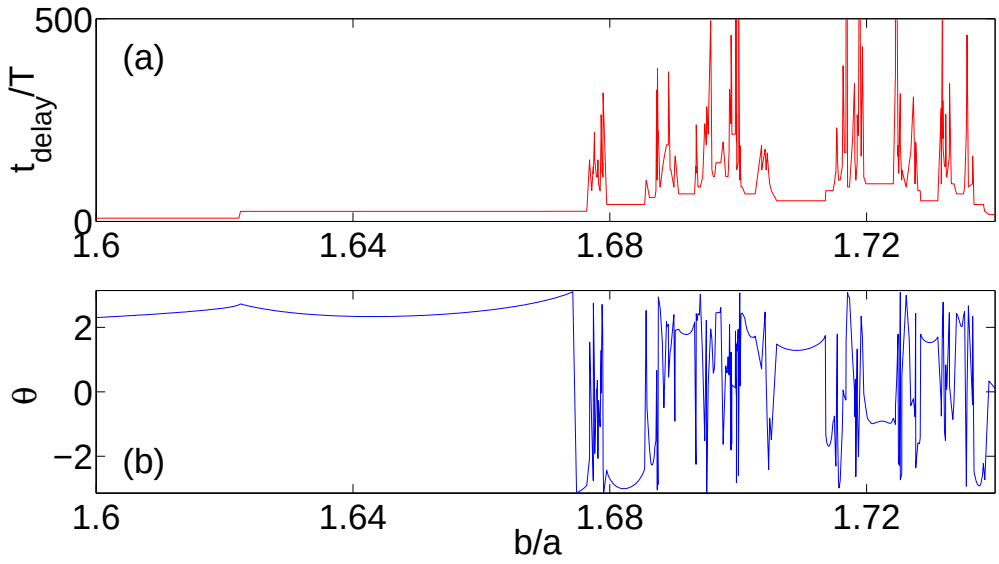

Fig. 18. (a) Delay-time function $t_{delay}(b)[\mathrm{mod}(T)]$ and (b) angle function $\theta(b)[\mathrm{mod}(2\pi)]$ for $\xi = 0.2$.

more periodic orbits of periods of multiples of 2π can exist, e.g., the third possible periodic orbit has period 6π. Physical reality requires, however, $n_s(\rho) > 1$ so that the truncation is necessary. Besides the periodic orbits of periods 2π and 4π, there are an infinite number of quasiperiodic orbits in the interaction region. When the time-dependent perturbation is turned on, unstable periodic orbits are created, some of these quasiperiodic orbits survive, forming KAM tori, and nonattracting chaotic sets arise through the typical mechanism of homoclinic/heteroclinic intersections between the stable and the unstable manifolds of the unstable periodic orbits. As the intensity ξ of the perturbation is increased, the regions containing the KAM tori shrink and the chaotic regions become more extensive in the phase space. A typical phase-space structure is shown in Fig. 19(a), where we observe both KAM tori and chaotic regions surrounding the central KAM island. Transient chaos is thus nonhyperbolic in this case. We note that, an analogous class of systems in classical mechanics exists, namely soft-wall billiards with repulsive potentials, for which certain rigorous results on chaotic dynamics are available [71–73].

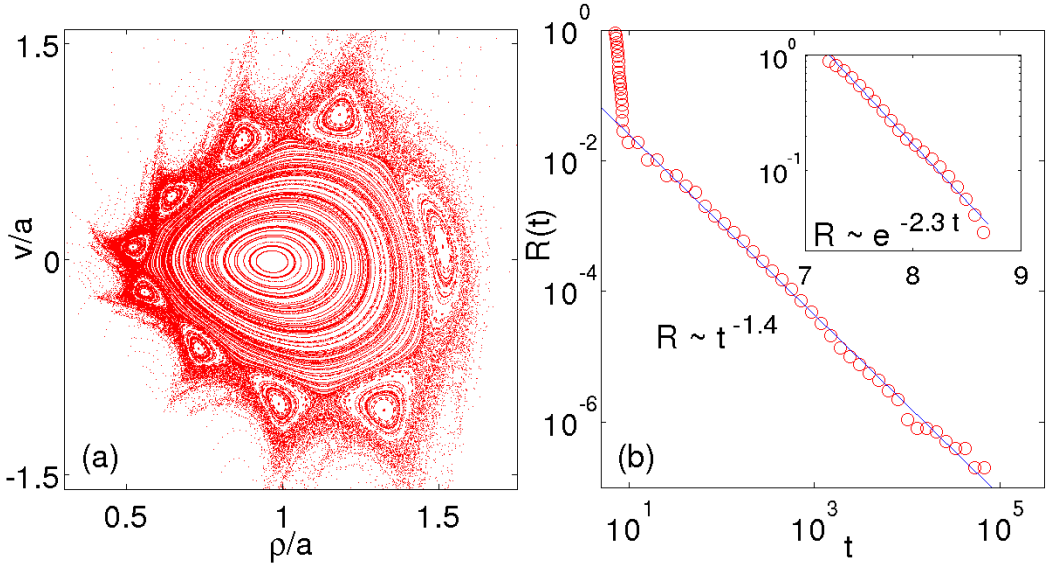

Fig. 19. (a) Phase-space structure on a Poincaré surface of section for $\xi = 0.2$. There are both KAM islands and chaotic regions, indicating nonhyperbolic transient chaos. The data points are sampled at $t = mT$ for $m \in \mathbb{N}$. (b) Fraction of light rays remaining in the interaction region as a function of time. We see that the decay is mostly algebraic, except for the initial small-time interval where the decay is exponential as demonstrated by the plot in the inset.

That the transient chaotic dynamics is nonhyperbolic can be further verified by examining the decay law of light rays. In particular, we define $R(t)$ to be the fraction of a large number of light rays (or photons in the short wavelength limit) still remaining in the interaction region $\rho < \rho_{max}$ at time t. Because of the time-dependent nature of the refractive index, we launch a large number of incident light rays successively and uniformly distributed in one period T of the external perturbation $\Delta n(t)$. The decay law of the light rays is shown in Fig. 19(b), where we see that $R(t)$ decreases exponentially for small t but algebraically for most of the time interval considered. We have, for $t < 8.7$, $R(t) \sim e^{-\alpha t}$ where $\alpha \approx 2.3$, and for $t \geq 8.7$, $R(t) \sim t^{-\beta}$ where $\beta \approx 1.4$.

4.4. Transient chaos in systems with time-independent refractive index

To demonstrate the generality of transient chaos in optical-metamaterial systems, we now consider a class of systems in which the refractive index is time-independent. In contrast to the time-dependent case where chaos has been uncovered previously [59], there has been no study of chaos in time-independent metamaterial systems. Our system consists of three equally spaced, static, volcano-shaped refractive index potentials, as shown in Figs.20(a) and 20(b). The Lagrangian of the system is of the same form as Eq.(4.2) except that now the refractive index is constant. Moreover, due to the loss of the central symmetry in the potential, an additional dynamical variable θ_v, the velocity angle with respect to the $+x$ direction, is needed to describe the dynamics. We obtain

$$\begin{aligned} \dot{x} &= \cos\theta_v / n(x,y), \\ \dot{y} &= \sin\theta_v / n(x,y), \\ \dot{\theta_v} &= (d\hat{\mathbf{v}}/d\theta_v) \cdot \nabla n / n^2, \end{aligned} \tag{4.8}$$

where $\hat{\mathbf{v}}$ is the unit vector in the velocity direction, and the derivatives are with respect to any affine parameter. In this system, the characteristics of transient chaos can be quite different in terms of whether the three refractive index potentials overlap. Figures 20(a) and 20(b) show two different configurations of the potentials. In Fig.20(a) where the potentials are spatially separated, there are stable periodic orbits in each potential region and unstable orbits circling the three potentials. In the overlapping case [Fig.20(b)], some of the stable orbits are destroyed, giving rise to complicated

trajectories. In this case, light ray trajectories can bounce back and forth between the original stable orbits within a single potential region and the unstable orbits that connect the three potentials, forming new unstable periodic orbits.

For the time-independent case, two convenient dynamical variables characterizing the transient dynamics are the impact parameter and the angle of incident light ray. To be concrete, we focus on scattering functions and the decay law with respect to variation in the impact parameter. An example of sensitive dependence of the trajectories on initial conditions is shown in the bottom panels of Fig. 20. In the non-overlapping potential case, the stable orbits inside each potential region cannot be reached by the trajectories starting from outside, i.e., the stable and unstable orbits are well separated. Figure 20(c) shows two distinct trajectories from two extremely closed initial impact parameters. For the overlapping case, Figs. 20(d) and 20(e) show two different trajectories from two nearby impact parameters. One can still see that the light ray encircles around the original stable orbits within the single potential region but finally leaves, due to the fact that the overlapping regions break the original stable orbits and connect them to the regions outside.

Typical scattering functions, where the incident angle of the light rays is fixed to be along the $+x$ direction, and the associated light-ray decay law are shown in Fig.21. We observe typical features of transient chaos. As shown in Fig.21(c), the decay law is exponential in this case, indicating the hyperbolic nature of the transient chaotic dynamics. The physical reason is that, since the potentials are non-overlapping, the stable and unstable periodic orbits are well separated in the phase space. Since decay law is meaningfully defined by light rays from outside the interaction region in all directions with random impact parameters, the KAM islands surrounding the stable periodic orbits are isolated from the regions outside and so are inaccessible to these rays, as shown in Figs. 22(a) and 22(b). For the overlapping-potential case, the dynamics is nonhyperbolic, as demonstrated by the phase-space structures shown in Figs. 22(c) and 22(d). In this case, three potentials penetrate into each other so that the originally inaccessible KAM islands are now accessible to light rays initiated afar from the interaction region, leading to an algebraic decay law, as shown in Fig.21(f).

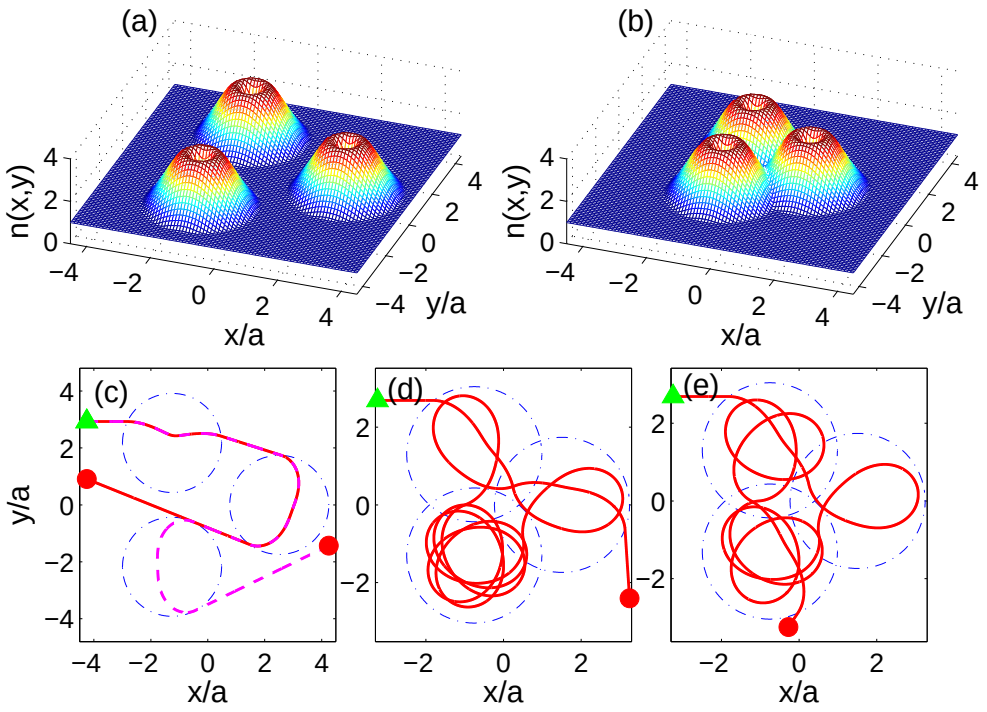

Fig. 20. Time-independent effective-index distribution for (a) three separated potentials $d = (2.5/\sqrt{3})r_{max}$, and (b) three overlapping potentials $d = (1.5/\sqrt{3})r_{max}$. Sensitive dependence of light ray trajectories on initial conditions are shown in (c-e). The dash-dotted circles, (green) triangles and (red) circles have the same meaning as in Fig.17. For the non-overlapping potential case (a), we show two trajectories in (c). The trajectory marked by the solid lines is for $b = 2.92724527$, and the one marked by dashed line is for a slightly different b value (increased by 10^{-8}). In (d) $b = 2.69012$, and (e) $b = 2.69013$, two distinct trajectories from two close impact parameters for the overlapping potential case (b) are shown.

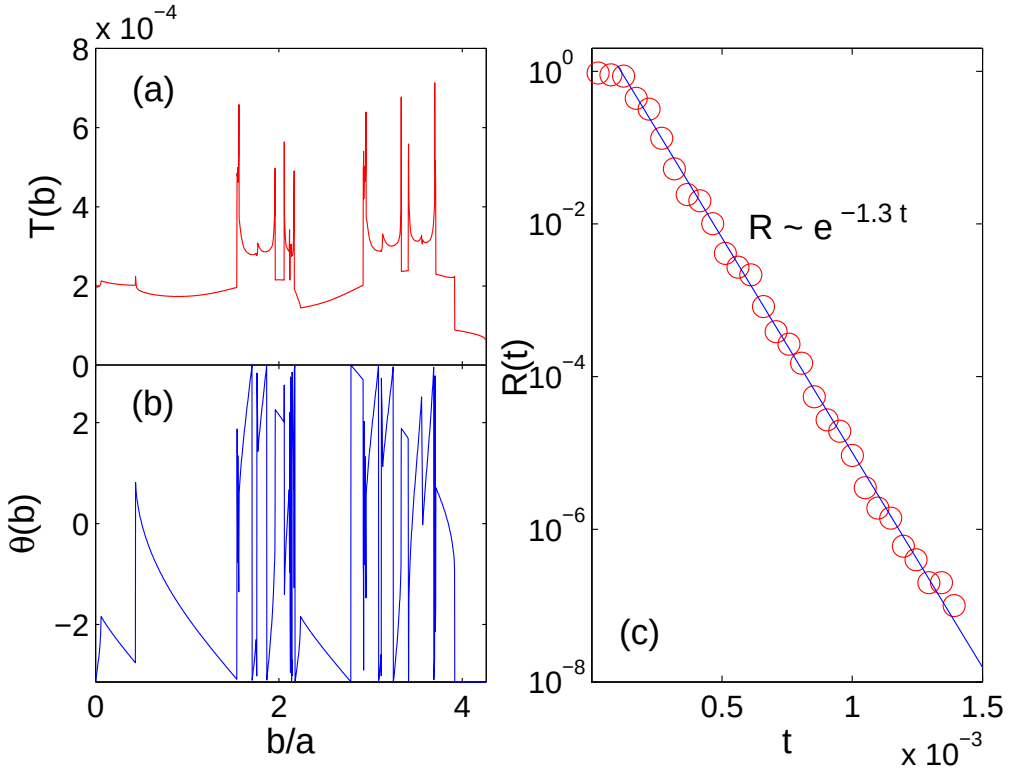

Fig. 21. For the non-overlapping refractive-index potential case ($d = (2.5/\sqrt{3})r_{max}$), (a,b) scattering functions and (c) exponential light-ray decay law. For the overlapping case ($d = (1.5/\sqrt{3})r_{max}$), (d,e) scattering functions and (f) algebraic light-ray decay law.

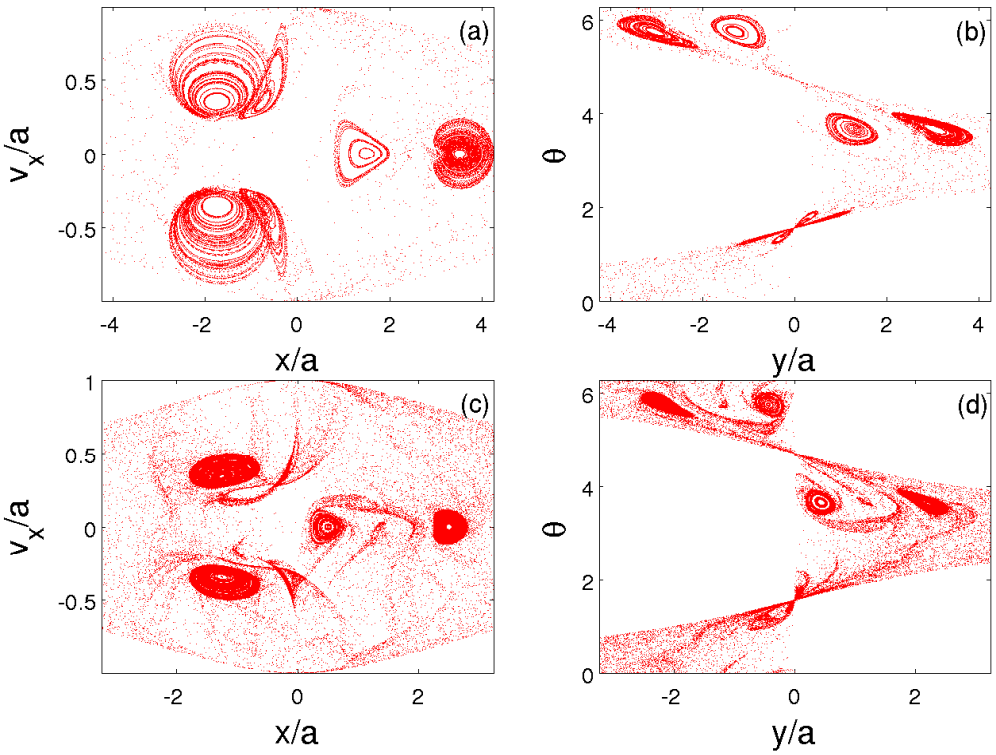

Fig. 22. Phase-space structure for the non-overlapping (a,b) and overlapping (c,d) potential cases. The points are sampled when the direction of velocity (represented by θ_v) forms $\pi/2$ angle with respect to the polar angle ϕ. This angle can be adjusted so that the resulting phase-space diagram looks similar but with each KAM island rotated.

There is then a crossover from exponential to algebraic decay as a system parameter changes so that the refractive-index potentials begin to overlap with each other, a known phenomenon in chaotic scattering in potential systems [74, 75].

4.5. Conclusion

We have demonstrated transient chaotic dynamics of light rays in optical metamaterials under time-dependent perturbations, which can be realized by an external electromagnetic field. The transient dynamics is typically nonhyperbolic in this case. We have also demonstrated that, even without the external time-dependent perturbations, transient chaos can arise from a class of static refractive-

index potential configurations. To our knowledge, chaos in optical metamaterial systems with static refractive index has not been observed previously. A rigorous mathematical understanding of the chaotic dynamics in optical metamaterials is not available at the present, but insights can be obtained from previous mathematical works on chaos in soft-wall billiards [71–73]. Based on the recently established connection between optical metamaterial and in relativistic gravitational systems [59], our results reinforce the idea that complex chaotic dynamics in the latter can potentially be observed and tested in laboratory experiments using optical metamaterials.

5 . EMERGENCE OF SCALING ASSOCIATED WITH COMPLEX BRANCHED WAVE STRUCTURES IN OPTICAL MEDIUM

Branched wave structures, an unconventional wave propagation pattern, can arise in random media. Experimental evidence has accumulated, revealing the occurrence of these waves in systems ranging from microwave and optical systems to solid-state devices. Experiments have also established the universal feature that the wave-intensity statistics deviate from Gaussian and typically possess a long-tail distribution, implying the existence of spatially localized regions with extraordinarily high intensity concentration ("hot" spots). Despite previous efforts, the origin of branched wave pattern is currently an issue of debate. We here propose a "minimal" model of wave propagation and scattering in optical media, taking into account the essential physics for generating robust branched flows: (1) a finite-size medium for linear wave propagation and (2) random scatterers whose refractive indices deviate continuously from that of the background medium. We find, through extensive numerical simulations and a detailed theoretical analysis, that branched wave pattern can emerge as a general phenomenon in wide parameter regime in between the weak-scattering limit and Anderson localization. The basic physical mechanisms to form branched waves are breakup of waves by a single scatterer and constructive interference of broken waves from multiple scatterers. Despite simplicity of our model, analysis of the scattering field naturally yields an algebraic (power-law) statistic in the high wave-intensity distribution, indicating that our model is able to capture the generic physical origin of these special wave patterns. The insights so obtained can be used to better understand the origin of complex extreme wave patterns, whose occurrences can have significant impact on the performance of the underlying physical systems or devices.

5.1. Method

In this chapter, we focus on wave propagation in two-dimensional optical medium and propose a class of models for branched wave patterns which contain two basic physical elements: (1) a uniform medium of finite size and (2) spatially localized scatterers randomly distributed in the medium, the refractive indices of which deviate from that of the background medium. The deviations can occur in

both ways which, in the case of negative deviation, may correspond to scatterers that are effectively negative-indexed, or *metamaterials*. The second element is required for generating dynamics beyond simple linear wave propagation. We shall demonstrate that such a minimal model can generate robust branched wave patterns, regardless of the detailed distribution of the refractive-index deviations associated with the random scatterers. We will derive theoretically that the model can naturally yield an algebraic (or power-law), long-tail type of distribution of the wave intensities.

More specifically, the model, approach, and findings of our study can be described, as follows. We consider the setting where a polarized monochromatic light propagates in a dielectric optical medium with random structural imperfections characterized by random refractive-index disorders (scatterers) of size comparable to the wavelength. Our numerical scheme employs the standard finite-difference frequency-domain (FDFD) method [89–92] to calculate the intensity of scattered field through multiple scatterers. In the weak scattering limit, i.e., when the wavelength λ is much smaller than the mean free path l, we obtain striking branching flow structures of propagating light, similar to those observed in the 2DEG and microwave transport experiments. As the spatial density of the scatterers is increased, the intensity patterns exhibit more pronounced fractal-like behavior, where branches of extraordinarily high intensities tend to enhance themselves when forking into narrower and even smaller paths. Anderson localization of light is also observed as the mean free path approaches the strong scattering limit ($l \sim \lambda$). Our extensive numerical computation also confirms that the branched structure can result from the caustics of the flow rather than the valleys of the random scatterers. We find that branched waves generically arise in the regime between weak scattering and strong localization of light waves.

In order to obtain a comprehensive understanding of the occurrence of branched waves in optical media and also to uncover their statistics, we develop a detailed analytic theory. Utilizing the Green's function method, we treat the scattering of two-dimensional polarized light wave off a single scatterer and obtain a theoretical explanation for the reason why the wavelength needs to be comparable to the size of the scatterer in order for noticeable large fluctuations of branching strands to

be observed. In contrast to the existing theory [86] which deals with stretches and folds in classical ray dynamics in a concrete and somewhat abstract manner, our theory enables us to *visualize* the branching flow structures of the scattered light intensities in different angular directions. Based on the results from scattering off a single scatterer, we next extend our treatment to multiple scatterers. In this case, coherent backscattering and recurrent multiple scattering become important, and they together contribute dominantly to the formation of extremely large amplitude events. This unstable branch stretching and accumulation process is highly sensitive to the scatterers' spatial distribution and thus is critical to the formation of fractal-like wave patterns. Because of the large intensity fluctuations caused by wave interference and the complexity of random-scatterer configuration, it is essential to focus on the statistical distribution function of light intensities. We have succeeded in deriving a formula for the distribution function of high intensities, which follows an algebraic (power-law) scaling law in the weak-scattering limit. This means that, associated with the branched waves, there are points in the space at which exceedingly large intensities can arise, the "hot" spots, in contrast to situations governed by Gaussian type of intensity distributions [93–96]. Note that the algebraic distribution was previously observed in electronic transport in 2DEG systems [86]. In the optical media, however, away from the weak-scattering limit (e.g., $\lambda/l \sim 0.35$), our theory predicts a small deviation from the algebraic scaling law, but the overall distribution is still markedly long-tailed.

A brief account of some of the above results has been published [97]. The purpose here is to provide a comprehensive treatment with a detailed theoretical analysis and extensive numerical results. The chapter is organized as follows. In Sec. 5.2, we describe our model and present extensive numerical evidence of branched wave patterns in optical media with negative- and positive-index disorders, and a mixture of both. In Sec. 5.3, we develop a detailed analytic theory based on electromagnetic wave scattering to uncover the physical origin underlying the emergence of branched wave structures. The theory allows us to predict the significant statistical behaviors of these complex wave patterns, which are verified numerically. Conclusions and discussions are presented

in Sec. 5.4.

5.2. Numerical results

We consider a polarized, monochromatic, Gaussian light beam propagating in a dielectric medium of refractive index n_0, where the medium has embedded within itself N random scatterers. The spatial distribution function of the refractive index for the whole system can be written as

$$n(\mathbf{r}) = n_0 + \sum_{i=1}^{N} \Delta n_i \exp[-|\mathbf{r} - \mathbf{r}_i|^2/(2\sigma^2)], \tag{5.1}$$

where Δn_i is the magnitude of the refractive index of the ith scatterer relative to that of the medium, and $\mathbf{r} = (x, y)$ is a two-dimensional vector. Each scatterer is characterized by a Gaussian-shaped refractive index profile, whose effective radius is σ. To simulate the scattering of electromagnetic waves, we use the standard FDFD method [92]. The wavelength is chosen to be $\lambda = 1\mu$m so that the scattering strength ratio is $\lambda/l \sim 0.35$.

Figures 23(a-d) show, for a rectangular medium of size $35\mu\text{m} \times 70\mu\text{m}$ and $N = 300$, four typical cases of the distribution of the scattering field strength, where the scatterers have negative refractive-index variations ($\Delta n_i < 0$) for panels (a,b), and positive variation ($\Delta n_i > 0$) for panel (c), and a mixed distribution of negative and positive variations for panel (d). Signatures of branched wave patterns, especially a fractal-like branching structure, are apparent in all cases. Numerically, we observe that the shape of the refractive-index distribution associated with the random scatterers does not have a significant effect on the emergence and the statistical properties of the branched wave structures. However, in order to preserve high numerical accuracy and reduce artificial reflection effect, we have chosen some smoothly varied shape, such as the Gaussian shape. As will be derived analytically, in order to observe sharp, narrow, branch-like flows, the sizes of the scatterers should be comparable to the wavelength λ. Note that, the wave patterns for the negative and positive variation cases exhibit somewhat different branched forking structures. This is largely due to the fact that higher refractive-index regions attract light rays while lower refractive-index regions repel them. In the short-wavelength limit, the negative-indexed scatterers are equivalent to repulsive potential hills, while the positive ones are effectively attractive potential wells for light rays. In both cases, chaos

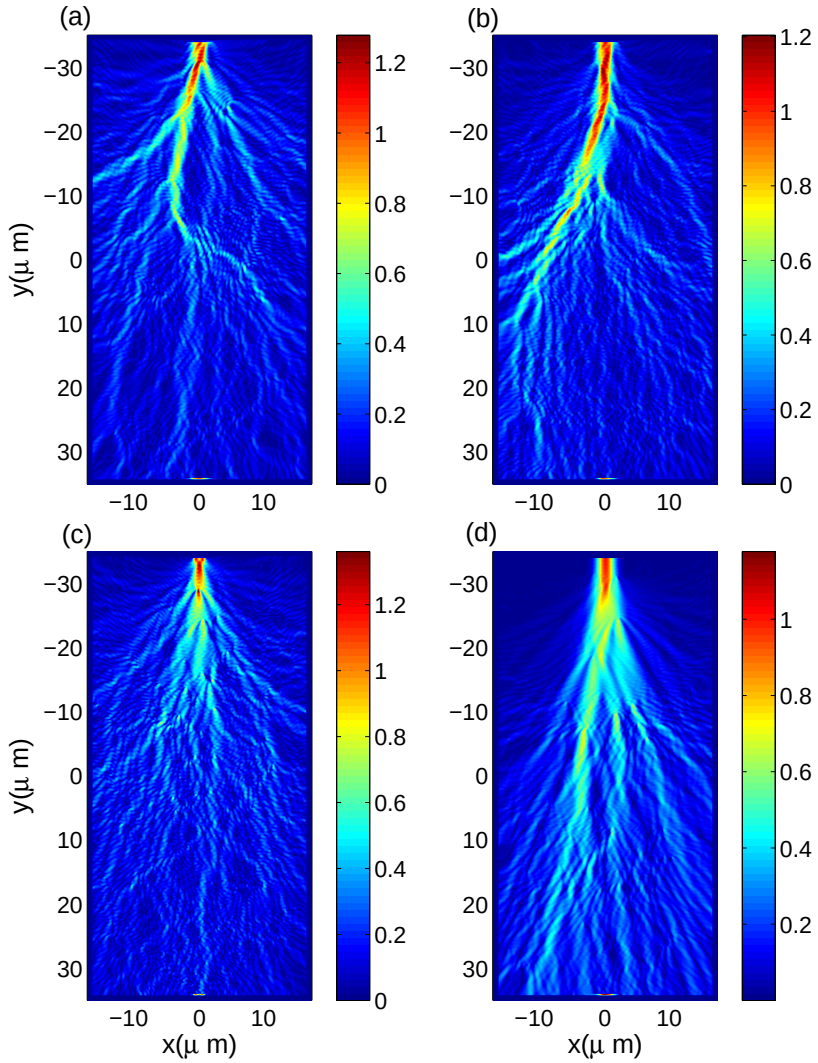

Fig. 23. For a rectangular optical medium of size 35μm $\times$ 70μm with $N = 300$ spatially localized, Gaussian-shaped scatterers, typical spatial distributions of the magnetic field strength $|H|$ of the scattered waves. In each case, an external polarized, monochromatic, Gaussian wave of width $w = 1\mu$m and unit intensity is sent from the top of the region. For panels (a) and (b), the refractive-index variations are negative: $\Delta n_i = -0.5$. The variation is positive for panel (c): $\Delta n_i = 0.5$. For panel (d), Δn_i is randomly selected from the range $[-0.5, 0.5]$. Other parameters are the same for all panels: $n_0 = 1$, $\lambda = 1\mu$m, and $\sigma = 0.22$. We observe signatures of branched, fractal-like wave patterns in all cases.

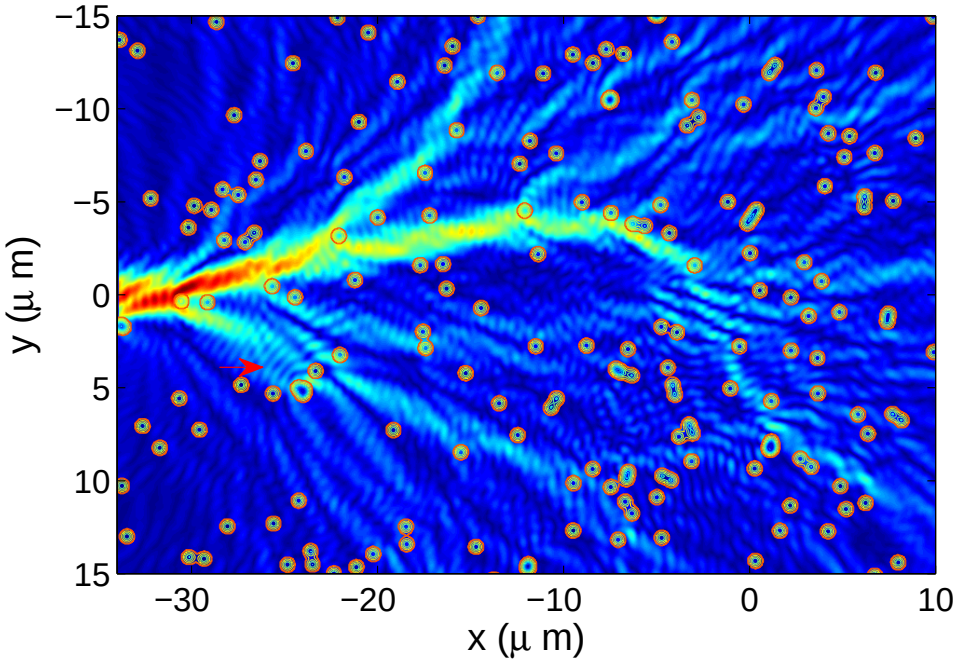

Fig. 24. Positions of scatterers (marked by red circles) on top of various wave paths. Intensive wave branches tend to go through various boundaries of scatterers instead of passing through the various smooth valleys in between. Red arrow marks the position where interference fringes are observed.

can arise in the zero wavelength limit.

Figure 24 shows the positions of the random scatterers superimposed on top of the branched wave pattern. A feature typical of the observed fractal-like wave patterns is that the wave branches tend to pass along the sides of the scatterers instead of going through the smooth valleys among the scatterers. This feature appears to be shared by electronic branched wave patterns in 2DEG systems [85, 86], where it was suggested that the wave branches may result from caustics in the corresponding classical regime. As for 2DEG systems, we also observe fringe patterns (e.g., marked by a red arrow in Fig.24), which are separated in space by about $\lambda/2$. It is known that coherent backscattering [98] of light by disorders is responsible for the formation of these fringe patterns.

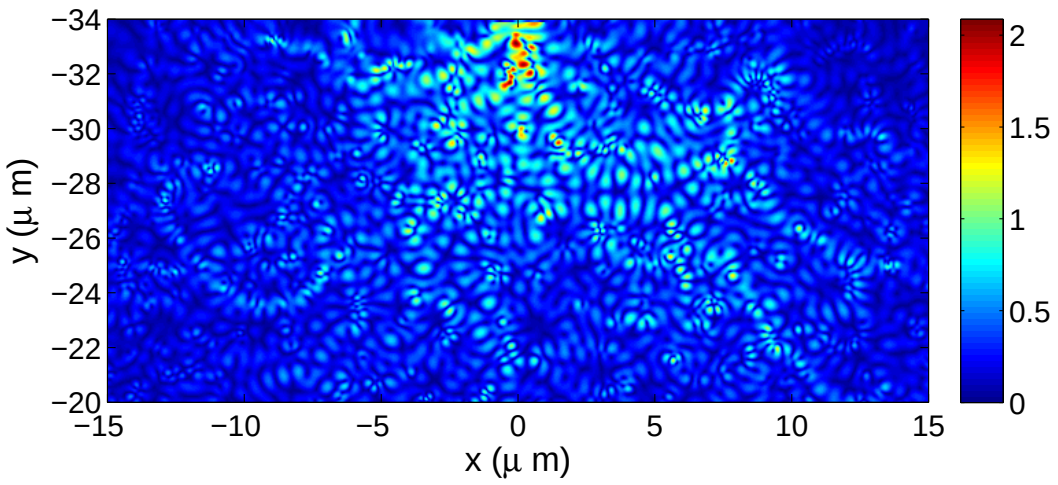

Fig. 25. Emergence of localization of light as the number of disorders is increased to $N = 2000$. Other parameters are the same as in Fig.23.

More specifically, light backscattered by the disorders (in Fig. 24, close to the arrow along the propagating direction of light) tends to interfere with the forward propagating light, giving rise to the fringes separated by half-wavelength.

To gain more physical insights, we increase the scattering strength ratio to some value close to the Ioffe-Regel criterion defined by $kl < 1$ so that localization of light is anticipated [99, 100]. For $\lambda/l \sim 1$, with a small imaginary part added to the dielectric constant of the scatterer to model possible absorption effects, we observe extremely localized light-wave pattern, as shown in Fig.25. The simulation is performed for media of the same size as in Fig. 23, but for clarity we show only the upper part of the region because most light in the strong localized state concentrates within this region. As the number of scatterers is increased, the probability of light paths connected by them to form cycles increases as well. Due to the time reversal symmetry of light propagation, paths having the same cycles but propagating in the opposite direction interfere constructively with the original circle paths, giving rise to strongly localized concentration of light intensities. In fact, as strong-scattering regime is approached, the system exhibits a transition similar to that typically seen in an electronic system, which is transformed from a conducting to an insulating (localized) state.

5.3. Emergence of branched waves and their scaling behavior: theory

The problem setting is wave propagation in a two-dimensional optical medium with randomly positioned scattering centers. The material is assumed to be isotropic and *linear*, it is neither dispersive nor dissipative, and there is no source (free charge or current). For disorders with centrosymmetric refractive index distribution, the propagating direction of light wave with linear polarization is confined within a two-dimensional plane [97]. To be concrete, we focus on the TE mode, for which the magnetic field strength is given by $\mathbf{H} = H\mathbf{e}_z$. The Maxwell's equations for $\mathbf{H}$ lead to

$$\nabla \times \left(\frac{1}{\varepsilon} \nabla \times \mathbf{H} \right) = k^2 \mu \mathbf{H}, \tag{5.2}$$

where $k = \omega/c$ is the vacuum wave vector, ε and μ are the relative permittivity and permeability, respectively. The refractive index is $n_0 = \sqrt{\varepsilon\mu}$. For polarized light, Eq. (5.2) becomes the following Helmholtz equation for the scalar field H:

$$\left(\nabla^2 + k^2 n^2 \right) H = \frac{\nabla n}{n} \cdot \nabla H. \tag{5.3}$$

The goal of our theoretical analysis is to calculate the scattering field and its statistical distribution throughout the medium. Our approach is to first analyze the field from a single scatterer and then extend the result to multiple scatterers to obtain the statistical properties of the resulted wave intensity. We assume that the random scatterers are far away from each other as compared with their sizes, which can be ensured if they are sparsely distributed in the medium. The shape of the random scatterers will also be taken into account in the analysis.

5.3.1. Scattering wave field from a single scatterer

Consider a single scatterer located at the origin. Without loss of generality, we set $n_0 = 1$. For the single-scatterer system we use approximated Gaussian shaped disorders as in our numerical computation, but analysis indicates that the shape of the disorder does not have a significant impact on the statistical properties of the wave intensity distribution.

To proceed, we decompose the magnetic field H into an incident and a scattering part, i.e., $H = H^i + H^s$. The incident field is a plane wave $H^i = e^{ikx}$, whereas the scattering part is the

response of the small scatterer to the incident plane wave. If n_0 were not unity, the plane wave should be e^{ikn_0x} instead. For field far away from the scatterer, i.e., $r \gg \sigma$, Eq. (5.3) becomes

$$\left(\nabla^2 + k^2\right) H^s(\mathbf{r}) = f_1 + f_2 + f_3, \tag{5.4}$$

where

$$\begin{aligned} f_1(\mathbf{r}) &= -(\nabla^2 + k^2 n^2) H^i, \\ f_2(\mathbf{r}) &= \nabla H^i \cdot \nabla n/n, \\ f_3(\mathbf{r}) &= \nabla H^s \cdot \nabla n/n. \end{aligned}$$

At far field where $H^i \gg H^s$ is satisfied, only f_1 and f_2 contribute to the lowest-order approximation. In particular, to the lowest order, both f_1 and f_2 contain the $r^{-1/2}$ term at far field of H^s, whereas f_3 has the r^{-1} term. It is thus reasonable to consider contributions from f_1 and f_2 only. Higher-order corrections due to the source term f_3 can be obtained by using recursive iterations, but their contributions to the wave field are insignificant and thus will not be included in our analysis. The Green's function associated with Eq. (5.4) is

$$\left(\nabla^2 + k^2\right) G(\mathbf{r}, \mathbf{r}') = -\delta(\mathbf{r} - \mathbf{r}').$$

The standard solution to the Green's function in two dimensions is given by

$$G(\mathbf{r}, \mathbf{r}') = \frac{i}{4} h_0^{(1)}(k|\mathbf{r} - \mathbf{r}'|),$$

where $h_0^{(1)} = J_0 + iY_0$ is the Hankel function of the first kind. The scattering field can then be written as the summation of two convolution operations:

$$H^s(\mathbf{r})_{r \gg \sigma} \approx \sum_{j=1,2} (G * f_j)(\mathbf{r}),$$

where $H_j^s(\mathbf{r}) = (G * f_j)(\mathbf{r})$, $(j = 1, 2)$. Physically, the two scattering fields H_1^s and H_2^s result from the inhomogeneity $n(\mathbf{r})$ in the refractive-index profile and its spatial variations $\nabla n(\mathbf{r})$, respectively, as shown in Fig. 26.

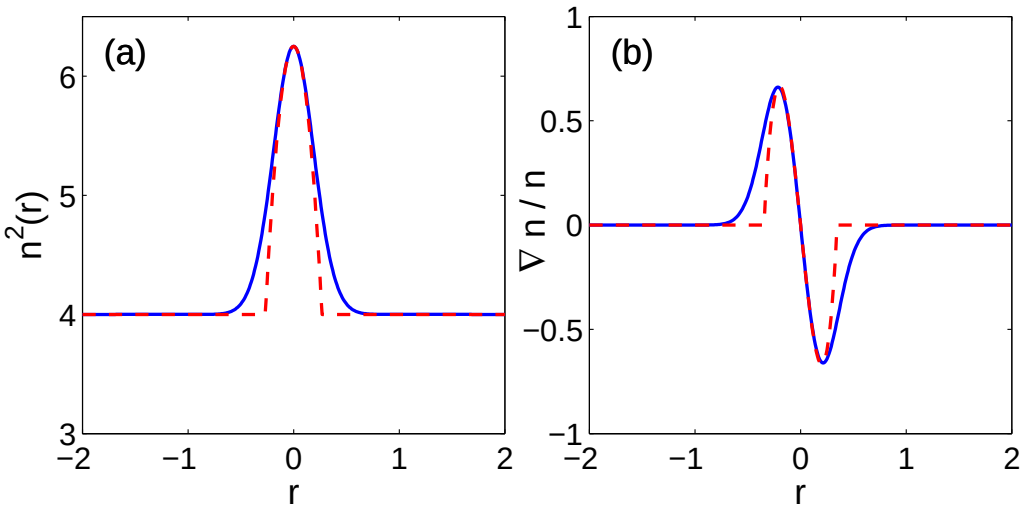

Fig. 26. Approximations of (a) n^2 and (b) $\nabla n/n$ as functions of the distance from center of the scatter. Blue solid lines represent the refractive-index profiles of the Gaussian-shaped scatterer and the red dashed lines are the polynomial approximations. The typical parameters shown here are $n_0 = 2$, $\Delta n = 0.5$, $\sigma = 0.2\mu$m, $\alpha = 1$, and $\beta = 2/3$.

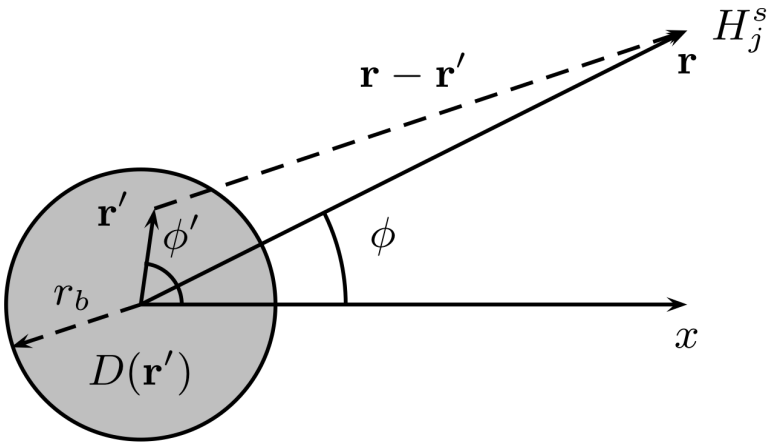

Fig. 27. Integration domain $D(\mathbf{r}')$ of a single scatterer located at the origin with a truncated radius r_b. The incident beam is from -x direction and the scattered field H_j^s is evaluated at far field $\mathbf{r}$.

The scattering fields due to f_1 and f_2 can be calculated separately. For example, in order to obtain H_1^s analytically, we approximate the refractive index of the scatterer as

$$n^2(\mathbf{r}) \approx \begin{cases} (1+\Delta n)^2 - \Delta n(1+\Delta n)\left(\frac{r}{\alpha\sigma}\right)^2, & r \le r_b, \\ 1, & r > r_b, \end{cases} \tag{5.5}$$

where

$$r_b = \alpha\sigma\sqrt{\frac{\Delta n+2}{\Delta n+1}}$$

is the truncated boundary of the scatterer, and α is the parameter that controls the width of variation in n^2, as shown in Fig. 26(a). This form of the refractive index function with a finite domain of disorder profile allows us to evaluate analytically the scattering field at far field by integrating the convolution, which requires the asymptotic form of the Hankel function at far field:

$$h_0^{(1)}(x \gg \frac{1}{4}) \sim (\frac{\pi x}{2})^{-1/2}\exp(i[x-\frac{\pi}{4}]).$$

The integration is confined within the shaded area in Fig. 27, i.e., $D(\mathbf{r}') : |\mathbf{r}'| < r_b$. The conditions to ensure the validity of the far-field approximation $x = k|\mathbf{r}-\mathbf{r}'| \gg 1/4$ can be estimated, as follows. For $\Delta n = -0.5$, $\lambda = 1\mu$m, $\sigma = 0.22$, and $\alpha = 1$, we have $r_b \approx 0.38$ μm, and $r > 2[10\cdot(1/4)/k + r_b] \approx 1.56$ μm. This means that, in a 35 μm $\times$ 70 μm medium, we can have up to 1000 disorders while still maintaining the sparsity condition, provided that the disorders are arranged on a lattice. Since, in our simulation, the disorders are randomly placed in the medium, the acceptable maximum number of disorders is considerably less. Using the asymptotic form of the Hankel function, the field $H_1^s(\mathbf{r})$ becomes

$$\begin{aligned} H_1^s(\mathbf{r})_{r\gg r_b} &= \iint\limits_{D(\mathbf{r}')} d\mathbf{r}'\; G(\mathbf{r},\mathbf{r}')f_1(\mathbf{r}') \\ &= \iint\limits_{D(\mathbf{r}')} d\mathbf{r}'\; \frac{i}{4}\, h_0^{(1)}(k|\mathbf{r}-\mathbf{r}'|)(-\nabla'^2 - k^2n^2)\, e^{ikx'} \\ &\approx \frac{i}{4}\sqrt{\frac{2}{\pi}}\, e^{-i\frac{\pi}{4}}\, k^{3/2} \\ &\quad \cdot\Delta n\left[\frac{(\Delta n+1)}{\sigma^2} I_1^{(2)} - (\Delta n+2) I_1^{(0)}\right], \end{aligned}$$

where the integrals $I_1^{(\ell)}(\mathbf{r})$ of orders $\ell = 0, 2$ are of the following form:

$$I_1^{(\ell)}(\mathbf{r}) = \iint\limits_{|\mathbf{r}'|<r_b} d\mathbf{r}'\; r'^{\ell}\; \frac{e^{ik(|\mathbf{r}-\mathbf{r}'|+x')}}{\sqrt{|\mathbf{r}-\mathbf{r}'|}}.$$

Similarly, for $H_2^s(\mathbf{r})$ resulting from the source term f_2, we expand $\nabla n/n$ as

$$\frac{\nabla n}{n} \approx \begin{cases} \frac{\Delta n}{1+\Delta n}\left(1-\frac{\beta r^2}{2\sigma^2}\right)\left(-\frac{\mathbf{r}}{\sigma^2}\right), & r \le r_b', \\ 0, & r > r_b', \end{cases} \tag{5.6}$$

where

$$r_b' = \sigma\sqrt{\frac{2}{\beta}}.$$

An approximate form of $\nabla n/n$ is shown in Fig. 26(b), where we use matched values of α and β so that the boundaries are identical for both integration domains, i.e., $r_b = r_b'$. Under these approximations, H_2^s can be written as

$$\begin{aligned} H_2^s(\mathbf{r})_{r\gg r_b'} \;\approx\; & -\frac{1}{4}\sqrt{\frac{2}{\pi}}\, e^{-i\frac{\pi}{4}}\, k^{1/2} \\ & \cdot\frac{\Delta n}{(1+\Delta n)\sigma^2}\left[\frac{\beta}{2\sigma^2} I_2^{(2)} - I_2^{(0)}\right], \end{aligned}$$

where the integrals $I_2^{(\ell)}$ for orders $\ell = 0, 2$ are defined to be

$$I_2^{(\ell)}(\mathbf{r}) = \iint\limits_{|\mathbf{r}'|<r_b'} d\mathbf{r}'\; r'^{\ell}\; x'\; \frac{e^{ik(|\mathbf{r}-\mathbf{r}'|+x')}}{\sqrt{|\mathbf{r}-\mathbf{r}'|}}.$$

To calculate $I_j^{(\ell)}$'s, we use polar coordinates, as depicted in Fig. 27. In the region $r \gg r_b$, the approximations

$$|\mathbf{r}-\mathbf{r}'| \approx r - \hat{\mathbf{r}}\cdot\mathbf{r}' = r - r'\cos(\phi-\phi')$$

and

$$\frac{1}{\sqrt{|\mathbf{r}-\mathbf{r}'|}} \approx r^{-1/2}\left[1+\frac{1}{2}\frac{r'}{r}\cos(\phi-\phi')\right],$$

hold, where $\hat{\mathbf{r}}$ is the unit vector in the direction of $\mathbf{r}'$, ϕ and ϕ' (cf. Fig. 27) are the polar angles of $\mathbf{r}$ and $\mathbf{r}'$, respectively. It can be shown that all the integrals involved in the two scattering fields have the general form

$$\begin{aligned} I_{\tau\mu\nu}(r,\phi) = & \int_0^R dr' \int_0^{2\pi} d\phi'\; r'^{\tau}\cos^{\mu}\phi'\cos^{\nu}(\phi-\phi') \\ & \cdot\exp(ikr'[\cos\phi' - \cos(\phi-\phi')]), \end{aligned} \tag{5.7}$$

where R denotes r_b or r_b', and $\tau, \mu, \nu \in \mathbb{N}$. More specifically, $I_j^{(\ell)}$ can be expressed using $I_{\tau\mu\nu}$'s,

$$\begin{aligned}
I_1^{(0)} &= e^{ikr}\left[r^{-1/2}I_{100} + \frac{1}{2}r^{-3/2}I_{201}\right], \\
I_1^{(2)} &= e^{ikr}\left[r^{-1/2}I_{300} + \frac{1}{2}r^{-3/2}I_{401}\right], \\
I_2^{(0)} &= e^{ikr}\left[r^{-1/2}I_{210} + \frac{1}{2}r^{-3/2}I_{311}\right], \\
I_2^{(2)} &= e^{ikr}\left[r^{-1/2}I_{410} + \frac{1}{2}r^{-3/2}I_{511}\right].
\end{aligned} \tag{5.8}$$

A key step in obtaining the scattering field is then to integrate $I_{\tau\mu\nu}(r,\phi)$. Take I_{201} for example. We first integrate the ϕ' part by expressing the exponent as

$$\cos\phi' - \cos(\phi - \phi') = \sqrt{2 - 2\cos\phi}\ \sin(\theta - \phi'),$$

where

$$\sin\theta \equiv \frac{1-\cos\phi}{\sqrt{2-2\cos\phi}}, \ \text{ and } \ \cos\theta \equiv \frac{\sin\phi}{\sqrt{2-2\cos\phi}}.$$

The integral I_{201} then becomes

$$\begin{aligned}
I_{201}(r,\phi) &= \int_0^{r_b} dr' r'^2 \int_0^{2\pi} d\phi' \cos(\phi - \phi') \\
&\quad \cdot \exp[ikr'\sqrt{2-2\cos\phi}\ \sin(\theta - \phi')] \\
&= 2\pi i \sin(\phi - \theta) \\
&\quad \cdot \int_0^{r_b} dr' r'^2 J_0'(kr'\sqrt{2-2\cos\phi}) \\
&= -2\pi i \sin(\phi-\theta)\frac{r_b^2 J_2(kr_b\sqrt{2-2\cos\phi})}{k\sqrt{2-2\cos\phi}} \\
&= -\pi i k^{-1} r_b^2 J_2(kr_b\sqrt{2-2\cos\phi}),
\end{aligned}$$

where in the last step, we have used $\sin(\phi-\theta) = \sqrt{2-2\cos\phi}/2$. All the integrals are Bessel functions, or more generally, hypergeometric functions. After evaluating all $I_{\tau\mu\nu}$ integrals, we obtain the final scattering fields as

$$\begin{aligned}
H_1^s(r,\phi)_{r\gg r_b} &= a_{11}\frac{e^{ikr}}{r^{1/2}}\Phi_1(\phi) + a_{12}\frac{e^{ikr}}{r^{3/2}}\Psi_1(\phi), \\
H_2^s(r,\phi)_{r\gg r_b} &= a_{21}\frac{e^{ikr}}{r^{1/2}}\Phi_2(\phi) + a_{22}\frac{e^{ikr}}{r^{3/2}}\Psi_2(\phi),
\end{aligned} \tag{5.9}$$

where the angular functions are

$$\begin{aligned}
\Phi_1(\phi) &= \frac{J_2(kr_b\sqrt{2-2\cos\phi})}{2-2\cos\phi}, \\
\Psi_1(\phi) &= \frac{J_3(kr_b\sqrt{2-2\cos\phi})}{\sqrt{2-2\cos\phi}}, \\
\Phi_2(\phi) &= \frac{J_3(kr'_b\sqrt{2-2\cos\phi})}{\sqrt{2-2\cos\phi}}, \\
\Psi_2(\phi) &= \frac{J_4(kr'_b\sqrt{2-2\cos\phi})}{2-2\cos\phi},
\end{aligned} \tag{5.10}$$

and the coefficients a_{ij}'s are given by

$$\begin{aligned}
a_{11} &= -4\pi k^{-1/2}\left(\frac{i}{4}\sqrt{\frac{2}{\pi}}e^{-i\frac{\pi}{4}}\right)\frac{\Delta n(\Delta n+1)r_b^2}{\sigma^2}, \\
a_{12} &= \pi i k^{-1/2}\left(\frac{i}{4}\sqrt{\frac{2}{\pi}}e^{-i\frac{\pi}{4}}\right)\frac{\Delta n(\Delta n+1)r_b^3}{\sigma^2}, \\
a_{21} &= 2\pi k^{-3/2}\left(\frac{i}{4}\sqrt{\frac{2}{\pi}}e^{-i\frac{\pi}{4}}\right)\frac{\Delta n r'_b}{(\Delta n+1)\sigma^2}, \\
a_{22} &= -\pi i k^{-3/2}\left(\frac{i}{4}\sqrt{\frac{2}{\pi}}e^{-i\frac{\pi}{4}}\right)\frac{\Delta n r'^2_b}{(\Delta n+1)\sigma^2}.
\end{aligned} \tag{5.11}$$

By considering only the lowest order $r^{-1/2}$, we can write the scattering field in the form

$$H^s(r,\phi)_{r\gg r_b,r'_b} = \frac{e^{ikr}}{r^{1/2}}\Phi(\phi), \tag{5.12}$$

where $\Phi(\phi) = a_{11}\Phi_1(\phi) + a_{21}\Phi_2(\phi)$. While Eq.(5.12) is derived under the assumption $n_0 = 1$, the cases where n_0 is not unity can be treated by using the simple substitutions $k \to kn_0$ and $\Delta n \to \Delta n/n_0$.

Figures 28(a) and 28(b) show the behavior of the angular part $\Phi(\phi)$ for two distinct cases, corresponding to extreme cases of small and large scatterer-wavelength ratios, respectively. When the ratio r_b/λ is small [Fig. 28(a)], the scattering field is nearly uniform in all directions from the scatterer. In contrast, as the size of the scatterer is increased so that r_b/λ becomes large, the energy associated with the incident wave concentrates mostly in the incident direction, leaving oscillating fields of small amplitude in other directions, as shown in Fig. 28(b). The inset of Fig. 28(b) indicates the oscillatory behavior of the scattering field, which represents the branched but somewhat weak wave flow patterns in different directions. An optimal ratio r_b/λ can be found in between the

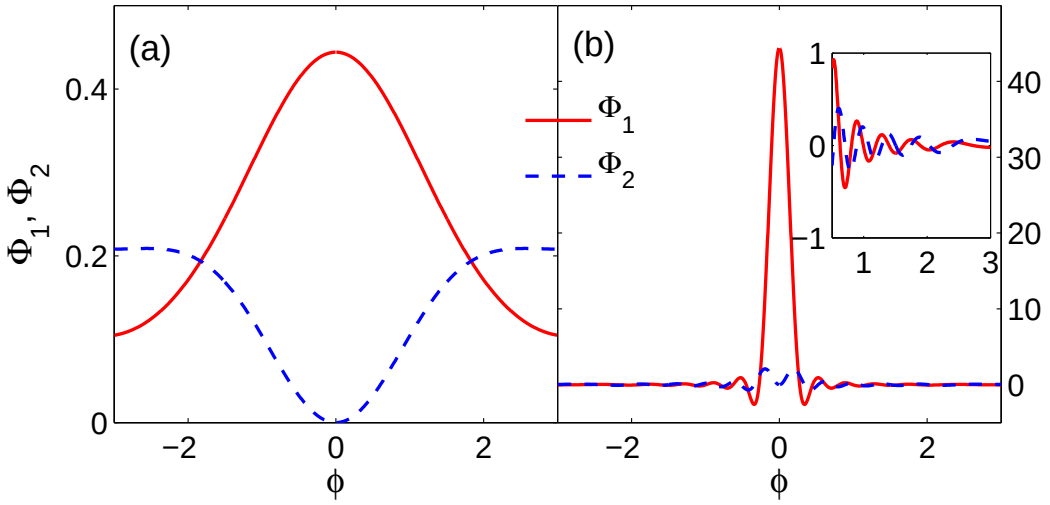

Fig. 28. Angular distributions of the scattering field $H^s(r = const., \phi)$ for two different scatterer-wavelength ratios (r_b/λ). Assuming $r_b = r_b'$, we compute the angular functions Φ_1 and Φ_2 corresponding to scattered fields of order $r^{-1/2}$ under two cases: (a) $r_b/\lambda = 0.3$ and (b) $r_b/\lambda = 3$. The inset of (b) shows the oscillating behavior for $\phi > 0.5$.

two cases shown in Fig. 28, implying that the branched structure emerges only when the size of the scatterer is comparable to the incident wavelength.

The scattering field structure calculated directly from Eq. (5.9) is shown in Fig. 29. In the forward ($+x$) direction, the strength of the scattering field decreases with the radius and the field is composed of a series of magnified flows radiating in all directions. This faithfully reproduces the typical behavior of the scattering field obtained from direct FDFD simulation where the main wave branches fork into smaller ones when encountering refractive index disorders. Note that in Figs. 29(e) and 29(f), both the $r^{-1/2}$ and $r^{-3/2}$ terms have been taken into account, but the $r^{-3/2}$ term is significantly weaker than the $r^{-1/2}$ term in magnitude [as evidenced in Figs. 29 (a-d)], providing further validation of Eq. (5.12).

Our expression for the scattering field of a single scatterer provides qualitative explanation as to why a highly non-uniform structure associated with the field can arise. In particular, the analytic

result explains, instead of a uniform spread of the scattering field in all directions, it tends to form a branched structure with hot spots. In the presence of multiple scatterers, each scattering event gives rise to a few dominant branches that spread out to far field. Some of the remaining scatterers are located within the large branches while most other scatterers are located outside any large branched structure. These latter group of scatterers are essentially not affected by the scattering field. Second-stage scattering will also induce some large branches, which can possibly "meet" with the branches from the first-stage scattering and generate constructive interference. Highly localized structure of the field can result from such interference. The probabilities of destructive and constructive interferences are approximately the same. However, since the higher-level scattering fields are necessarily weaker than the ancestor wave branches, the already generated intense branches cannot be eliminated, especially for the branches near the center direction of the propagation. This provides a plausible explanation as to why in most cases the strongest branch in our simulation either is along the center direction or titles slightly to one side. The former is due to equal probabilities that the random scatterers appear on both sides of the main propagation direction, and the latter is caused by the asymmetric distribution of the refractive index of the scatterer on both sides. This branch-accumulation process is extremely sensitive to the disorders' spatial distribution, leading to the emergence of branched wave patterns.

5.3.2. Multiple disorders

Based on the results from a single scatterer, we now analyze the scattering field due to multiple random scatterers. Although a general analysis of coherent scattering of light in random medium has been available for many years (see, for example, Ref. [98]), our focus here is on the emergence and statistical properties of branched waves. To make analysis feasible, we assume that all scatterers have the same size and are relatively far from each other: $r_{ij} \gg r_b$, as shown in Fig. 30, where r_{ij} is the distance between scatterers i and j, and r_b is the size of each scatterer. The scatterers can then be regarded as weakly correlated, rendering applicable our analysis leading to Eq.(5.12) of the scattering field from a single scatterer. Let i denote the primary scatterer and consider another scat-

terer, denoted by j. Waves scattered from i can undergo a secondary scattering process off scatterer j. Let the original incident wave direction be $+x$ and the direction from i to j be $+x'$. The primary scattering field is the incident wave of secondary scattering off scatterer j. The transformation from frame (x',y') to frame (x, y) is

$$\mathbf{r} = \mathbf{R}(\phi_j)\mathbf{r}' + \mathbf{r}_{ij},$$

where $\mathbf{R}(\phi_j) = \begin{pmatrix} \cos\phi_j & -\sin\phi_j \\ \sin\phi_j & \cos\phi_j \end{pmatrix}$ is the rotation operator. According to Eq. (5.12), we write the scattering field from scatterer i in the vicinity of scatterer j as

$$\begin{aligned} \frac{e^{ik|\mathbf{R}\mathbf{r}'+\mathbf{r}_{ij}|}}{\sqrt{|\mathbf{R}\mathbf{r}'+\mathbf{r}_{ij}|}}\Phi(\phi) &\approx \frac{e^{ikr_{ij}}e^{ikr'\cos\phi'}}{\sqrt{r_{ij}+r'\cos\phi'}}\Phi(\phi_j) \\ &\approx \frac{e^{ikr_{ij}}}{\sqrt{r_{ij}}}\Phi(\phi_j)e^{ikx'}. \end{aligned}$$

Since the $e^{ikx'}$ term is now the incident plane wave for the secondary scattering process, to the lowest order $r^{-1/2}$, the scattering fields from the first and second stages differ by only a fixed pattern factor. To define this factor properly, we consider three scatterers (denoted by i, j, ℓ) through which the light passes successively, forming a multiple scattering process. The cumulative factor can then be defined as

$$q_{i,j,\ell} = \frac{e^{ik|\mathbf{r_j}-\mathbf{r_i}|}}{\sqrt{|\mathbf{r_j}-\mathbf{r_i}|}}\,\Phi\left[\arccos(\mathbf{e}_{ij}\cdot\mathbf{e}_{j\ell})\right],$$

where $\mathbf{e}_{ij}$ is the unit vector in the direction of $\mathbf{r}_j - \mathbf{r}_i$.

Let the subscript 0 denote infinity where the incident wave is originated, and assume that the incident wave beam is first scattered by only one scatterer, labeled by 1. Treating the field point j as another scatterer, we obtain the total field from all possible scattering paths,

$$q_{0,1,j} + \sum_i q_{0,1,i}q_{1,i,j} + \sum_{i,\ell} q_{0,1,i}q_{1,i,\ell}q_{i,\ell,j} + \ldots. \tag{5.13}$$

If the scatterers are randomly distributed, the summation over the same scattering level will not cause order-of-magnitude changes in the scattering field, due to the fact that complex variables of similar magnitude but of random phases will cancel each other, generating a complex number close to the origin in the complex plane. In order to obtain an analytic expression for the total scattering

field so that its statistical properties can be analyzed, we need to make approximations on each $q_{i,j,\ell}$ term. Specifically, we write

$$q_{i,j,\ell} \approx q(\rho, \varphi) = \rho^{-1/2} \exp(ik\rho)\Phi(\varphi),$$

where ρ is the distance between each pair of scatterers and φ is the angle determined by the relative positions of the three consecutive scatterers. Under this approximation, the sum of the first m terms in Eq. (5.13) becomes

$$S_m = q + q^2 + q^3 + \cdots + q^m.$$

Letting $q = ae^{i\theta}$, where $a \geq 0$, we get the sum of the geometric series $S_\infty = ae^{i\theta}/(1 - ae^{i\theta})$. Similar to geometric series of real numbers, $a \in [0, 1)$ is the condition that guarantees the convergence of the sum. In our case, this condition is satisfied because we assume weakly correlated scatterers so that $a \to 0$. The total intensity of the scattering field is then

$$I(\rho, \varphi) = |S_\infty|^2 = \left| \frac{ae^{i\theta}}{1 - ae^{i\theta}} \right|^2.$$

Under the assumption that $a \to 0$, the intensity can be written as

$$\begin{aligned} I &= \left| \frac{ae^{i\theta} - a^2}{1 - 2a\cos\theta + a^2} \right|^2 \\ &\approx \frac{a^2}{1 - 4a\cos\theta} \approx a^2 + 4a^3\cos\theta. \end{aligned}$$

To the lowest order, the intensity can be expressed in the following simple form:

$$I = \frac{|\Phi(\varphi)|^2}{\rho}, \tag{5.14}$$

which is similar to that in the case of a single scatterer. This is reasonable because, under the assumption of weakly correlated scatterers, contributions from higher-level scattering processes are negligibly small.

5.3.3. Scaling laws for intensity distribution

The probability distribution of the intensity of the scattering field can be obtained if the distributions of the position parameters ρ and φ are available. To be concrete, denote $f_{\rho,\varphi}(\rho, \varphi)$ as the

joint probability density function (PDF) of random variables ρ and φ. The expression $I = I(\rho, \varphi)$ alone is not sufficient to derive the PDF of the intensity. What is needed is an auxiliary function $J = J(\rho, \varphi)$. We have

$$f_I(I) = \int f_{I,J}(I, J)dJ = \int \frac{f_{\rho,\varphi}(\rho(I, J), \varphi(I, J))}{\left|\det\left(\frac{\partial(I,J)}{\partial(\rho,\varphi)}\right)\right|}dJ, \tag{5.15}$$

where $\frac{\partial(I,J)}{\partial(\rho,\varphi)}$ is the Jacobian matrix associated with the corresponding transformation. The joint PDF of the variables in the polar coordinate is proportional to the unit area of the two-dimensional plane, $f_{\rho,\varphi} \sim \rho$, and a proper choice for $J(\rho, \varphi)$ is $J = \varphi$. We then obtain the following algebraic scaling law of the PDF with respect to the intensity of the scattering field:

$$f_I(I) \propto I^{-\gamma}, \tag{5.16}$$

where $\gamma = 3$ for our minimal model.

To verify the algebraic scaling law, we carry out extensive FDFD computations for different realizations of random scatterers of different densities, which are uniformly distributed within a 35μm $\times$ 70μm rectangular dielectric medium, as shown in Figs. 31 and 32 for two cases. From these results (and many other cases as well), we observe branched wave patterns and the associated algebraic scaling law for the high intensity distribution of the large branches, as predicted by our theory. Especially, when the random scatterers are weakly correlated, the algebraic (or power-law) scaling behavior is quite robust, implying the existence of "hot" branches with extremely high local intensities. As the density of the random scatterers is decreased, this hallmark of branched waves tends to be somewhat weakened because, when the scatterers are further apart, the intensity of the wave scattered from one scatterer may already have weakened significantly before reaching the next scatterer, making it less probable for fields from different levels of scattering to interfere constructively.

5.3.4. Effect of shape of random scatterer

Our theoretical analysis and numerical simulations indicate that the shape of the random scatterer has little effect on the scaling law associated with the intensity of the branched wave patterns. The

shape, however, can affect the weight of each of the r^n term as well as the weights of the H_1^s and H_2^s terms in, for example, the scattering fields in Fig. 29. Because the total scattering field is the sum of all terms, a change in the shape of the scatterer can induce a change in the pattern of the scattering fields. But if the scatterers are sparse in the medium, the effect can still be quite small. Additional insights can be obtained by examining the process leading to the scattering intensity given by Eq. (5.14). When we perform the integration to obtain the PDF of intensity, the polar angle ϕ part only contributes to the normalization constant while the exponent value -3 remains unchanged. This treatment is valid for the lowest-order approximation of intensity, in which the scatterer shape can only affect the angular ϕ part and therefore will not affect the field intensity distribution. When high-order terms are included, the polar angle may become important, in which case the shape of the scatter can affect the algebraic scaling exponent in the branched wave intensity distribution.

5.4. Conclusions and discussions

Branched structures are an extreme type of wave phenomena that were historically documented in oceanography. Recent experimental efforts have demonstrated, however, that they can occur in a wide variety of physical systems such as two-dimensional electron gas, superfluid Helium, microwave systems, optical fibers, and optical cavities. Despite the intense efforts, the physical origin of branched waves remains to be elusive and an actively debated issue. For example, earlier it had been thought that nonlinearity, or weak nonlinearity, should be a necessary condition for branched waves, but very recent experiments demonstrated that even linear medium can generate these waves [84, 88]. It seems from all previous works, though, that random wave scattering is a necessary condition for the emergence of branched waves. In many experiments, significant deviations of the light intensity from the Gaussian distribution were observed. In fact, a characteristic feature of branched waves is the "long-tail" distribution in their intensities, leading to localized regions in the space with significantly higher intensity than those in the rest. A paradigmatic model that contains absolutely the minimal physical ingredients necessary for branched waves is needed to understand the origin of these exotic waves.

We have proposed a minimal model to explain the emergence of branched waves. Our model contains two essential ingredients: (1) a finite medium for linear wave propagation, and (2) random scatterers in the medium whose physical properties deviate from those of the background medium. To facilitate computation and theoretical analysis, we have considered wave systems in two dimensions. For numerical simulations we assume a generic form of the refractive-index distribution function for each scatterer. For analytic treatment, we have used an approximate form of the index function. In both cases, robust branched wave patterns in a wide range of system parameters with algebraic (power-law) tails in the distribution of the wave intensity have been observed or predicted, indicating that branched waves are a general phenomenon, regardless of the difference in the physical properties of the random scatterers. Our analysis suggests that the origin of branched waves can be attributed to two basic phenomena: (1) break-up of wave by a single scatterer, and (2) constructive interference of "broken waves" by multiple scatterers randomly located in the space. Note that these two phenomena are fairly "elementary" in wave physics, and we believe that they explain why branched waves should be a universal phenomenon in all kinds of wave systems. Although our computations and analysis are for optical waves, the physical insights should be applicable to many other wave systems in various areas of science and engineering.

We mention that, in electromagnetics, coherent multiple scattering of light through random media was studied extensively in the past [98,101,102], although these studies were not directly pointed at the phenomenon of branched wave structures. A related phenomenon is Anderson localization of light in random media. In particular, a basic theory in the scattering of electromagnetic waves in random media is the scaling theory of localization [103], where the scattering strength, characterized by the ratio of wavelength λ and the math free path l, increases as l decreases. In the classical limit where $\lambda/l \ll 1$, phase correlation is weak so that the approximation of self-avoiding multiple scattering can be used. However, in the strong scattering limit, constructive and destructive wave interferences become dominant. In this case, one has $\lambda \sim l$, and the phenomenon of light localization emerges, similar to the phenomenon of Anderson localization in condensed matter physics [104].

In fact, Anderson localization of light was theoretically predicted [99, 100] and experimentally confirmed [105–108].

The study of complex wave patterns in optical media and their underlying physical mechanism can have broader applications. For example, structural disorders are inherent to the fabrication process of many optical devices such as photonic crystals [109, 110], and the occurrence of extremely high intensity wave branches can be detrimental to the device operation due to the random nature of the waves. Even worse, the existence of hot spots of excessive intensities associated with the branched wave structures can cause irreversible damage to the device. On the other hand, since the random, spatially localized disorders that we treat in this chapter can have positive or negative refractive constants, our work may be relevant to the extremely active field of optical metamaterials [111, 112] and devices. From a different perspective, the possibility that branched waves with hot spots can be induced in realistic optical media implies potential applications in defense, where defeating adversarial systems using electromagnetic waves is of significant interest. Suppose an adversarial system that contains some optical media poses a threat. Inducing branched waves in the media may cause desirable damages to the intended operation of the system.

A final remark is that, the algebraic scaling exponent $\gamma = 3$ in the intensity distribution of branched waves is obtained for Gaussian type of refractive-index distribution function or its approximation for random scatterers. Deviation from the Gaussian shape can cause the scaling exponent to be different. Thus, in general we do not anticipate to obtain the exponent value of 3 associated with branched waves. However, the algebraic scaling relation or the long-tail behavior is generic for branched waves arising in different fields.

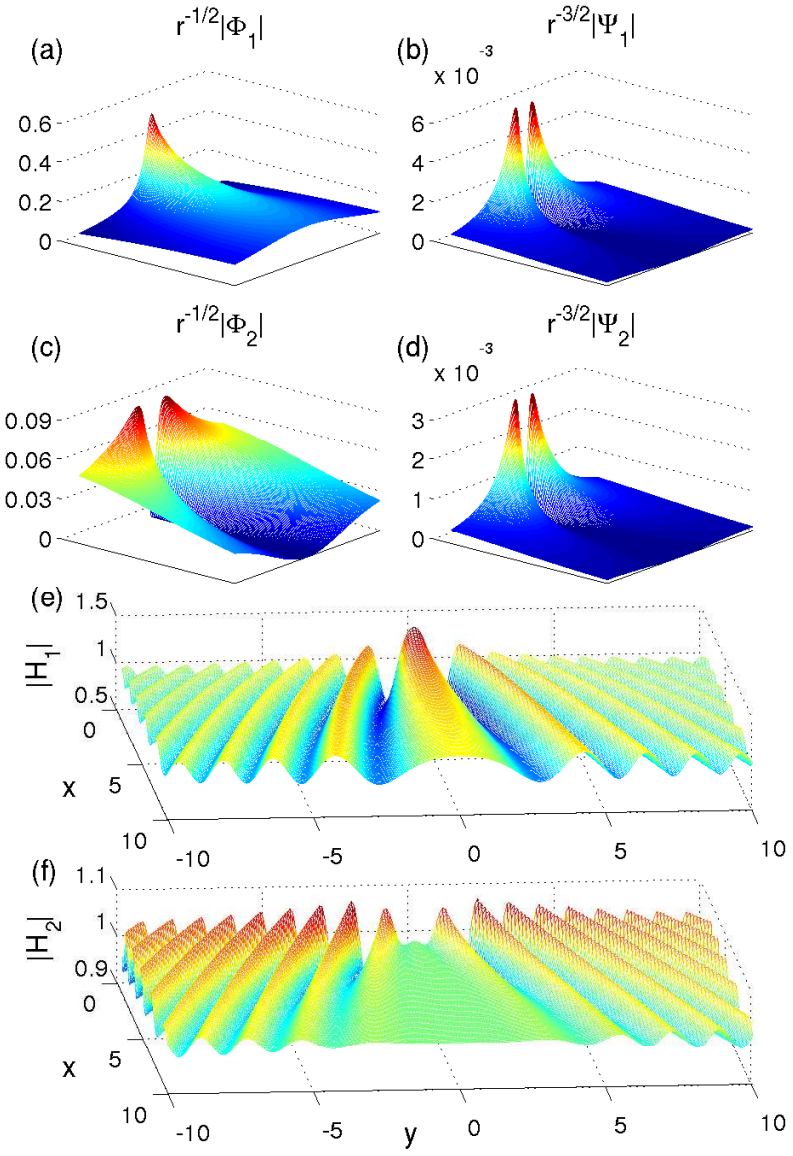

Fig. 29. Forward ($+x$) scattering fields. Panels (a) and (c) show the magnitude of forward scattering fields of order $r^{-1/2}$ from the source term f_1 in Eq. (5.4), while panels (b) and (d) show the field magnitude of order $r^{-3/2}$ from the source term f_2, which are much smaller at far field. The total field magnitude $|H_1|$ and $|H_2|$ from two source terms are shown in (e) and (f), respectively. The incident wave (of wavelength $\lambda = 1\mu$m) is sent in the $+x$ direction on a scatterer located at the origin. The parameters characterizing the refractive-index function of the scatterer are $\sigma = 0.22\mu$m and $\Delta n = -0.5$.

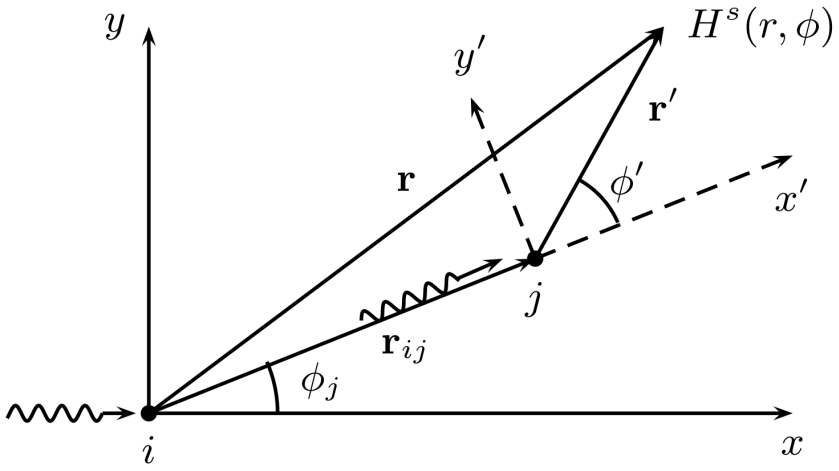

Fig. 30. Multiple scattering from two scatterers, labeled as i and j and separated by distance $|\mathbf{r}_{ij}|$. In the case of well-separated scatterers, the final scattering field can be interpreted as a cumulative scattering process by multiple scatterers, with each individual scattering event being analogous to the scattering of a single disorder.

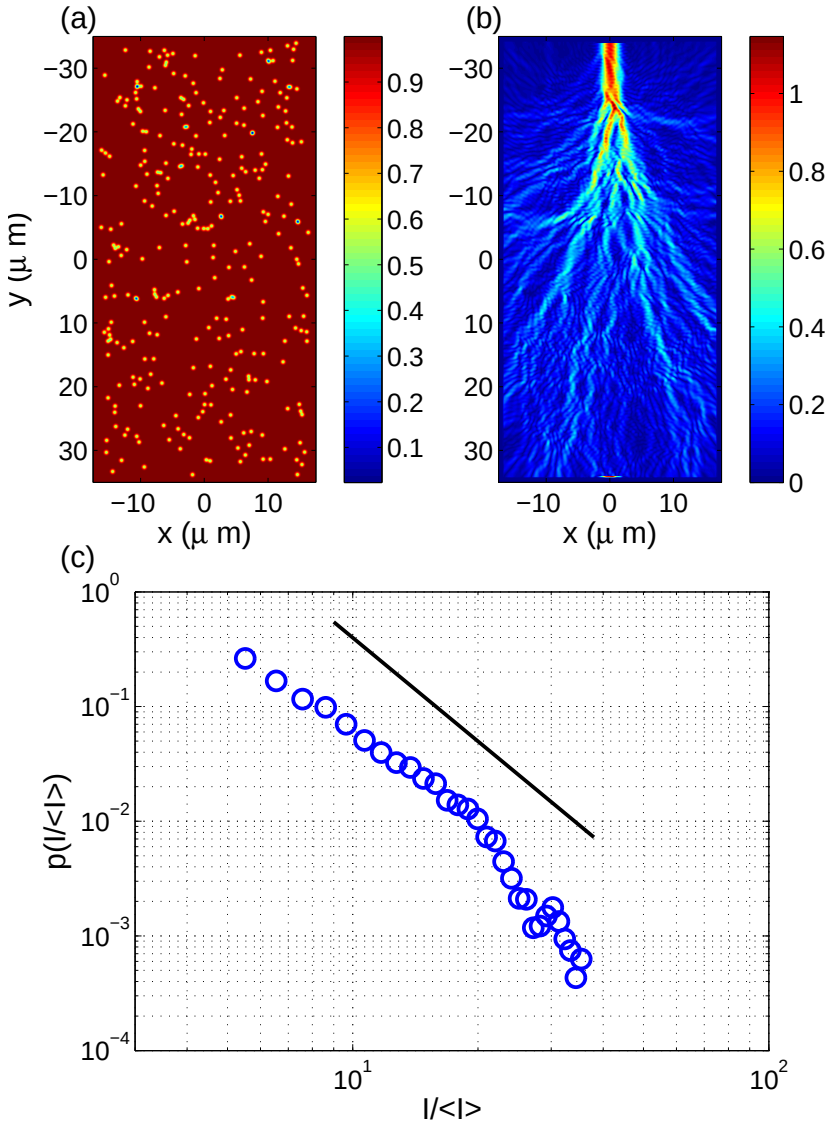

Fig. 31. (a) Distribution of 300 random scatterers in a $35\mu\text{m} \times 70\mu\text{m}$ uniform medium. (b) Branched wave magnitude from FDFD simulation. The incident wave is uniform with width λ and sent in the $+y$ direction, where $\lambda = 1\mu\text{m}, n_0 = 1, \Delta n = -0.5, \sigma = 0.22\mu\text{m}$. (c) Numerically obtained scaling law of the high intensity distribution (blue circles) and the theoretical prediction (solid line $\sim I^{-3}$). Slight deviation from the predicted pow-law scaling is observed at extreme high intensities due to the violation of sparse scatterer assumption in theory.

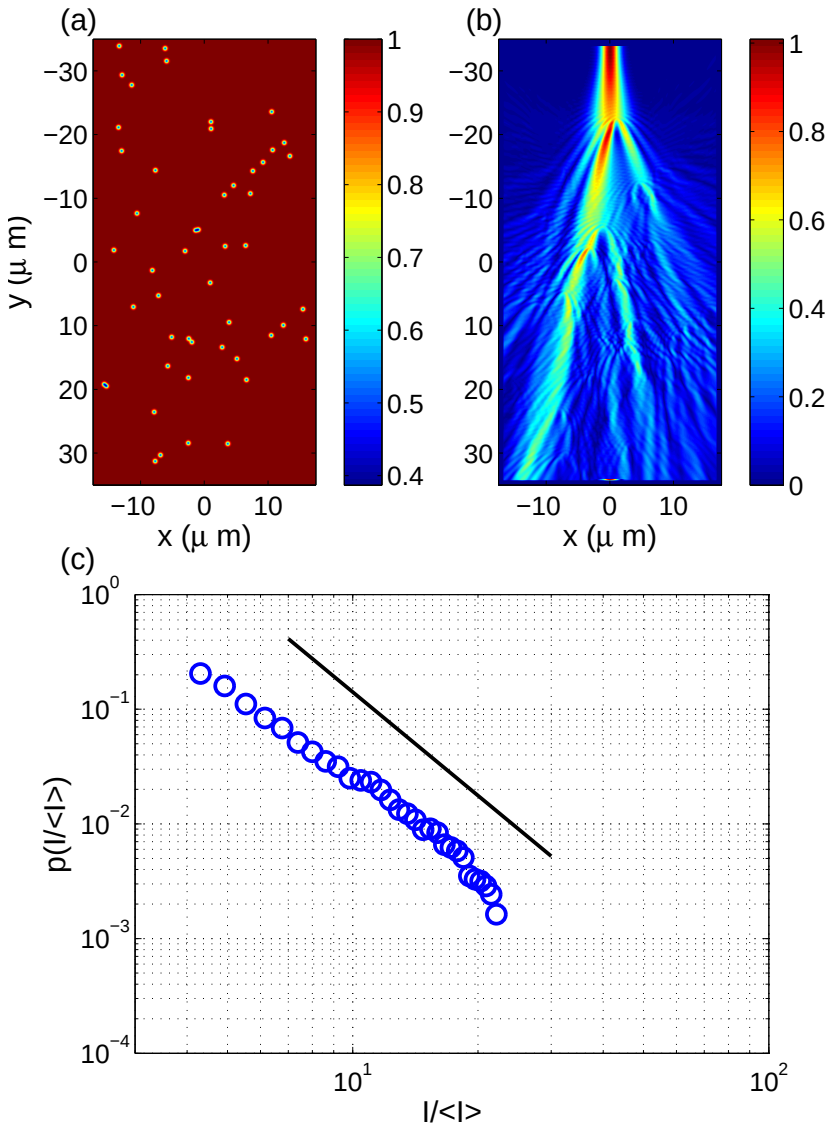

Fig. 32. (a) Distribution of 50 random scatterers in a 35μm $\times$ 70μm uniform medium. (b) Branched wave magnitude from FDFD simulation. The incident wave is uniform with width λ and sent in the $+y$ direction, where $\lambda = 1\mu\text{m}, n_0 = 1, \Delta n = -0.5, \sigma = 0.23\mu\text{m}$. (c) Numerically obtained scaling law of the high intensity distribution (blue circles) and the theoretical prediction (solid line $\sim I^{-3}$).

6 . CYCLIC COMPETITION OF MOBILE SPECIES ON CONTINUOUS SPACE: PATTERN FORMATION AND COEXISTENCE

6.1. Background

All existing microscopic models of the competition dynamics of dispersing species assume lattices as the underlying spatial structure on which movements of individuals and their interactions with neighboring individuals occur. While there were efforts to investigate the effect of shortcuts among non-adjacent sites on the competition dynamics [140, 141], in these models the space is still discrete. Considering that, in realistic ecosystems, the physical space that supports the dynamics is continuous, it is of interest to ask what might happen to RPS dynamics and species coexistence in a continuous space. The purposes of this chapter is to study this issue. In particular, we construct a continuous-space RPS model for mobile species and address one fundamental question: what is the role of species-interaction range in coexistence? This issue has not been investigated in previous discrete-space models, as the interaction range was usually limited to neighboring individuals. In our continuous-space model, the interaction range becomes a physical parameter that can be adjusted. Since, in discrete-space models, mobility is the single most important parameter whose effect on species coexistence has been the focus of most previous works, our continuous-space model allows us to explore the fundamental interplay between two parameters, i.e., mobility and interaction range, with respect to coexistence/extinction.

Our main results are the following. (1) When the interaction scale in the continuous space is increased, the probability of coexistence exhibits a non-monotonic behavior with one local minimum and one local maximum, regardless of the size of the continuous space. Close to the minimum, a switching behavior in the spatial patterns occurs between spiral and plane waves, as a result of the collision of spirals and stochastic effects. (2) Contrary to the basic result from the discrete-space models that high mobility induces extinction, we find that the role of mobility as to whether it promotes or prevents coexistence depends on the range of spatial interaction. To substantiate these findings, we have derived a theoretical model based on nonlinear partial differential equations

(PDEs) to analyze some of the results obtained from direct simulations of RPS dynamics. The PDE model can successfully reproduce the dependence of the spiral wavelength on the interaction range as well as the switch from plane waves to spiral waves. However, the model cannot reproduce the non-monotonic coexistence probability due to the absence of intrinsic stochastic effect. Our continuous-space RPS model enriches greatly the possibilities to explore and predict the dynamics of cyclically interacting species in a physically more realistic way, facilitating experimental research on species competitions and biodiversity.

In Sec. 6.2, we describe the RPS model on continuous space and investigate species coexistence with respect to interaction range, pattern formation, and individual mobility. In Sec. 6.3, a PDE model is proposed to explain the results produced by stochastic model and an explanation for the transition between spiral- and plane-wave patterns in terms of examining the wavelength. In Sec. 6.4, we study an alternative model for specie coexistence by separating competition and reproduction in the RPS game. Conclusions are presented in Sec. 6.5.

6.2. Competition dynamics on continuous space

6.2.1. Model description

We consider three cyclically competing subpopulations (referred to as A, B and C) on a square cell of linear size $L = 1$ under periodic boundary conditions. The species compete with each other for limited resources according to the following general rules:

$$\begin{aligned} AB &\xrightarrow{u} AA, \\ BC &\xrightarrow{u} BB, \\ CA &\xrightarrow{u} CC, \end{aligned} \tag{6.1}$$

which occur only if the distance between two individuals is less than r, the interaction radius. At each simulation step, a randomly chosen individual i from one species eliminates, within its interaction range, one individual j from the next species in the cycle at rate u. At the same time, i reproduces at the position of j. In this sense, competition and reproduction occurs simultaneously and the two processes are combined. Mobility is incorporated into the dynamics such that individu-

als can move to a random position within the same range of radius r, and this occurs at rate s. The probabilities of competition and movements are normalized by $(u + s)$, i.e., their probabilities are $u/(u + s)$ and $s/(u + s)$, respectively. In the absence of mobility, the probability of competition is 1, regardless of the value of u. Individuals from all three species are represented by points in the plane at different locations. Initially the plane is randomly populated with individuals from all three species. To make an unbiased comparison for different population sizes, we normalize the radius r by the average distance between individuals: $R = r\sqrt{N}$, with N being the total population size.

6.2.2. Species coexistence and pattern formation

We first study the case where mobility is absent and focus on the effect of interaction range on the coexistence probability p_{coex}. The results are shown in Fig. 33. We find that, when the radius R is close to zero, the system reaches a trivial, static coexistence state where the average distance between individuals is greater than the interaction range, so effectively there are no interactions among most individuals and no death/birth can occur, in contrast to what can happen in a dynamic equilibrium. As R exceeds the critical value $R_T \approx 1.0$, the system experiences an abrupt transition to a dynamical coexistence state in which all species survive in the form of certain spatial patterns. When R is increased from R_T, p_{coex} exhibits a non-monotonic behavior, reaching a local minimum at R_{Min} and a local maximum at $R_{Max} > R_{Min}$. This is counterintuitive because one may expect a monotonic decrease in p_{coex} based on the existent result in the literature that local interactions ensure coexistence while it is lost at larger scales [118, 119]. However, our results demonstrate a nontrivial transition in p_{coex} from small to large values with an optimal degree of coexistence occurring for $R = R_{Max}$. We observe further that coexistence is ruled out for large interaction range, which is consistent with the results from *E.coli* experiment [118, 119].

For $R \lesssim R_{Max}$, the underlying spatial pattern switches between spiral and plane waves in time, as shown in Fig. 34 (top row). Both types of patterns are relatively stable to generate coexistence but, due to the stochastic effect, intermittent switches between the patterns occur. The evolutions of species densities (ρ_a, ρ_b, or ρ_c) associated with the two types of patterns are also quite different.

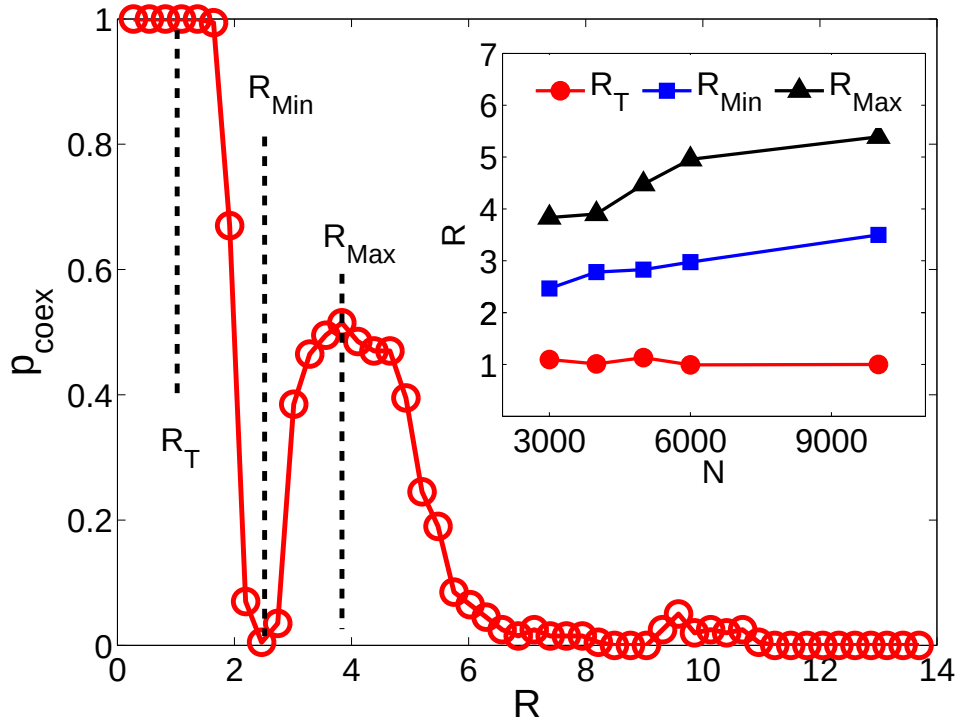

Fig. 33. Coexistence probability p_{coex} as a function of the radius R of interaction range in the absence of individual mobility for $N = 3000$, $L = 1$, where p_{coex} is defined to be the ratio of the number of the survival cases to the total number (200) of independent simulation realizations. The probability is calculated after a transient time $T \propto N$ from random initial configurations with the same densities of three species. The inset shows the dependence of R_T, R_{Min} and R_{Max} on the population size N.

In particular, in the spiral-wave phase each density exhibits relatively high frequency oscillations as compared to the plane-wave phase [Fig. 34(a)]. Figure 34(b) shows the average densities of the three species over a time window. Typical patterns occurring near the switching points are also shown in Fig. 34 (bottom row, left two panels). The transition from plane to spiral wave patterns occurs due to the stochasticity-induced penetration of individuals of one species into the domain of neighboring species and exclusion of individuals of the next species in the cyclic loop. At the mixing point, due to the cyclic competition, three species twist and form spiral waves, breaking the plane wave. On the other hand, the transition from spiral to plane wave can be ascribed to the collision of two large local spiral waves. After they collide and vanish, the outgoing wavefront becomes approximately straight, decreasing significantly the curvature of the wave. Thus, when the wavelength of spiral waves is proper, stochastic effects intrinsic to the underlying dynamical system can trigger the transition. In general, the probability of finding the switch between spiral and plane waves is related with the probability of species coexistence. There are two major directions along which the plane wave can travel: axial and diagonal directions, as shown in Fig. 34 (bottom row, right two panels), due to the symmetry in both orthogonal axes. It is noteworthy that spiral waves are quite common in excitable media and population dynamics [142–146], and traveling waves have been found in a number of cyclic populations [147]. However, the switch between the two types of waves is rarely studied, especially in stochastic systems. In this regard, our work provides quantitative insight into this issue.

Since the nontrivial relations between the normalized selection range R and the coexistence probability P_{coex} and the pattern switch are for the special case of $L = 1$, it is of interest to justify the validity of such results in general cases. We take into account the effect of the size of the square lattice on the coexistence curve by defining a rescaled selection range $R_L \equiv (r/d-1)/L+1$, where $r \in [0, L]$ is the physical or original selection range, and $d = L/\sqrt{N}$ is the average distance between two neighboring individuals when individuals are uniformly distributed on the square cell initially. For $L = 1$, we have $R_L(L = 1) = r\sqrt{N} = R$ so that the rescaled selection range R_L reduces to

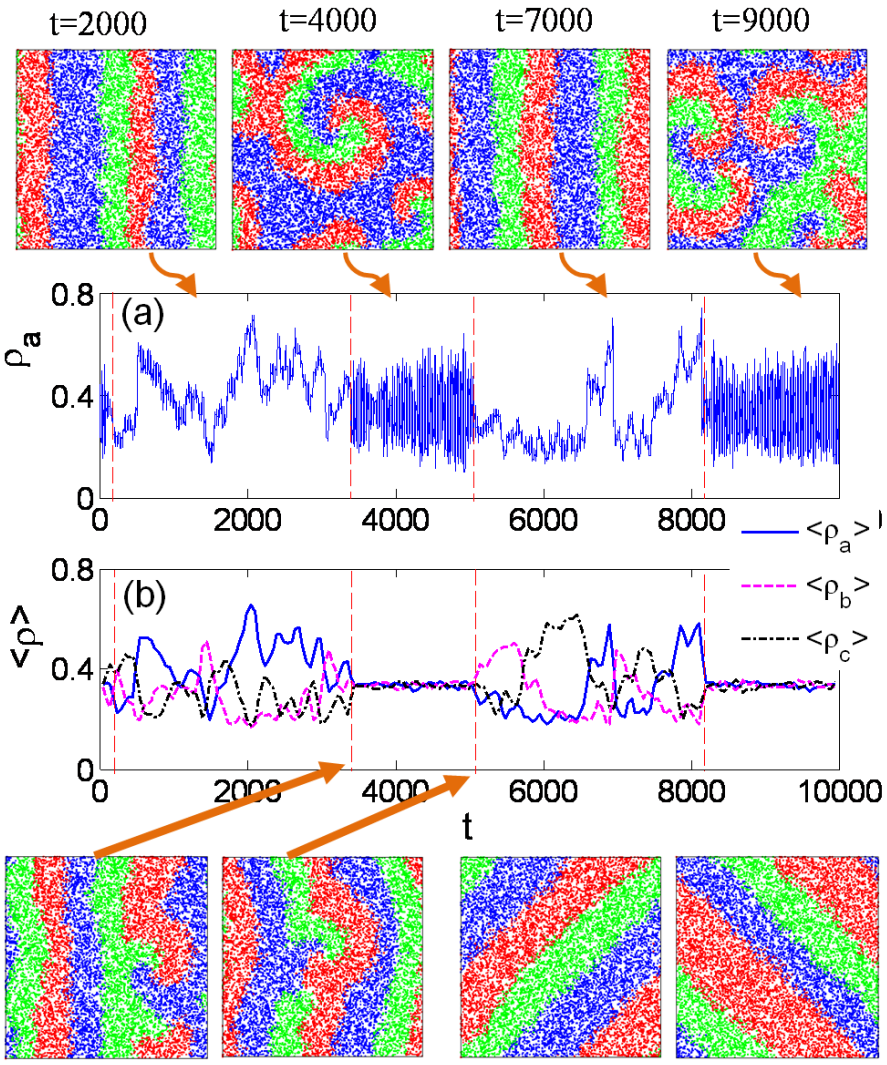

Fig. 34. For $N = 10000$ and $R = 4.25$, pattern transition between plane waves and spiral waves (top row), (a) the corresponding time series of species density ρ_a, (b) average species density $\langle\rho_a\rangle$, $\langle\rho_b\rangle$, $\langle\rho_c\rangle$, typical patterns about the transition point (two left panels, bottom row), and plane wave traveling along diagonal directions (two right panels, bottom row). Red (gray) , blue (dark gray), and green (light gray) represent species A, B, and C, respectively. The rapid oscillations in the density are due to the fact that, in the spiral-wave phase, the curved boundaries between different species generate relatively large interaction areas so that many more individuals can interact with others in a random manner. The average species density $\langle\rho\rangle$ is taken by down-sampling the original time series and the average values are taken over 100 time steps.

the normalized selection range R shown in Figure 33. The interpretation of R_L is understood as follows. The average distance d between neighboring individuals is the first critical distance above which the system experiences an abrupt transition from static to dynamical coexistence, thus we set d to be the unit of the selection range. The scale factor $1/L$ is used to normalize the size of the square cell. The rescaled selection range R_L can ensure $R_L = R = 1$ when $r = d$. Figure 35 shows the effect of the cell size associated with different population N on the coexistence probability p_{coex}. We can see that p_{coex} does not depend on the size of the square lattice except for small populations, e.g., $N = 1500$ and $N = 2000$, where the stochastic effect becomes more prominent, suppressing coexistence because of the spatial non-uniformity, leading to lower peak values of p_{coex}. In contrast, for $N > 2000$, the curves of $p_{coex} \sim R_L$ collapse into a single one, regardless of the size of the square cell, indicating that the size L has little effect on coexistence.

Although the cell size L with respect to the rescaled selection range R_L has little effect on the coexistence behavior and the spatial pattern, it is of interest to explore how the cell size L influences the pattern switch for fixed physical selection range r. We have thus carried out simulations by fixing the density of individuals and choosing some typical values of r. As shown in Fig. 36(a), r is chosen to be at the peak of the coexistence probability P_{coex} for $L^2 = 2$. The switch between spiral and plane waves is found to be quite common under this condition [Fig. 36(a)]. However, for the same value of r, when L^2 is reduced to $1/2$, the pattern switches no longer occur and two species become extinct [Fig. 36(a)]. This phenomenon can be explained by taking the relationship between L and R_L into account. For fixed values of r and species densities, according to the definition of the rescaled selection range R_L, we have $R_L \sim 1/L$. If L is reduced, R_L is enhanced, resulting in a change in R_L from that associated with the local maximum of P_{coex} to that in the extinction region, as shown in Fig. 35. Further insights can be obtained by examining the wavelength, which is determined exclusively by r, irrespective of the value of L. When L is reduced for fixed r, the wavelength becomes relatively larger as compared to L and exceeds the cell size, leading to extinction. We have also examined the values of r about the local minimum value of P_{coex}. As

shown in Fig. 36(c), for $L^2 = 5/6$, there are switches between the two kinds of patterns. However, when L^2 is increased to 2, switches can never occur [Fig. 36(d)] because R_L due to the increase of L is changed to the left side of the local minimum, which is outside of the pattern switch region. We have also studied the size effect on the spatial patterns for other values of r. The effect can be explicitly predicted in terms of the change in the rescaled selection range R_L. All these imply that the cell size has a great influence on the spatial pattern for a fixed physical selection range. The spatial patterns are thus determined by the rescaled selection range R_L with respect to different cell sizes.

6.2.3. Role of individual mobility

We next investigate the role of individual mobility. A macroscopic mobility can be defined by rescaling the mobile rate s of individuals using the system population N according to $M \equiv s/N$ [132, 133]. We find that mobility can either promote or hamper coexistence, depending on the interaction radius R, in contrast to previous results [132] that large mobility typically leads to extinction. For $R \approx R_{Min}$, the coexistence probability p_{coex} can be enhanced by mobility, as shown in Fig. 37(a). We see that there exists an optimal value of mobility M at which p_{coex} is considerably larger than that without mobility, suggesting a positive role of mobility on continuous plane in promoting coexistence. However, in other regions of R values, p_{coex} can be reduced by increasing M, as shown in Fig. 37(b). These results reveal a more complicated role of mobility in ecosystems than previously thought: species movements to gain essential life-sustaining resources can either facilitate or jeopardize coexistence. Species movements are somewhat equivalent to the expansion of interaction range in the sense that individuals outside the range of a certain individual can be reached when the individuals are mobile. We can thus rescale the value of R by the mobility and the resulting curve in Fig. 33 would shift to the left by a small amount so that the value of p_{coex} at R_{Min} is augmented. This phenomenon is illustrated in Fig. 38. We can see that not only at $R \approx R_{Min}$ (as evidenced in Fig. 37), but also within a relatively large region of the selection range around $R \approx R_{Min}$ can mobility promote biodiversity. In the meantime, the negative role of

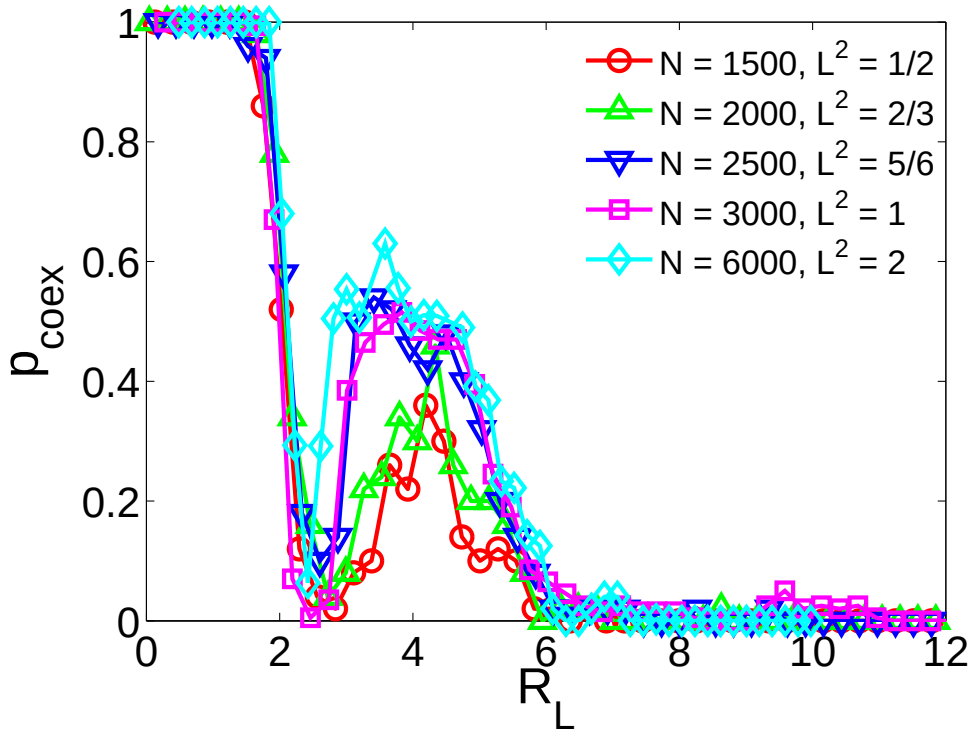

Fig. 35. The effect of the size of the square cell on the coexistence probability p_{coex} with respect to the rescaled selection range R_L. We compute coexistence curves for five different combinations of the cell size L and the total population N. The non-monotonic behavior of $p_{coex} \sim R_L$ is independent of the cell size, as indicated by the collapse of the three curves into a single one for $N = 2500, 3000, 6000$. The peaks for $N = 1500$ and 2000 are lower, due to a relatively stronger stochastic effect for smaller values of N.

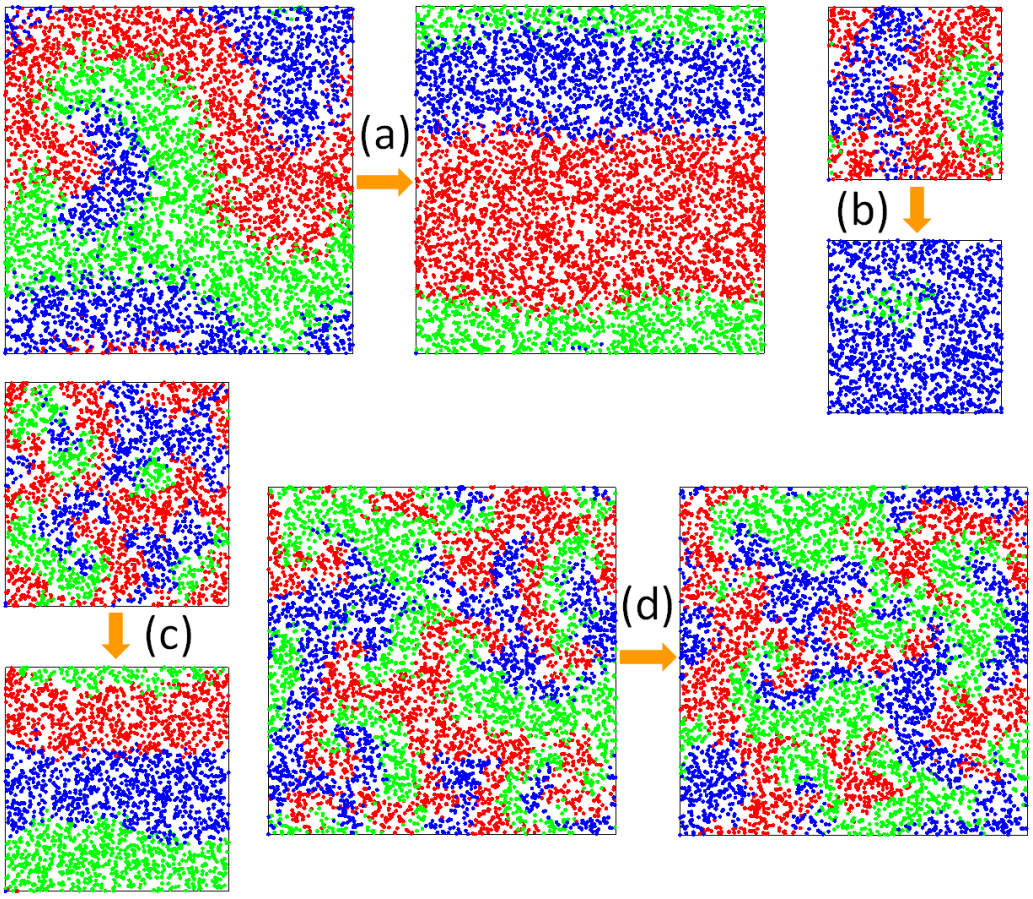

Fig. 36. Spatial patterns at physical selection range $r = 0.0913$ for (a) cell size $L^2 = 2$ and (b) $L^2 = 1/2$, and at $r = 0.0365$ for (c) cell size $L^2 = 5/6$ and (d) $L^2 = 2$. For all these patterns, the density N/L^2 of individuals is fixed to be 3000. In (a), the rescaled selection range $R_L = 3.82$, which corresponds to the R_{Max} in Fig. 35. Spiral waves and plane waves can switch between each other at this R_L. In (b), species go extinct for smaller cell size than (a), because $R_L = 6.66$, is in the extinction region. In (c), $R_L = 2.10$, close to R_{Min} in Fig. 35; while in (d), by increasing L, R_L decreases to 1.71, which is outside of the pattern switch region (the peak), so that pattern switch never occurs. The color (grayscale) scheme is the same as in Fig.34.

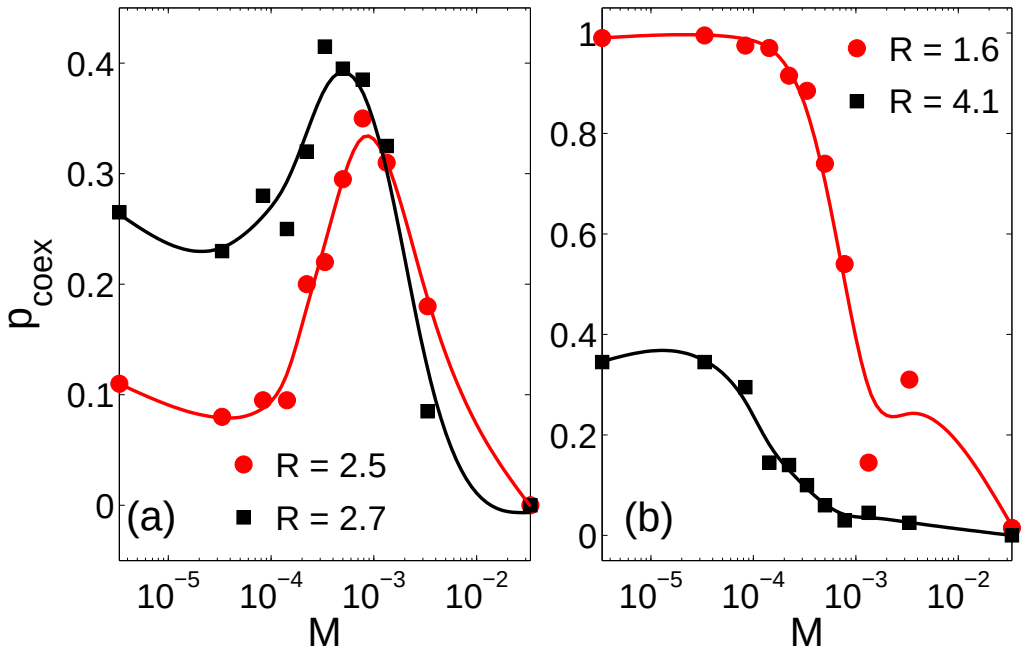

Fig. 37. For $N = 3000$, coexistence probability p_{coex} as a function of the individual mobility M for different values of interaction range R. (a) For $R = R_{Min} = 2.5$, a proper value of M can considerably enhance the coexistence probability p_{coex}. (b) In other region of R, as is M increased, coexistence is always inhibited.

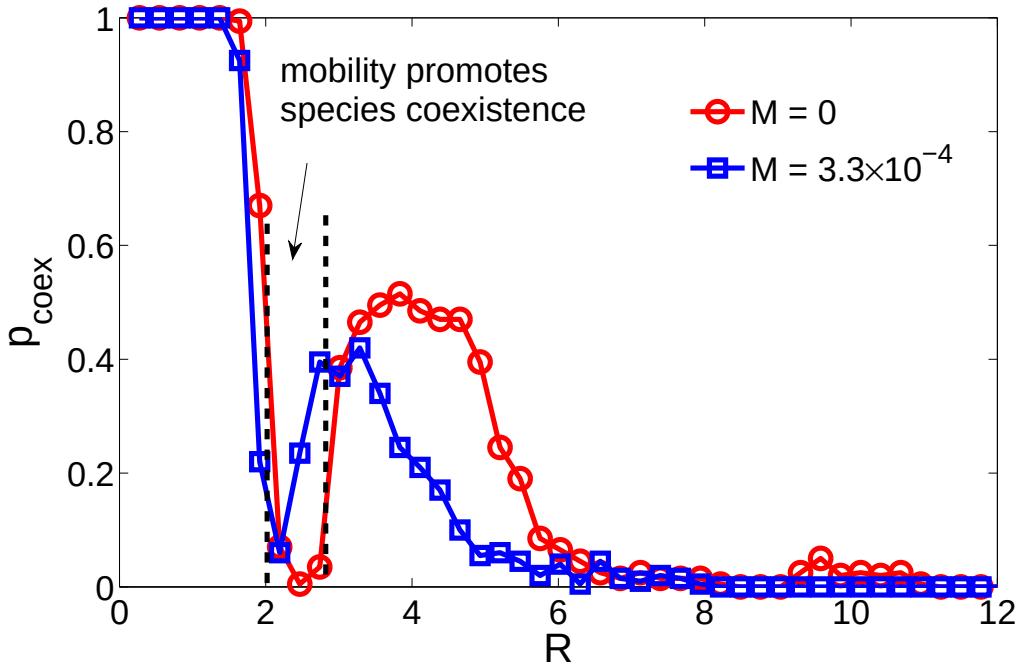

Fig. 38. Comparison of the coexistence curves for $M = 0$ and $M = 3.3 \times 10^{-4}$ ($u = s$), where the population size is $N = 3000$. When mobility is present, in the region between two dashed lines, mobility promotes coexistence. Other parameters are the same as in Fig. 33.

mobility in biodiversity can also be seen in other regions of Fig. 38 around the peak of p_{coex}.

6.3. PDE model and explanation for the coexistence-extinction transition

6.3.1. Derivation of PDE model

We now derive a set of partial differential equations based on the complex Ginsburg-Landau equation (CGLE) to explain our numerical findings. The starting point is to decompose the reaction $AB \longrightarrow AA$ as $AB \longrightarrow A\oslash + A\oslash \longrightarrow AA$, where $\oslash$ denotes an empty position. The two reactions occur simultaneously within the range of radius R. Let $a(\boldsymbol{r}, t)$, $b(\boldsymbol{r}, t)$ and $c(\boldsymbol{r}, t)$ denote the densities at position $\boldsymbol{r}$ and time t for the three subpopulations, respectively. We obtain the

following PDEs:

$$\begin{aligned}
\partial_t a(\boldsymbol{r},t) = \quad & D\Delta[a(\boldsymbol{r},t)+c(\boldsymbol{r},t)] + [1-\rho(\boldsymbol{r},t)]\tfrac{1}{S_R}\cdot \\
& \textstyle\int_{G_{\boldsymbol{r}}} d\boldsymbol{r}' a(\boldsymbol{r}',t) - a(\boldsymbol{r},t)\tfrac{1}{S_R}\int_{G_{\boldsymbol{r}}} d\boldsymbol{r}' c(\boldsymbol{r}',t), \\
\partial_t b(\boldsymbol{r},t) = \quad & D\Delta[b(\boldsymbol{r},t)+a(\boldsymbol{r},t)] + [1-\rho(\boldsymbol{r},t)]\tfrac{1}{S_R}\cdot \\
& \textstyle\int_{G_{\boldsymbol{r}}} d\boldsymbol{r}' b(\boldsymbol{r}',t) - b(\boldsymbol{r},t)\tfrac{1}{S_R}\int_{G_{\boldsymbol{r}}} d\boldsymbol{r}' a(\boldsymbol{r}',t), \\
\partial_t c(\boldsymbol{r},t) = \quad & D\Delta[c(\boldsymbol{r},t)+b(\boldsymbol{r},t)] + [1-\rho(\boldsymbol{r},t)]\tfrac{1}{S_R}\cdot \\
& \textstyle\int_{G_{\boldsymbol{r}}} d\boldsymbol{r}' c(\boldsymbol{r}',t) - c(\boldsymbol{r},t)\tfrac{1}{S_R}\int_{G_{\boldsymbol{r}}} d\boldsymbol{r}' b(\boldsymbol{r}',t),
\end{aligned} \tag{6.2}$$

where D is a diffusion constant induced by the finite interaction range, $G_{\boldsymbol{r}}$ specifies the circular interaction domain of radius R centered at $\boldsymbol{r}$, $\rho(\boldsymbol{r},t)$ is the total species density and S_R is the area of the interaction domain $G_{\boldsymbol{r}}$. We use the average density within the interaction range to approximate the density at the center. To explain the construction of the PDE model, we consider the density of one species, say $a(\boldsymbol{r},t)$. Firstly, the increment in $a(\boldsymbol{r},t)$ with time at position $\boldsymbol{r}$, $\partial_t a(\boldsymbol{r},t)$, is proportional to the probability of empty space density $1-\rho(\boldsymbol{r},t)$ and the average density of its own species within its interaction range $(1/S_R)\int_{G_{\boldsymbol{r}}} d\boldsymbol{r}' a(\boldsymbol{r}',t)$, according to the reaction rule $A\oslash \longrightarrow AA$. Secondly, the decrement of the density of species A with respect to time, $-\partial_t a(\boldsymbol{r},t)$, is proportional to the density of itself $a(\boldsymbol{r},t)$ and its prior species in the cycle within the interaction range $(1/S_R)\int_{G_{\boldsymbol{r}}} d\boldsymbol{r}' c(\boldsymbol{r}',t)$, according to the reaction rule $CA \longrightarrow C\oslash$. However, to incorporate the long-range interaction parameterized by selection range R, diffusions of both A and C should be taken into account, which are characterized by two diffusion terms $D\Delta[a(\boldsymbol{r},t)+c(\boldsymbol{r},t)]$. The diffusion term on the right-hand side of the first equation in Eq. (6.2) thus characterizes the copying of an individual from prior specie to the neighborhood of an individual from next species; while other terms in the equation correspond to the competition and reproduction. Although mobility

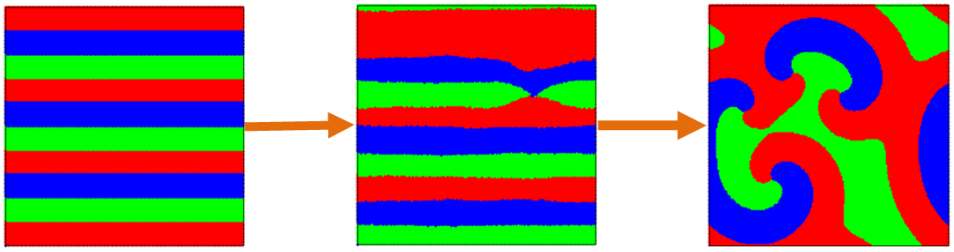

Fig. 39. Pattern transition from a plane to a spiral wave as predicted by the theoretical PDE models. Red (gray), green (light gray), and blue (dark gray) represent species A, B, and C, respectively.

in the stochastic model is not explicit, a finite interaction range plays the same role in individual mobility as the diffusion term in the PDE model.

We solve Eq. (6.2) numerically by discretizing the unit space into a $K \times K$ square lattice so that solving three partial differential equations is equivalent to solving $3K^2$ ordinary differential equations. In particular, let $a(r_1, r_2, t)$, $b(r_1, r_2, t)$, and $c(r_1, r_2, t)$ denote the species densities at site $(r_1, r_2), (r_1, r_2, = 1, \ldots, K)$ and at time t for A, B, C, respectively, where r_1, r_2 are the coordinates of the two spatial dimensions. The terms containing the diffusion operator Δ can be approximated by using the finite-difference method:

$$\begin{aligned} \Delta a(r_1, r_2) &\approx [a(r_1 - 1, r_2) + a(r_1 + 1, r_2) + a(r_1, r_2 - 1) \\ &+ a(r_1, r_2 + 1) - 4a(r_1, r_2)]/(\delta r)^2, \end{aligned}$$

subject to periodic boundary conditions. Here $\delta r = L/K$ denotes the grid size. The integration term

$$\frac{1}{S_R} \int_{G_{\boldsymbol{r}}} d\boldsymbol{r}' a(\boldsymbol{r}', t)$$

is thus replaced by the sum

$$\frac{1}{N_R} \sum_{m,n,a(m,n,t) \in G(r_1, r_2)} a(m, n, t),$$

where $G(r_1, r_2)$ represents the circular interaction range with radius R centered at site (r_1, r_2), and N_R is number of sites inside $G(r_1, r_2)$. The whole system is then transformed to a set of coupled

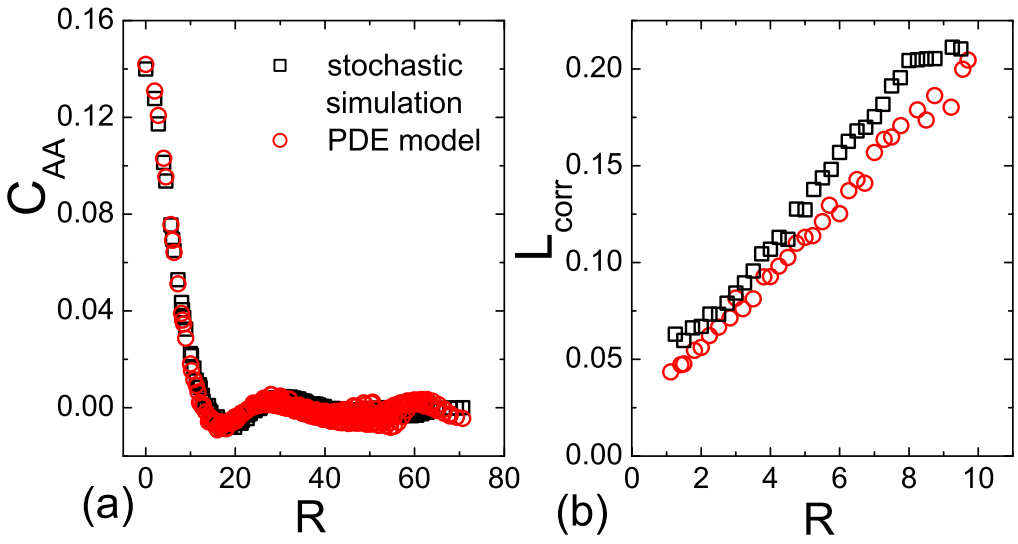

Fig. 40. For $N = 10000$, dependence of spatial correlation C_{AA} (a) and correlation length L_{corr} (b) on the interaction range R from both stochastic simulation ($R = 2.5$) and the PDE model ($D = 0.00045R^2$), where C_{AA} as a function of R is obtained from Eqs. (6.3) and (6.4). Here, we select a spatial position $\mathbf{r}$ and calculate C_{AA} as a function of $|\boldsymbol{r} - \boldsymbol{r}'|$ according to Eq. (6.3). We then count all C_{AA}'s with the same $|\boldsymbol{r} - \boldsymbol{r}'|$ and calculate an average of them, which yield C_{AA} as a function of the normalized distance R.

ordinary differential equations and can be solved using any standard numerical integration method. To incorporate stochasticity intrinsic to the evolutionary dynamics in the game framework, we add a small noise term in the PDEs, which results in switchings from plane to spiral waves [Fig. 39]. However, the imposed stochastic terms is incapable of producing the non-monotonic dependence of the coexistence probability on the interaction radius because the intrinsic stochasticity, which is essential to the evolution of the ecosystem, cannot be described exactly by an extra term that is independent of the system dynamics.

6.3.2. Wavelength and spatial correlation

Assessing the wavelength of the spiral waves is key to understanding the transition from coexistence to extinction as the interaction radius R is increased. The wavelength can be determined by

the method in Ref. [133]. Specifically, the spatial correlation function of one of the species, say A, between locations $\boldsymbol{r}$ and $\boldsymbol{r}'$ can be defined as

$$C_{AA}(|\boldsymbol{r}-\boldsymbol{r}'|) = \langle a(\boldsymbol{r},t)a(\boldsymbol{r}',t)\rangle - \langle a(\boldsymbol{r},t)\rangle\langle a(\boldsymbol{r}',t)\rangle, \tag{6.3}$$

where $\langle \dots \rangle$ denotes the time average after the system has reached a steady state. The final spatial correlation C_{AA} is given by the average of all correlation values that have the same spatial length,

$$C_{AA}(l) = \frac{1}{N_{\boldsymbol{r},\boldsymbol{r}'}} \sum_{|\boldsymbol{r}-\boldsymbol{r}'|=l} C_{AA}(|\boldsymbol{r}-\boldsymbol{r}'|). \tag{6.4}$$

To compare results from different simulation settings, we multiply the length l by $\sqrt{N}$ to yield R. The wavelength is proportional to the critical spatial correlation: $C_{AA}(L_{corr}) \equiv C_{AA}(0)/e$ [133]. The results of wavelength calculation from the stochastic simulation and the PDE model are displayed in Fig. 40. For the spatial correlation function [Fig. 40(a)], the results from both approaches agree well with each other for large values of R, validating our PDE model. Furthermore, we observe from Fig. 40(b) that L_{corr} is approximately a linearly increasing function of R, suggesting the relation $D \sim R^2$.

The coexistence-extinction transition in Fig. 33 can then be understood based on the spatial patterns associated with the correlation between the wavelength and the interaction radius, as follows. For $R = R_{Max}$, we have numerically found that species coexist through two anti-spiral waves whose wavelength approaches the size of the entire square region. The anti-spiral waves are relatively stable, leading to the local maximum in p_{coex}. As R is increased from R_{Max}, due to the linear correlation, the wavelength will exceed the size of the square and extinction becomes more likely, as reflected by the sharp decrease in p_{coex}. For $R \lesssim R_{Max}$, the wavelength is decreased together with an increase in the number of spirals. In this case, collisions of spirals begin to occur, leading to transitions between the spiral and plane waves, which suppress coexistence. This effect leads to a local minimum in p_{coex} at R_{Min} on the left hand side of R_{Max}. However, for smaller values of R, the spatial region is shared by a number of spiral waves of small wavelength. The collision among some of them will be accompanied by the generation of some new small spirals, which will

not affect the dynamical equilibrium of the system. As a result, the coexistence probability is large. This phenomenon is consistent with previous results from discrete-lattice models in the literature that small interaction scales ensure species coexistence. In fact, when the wavelength of spirals is small compared to the size of the spatial region, plane waves are unlikely to arise [148].

6.4. Alternative model: separating reproduction from competition

We consider a more general scenario by separating competition and reproduction in the model in Section 6.2. We aim to examine whether the non-monotonic behavior in the coexistent probability and the switchings of spatial patterns hold for this more realistic interaction. In this new model, three subpopulations interact with each other on a square cell of linear size L as follows:

$$\begin{aligned} AB &\longrightarrow A\oslash,\ \ A\oslash \longrightarrow AA, \\ BC &\longrightarrow B\oslash,\ \ B\oslash \longrightarrow BB, \\ CA &\longrightarrow C\oslash,\ \ C\oslash \longrightarrow CC, \end{aligned} \tag{6.5}$$

where $\oslash$ stands for empty site. As before, the competition and reproduction occur only in a circular region of radius r. At each simulation step, a randomly selected individual i kills one individual j from next species. At the same time, i leaves its offspring at a random location within the interaction range. Initially, the cell is randomly occupied by three species whose densities are approximately identical. The main difference between this model and the model (6.1) lies in the locations of the offsprings. Specifically, in model (6.1), the offspring of an individual replaces another individual from the next species in the cycle; whereas in the model (6.6), the place of birth is random.

Stochastic simulations are carried out for different values of the interaction radius R, as shown in Fig. 41. The coexistence probability p_{coex} exhibits a non-monotonic behavior with respect to R with a peak at about $R = 4$, analogous to the result from model (6.1). This implies that the non-monotonic dependence of species coexistence on interaction range is an intrinsic feature of cyclic competition dynamics on continuous space, regardless of the place of the birth of descendants. Spatial patterns and time series of the species densities are displayed in Fig. 42(a). We observe

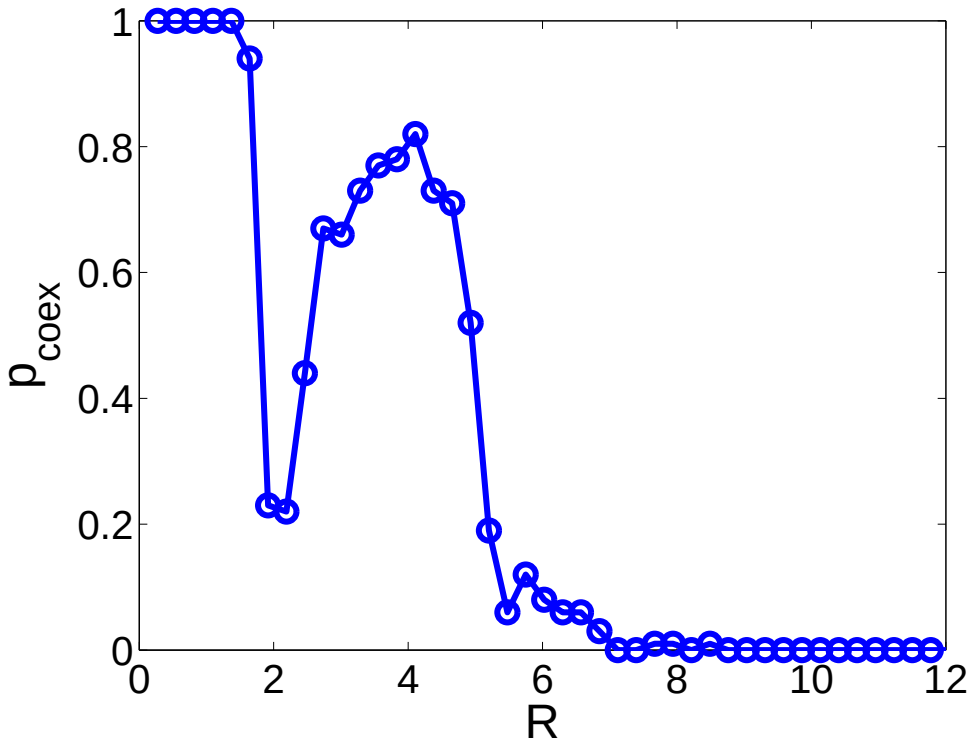

Fig. 41. Coexistence probability p_{coex} as a function of normalized interaction radius R in model (6.6) in the absence of individual mobility. Other parameters are the same as in Fig. 33.

switchings between spiral and plane waves, where the time series of the former exhibit fluctuations with higher frequency than the latter.

Since the birth locations of offsprings are random, we study the spatial distribution of species associated with two types of wave patterns. Since the resources within the square cell are limited and fixed, the spatial distribution of species indicates resources utilization. For example, if individuals are uniformly distributed on the space, resources are fully used and the competitions among species are relatively mild. In contrast, if species disperse inhomogeneously on the space, some areas with high species densities are faced with severe competition due to the shortage of resources. To characterize the resource utilization, we investigate the overlap in the interaction ranges among individuals, which can be simply measured by the distance among individuals. To be concrete, we

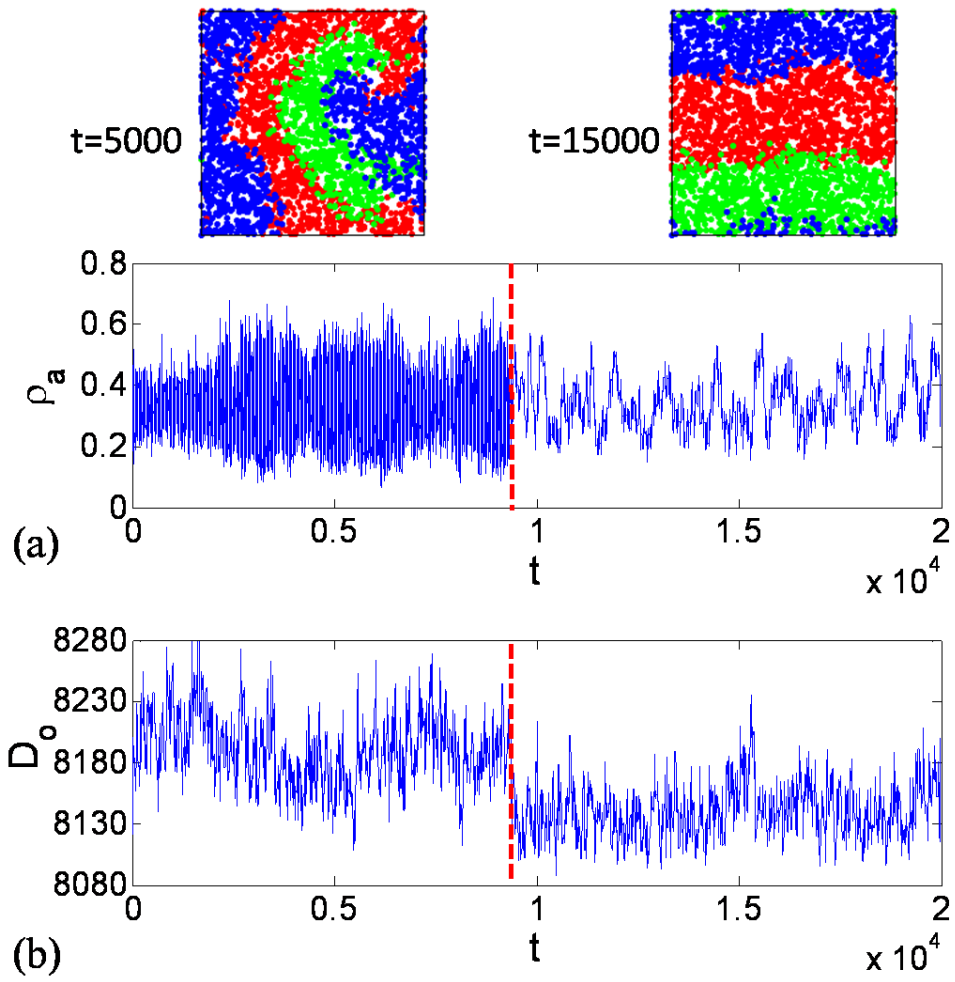

Fig. 42. For model (6.6) with $N = 3000$ and $L = 1$, (a) spatial patterns and the corresponding time series of species density ρ_a and (b) time series of the overlapping distance D_o in the interaction range. The color (grayscale) scheme for spiral and plane waves is the same as in Fig.34.

define the overlapping distance between individuals i and j as

$$D_{ij} = \begin{cases} 2r - d_{ij}, & \text{if } d_{ij} < 2r \\ 0, & \text{otherwise,} \end{cases} \tag{6.6}$$

where d_{ij} is the distance between i and j. Then the total overlapping distance is

$$D_o = \sum_{i,j=1,i\neq j}^{N} D_{ij}. \tag{6.7}$$

The lower the value of D_o, the more the resources are utilized. The time series of D_o corresponding to p_{coex} for spiral waves and plane waves are shown in Fig 42(b). We find that plane waves tend to benefit more from the utilization of resources that spiral waves. This is due to the fact that the boundaries among species associated with plane waves are shorter than those with spiral waves. Since competition and reproduction occur near the boundaries among different species, the spiral waves with longer boundaries can induce more spatial heterogeneity caused by reproduction at random locations.

6.5. Conclusion

In conclusion, we have generalized cyclic-competition dynamics to continuous space and addressed a key issue: the interplay between interaction range and species mobility and its role in coexistence. Model predictions in both the small and large limits of the interaction range are consistent with those from the *E.coli* experiments. In the intermediate interaction range, our study predicts a non-monotonic behavior in the coexistence probability, which is independent of the size of the square cell, the populations size and the relationship between competition and reproduction. Near the local minimum of the probability, a transition between spiral and plane wave patterns arises, where coexistence can be greatly enhanced through a proper choice of the mobility. When the reproduction process is separated from the competition, the plane waves of species organization benefits more from the utilization of resources than the spiral waves. We have derived a general PDE model with results that agree with those from direct stochastic simulations of the competition dynamics. Our work provides a more comprehensive and physical understanding of the dynamics of cyclically competing populations with respect to the fundamental issue of coexistence.

7 . BASINS OF COEXISTENCE AND EXTINCTION IN SPATIALLY EXTENDED ECOSYSTEMS OF CYCLICALLY COMPETING SPECIES

7.1. The rock-paper-scissors game

Species diversity is ubiquitous in nature. Uncovering the factors that support biodiversity is a fundamental problem in interdisciplinary science. Essential to biodiversity is species coexistence, a problem that has been investigated experimentally, computationally and theoretically [114, 117, 149–155]. In this regard, empirical observations from experimental studies suggested non-hierarchical, cyclic competitions among species as an important mechanism for species coexistence, the essential features of which can be captured by the childhood game "rock-paper-scissors" (RPS) [115]. In a RPS game, three strategies form a cyclic loop and any strategy can defeat the one next to it in the loop. Indeed, cyclic competitions of the RPS nature have been found in different contexts in ecosystems and in laboratory experiments as well. Typical examples include colicinogenic microbes' competition [120], mating strategies of side-blotched lizards in California [139], and competition among mutant strains of yeast [138] and coral reef invertebrates [137]. In computational and theoretical exploration of species coexistence, the RPS game has been a paradigm [156], where it was found that the incorporation of spatial structure is absolutely necessary to model the competition dynamics in real ecosystems [118, 156]. This is due to the fact that, for well-mixed populations under global interactions, macroscopic population models based on ordinary differential equations (ODEs) predicted that species coexistence is unstable in the RPS game [114]. That is, stochastic effects and small external perturbation can typically destroy species coexistence, in contrast to empirical observations. Computational studies have shown that, when spatial structure is introduced into the RPS game, species coexistence can become stable and robust, which is consistent with experimental observations [118, 119, 157]. For example, in both simulations and E. coli experiments [118], it was found that local interactions and dispersal enable coexistence of all three species in the RPS game while coexistence is lost when the ecological processes take place over large scale so that the spatial structure is effectively averaged out. Notice that, two features appear

in the RPS game model when spatial structures are taken into account: (1) the underlying dynamics becomes spatiotemporal as the RPS competitions now occur in space, (2) the model becomes *microscopic* as competitions must now be treated at the level of species individuals, in contrast to the macroscopic population models described by ODEs.

Spatially extended RPS game models thus provide a powerful, microscopic paradigm to address various fundamental issues associated with species coexistence in realistic ecosystems. For example, when competitions are deemed to occur on space, the issue of species mobility becomes important [158, 159]. Indeed, mobile behaviors ranging from bacteria run to animal migration play an important role in species coexistence. In the work of Reichenbach et al. [158, 159], a critical mobility value has been identified, below which species stably coexist in the form of moving spiral waves on spatially extended scales, whereas above the critical mobility, the wavelength of the spiral waves exceeds the size of the underlying spatial structure, resulting in extinction of two species with only one surviving species [158, 159]. The formation of moving spiral waves induced by stochastic interactions at a microscopic level is a surprising finding, since these waves arise mostly in models based on partial differential equations (PDEs). This finding has stimulated a series of subsequent works. For example, in Refs. [132, 134], instability of the spatial patterns and the effect of noise were investigated. In Ref. [160], it was found that breaking the conservation law was crucial for the formation of spiral waves. In Ref. [161], a zero-one behavior was revealed in that the weakest species has the highest survival probability. The effect of zero-sum and non-zero sum in the payoff matrix in the RPS game was investigated in Refs. [162] and [163], respectively. It was reported in Ref. [164] that intraspecific epidemic spreading can promote species coexistence, whereas interspecies epidemic spreading tends to suppress species coexistence. In Ref. [165], it was reported that intraspecific competition can effectively promote biodiversity. The RPS game has also been extended to more than three species in Ref. [166] and to spatial small-world networks in the presence of shortcuts [140, 141]. In a fairly recent work [167], entropy production has been used to characterize non-equilibrium behavior in the RPS game.

In a recent Rapid Communication [136], we proposed to explore the concept of attraction basin in spatially extended PRS game dynamics. This was motivated by the consideration that basin structure provides a more comprehensive characterization of the non-equilibrium dynamics in the RPS game. In contrast to most previous works where computations and analysis were carried out with respect to a single initial configuration with identical species densities, basin structure obtained from all possible initial densities of species can yield a "global" picture of the coexistence dynamics. In Ref. [163], the authors studied the fixation probability in the deterministic RPS game, which depends on the initial densities of three species, with respect to both zero-sum and non-zero sum assumptions in finite populations. A graphical representation analogous to the method in [136] is exploited to characterize the fixation probability. This issue, however, is somewhat different from species coexistence in mobile populations. In nonlinear dynamics, the basins of attraction and the boundaries among different basins are a fundamental problem [168]. In our work, the basin structures were investigated for RPS game dynamics of mobile individuals. The purpose of this chapter is to provide a more extensive treatment of the problem of basins in spatially extended RPS game models. In particular, we propose a different method to explore basins by resorting to the convergence time for different initial configurations. This time can not only distinguish the boundaries among extinction and coexistence basins, but also reveal the intrinsic difference within each extinction basin. Such a difference cannot be detected using the final-state characterization method [136]. Going beyond the model in Ref. [136] that treated only mobile populations with cyclic competition on lattice, here we consider two additional types of model extension: (i) mobile populations with intraspecific competitions, and (ii) populations dispersing on a continuous geographical space with adjustable interaction ranges. Results of basins are obtained from both microscopic, stochastic simulations and models based on PDEs, and a good agreement between the two types of results is demonstrated with respect to the structures of coexistence and extinction basins. We note that the area of the coexistence basin in the phase space provides a meaningful measure of biodiversity, which is unable to be quantified when identical initial densities are used as in most previous works. In all cases considered

in this chapter, the extinction basins show a universal rotational structure toward the central point in the phase space. The investigation of basins leads to *quantitative* insights into the evolutionary dynamics in spatial RPS game under various conditions.

In Sec. 7.2, we describe the spatial RPS model with mobile individuals and two methods for computing attraction basins. In Sec. 7.3 and 7.4, we apply the basin characterizations to RPS games with intraspecific competitions on lattice and games on continuous geographical space, respectively. Conclusions are presented in Sec. 7.5.

7.2. Basins of coexistence and extinction

7.2.1. Model of RPS games in spatially extended ecosystems

The cyclic-competition model with mobile individuals was originally proposed in Ref. [150, 158], where each site of a square lattice with periodic boundary condition can be occupied by an individual from one of the three species or left empty so that the system has a finite carrying capacity. Interactions and dispersing behaviors among neighboring sites are described by the following set of rules:

$$AB \xrightarrow{\sigma} A\varnothing, \qquad BC \xrightarrow{\sigma} B\varnothing, \qquad CA \xrightarrow{\sigma} C\varnothing, \tag{7.1}$$

$$A\varnothing \xrightarrow{\mu} AA, \qquad B\varnothing \xrightarrow{\mu} BB, \qquad C\varnothing \xrightarrow{\mu} CC, \tag{7.2}$$

$$A\square \xrightarrow{\epsilon} \square A, \qquad B\square \xrightarrow{\epsilon} \square B, \qquad C\square \xrightarrow{\epsilon} \square C, \tag{7.3}$$

where A, B and C denote the three cyclically competing species, $\varnothing$ represents empty sites and $\square$ denotes any species or empty sites. Relation (1) denotes the cyclic competitions, i.e., one species preys on a less-predominant species in the cycle (e.g., A can kill B, B out-competes C, C in turn out-competes A, leaving behind empty sites). Relations (2) represents reproduction of an individual at a neighboring empty site with rate μ. Relation (3) defines migration by position exchange between two neighboring individuals or between one individual and one of its neighboring empty sites. Migration occurs at rate ϵ. To be concrete, at each time step, a randomly chosen individual interacts with or moves to one of its nearest neighbors at random. For the pair of neighboring sites, cyclic competition, reproduction and migration occur at the probabilities $\sigma/(\mu+\sigma+\epsilon)$, $\mu/(\mu+\sigma+\epsilon)$

and $\epsilon/(\mu+\sigma+\epsilon)$, respectively, so that the rates of competition, reproduction and migration are normalized. Whether the interaction can successfully occur is determined by the states of both sites. For example, if reproduction is chosen but there are no empty sites, the reaction fails. According to the theory of random walk [169], individual mobility M is defined as $M=\epsilon(2N)^{-1}$, to which the number of sites explored by one mobile individual per unit time is proportional. An actual time step is defined when each individual has interacted with others once on average. In other words, in one actual time, N pairwise interactions will have occurred.

In Ref. [136], we introduced the concept of attraction basin in the RPS game. Let n_0 be the fraction of empty site. For example, we can fix n_0 to be 10% of the N lattice sites. Since the initial densities of three species satisfy $n_a+n_b+n_c=1-n_0$, all possible combinations of n_a, n_b and n_c define a triangular region. The phase space at time $T=0$ can thus be represented by the simplex S_2 defined by this triangle. There are four possible final states, corresponding to three extinction states, each converging to one of the three single species, and a coexistence state. In the phase space S_2, the coordinates of a point denote a combination of the initial densities of the three species, and we can use four different colors to represent the final states. The basins can thus be defined by regions in S_2, within which initial densities converge to the same final state. Alternatively, the basins can be characterized by the convergence time t_c for each point in S_2. Note that different initial states in the same basin cannot be distinguished by the final state, but their convergence times t_c can be quite different. For computational convenience, we use the quantity $1/t_c$ to distinguish different points in S_2.

In Ref. [158], a critical mobility $M_c=(4.5\pm0.5)\times10^{-4}$ was derived for identical initial densities of three subpopulations. For $M<M_c$, species can stably coexist while for $M>M_c$ only one species can survival finally and coexistence is lost. We investigate basins of coexistence and extinction in the two regions separated by M_c by varying M. Numerical simulations are implemented for a large time T that scales with the system size N. To make an unbiased comparison with previous works, we assume equal reaction probabilities for reproduction and competition rates, i.e.,

$\mu = \sigma = 1$. The mobility M is thus the only control parameter of the system. In our simulations, square lattices with 100×100 sites are used and the simulation time is chosen to be $T = 5000$ to ensure that the final state can be reached from any initial point in S_2.

7.2.2. Basin structure from microscopic simulations

Figures 43(a-e) show the basin structures in S_2 for different values of M for both regions of $M < M_c$ and $M > M_c$. The basins for all values of M exhibit rotational symmetry around the center point of S_2. For $M < M_c$, e.g., (a) $M = 5 \times 10^{-5}$, (b) $M = 1 \times 10^{-4}$, and (c) $M = 3 \times 10^{-4}$, there exists a coexistence basin at the central area of S_2 and three extinction basins are rotationally entangled around the coexistence basin. As M is increased, the coexistence basin shrinks toward the center point together with the expansion of the three extinction basins. This indicates that population mobility tends to inhibit coexistence for $M < M_c$, as the area of coexistence basin decreases by increasing M. In previous works that focus on identical initial densities of species (corresponding to the a single point in S_2, its center), the effect of mobility on coexistence cannot be revealed in this parameter region where species can always coexist. The basins thus provide a global picture of the coexistence problem. At the boundaries among different basins, the final state depends sensitively on the initial state and small initial perturbations can drive the system to an entire different final state. As soon as M exceeds the critical value M_c, the coexistence basin vanishes, as exemplified by Fig. 43(d) for $M = 1 \times 10^{-3}$. We see that, in this case, the phase space S_2 is shared exclusively by three extinction basins. The center point is where all three basins meet. At this point, the final convergence state is hard to be predicted due to the presence of stochastic effect and the sensitivity of final state to small variations in the initial densities. Further increase of M, e.g., (e) $M = 5 \times 10^{-3}$ leads to the same structure of extinction basins as shown in Fig. 43(d) for $M = 1 \times 10^{-3}$. We can expect the same basin structures for very large values of M, which correspond to the well-mixed and globally interacting case without the restriction of lattice links. Our finding is thus consistent with the known result that global interactions can exclude coexistence in the RPS game.

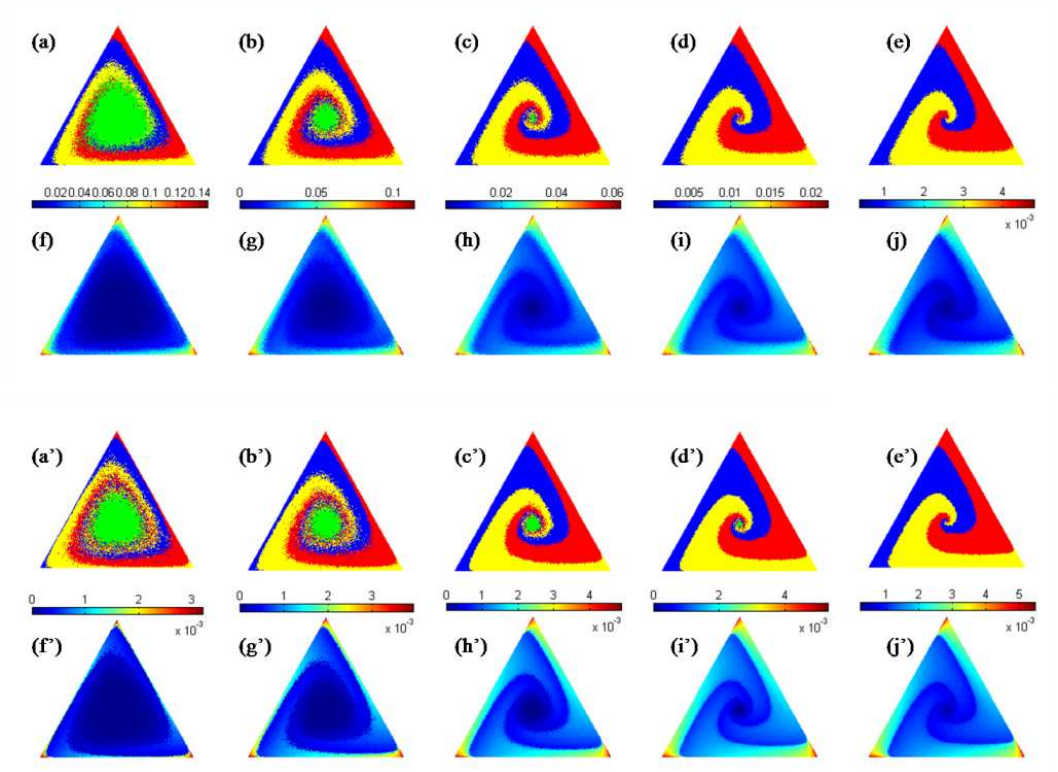

Fig. 43. Basin structures of mobile individuals with cyclic competition on lattice for different values of mobility by using the characterizations of final state and convergence time. Panels (a-e) are the basins obtained by using the final state for $M = 5 \times 10^{-5}$, 1×10^{-4}, 3×10^{-4}, 1×10^{-3} and 5×10^{-3}, respectively. Panels (f-j) are the basins obtained by using the convergence time. The mobility values in (f-j) are the same as those in (a-e), respectively. Panels (a'-j') are the basins obtained by the PDEs under the same set of mobility values as in (a-j). The final state is represented by one of the four colors at each point from stochastic simulations using 30 random realizations of the cyclic competition dynamics, under the same initial condition, on a given 100×100 square lattice. Blue, yellow and red denote the three single-species states composed of species A, B and C, respectively. Green denotes coexistence of species in the steady state. For each realization, the simulation consists of $5000 \times N$ time steps. We have checked that $5000 \times N$ time steps are sufficient long for the system reaching a steady state.

Basin structures obtained by using the inverse $1/t_c$ of convergence time in the phase space S_2 is shown in Figs. 43(f-j), corresponding to panels (a-e), respectively. We see that $1/t_c$ offers a detailed characterization of the different states within each extinction basin, where $1/t_c$ decreases along the rotational structure of the basin toward the central area. An interesting behavior is that the boundaries of basins can be identified solely based on t_c in the sense that there is sharp transition in $1/t_c$ from one extinction basin to another when crossing the boundary. For the coexistence basin, since species can always coexist, t_c in the basin tends to ∞ and $1/t_c$ equals zero, so all points appear identical in the coexistence basin. The boundary between the coexistence and extinction basins is thus unequivocal since t_c in the extinction basins is always finite.

7.2.3. Basin structure from PDE model

The PDEs can be derived by a continuous approximation for the three reactions among geographically neighboring individuals. Let $n_a(\mathbf{r},t)$, $n_b(\mathbf{r},t)$ and $n_c(\mathbf{r},t)$ be the densities of populations A, B and C at time t and site $\mathbf{r}=(r_1,r_2)$ in the two-dimensional space, respectively. Neighbors are located at $\mathbf{r}\pm\delta r\cdot\mathbf{e}_i$, where $\{\mathbf{e}_i\}$ ($i=1,2$) are the base vectors of the two-dimensional lattice. We have, for the average value of an arbitrary population $a(\mathbf{r},t)$, the following evolutionary equation:

$$\begin{aligned}\partial_t n_a(\mathbf{r},t) = \frac{1}{z}\sum_{\pm,i=1}^{2}\{&2\epsilon[n_a(\mathbf{r}\pm\delta r\cdot\mathbf{e}_i,t)-n_a(\mathbf{r},t)]\\ +\;&\mu n_a(\mathbf{r}\pm\delta r\cdot\mathbf{e}_i,t)[1-n_a(\mathbf{r},t)-n_b(\mathbf{r},t)-n_c(\mathbf{r},t)]\\ -\;&\sigma n_c(\mathbf{r}\pm\delta r\cdot\mathbf{e}_i,t)n_a(\mathbf{r},t)\},\end{aligned} \tag{7.4}$$

where z is the number of nearest neighbors of each lattice site. On the right-hand side of the equation, the first term denotes the exchange process, where the neighbors moving into a site and the individual at this site moving out to its neighbors will induce an increase and a decrease in $n_a(\mathbf{r})$, respectively. The second term describes the increase in $n_a(\mathbf{r})$ due to reproduction, and the third term characterizes the decrease in $n_a(\mathbf{r})$ due to competition. We set the length of the lattice to unity and, hence, the distance between two nearest neighbors is $\delta r=1/\sqrt{N}$. For $N\to\infty$ and the lattice size fixed to

1, $\delta r \to 0$. Thus $\mathbf{r}$ can be treated as a continuous variable. Using Taylor expansion to the second order, we have

$$\begin{aligned} & n_a(\mathbf{r} \pm \delta r \cdot \mathbf{e}_i, t) \\ = \quad & n_a(\mathbf{r}, t) \pm \delta r \partial_i n_a(\mathbf{r}, t) + \frac{1}{2}\delta r^2 \partial_i^2 n_a(\mathbf{r}, t) + O(\delta r^2). \end{aligned}$$

The first term on the right-hand side of the Eq. (7.4) becomes

$$\frac{2\epsilon}{z} \sum_{\pm, i=1}^{2} [n_a(\mathbf{r} \pm \delta r \cdot \mathbf{e}_i, t) - n_a(\mathbf{r}, t)] = \frac{\epsilon}{2}\delta r^2 \partial_i^2 n_a(\mathbf{r}, t).$$

By rescaling the exchange rate ϵ with system size N and a fixed (diffusion) constant M according to

$$\epsilon = 2MN, \tag{7.5}$$

we have

$$\frac{\epsilon}{2}\delta r^2 = M, \tag{7.6}$$

where $\delta r = 1/\sqrt{N}$. For other terms in the Eq. (7.4), only the zeroth-order contributions to $n_a(\mathbf{r}, t)$ in the expansion of $n_a(\mathbf{r} \pm \delta r \cdot \mathbf{e}_i, t)$ are important in the large system-size or the $\delta r \to 0$ limit. These considerations lead to the following set of PDEs:

$$\begin{aligned} \partial_t n_a &= M\nabla^2 n_a + \mu n_a(1-\rho) - \sigma n_c n_a, \\ \partial_t n_b &= M\nabla^2 n_b + \mu n_b(1-\rho) - \sigma n_a n_b, \\ \partial_t n_c &= M\nabla^2 n_c + \mu n_c(1-\rho) - \sigma n_b n_c, \end{aligned} \tag{7.7}$$

where $\rho = n_a(\mathbf{r}, t) + n_b(\mathbf{r}, t) + n_c(\mathbf{r}, t)$ is the local species density and $1 - \rho$ denotes the density of empty sites. Basin structures in the PDE model can be obtained by numerically solving the equations for random initial species densities. Specifically, for an arbitrary density, at $t = 0$, only one quantity of $n_a(r_x, r_y)$, $n_b(r_x, r_y)$ and $n_c(r_x, r_y)$ is equal to one and the other two are zero, the probability of which is determined by the initial densities of n_a, n_b and n_c altogether. For the PDEs, extinction is defined when the density of any species is less than $1/N$. The species preyed by the extinction species is the exclusive survivor. The definition takes into account the physical meaning of survival in that the number of survival species cannot be less than one.

The results of basins from the PDE model are shown in Figs. 43(a'-j'), which correspond to the stochastic simulation results in (a-j), respectively. We see that the results from the PDE model are in good agreement with simulations in terms of both the basin structures and the areas of coexistence and extinction basins for different values of individual mobility. The stochastic fluctuations in the basins obtained from the PDE model is a result of the initial randomness of species densities [$n_a(r_x, r_y)$, $n_b(r_x, r_y)$ and $n_c(r_x, r_y)$] used in the numerical solution of the PDEs.

Our exploration of basin structures in terms of the final convergence state, the inverse of the survival time, and the PDE model thus provides a more complete picture concerning the emergence and loss of biodiversity in the spatial RPS game in the presence of individual mobility.

7.3. Basins of spatial RPS dynamics with intraspecific competition

In nature, intraspecific competitions are quite common [170–173]. Individuals within the same species do compete for essential life-sustaining resources such as food, water, light, and opposite sex, etc.. Intraspecific competitions can have a significant impact on species diversity in both predator-prey-like interaction and cyclic-competition systems. Intraspecific competition is also quite common in various food chains. Here we explore the basin structure in the presence of intraspecific competitions, which can be incorporated in the game model in Sec. 7.2 as follows:

$$AA \xrightarrow{p} A\varnothing, \qquad BB \xrightarrow{p} B\varnothing, \qquad CC \xrightarrow{p} C\varnothing, \tag{7.8}$$

where $\varnothing$ represents empty sites. Due to the competition of two neighboring individuals in the same species, one individual will die at random and leave its site empty at rate p. Intraspecific competition occurs with probabilities $p/(p+\mu+\sigma+\epsilon)$ and the rates of inter-species competition, reproduction and motion are normalized by $p+\mu+\sigma+\epsilon$ as well. We set the summation of intraspecific competition, interspecific competition, and reproduction rates to be 2, i.e., $p+\sigma+\mu=2$ so that the dependence on the mobility probability ϵ is the same as compared to models in Sec. 7.2.

Using the continuous approximation, we can derive a PDE model from the four types of reactions for spatiotemporal dynamics of RPS game under intraspecific competition [165]. The model is given

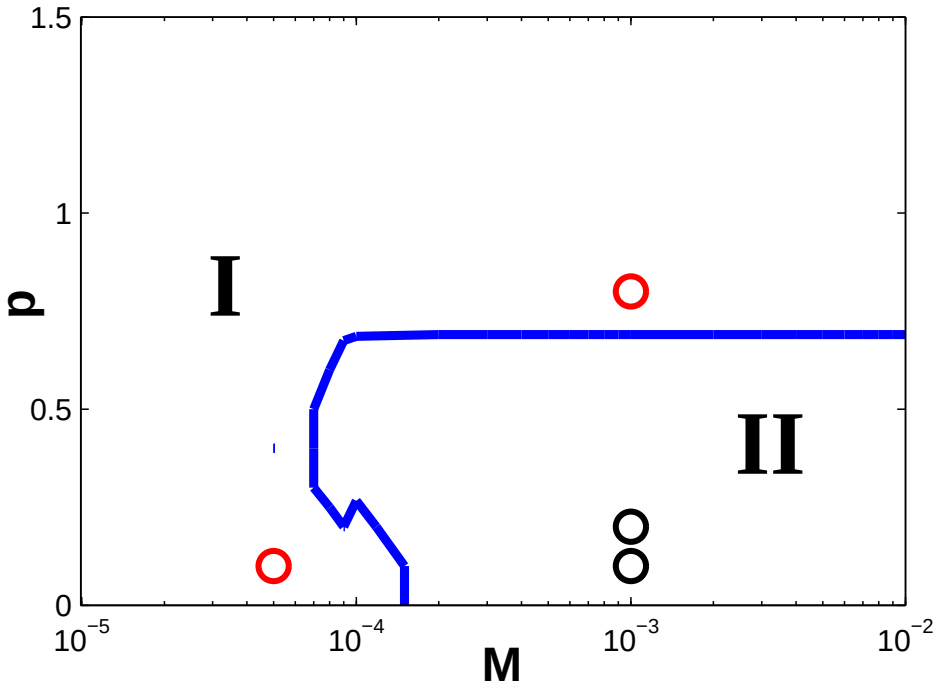

Fig. 44. Dependence of extinction probability on the intraspecific competition rate p and mobility M, where regions I and II denote coexistence and extinction behaviors, respectively. Simulation results are obtained by averaging over 50 random initial configurations on a lattice of size 100×100. The boundary between regions I and II are obtained by the PDE model Eq. (7.9). We select four sets of parameter combinations to explore the basin structures.

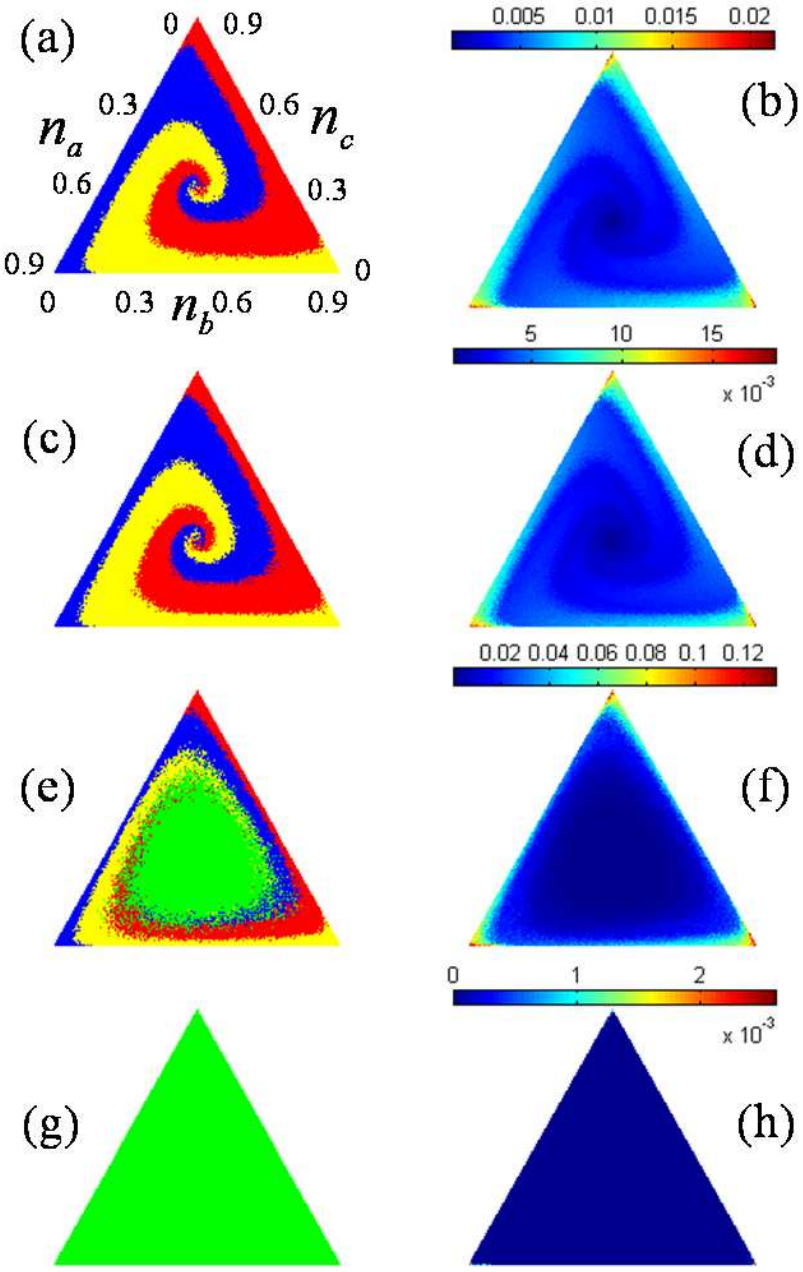

Fig. 45. Basins of mobile individuals with inter-species and intraspecific competitions on lattices for (a,b) $M = 1 \times 10^{-3}$ and $p = 0.1$, (c,d) $M = 1 \times 10^{-3}$ and $p = 0.2$, (e,f) $M = 5 \times 10^{-5}$ and $p = 0.1$, and (g,h) $M = 1 \times 10^{-3}$ and $p = 0.8$. Panels (a), (c), (e), and (g) are obtained by the final-state criterion, and panels (b), (d), (f) and (h) are calculated according to the convergence time. Other simulation parameters are the same as for Fig. 44.

by

$$\begin{aligned} \partial_t n_a &= M\nabla^2 n_a + \mu n_a(1-\rho) - \sigma n_c n_a - (p/2) n_a n_a, \\ \partial_t n_b &= M\nabla^2 n_b + \mu n_b(1-\rho) - \sigma n_a n_b - (p/2) n_b n_b, \\ \partial_t n_c &= M\nabla^2 n_c + \mu n_c(1-\rho) - \sigma n_b n_c - (p/2) n_c n_c. \end{aligned} \tag{7.9}$$

Numerical solution of the PDEs yields two dynamical regions in the parameter space, as shown in Fig. 44, where region I corresponds to coexistence and region II to extinction. In each region, we select two groups of parameter combinations (M, p) to explore the basin structures. The chosen points are marked in Fig. 44. Results from direct stochastic simulations are shown in Fig. 45. For the two points in the extinction region [(a) and (c)], we observe three entangled extinction basins that meet at the center of the phase space S_2, which is similar to the basins in the absence of intraspecific competition in Sec. 7.2. In this region, intraspecific competition is not sufficient to induce the coexistence basin. In contrast, in the coexistence region [(e) and (b)], a large area of coexistence basin dominates the central area of S_2. In particular, for strong intraspecific competition (large value of p), the phase space S_2 is almost exclusively a coexistence basin and the extinction basins almost vanish [Fig. 45(g)]. Such a domination of the coexistence basin is general for large values of p, indicating that coexistence is strongly promoted by intraspecific competitions. The inverse of the convergence time $1/t_c$ identifies the boundaries among different extinction basins and between the extinction and coexistence basin. Within each extinction basin, $1/t_c$ decreases along the rotational direction of the basins toward the central area, which is similar to the situation without intraspecific competition. Another feature is that the rising of coexistence basin when p exceeds the critical value 0.7 is quite sharp. That is, for $p < 0.7$ in the extinction region, coexistence basin does not exist. For $p > 0.7$, a vast area of coexistence basin arises and dominates the phase S_2 associated with the loss of the extinction basins. In this regard, the phase transition from extinction to coexistence at the critical value $p = 0.7$ is of the first order.

7.4. Basins of RPS dynamics on continuous space

Most existing models based on stochastic interactions assume discrete lattices as the underlying spatial structure, on which cyclic competition, reproduction and movement occur among neighbor-

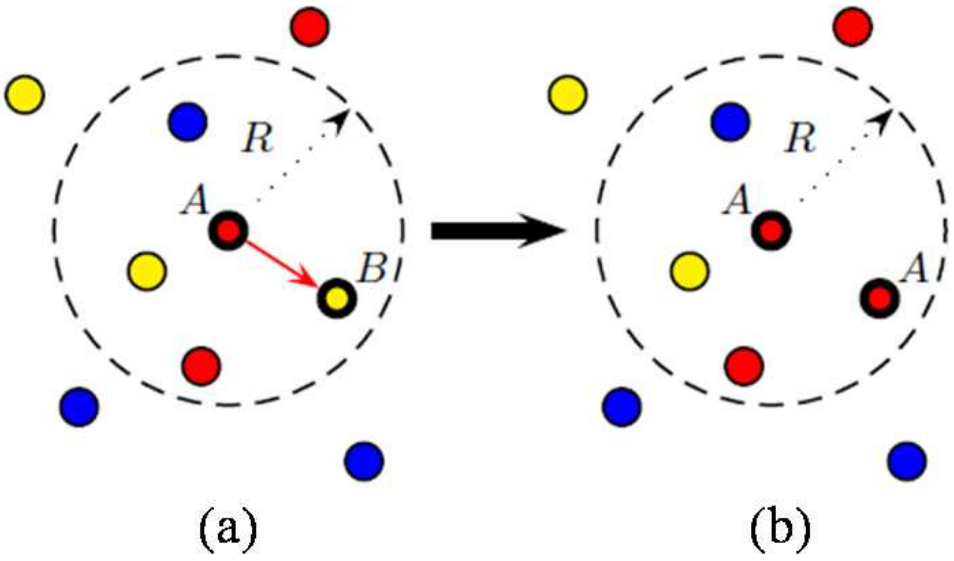

Fig. 46. Schematic illustration of continuous-space model. Three subpopulations, A, B and C represented by red, yellow and blue, respectively, dominate each other in a cyclic manner. (a) An individual belonging to A randomly selects an individual B within its selection range R, where B is next to A in the cyclic competing loop. (b) The A individual kills the B individual and at the same time replicates itself. If within the interaction range, an individual cannot find any inferior individual, nothing happens.

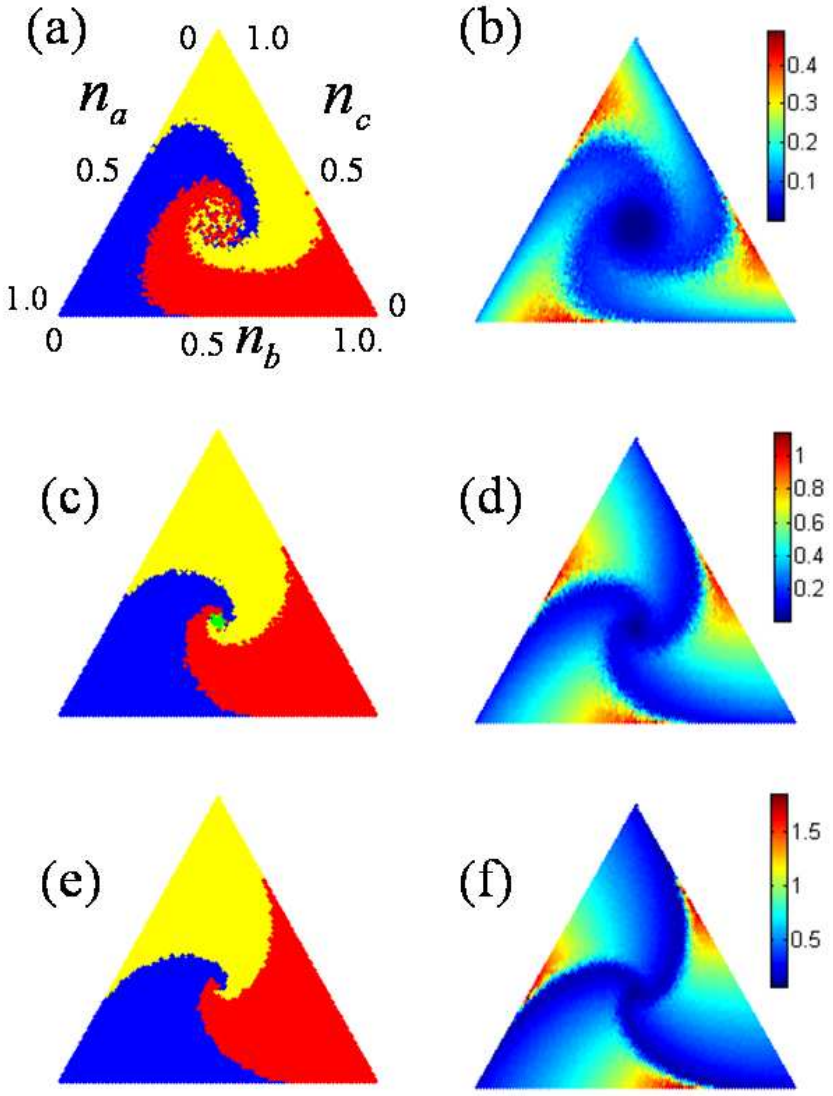

Fig. 47. Basins of cyclically competing subpopulations on continuous geographical space for (a,b) the interaction radius $R = 0.045$, (c,d) $R = 0.07$ and (e,f) $R = 0.1$. Panels (a), (c) and (e) are obtained according to the final-state criterion while panels (b), (d) and (f) are calculated according to the convergence-time criterion. The number of individuals is fixed at 3000 and size of the square cell is 1×1. Each point in the phase space is obtained by 100 different realizations. The initial positions of individuals in the geographical space are random.

ing sites. In such a case, the underlying geographical space is discrete. In realistic ecosystems, the intrinsic geographical space can be continuous. In this section, we study RPS dynamics with individuals dispersing on a continuous space, which allows the effect of nonlocal interactions on species coexistence to be studied in terms of basin structures. In our model, we assume that individuals of the three species are randomly dispersed on a square cell of linear size $L = 1$ under periodic boundary conditions. A competition occurs only if the geographical distance between two cyclic individuals is less than the interaction radius R, as schematically illustrated in Fig. 46. At each simulation step, an individual is randomly selected. For example, in Fig. 46(a), an individual belonging to species A is chosen. After this, within the interaction range, the A individual randomly kills an individual belonging to B which is next to A in the cyclic competition loop. At the same time, the A individual reproduces itself at the position of the B individual. If the A individual cannot find any B individual within the range, no interaction occurs. The rate of killing is σ. Note that the absolute value of the rate σ only affects the evolution speed of the system but does not influence the convergence toward the final state. The radius R of interaction range is thus the sole physical parameter in the model.

We calculate the basins in the simplex S_2 by using different initial densities of three species. Because of the absence of empty sites in the continuous space, the range of S_2 is unity. Basin structures for different values of R obtained from stochastic simulations are shown in Fig. 47. In particular, we observe that the area of the coexistence basin is a *non-monotonic* function of R. When R is increased to 0.045, coexistence is lost, as shown in Fig. 47(a), and there is an entangled and disordered region in the central area where small deviations in the initial densities could lead to completely different final extinction states. This behavior is distinct from those in the lattice models treated in Secs. 7.2 and 7.3. Except the central region, three extinction basins exhibit a rotational symmetry around the central point, similar to the behavior in the lattice models. As R reaches 0.07 [Fig. 47(c)], a small coexistence basin re-emerges at the center and the degree of rotation of the three extinction basins is reduced as compared to that in Fig. 47(a). This behavior is contrary to the existing result from

lattice models in the literature that local interactions promote coexistence while it is lost at larger interaction scale. For larger interaction range, e.g., $R = 0.1$ [Fig. 47(e)], coexistence basin vanishes again and the rotational degree of extinction basins is reduced further. We have examined that for R larger than 0.1, the phase space S_2 is shared exclusively by three extinction basins. The phase-space structures obtained by the convergence-time t_c in Figs. 47(b,d,f) are consistent with those from the final-state criterion. In particular, the characteristics of the behavior of t_c in each extinction basin are qualitatively similar for discrete-lattice and continuous-space models. While the basin structures exhibit some small difference for small [Figs. 47(a)] and large [Figs. 47(e)] values of R, extinction is the exclusive outcome in these cases.

7.5. Conclusion

In conclusion, we have studied basins of species coexistence and extinction in three spatial RPS game models: (1) mobile species on lattice, (2) mobile species on lattice with intraspecific competition, and (3) mobile species on continuous space. Two criteria are used to characterize the basin structures in the phase space S_2: the final state and the convergence time. We have found that for all three models, three extinction basins spirally entangle around the center point in S_2. About the center, a coexistence basin can emerge, depending on the parameters of the underlying spatiotemporal dynamical system. The boundaries among basins can be distinguished by the final convergence state and the fine structure within each single basin can be resolved by the convergence time, which exhibits a general behavior in that it increases along the spiral of the basin toward the central area, signifying a dependence of the degree of extinction (within the same basin) on initial configurations. There is a sharp transition in the convergence time at the boundary between two extinction basins, so the boundary can also be identified by this time. In the coexistence basin, the convergence time tends to infinity, separating the coexistence from extinction basins in a straightforward manner.

For each model, a set of PDEs can be derived to capture the basic features of the spatiotemporal evolutionary dynamics and we find that the PDEs can generate basin structures that are consistent with those from microscopic stochastic simulations. While our computational efforts establish a

plausible picture for the basin structures associated with the evolutionary dynamics of cyclically competing species on spatially extended scales and thereby provide deeper insights into the species coexistence problem, the dynamical origin of the emergence of the basin structure revealed in this chapter is not understood at the present. Further efforts in this direction are required.

8 . PATTERN FORMATION, SYNCHRONIZATION AND OUTBREAK OF BIODIVERSITY IN CYCLICALLY COMPETING GAMES

8.1. Background

Biodiversity is ubiquitous in nature and fundamental to evolution in ecosystems [114, 174, 175]. Evolutionary game theory [117, 176–179] has been used as a paradigm to address the coexistence of competing species, which is the key to sustaining biodiversity. Cyclic, non-hierarchical competitions have been observed in a plethora of real ecosystems, ranging from microbes to mating strategies of side-blotched lizards in California [120, 180–182]. To understand the role of the competitions in biodiversity, *microscopic* game models based on stochastic interactions on spatially extended scales using, e.g., the classical rock-paper-scissors games, have been exploited to understand the dynamics of species coexistence [120]. More recently, the role of mobility in coexistence has also been investigated [130, 183–185] with the finding that strong *local* mobility can cause non-local interactions, which under certain circumstances tend to hamper coexistence through the formation of moving spiral waves of population densities in the physical space [184].

In this chapter, motivated by the ubiquity of long-distance, seasonal migrations in nature, we address their effect on species coexistence. We find a striking phenomenon: long-range migration in combination with local dispersal can promote and stabilize species coexistence. In particular, we consider species movements on two distinct spatial scales: intra-patch and inter-patch migrations. The resulting microscopic model based on stochastic interactions, as will be explained, is quite different from the classical, coupled patchy models described by deterministic differential equations [155, 186]. We will show that migrations at the distinct spatial scales can result in species coexistence in *target* wave patterns [187]. Associated with coexistence, synchronization and time-lagged synchronization emerge among spatial patterns in different patches, stabilizing coexistence. The time-lagged synchronization can potentially be used to predict the spatiotemporal evolution of species. In addition, we find that rare mutations, in combination with long-range migrations, can induce a spontaneous outbreak of biodiversity. Our results not only provide insights into the

dynamics of global oscillations induced by long-distance interactions among cyclically competing species [188], but also have implications to the emergence and maintenance of order from randomness and disorder in natural and social systems through self-organization in the absence of any central control.

8.2. Model description

We consider multiple-patch systems of three subpopulations (referred to as a, b and c) under both intra- and inter-patch migration. Within each patch, a, b and c interact with each other according to the following rules: (1) $ab \xrightarrow{u} a\varnothing$, $bc \xrightarrow{u} b\varnothing$, $ca \xrightarrow{u} c\varnothing$; (2) $a\varnothing \xrightarrow{\sigma} aa$, $b\varnothing \xrightarrow{\sigma} bb$, $c\varnothing \xrightarrow{\sigma} cc$; and (3) $a\odot \xrightarrow{\varepsilon} \odot a$, $b\odot \xrightarrow{\varepsilon} \odot b$, $c\odot \xrightarrow{\varepsilon} \odot c$, where $\varnothing$ represents empty sites and $\odot$ represents any species or empty sites. Relations (1-3) define competition, reproduction and intra-patch migration that occur at the rates u, σ and ε, respectively. The occurrence probabilities are normalized by $(u+\sigma+\varepsilon)$. Since our focus is on the role of mobility, we set $u=\sigma=1$ without loss of generality. The individual mobility is defined as $M=\varepsilon(2N)^{-1}$, which is proportional to the number of sites explored by one individual per time step [184]. Initially, individuals are randomly located over all patches, each of which is represented by a lattice of $L \times L$ sites with open boundary conditions. At each simulation step, a random pair of neighboring sites is selected for one interaction from (1-3) according to their probability. Whether the chosen interaction can actually occur is determined by the states of both sites. An actual time step t is defined when each individual has experienced interaction once on average, i.e., in one time step N pairwise interactions will have occurred. Inter-patch migration is a type of long-distance species movements among different patches. In a certain period, a mutual migration takes place among patches, where one randomly selected individual migrates from one patch to a random location in the target region of another patch and vice versa (see Fig. 48). The speed of inter-patch migration is determined by the parameter T_m, the actual time between two successive mutual migrations.

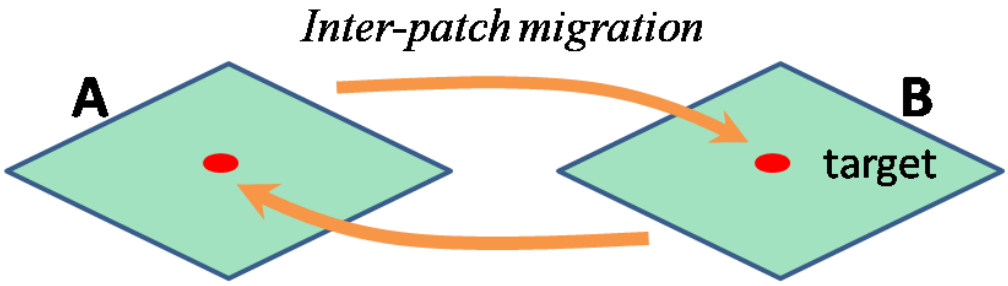

Fig. 48. Illustration of inter-patch migration in a two-patch ecosystem with open boundary conditions. There is a periodic migration between two patches: at each time step nT_m ($n = 1, 2, \ldots$), one randomly selected individual migrates from patch A to patch B and vice versa. The the migration (target) region can be of any size and at any location in the patch. If the target area contains several sites, we randomly pick one site. If there are more than two patches, each migration individual first randomly chooses a patch and then occupies a target site, regardless of the original individual at the site. The individual with inter-patch migration leaves its site empty in the original patch.

8.3. Results on multiple forms of synchronization

We first study an ecosystem of two patches, where a single target region is located at the center of each patch for inter-patch migration (Fig. 49). Without the migration, in each patch two species will become extinct and only one species can prevail. When inter-patch migration occurs, a predominant species can arise due to the difference in the initial densities at $t \approx 2500$, as shown in Fig. 49. After this event, species superior to the dominant one in the cyclic-competition loop appear around the target points in both patches, inducing target waves emanating from their respective target points and propagating outward. For large times, the target waves from the two patches tend to synchronize with each other at $t = 25000$. When synchronization occurs, it can be maintained and there is then a strong order in the system dynamics. We have examined a three-patch systems starting from single specie on each patch and a four-patch systems when the target locations deviate from the centers of patches. e.g., at the corner of each patch. We observe synchronized target waves as well.

The area of target in each patch can have a significant influence on the pattern formation and

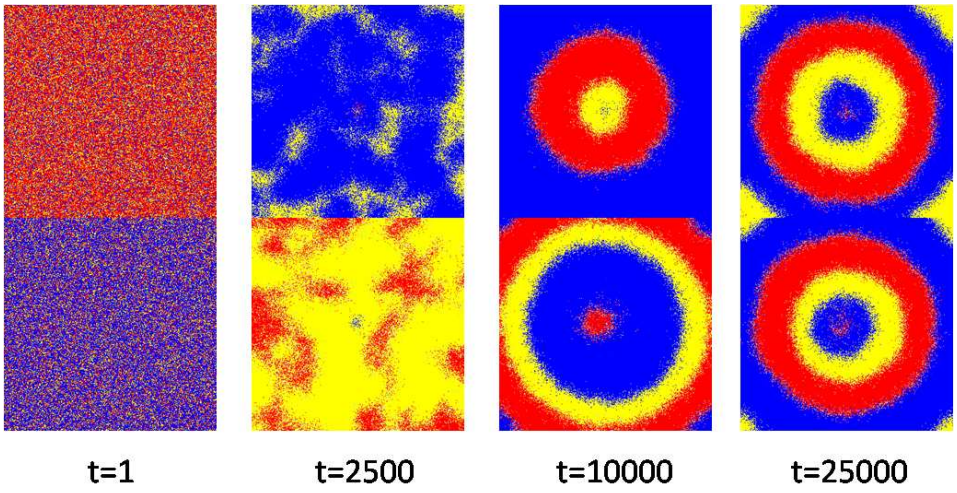

Fig. 49. Emergence of target waves and pattern synchronization in a two-patch system with initially mixed populations for $M = 0.7 \times 10^{-4}$ and $T_m = 1$. Each patch has size 300×300 and target is at center. The initial densities of species in the first patch are $\rho_a = 0.6$ and $\rho_b = \rho_c = 0.2$, and in the second patch are $\rho_b = 0.6$ and $\rho_a = \rho_c = 0.2$. Red, blue and yellow colors represent the three species a, b and c, respectively, and empty sites are denoted by gray.

synchronization. As shown in Fig. 50, we observe synchronization of target waves when the target area is small. In this case, time series of densities of a particular species in the three patches exhibit a phase-synchronized behavior. For a large target area, a strikingly different type of synchronization occurs: time-delayed synchronization. In this case, the time series of species densities from the three patches exhibit the same period T but there is a time lag of about T/N_p among them, where N_p is the number of patches [Fig. 50(b-d)]. Time series of species densities can be used to characterize the correlation and difference among target-wave patterns from different patches.

We introduce an order parameter defined by the phase difference between the species densities, as shown in Fig. 50(b). Specifically, the average period can be computed by the time interval between two neighboring peaks. Since the densities in the three patches exhibit similar oscillating behaviors, we define an average period $\langle T\rangle$ obtained from, say ρ_a in three patches. We can then calculate the order parameter of phase synchronization between each pair of patches. For example, for B and C, the order parameter η_{BC} reads

$$\eta_{BC} = 1 - \frac{\langle \min(\Delta t_{BC}, \langle T\rangle - \Delta t_{BC})\rangle_{BC}}{\langle T\rangle/2}, \tag{8.1}$$

where $\langle\cdots\rangle_{BC}$ stands for the average over all pairs of neighboring peaks in B and C and the value of $\min(\Delta t_{BC}, \langle T\rangle - \Delta t_{BC})$ is always less than $\langle T\rangle/2$. If ρ_a's from B and C display a phase coherence, Δt_{BC} tends to zero and η_{BC} approaches unity. If the phases are incoherent, η_{BC} tends to zero. The overall order parameter η can be defined by the average of order parameters over all patches: $\eta = (\eta_{AB} + \eta_{AC} + \eta_{BC})/3$. Lag synchronization, however, needs to be characterized by all pairs of order parameters. Since the time delay for each pair is $T/3$, for lag synchronization we have $\eta_{AB} = \eta_{AC} = \eta_{BC} = 1/3$.

The order parameter enables us to quantify the dependence of pattern synchronization on both M and T_m. As shown in Fig. 51, for $M < 2 \times 10^{-5}$, target waves become unstable and break into small spiral waves (the three insets in region I). Once spiral waves have appeared, they are robust, making the appearance of target waves difficult. For large values of T_m, because of the low inter-patch migration frequency, species coexistence in each patch is ruled out. Based on these results, we

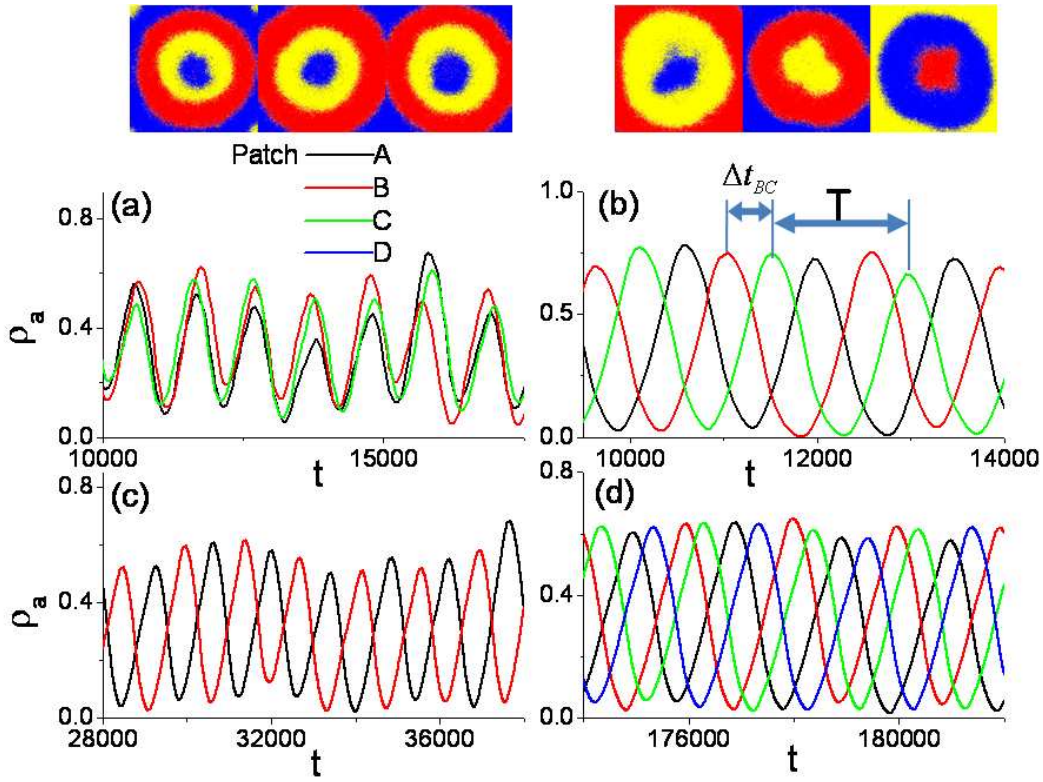

Fig. 50. (a) Phase synchronization and (b) time-delayed synchronization among target waves patterns in a three-patch system for small and large migration-target area, respectively. The parameters are $M = 0.8 \times 10^{-4}$ and $T_m = 1$. (c) Time-delayed synchronization for a two-patch ($M = 0.6 \times 10^{-4}$) and (d) a four-patch ($M = 1.2 \times 10^{-4}$ and $T_m = 1$) system, where the evolutions of densities of species whose distances from the central target site are less than $L/2$ are displayed. The target radii for synchronization and lag synchronization are 15 and 40, respectively and $L = 300$.

have identified three regions in the parameter space: (I) spiral-wave region, (II) target-wave region and (III) extinction region. Of interest is region II where synchronization occurs as a result of both intra- and inter-patch migration.

To gain further insights into pattern synchronization, we study the number of rings n_r associated with the target waves when synchronization occurs. Without loss of generality, we consider two patches A and B. In each patch, the central species a is surrounded by b and b is surround by c. The average length L_r of an arbitrary species in A is

$$L_r = \mathbb{T}V = \frac{T_m V}{\langle \rho_B(c) \rangle - \langle \rho_B(b) \rangle}, \tag{8.2}$$

where V is the front propagation velocity of target waves and $\mathbb{T}$ is the time interval between two successful inter-patch migrations between two patches. Note that only when species c moves to the migration target can a new ring be generated. Because, at each time step, the individual that executes actual migration is random, the time interval $\mathbb{T}$ for patch A is determined by the average species densities $\langle \rho_B(c) \rangle$ and $\langle \rho_B(b) \rangle$ in patch B from which individuals migrate, and vice versa. Given the lengths of the rings, n_r is given by $n_r = L/(\sqrt{2}L_r)$. Since V does not depend on the inter-patch migration parameter T_m, the front propagation velocity V can be obtained by casting the cyclically competing game in the framework of complex Ginzburg-Landau equation (CGLE) [184]. The spreading velocity of the propagating wave fronts can be determined by linearizing the CGLE around the unstable point: $\partial_t z(\boldsymbol{r}, t) = M\Delta z(\boldsymbol{r}, t) + (c_1 - i\omega)z(\boldsymbol{r}, t) + o(z^2)$. The spreading velocity is $= 2\sqrt{c_1 M}$, where the coefficient is given by $c_1 = u\sigma/[2(3u + \sigma)]$. Due to pattern synchronization, the densities of species in patch A and patch B are identical: $\rho_A(b) = \rho_B(b)$ and $\rho_A(c) = \rho_B(c)$, we can then estimate the densities of species b and c in patch A during the propagation of the central ring occupied by a from zero to length L_r. The average density of c reads: $\langle \rho_A(c) \rangle = \int_{L_r}^{2L_r} [\pi(x + L_r)^2 - \pi x^2]/(L^2 L_r) dx = 4\pi L_r^2/L^2$. Analogously, the outside boundary of species b to the center ranges from 0 to L_r, yielding $\langle \rho_A(b) \rangle = 2\pi L_r^2/L^2$. Inserting $\langle \rho_A(c) \rangle$ and $\langle \rho_A(b) \rangle$ into Eq. (8.2) yields

$$n_r = \frac{L}{\sqrt{2}L_r} = \left(\frac{2T_m}{\pi L} \sqrt{\frac{u\sigma}{3u + \sigma} M} \right)^{-1/3}. \tag{8.3}$$

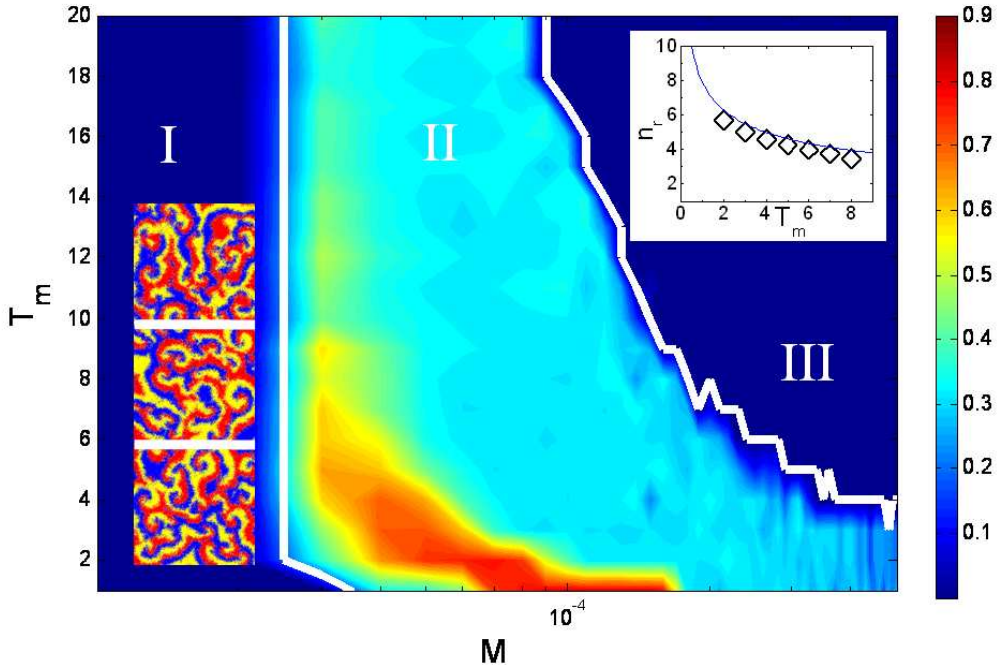

Fig. 51. In a three-patch system, dependence of the order parameter η on M and T_m. The radius of migration target is 10, centered at the lattice. Three phases are identified in the parameter space: (I) spiral waves, (II) target-wave region in which there is a synchronization subregion, and (III) extinction region defined by the criterion that in any patch at any time, the number of individuals in a species is less than three. The size of each patch is 300×300 and initially there is a single species in each patch. The inset at the upper-right corner is the dependence of n_r on T_m in the synchronization regime for $M = 10^{-5}$. The curve is the theoretical results from Eq. (8.3).

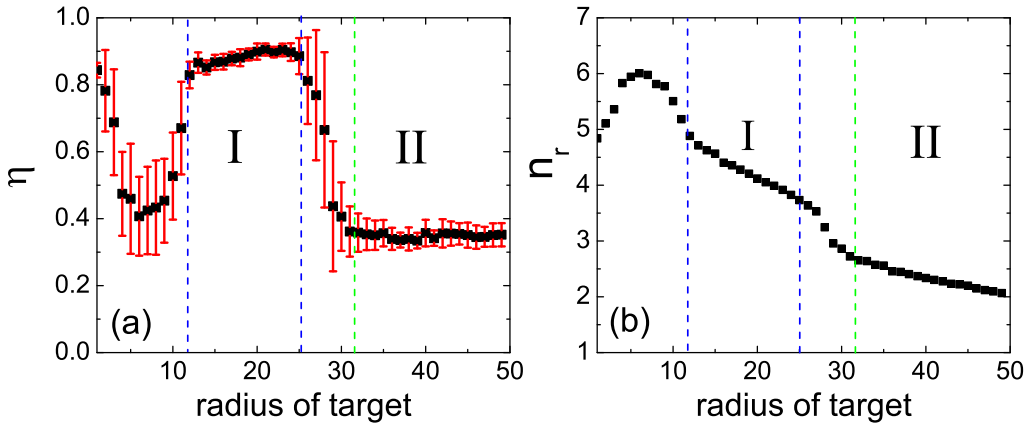

Fig. 52. For a three-patch (A, B, C) system, (a) mean value and standard deviation of order parameter η and (b) the number of rings n_r as a function of the radius of target region. Parameters are $L = 300$, $M = 0.8 \times 10^{-4}$ and $T_m = 1$. Data points are obtained from 20 independent realizations, where $\eta = (\eta_{AB} + \eta_{AC} + \eta_{BC})/3$ and the bars represent the standard deviations. There are three distinct dynamical behaviors: synchronization in region I, lag synchronization in region II, and disorder in other regions.

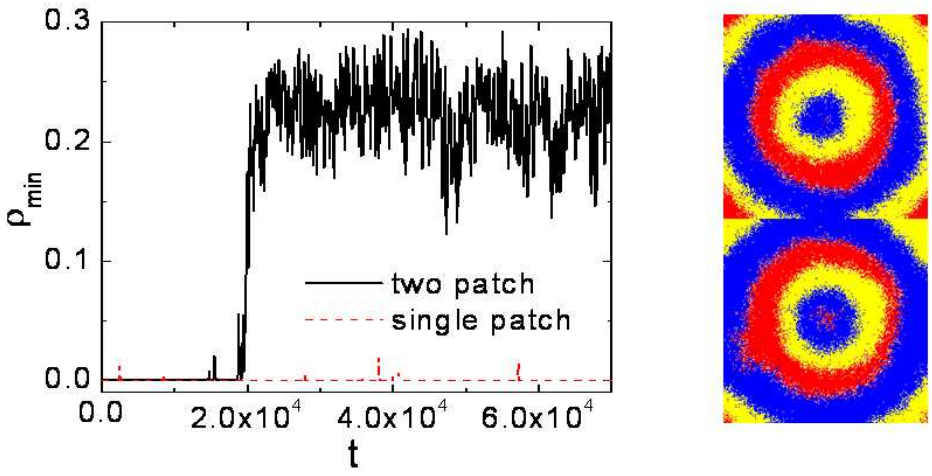

Fig. 53. In a two-patch system, outbreak of biodiversity from random, rare mutations in a single species world for $M = 0.7 \times 10^{-4}$ and $T_m = 2$. Each lattice size is 200×200 with a central target region, and the mutation probability for each individual is 10^{-7} at each time step. The quantity ρ_{min} is defined as the density of the least frequent species in a patch, averaged over the two patches. Synchronized target waves are associated with the outbreak of biodiversity.

The analytical result is in good agreement with numerical simulations (inset at the upper-right corner of Fig. 51). We have also investigated the transition from synchronization to lag synchronization as the target area is increased [Fig. 52(a)]. We see that the system experiences synchronization (single-site target), disorder, synchronization (region I), disorder and lag synchronization (region II). The number of rings n_r is confined to a certain range when synchronization behaviors occur, as shown in Fig. 52(b).

An interesting issue is whether the combination of two types of migrations can induce a *spontaneous* outbreak of biodiversity from rare mutations in a single species world. To address this, we consider a two-patch system with an identical single species. We randomly reset the state of each individual with a small probability p to mimic the effect of random mutations. We then examine the spatial patterns and the lowest density ρ_{min} of the species in each patch, where a near-zero value indicates extinction. As shown in Fig. 53, after a relatively long transient time, a sudden change

from zero in ρ_{min} occurs, signifying coexistence. Accompanying this are target wave patterns in both patches, ensuring persistence of all three species. This outbreak of biodiversity is triggered by the occasional appearance of new species in combination with the inter-patch migration. In contrast, without the inter-patch migration (effectively a single-patch environment), even though three species can occasionally appear simultaneously, the large differences among their densities will lead quickly to a predominant species, excluding the other two species, as represented by the small fluctuations of ρ_{min} about zero.

8.4. conclusion

In conclusion, our computations and analysis demonstrate that the interplay between intra- and inter-patch migrations in multi-patch ecosystems under cyclic competition can lead to remarkable target-wave patterns originated from stochastic interactions in the absence of any external control. These waves can form regardless of the area and the position of the migration target and the number of patches. Strikingly, depending on the area of the migration target, synchronization and lag synchronization in the target-wave patterns among different patches can occur. The synchronization state in fact stabilizes species persistence in a remarkable order, in contrast to the view that population synchronization is a cause for global population extinction, whereas lag synchronization enables prediction of the future spatiotemporal evolution of species based on current dynamical behavior. Analytic insights into the synchronization dynamics have been obtained through the theoretical framework of CGLE. We have also observed the phenomenon of outbreak of biodiversity from a single-species world through rare mutations. Our results are relevant to issues of pattern formation, control in excitable systems, and the origin of order arising from self-organization in social and natural systems.

9 . MULTI-ARMED SPIRALS AND MULTI-PAIRS ANTISPIRALS IN SPATIAL ROCK-PAPER-SCISSORS GAMES

Non-hierarchical cyclic competitions have been observed in a number of real ecosystems, ranging from colicinogenic microbes competition to mating strategies of side-blotched lizards in California [120,137–139,199]. The essential features of such competition can be captured by the childhood game "rock-paper-scissors" (RPS). In the game, species coexistence, as the key factor for maintaining biodiversity, has been given much attention, especially for the conditions that ensure species coexistence [115, 165, 200–205]. Both laboratory experiment and theoretical model have revealed that spatial structure by confining local interaction is necessary for stabilizing species coexistence [199]. Otherwise, stochastic effect and external perturbation can easily ruin biodiversity. Quite recently, individual mobility has been incorporated in the spatial RPS game [130, 183, 189, 192]. It has been found that individual mobility induces entangled moving spiral waves which preclude species from extinction [189]. The stochastic game has been casted into a set of partial differential equations by a continuous approximation [192]. In this thesis, we investigate the origin of multi-armed spiral waves and multi-pairs antispiral waves on the basis of the spatial RPS game with mobile individuals, which is unaddressed prior to our work. We find that the joint spiral waves can spontaneously arise due to the interaction of neighboring spirals and the type of the joint spirals is determined by the position and rotational directions of neighboring spirals. In particular, we discover a general set of seeds of species distribution, which is capable of producing multi-armed spirals with arbitrary numbers of arms and antispirals with arbitrary numbers of pairs. The diverse patterns generated from stochastic simulations are reproduced by solving a set of partial differential equations from specific initial conditions. We have also discussed the stability of the joint spiral waves with respect to individual mobility.

9.1. The RPS Model

We consider the spatial RPS game proposed in Ref. [189]. Nodes of a $L \times L$ square lattice with no flux boundary conditions sustain mobile individuals belonging to one of the three species, A, B

and C. Each node can either host one individual of a given species or it can be vacant. Vacant sites, denoted by $\otimes$, are also the so-called resource sites where individuals of species reproduce offspring. The dynamical process can be described as following:

$$AB \xrightarrow{1} A\otimes \quad , \quad BC \xrightarrow{1} B\otimes \quad , \quad CA \xrightarrow{1} C\otimes \tag{9.1}$$

$$A\otimes \xrightarrow{1} AA \quad , \quad B\otimes \xrightarrow{1} BB \quad , \quad C\otimes \xrightarrow{1} CC \tag{9.2}$$

$$A\odot \xrightarrow{\gamma} \odot A \quad , \quad B\odot \xrightarrow{\gamma} \odot B \quad , \quad C\odot \xrightarrow{\gamma} \odot C \tag{9.3}$$

where $\odot$ denotes any species or vacant sites. These reactions describe three processes, i.e. competition, reproduction and exchange, occurring only between neighboring nodes. In reaction (1), species A eliminates species B at a rate 1, whereby the node previously hosting species B becomes vacant. In the same manner species B can kill species C, and species C can kill species A, thus forming a closed loop. In reaction (2), individuals place an offspring to a neighboring vacant node $\otimes$ at a rate 1. Reaction (3) defines exchange process where an individual exchanges its position with an individual belonging any specie or an empty site at a rate γ. According to the theory of random walks [206], mobility of individuals M is defined as: $M = \gamma/2N$, where $N = L \times L$ and M represents the typical area explored by one mobile individual per unit time.

We apply stochastic algorithm developed by Gillespie to simulate the system's evolution, where the occurring probabilities of reactions are determined by their rates. In our model, competition and reproduction occur with probability $1/(\gamma + 2)$, whereas exchange (moving) occurs with probability $\gamma/(\gamma + 2)$. At each step, an individual is randomly selected to interact with one randomly selected neighboring site. In a Mote Carlo step, all individuals are selected once on average.

9.2. Multi-armed spiral patterns

A critical value $M_c = (4.5 \pm 0.5) \times 10^{-4}$ of mobility has been identified in Ref. [189]. Below M_c, three subpopulations can stably coexist in the form of moving spiral waves; while above M_c, the wave length of spirals exceeds the size of underlying lattice and biodiversity is lost. Here, we focus on the biodiversity region for $M < M_c$. In this region, by carrying out sufficient stochastic simulations from random initial distributions of species, we found there is chance to observe both

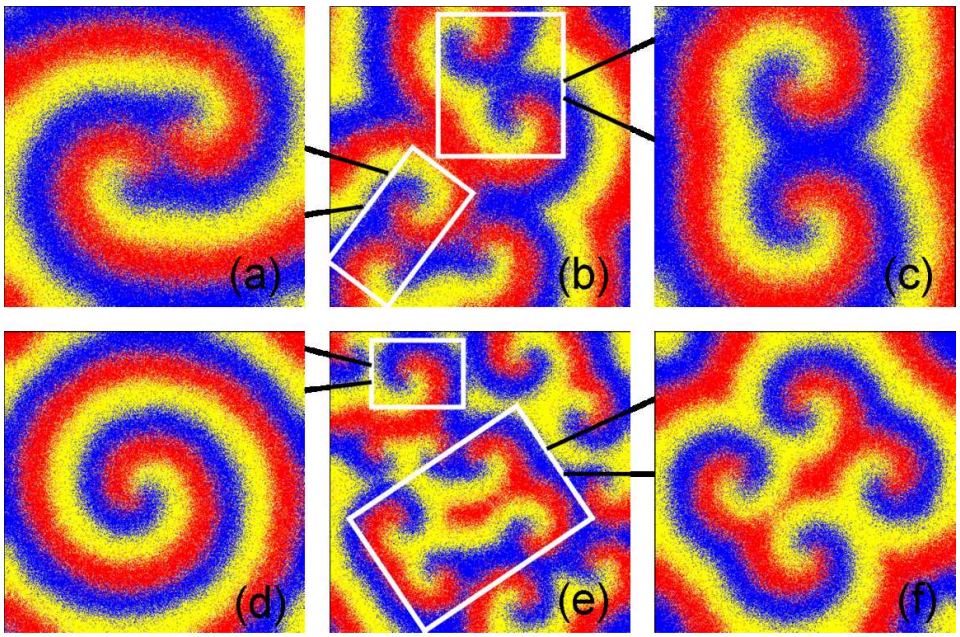

Fig. 54. Spatial patterns in RPS game for $M = 5.0 \times 10^{-5}$. Panels (b) and (e) are obtained from random distribution of three species initially. In panels (a), (c), (d), and (f), the system starts from specific seed distributions of three species. $L = 512$ for all panels.

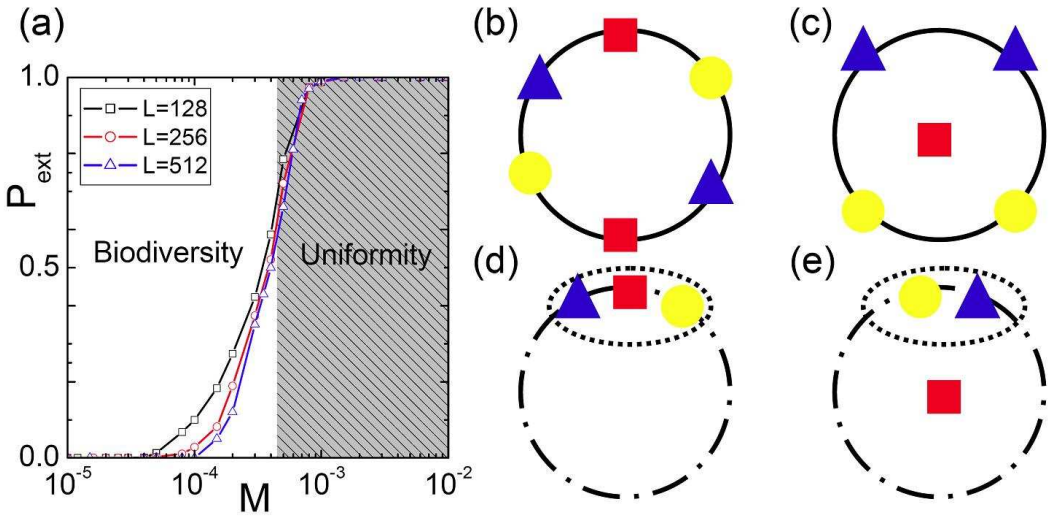

Fig. 55. In panel (a), extinction probability P_{ext} as a function of mobility M. Seed distribution of species for producing (b) two-armed spiral, (c) one pair antispiral, (d) multi-armed spirals with arbitrary numbers of arms and (e) antispirals with arbitrary numbers of pairs.

multi-armed spirals and multi-pairs antispirals, as shown in Fig. 54(b) and (e). In Fig. 54(b), there is a two-armed spiral and an one-pair antispiral, which are zoomed in in Fig. 54(a) and (c), respectively. A one-armed spiral and a two-pairs antispiral can be found in Fig. 54(e) and their enlarged versions are displayed in Fig. 54(d) and (f), respectively. We also found that these patterns can last for relative long time and then they may disappear or transform to single armed spirals with the initial conditions of species randomly distributing on the lattice. In the multi-armed spirals, the arms rotate in the same direction with the same speed, resulting exclusively from stochastic interactions among neighboring individuals. In the antispirals, the two spirals of a pair rotate with the same speed but in reverse directions. The identical rotational speed of sub-spirals in the waves ensures their stable existence. It worth mentioning that patterns in Fig. 54 are obtained from no flux boundary conditions, and we also examine the phase transition of system from biodiversity to uniformity with no flux boundary conditions. As shown in Fig. 55(a), a critical mobility M_c emerges at 4.5×10^{-4}, which is the same as the result of periodic boundary conditions in Ref. [189].

It is interesting to find that the multi-armed spirals and multi-pairs antispirals can arise from

some specific distribution of three subpopulations. As shown in Fig. 55(b) and Fig. 55(c), square, triangle and circle symbols stand for a small amount of three subpopulations which are placed on a lattice with no flux boundary condition. Other sites of the lattice are left empty. In the early stage, each pile of individuals expand due to reproduction. After the boundaries of different species encounter, populations begin to rotate because of the cyclic competition. Finally, after the systems reaching a non-equilibrium steady state, a two-armed spiral and a one-pair antispirals emerge. Let's see Fig. 55(b), the six pile of species placed around a circle are in the order A, B, C, A, B, and C. The six piles can be separated into two groups, each of which contains three species. During the evolution, each group form an arm. Due to the spatial symmetry of the two group, the wave lengthes, rotation speeds and directions of the two arms are the same, giving rise to a steady two-armed spiral (Fig. 54(a)). In contrast, to generate antispirals, we need to place an arbitrary species at the center of a circle and the other two species around the circle (Fig. 55(c)), leading to a steady one-pair antispiral (Fig. 54(c)).

By extending the simple configuration in Fig. 55(b) and (c), we discover a general route to generate multi-armed spirals with arbitrary numbers of arms and antispirals with arbitrary numbers of pairs. To articulate the method, we should define the basic cell in the initial distribution of species. As shown in Fig. 55(d), the cell of multi-armed spirals is composed of three species in the order A, B and C. The cell of antispiral contains two species except the central species. The central species can be arbitrary, but once the central species is fixed, the cell is fixed as well. For the multi-armed spirals, the number of arms is determined by the number of cells. In general, one arm can be formed by one cell, so that by adjusting the number of cells, one can obtain multi-armed spirals with any number of arms. For the antispiral, the number of cells equals the number of antispiral pairs. One-pair antispirals is different from this regulation, as shown in Fig. 55(c). Two cells with reverse orders are required to create one-pair antispirals, as shown in Fig. 55(e). Stochastic simulation results from a set of seed distribution with different numbers of cells are shown in top panels of Fig. 56 for multi-armed spirals and in top panels of Fig. 57 for multi-pairs antispirals, respectively. The patterns

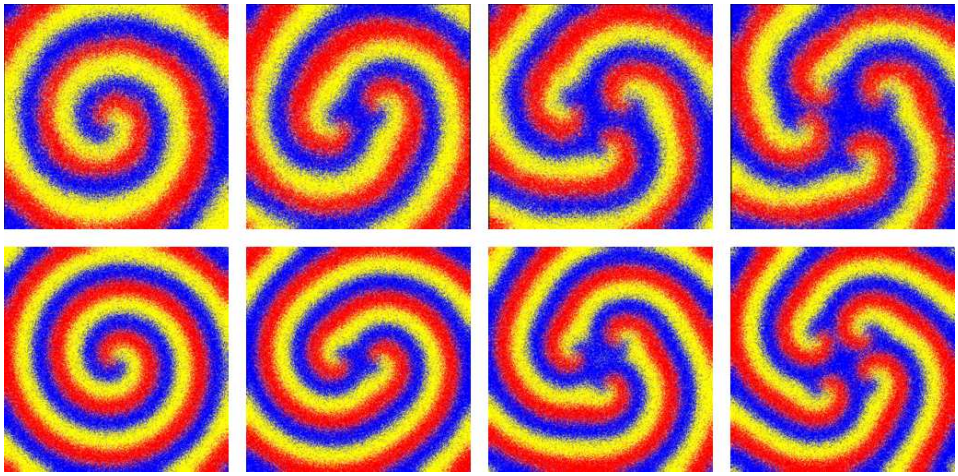

Fig. 56. Multi-armed spirals with one, two, three and four arms by stochastic simulations (top panels) and by solving PDEs (bottom panels). The parameters are $M = 5.0 \times 10^{-5}$ and $L = 512$.

justify the generate route to producing multi-armed spirals and multi-pairs antispirals.

It is noteworthy that a large number of arms or pairs is not stable because of the stochastic effect. Although all arms or pairs can be formed, after a while, some arms or pairs will be intruded by neighboring arms or pairs and disappear. The no flux boundary conditions are also necessary to generate the waves. In contrast, for periodic boundary conditions, the joint spirals in global scale will be destroyed and break into small spirals. The symmetry of the distribution of cells sustains the stability of multi-armed spirals and multi-pairs antispirals, and better symmetry lead to more stable waves. The radii of the circle and the number of individuals in each pile do not affect the wave patterns.

9.3. Predictions by PDE model and the spatial entropy

The patterns generated by stochastic simulations can be predicted theoretically by a set of partial differential equations (PDEs). As derived in the works of Reichenbach et al. [189, 192], starting

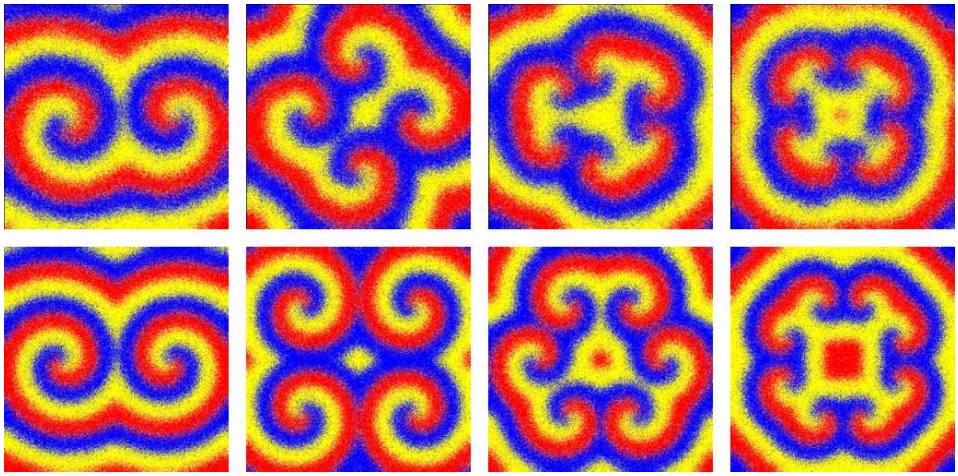

Fig. 57. Antispirals with one, two, three and four pairs by stochastic simulations (top panels) and by solving PDEs (bottom panels). The parameters are the same as in Fig. 56.

from rate equations and applying the continuous approximation, we have

$$\begin{aligned} \partial_t a(\mathbf{r},t) &= D\nabla^2 a(\mathbf{r},t) + a(\mathbf{r},t)(1-\rho) - c(\mathbf{r},t)a(\mathbf{r},t), \\ \partial_t b(\mathbf{r},t) &= D\nabla^2 b(\mathbf{r},t) + b(\mathbf{r},t)(1-\rho) - a(\mathbf{r},t)b(\mathbf{r},t), \\ \partial_t c(\mathbf{r},t) &= D\nabla^2 c(\mathbf{r},t) + c(\mathbf{r},t)(1-\rho) - b(\mathbf{r},t)c(\mathbf{r},t), \end{aligned} \tag{9.4}$$

where $a(\mathbf{r},t)$, $b(\mathbf{r},t)$ and $a(\mathbf{r},t)$ are the densities of species A, B, C at position $\mathbf{r}$ and time t, $\rho = a(\mathbf{r},t) + b(\mathbf{r},t) + c(\mathbf{r},t)$ is the local species density and $1-\rho$ denotes the density of empty sites. Eulerian difference method and Runge-Kutta method are applied to solve the PDEs. The initial conditions are $a(\mathbf{r}) = b(\mathbf{r}) = c(\mathbf{r}) = 0$ for all spatial coordinate $\mathbf{r}$ except the initial seed species in Fig. 55. In the coordinate of seed, one species's density is one and the others are zero. The patterns generated by numerically solving the PDEs are exhibited in the bottom rows of Fig. 56 and Fig. 57 for multi-armed spirals and multi-pairs antispirals, respectively. The theoretical patterns are in good agreement with simulation patterns. The colors in the theoretical patterns are determined by the densities of three species on all the spatial sites. For example, at an arbitrary location $(\mathbf{r})$ and time t, the site i is denoted by the color of species A with probability $a(\mathbf{r},t)$, by B' color with probability $b(\mathbf{r},t)$, and by C's color with probability $c(\mathbf{r},t)$.

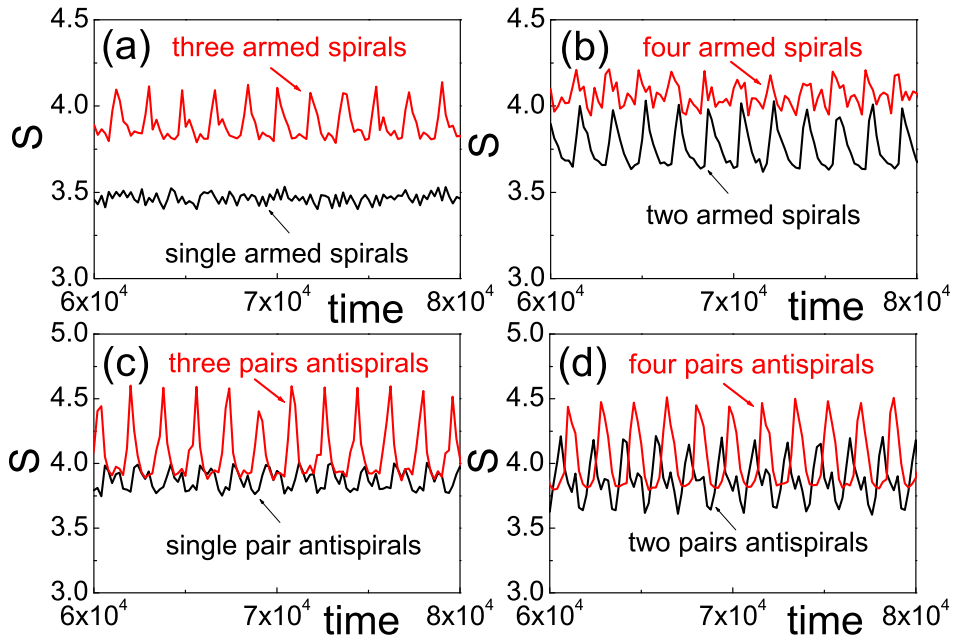

Fig. 58. The spatial entropy varying with time at $D = 5.0 \times 10^{-5}$ for multiple armed spirals and antispirals obtained from PDE method, single armed and three armed spirals in (a), two armed and four armed spirals in (b), two armed and three pairs antispirals in (c), four armed and four pairs antispirals in (d). The pattern formations are shown in bottom panels of Fig. 56 and Fig. 57 respectively. $L = 512$ for all panels.

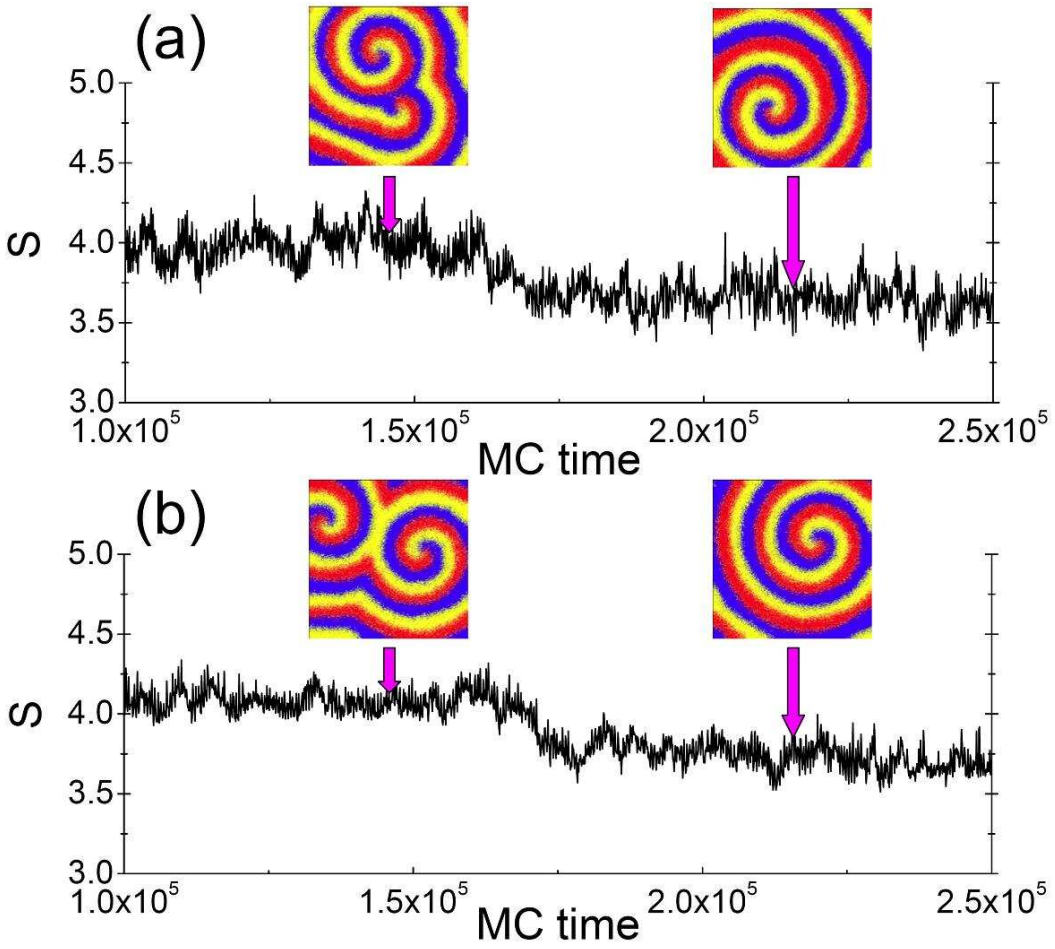

Fig. 59. The spatial entropy evolves with Monte Carlo (MC) time at $M = 4.0 \times 10^{-5}$ for two armed spirals in panel (a) and single pair antispirals in panel (b). It is notable that both two armed spirals and one pair antispirals become single armed spirals in the end, and patterns in panel (a) and panel (b) obtained at time of 1.45×10^5 and 2.15×10^5 respectively. $L = 512$ for all panels.

To quantitatively investigate the emergence of multi-armed spirals and multi-pairs antispirals, we define the spatial entropy of patterns according to Shannon entropy [208]:

$$S = -\sum_{i=1}^{z} p_i ln p_i \ , \tag{9.5}$$

where z is the number of the clusters formed by individuals of the same species and p_i is the probability of the cluster with size of x, $p_i = x/N$. Here, the size x is the number of individuals of the same species in the cluster. Fig. 58 shows spatial entropy of multi-armed spirals and multi-pairs antispirals as function of time with PDE method. Average values of spatial entropy are 3.4, 3.7, 3.8, and 4.0 for one-armed, two-armed, three-armed, and four-armed spirals respectively, while average values of spatial entropy are 3.8 for both one-pair and two-pairs antispirals, 4.0 for both three-pair and four-pairs antispirals. One can find that the spatial entropy of single spirals is smaller than that of multi-armed spirals and multi-pairs antispirals.

Since multi-armed spirals and multi-pairs spirals are unstable at too small or large mobility, without loss of generality, we investigate the evolvement of pattern and spatial entropy at $M = 4.0 \times 10^{-5}$ with stochastic algorithm. Fig. 59 shows the spatial entropy evolving with Monte Carlo (MC) time for two armed spirals and one pair antispirals which transform to the single armed spirals, and one can find that the two armed spirals and one pair antispirals emerge in the system at beginning, as shown in left insets of Fig. 59(a) and Fig. 59(b) respectively, while after long time evolving both two armed spirals and one pair antispirals become the single armed spirals, as shown in right insets of Fig. 59(a) and Fig. 59(b) respectively. In addition, the spatial entropy for both two armed spirals and one pair antispirals induces after the transformation.

9.4. Stability of spiral anti-spiral patterns

Finally, we examine the stability of spirals and antispirals with respect to the individual mobility M. The results are carried out from a number of independent realizations. The shadow and gray regions in Fig. 60 (a) denote one-armed spirals and two-armed spirals emerging stably in the system, respectively. There are three regions: for small values of M, e.g., $M < 1.0 \times 10^{-5}$, both single spiral and two-armed spiral break into a number of small spirals; for large values of M, e.g., $M >$

1.0×10^{-3}, biodiversity is lost and spirals disappear; for intermediate values of M, both spirals survive. The single spiral is more stable then the two-armed spiral and the latter can transform to the former. The similar phenomenon is also observed for multi-pairs antispirals. As shown in Fig. 60 (b), one-pair and two-pairs antispirals exist stably in the shadow and gray region respectively. There exhibit three regions and the one-pair is more stable then the two-pair, similar to the multi-armed spirals. The top panels of Fig. 60 demonstrate that at the boundaries of three regions, the two-pair antispirals reduces to single spiral.

Spatiotemporal patterns have been investigated extensively, ranging from chemical reactions on catalytic surfaces to propagating signals in aggregating microorganisms [209]. It is found that patterns in excitable media emerge primarily due to the instabilities induced by the interplay between the fast excitatory and slow recovery variables. This kind of mechanism explain well the multi-armed spirals and antispirals emerging in the Belousov- Zhabotinsky (BZ) reaction [195] as well as cardiac substrate [195], and aggregating amoeba D. discoideum [194]. However, multi-armed spirals and multi-pairs antispirals in our systems emerge because of cyclic interaction in populations of three species with the same mobility. In this chapter, we have explore the origin and stability of multi-armed spirals and multi-pairs antispirals in the spatial rock-paper-scissors game with mobile individuals. The two types of joint spirals are naturally observed by stochastic simulations. We have discovered a set of seed distributions of species, which is able to produce multi-armed spirals and multi-pairs antispirals with arbitrary numbers of arms and anti-pairs. The availability of the seed for producing the waves are justified by both stochastic simulations and a theoretical model described by a set of partial differential equations. The theoretical patterns is consistent with numerical patterns. We have also discussed the stability of multi-armed spirals and multi-pairs antispirals depending on the individual mobility. We found that in the intermediate mobility, both waves are relatively stable, whereas for low mobility, the spirals in the global scale breaks into small spirals and for high mobility, spirals disappear due to the loss of biodiversity. We have also found that large numbers of arms or anti-pairs weaken the stability of the joint spirals and the joint spirals with larger numbers

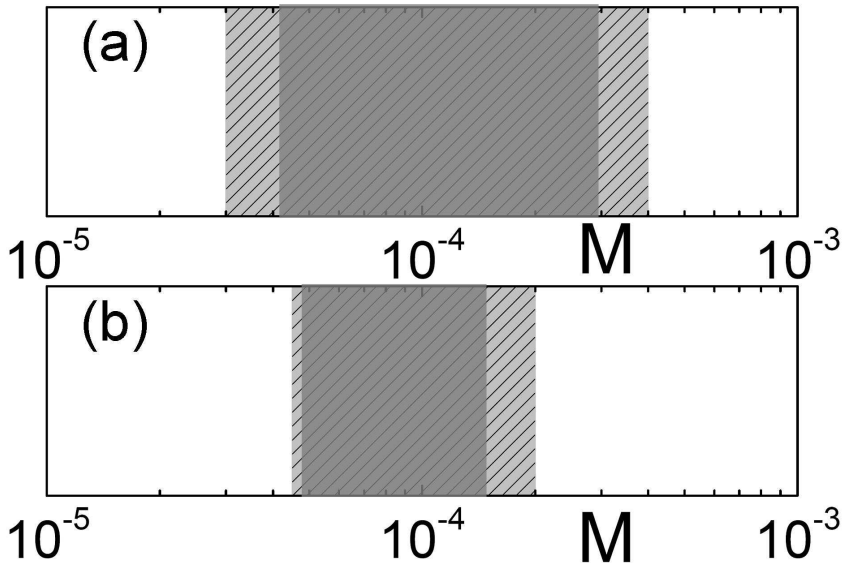

Fig. 60. The shadow and gray region indicate emerging stably of one- and two-armed spirals respectively in panel (a), and show appearing stably of one- and two-pairs antispirals respectively in panel (a). Results are obtained from 100 different independent realizations, $L = 512$.

of arms or anti-pairs can transform to less numbers of arms or anti-pairs. Our work gains insight into the pattern formation through stochastic processes rather than deterministic equations.

REFERENCES

[1] K. S. Novoselov, A. K. Geim, S. V. Morozov, D. Jiang, Y. Zhang, S. V. Dubonos, I. V. Grigorieva, A. A. Firsov, *Electric field effect in atomically thin carbon films*, Science **306**, 666 (2004).

[2] C. Berger, Z. Song, T. Li, X. Li, A. Y. Ogbazghi, R. Feng, Z. Dai, A. N. Marchenkov, E. H. Conrad, P. N. First, and W. A. de Heer, *Ultrathin epitaxial graphite: 2D electron gas properties and a route toward graphene-based nanoelectronics*, J. Phys. Chem. B **108**, 19912 (2004).

[3] K. S. Novoselov, A. K. Geim, S. V. Morozov, D. Jiang, M. I. Katsnelson, I. V. Grigorieva, S. V. Dubonos and A. A. Firsov, *Two-dimensional gas of massless Dirac fermions in graphene*, Nature **438**, 197 (2005).

[4] Y. Zhang, Y.-W. Tan, H. L. Stormer and P. Kim, *Experimental observation of the quantum Hall effect and Berry's phase in graphene*, Nature **438**, 201 (2005).

[5] C. W. J. Beenakker, *Colloquium: Andreev reflection and Klein tunneling in graphene*, Rev. Mod. Phys. **80**, 1337 (2008).

[6] A. H. Castro Neto, F. Guinea, N. M. R. Peres, K. S. Novoselov, and A. K. Geim, *The electronic properties of graphene*, Rev. Mod. Phys. **81**, 109 (2009).

[7] N. M. R. Peres, *Colloquium: The transport properties of graphene: An introduction*, Rev. Mod. Phys. **82**, 2673 (2010).

[8] S. Das Sarma, S. Adam, E. H. Hwang, and E. Rossi, *Electronic transport in two-dimensional graphene*, Rev. Mod. Phys. **83**, 407 (2011).

[9] X.-L. Qi and S.-C. Zhang, *The quantum spin Hall effect and topological insulators*, Phys. Today **63**, 33 (2010).

[10] M. Z. Hasan and C. L. Kane, *Colloquium: Topological insulators*, Rev. Mod. Phys. **82**, 3045 (2010).

[11] J. Tworzydlo, C. W. Groth, and C. W. J. Beenakker, *Finite difference method for transport properties of massless Dirac fermions*, Phys. Rev. B **78**, 235438 (2008).

[12] L. Huang, Y.-C. Lai, D. K. Ferry, S. M. Goodnick, and R. Akis, *Relativistic quantum scars*, Phys. Rev. Lett. **103**, 054101 (2009).

[13] L. Huang, Y.-C. Lai, and C. Grebogi, *Relativistic quantum level-spacing statistics in chaotic graphene billiards*, Phys. Rev. E **81**, 055203(R) (2010).

[14] L. Huang, Y.-C. Lai, and C. Grebogi, *Characteristics of level-spacing statistics in chaotic graphene billiards*, Chaos **21**, 013102 (2011).

[15] R. Yang, L. Huang, Y.-C. Lai and C. Grebogi, *Quantum chaotic scattering in graphene system*, Europhysics Letters **94**, 40004 (2011).

[16] M. C. Gutzwiller, *Chaos in Classical and Quantum Mechanics* (Springer, New York, 1990).

[17] H. J. Stöckmann, *Quantum Chaos: An Introduction* (Cambridge University Press, Cambridge, England, 1999).

[18] F. Haake, *Quantum Signatures of Chaos*, 2nd Edition (Springer, Berlin, 2001).

[19] E. J. Heller, *Bound-state eigenfunctions of classically chaotic Hamiltonian systems: scars of periodic orbits*, Phys. Rev. Lett. **53**, 1515 (1984).

[20] H. A. Weidenmüller and G. E. Mitchell, *Random matrices and chaos in nuclear physics: Nuclear structure*, Rev. Mod. Phys. **81**, 539 (2009).

[21] M. V. Berry and R. J. Mondragon, *Neutrino billiards: time-reversal symmetry-breaking without magnetic fields*, Proc. R. Soc. Lond. A **412**, 53 (1987).

[22] Boundary conditions are also an important issue in graphene systems, e.g., with respect to armchair or zigzag boundaries. See, for example, A. R. Akhmerov and C. W. J. Beenakker, *Boundary conditions for Dirac fermions on a terminated honeycomb lattice*, Phys. Rev. B **77**, 085423 (2008).

[23] V. Alonso and S. Vincenzo, *General boundary conditions for a Dirac particle in a box and their non-relativistic limits*, J. Phys. A: Math. Gen. **30**, 8573 (1997).

[24] P. Alberto, C. Fiolhais and V. M. S. Gil, *Relativistic particle in a box*, Eur. J. Phys. **17**, 19 (1996).

[25] V. Alonso, S. D. Vincenzo and L. Mondino, *On the boundary conditions for the Dirac equation*, Eur. J. Phys. **18**, 315 (1997).

[26] A. Chodos, R. L. Jaffe, K. Johnson, C. B. Thorn and V. F. Veisskopf, *New extended model of hadrons*, Phys. Rev. D **9**, 3471 (1974).

[27] A. Chodos, R. L. Jaffe, K. Johnson and C. B. Thorn, *Baryon structure in the bag theory*, Phys. Rev. D **10**, 2599 (1974).

[28] A. W. Thomas, *Chiral symmetry and the bag model: A new starting point for nuclear physics*, Adv. Nucl. Phys. **13**, 1 (1984).

[29] For example, M. E. Peskin and D. V. Schroeder, *An introduction to Quantum Field Theory* (Westview Press, 1995, Chapter 3).

[30] R. Stacey, *Eliminating lattice fermion doubling*, Phys. Rev. D **26**, 468 (1982).

[31] C. M. Bender, K. A. Milton and D. H. Sharp, *Consistent formulation of fermions on a Minkowski lattice*, Phys. Rev. Lett. **51**, 1815 (1983).

[32] F. J. Dyson and M. L. Mehta, *Statistical theory of the energy levels of complex systems. IV*, J. Math. Phys. **4**, 701 (1963).

[33] O. Bohigas and M. J. Giannoni, *Level density fluctuations and random matrix theory*, Ann. Phys. **89**, 393 (1975).

[34] G. Bohigas and M.-J. Giannoni, In *Mathematical and Computational Methods in Nuclear Physics*, Lecture Notes in Physics, Vol. 209 (Springer, Berlin, 1984).

[35] G. Bohigas, M.-J. Giannoni, and C. Schmit, *Characterization of chaotic quantum spectra and universality of level fluctuation laws*, Phys. Rev. Lett. **52**, 1 (1984).

[36] M. V. Berry, *Semiclassical theory of spectral rigidity*, Proc. R. Soc. London A **400**, 229 (1985).

[37] U. Stoffregen, J. Stein, H.-J. Stöckmann, M. Kuś, and F. Haake, *Microwave billiards with broken time reversal symmetry*, Phys. Rev. Lett. **74**, 2666 (1995).

[38] P. So, S. M. Anlage, E. Ott, and R. N. Oerter, *Wave chaos experiments with and without time reversal symmetry: GUE and GOE statistics*, Phys. Rev. Lett. **74**, 2662 (1995).

[39] L. M. Pecora, H. Lee, D.-H. Wu, T. Antonsen, M.-J. Lee and E. Ott, *Chaos regularization of quantum tunneling rates*, Phys. Rev. E **83**, 065201(R) (2011).

[40] M. C. Gutzwiller, *Chaos in Classical and Quantum Mechanics* (Springer, New York, 1990); H. J. Stöckmann, *Quantum chaos: an introduction* (Cambridge University Press, Cambridge, England, 1999); F. Haake, *Quantum Signatures of Chaos*, 2nd Edition (Springer, Berlin, 2001); E. J. Heller, Phys. Rev. Lett. **53**, 1515 (1984); H. A. Weidenmüller and G. E. Mitchell, Rev. Mod. Phys. **81**, 539 (2009).

[41] L. Huang, Y.-C. Lai, D. K. Ferry, S. M. Goodnick, and R. Akis, Phys. Rev. Lett. **103**, 054101 (2009); L. Huang, Y.-C. Lai, and C. Grebogi, Chaos **21**, 013102 (2011).

[42] K. S. Novoselov, A. K. Geim, S. V. Morozov, D. Jiang, Y. Zhang, S. V. Dubonos, I. V. Grigorieva, A. A. Firsov, Science **306**, 666 (2004); C. Berger, Z. Song, T. Li, X. Li, A. Y. Ogbazghi, R. Feng, Z. Dai, A. N. Marchenkov, E. H. Conrad, P. N. First, and W. A. de Heer, J. Phys. Chem. B **108**, 19912 (2004); K. S. Novoselov, A. K. Geim, S. V. Morozov, D. Jiang, M. I. Katsnelson, I. V. Grigorieva, S. V. Dubonos and A. A. Firsov, Nature **438**, 197 (2005); Y. Zhang, Y.-W. Tan, H. L. Stormer and P. Kim, Nature **438**, 201 (2005); A. H. Castro Neto, F. Guinea, N. M. R. Peres, K. S. Novoselov, and A. K. Geim, Rev. Mod. Phys. **81**, 109 (2009); S. Das Sarma, S. Adam, E. H. Hwang, and E. Rossi, Rev. Mod. Phys. **83**, 407 (2011).

[43] P. Strange, *Relativistic Quantum Mechanics with Applications in Condensed Matter Physics and Atomic Physics* (Cambridge University Press, Cambridge, UK, 1998).

[44] M. I. Katsnelson, K. S. Novoselov, and A. K. Geim, Nat. Phys. **2**, 620 (2006).

[45] W. H. Zurek, Phys. Rev. D **24**, 1516 (1981); *ibid*, Phys. Rev. D **26**, 1862 (1982); *ibid*, Rev. Mod. Phys. **75**, 715 (2003); *ibid*, Nature Phys. **5**, 181 (2009); R. Blume-Kohout and W. H. Zurek, Phys. Rev. Lett. **101**, 240405 (2008); M. Zwolak, H. T. Quan, and W. H. Zurek, Phys. Rev. Lett. **103**, 110402 (2009).

[46] D. K. Ferry, R. Akis, and J. P. Bird, Phys. Rev. Lett. **93**, 026803 (2004); R. Brunner, R. Akis, D. K. Ferry, F. Kuchar, and R. Meisels, Phys. Rev. Lett. **101**, 024102 (2008); A. M. Burke, R. Akis, T. E. Day, Gil Speyer, D. K. Ferry, and B. R. Bennett, Phys. Rev. Lett. **104**, 176801 (2010).

[47] S. Datta, *Electronic Transport in Mesoscopic Systems* (Cambridge Univ. Press, 1995)

[48] D. R. Smith and N. Kroll, Phys. Rev. Lett. **85**, 2933 (2000).

[49] R. W. Ziolkowski and E. Heyman, Phys. Rev. E **64**, 056625 (2001).

[50] R. A. Shelby, D. R. Smith, and S. Schultz, Science **292**, 5514 (2001); R. A. Shelby, D. R. Smith, S. C. Nemat-Nasser, and S. Schultz, Appl. Phys. Lett **78**, 489 (2001).

[51] J. Pacheco, Jr., T. M. Grzegorczyk, B.-I. Wu, Y. Zhang, and J. A. Kong, Phys. Rev. Lett **89**, 257401 (2002).

[52] C. G. Parazzoli, R. B. Greegor, K. Li, B. E. Koltenbah, and M. Tanielian, Phys. Rev. Lett **90**, 107401 (2003).

[53] G. Dolling, C. Enkrich, M. Wegener, C. M. Soukoulis, and S. Linden, Science **312**, 892 (2006).

[54] V. G. Veselago, Phys. Usp. **10**, 509 (1968).

[55] J. B. Pendry, Phys. Rev. Lett. **85**, 3966 (2000).

[56] N. Engheta, R. W. Ziolkowski, *Metamaterials: physics and engineering explorations* (Wiley & Sons, 2006).

[57] D. Schurig, J. J. Mock, B. J. Justice, S. A. Cummer, J. B. Pendry, A. F. Starr, and D. R. Smith, Science **314**, 977 (2006).

[58] J. Valentine, J. Li, T. Zentgraf, G. Bartal, and X. Zhang, Nature Materials **8**, 568 (2009).

[59] D. A. Genov, S. Zhang, X. Zhang, Nature Physics **5**, 687 (2009).

[60] E. Ott and T. Tél, Focus issue on chaotic scattering, Chaos **3**, 417 (1993).

[61] P. Gaspard, *Chaos, Scattering and Statistical Mechanics* (Cambridge University Press, Cambridge, UK, first edition, 1998).

[62] J. R. Dorfmann, *An Introduction to Chaos in Nonequilibrium Statistical Mechanics* (Cambridge University Press, Cambridge, UK, first edition, 1999).

[63] R. Klages, *Microscopic Chaos, Fractal and Transport in Nonequilibrium Statistical Mechanics* (World Scientific, Singapore, first edition, 2007).

[64] J. Aguirre, R. L. Viana, and M. A. F. Sanjuán, Rev. Mod. Phys. **81**, 333 (2009).

[65] In chaotic scattering, a scattering function contains an uncountably infinite number of singularities. Near any of the singularities, an arbitrarily small change in the input variable can cause a large change in the output variable. This is a sensitive dependence on initial conditions that signifies the appearance of chaos. Dynamically, chaotic scattering is due to the existence of non-attracting chaotic sets in the phase space [60, 64]. It is generally understood now that chaotic scattering is the physical manifestation of transient chaos [76] in open Hamiltonian systems.

[66] There is a long history of studying complicated dynamics in gravitational systems, starting from the work of Poincaré on the gravitational three-body problem [H. Poincaré, *Les Méthodes Nouvelles de la Mécanique* (Gauthier-villars, Paris, 1892)]. For a simplified three-body system the motion of the third body is generally chaotic before escape takes place as proved by Sitnikov [J. Moser, *Stable and Random Motions in Dynamical Systems* (Princeton University Press, Princeton, NJ, 1973)] and studied more recently by T. Kovács and B. Érdi [Cel. Mech. Dyn. Astron. **105**, 289 (2009)]. Petit and Hénon considered another class of restricted three-body problems and found chaotic scattering [J. M. Petit and M. Hénon, Icarus **66**, 536 (1988); M. Hénon, Physica D **33**, 132 (1988)]. Chaotic scattering has also been identified in a model of the motion of an incoming star toward a binary [P. T. Boyd and S. L. W. McMillan, Chaos **4**, 507 (1993)]. The escape of stars from galaxies has also been investigated [C. Siopis, H. E. Kandrup, G. Contopoulos, and R. Dvorak, Cel. Mech. Dyn. Astr. **65**, 57 (1997); A. F. Steklain and P. S. Letelier, Phys. Lett. A **352**, 398 (2006)], as well as the problem of light rays around black holes [A. P. S. de Moura and P. S. Letelier, Phys. Rev. E **61**, 6506 (2000)], and chaos in cosmological models [A. E. Motter and P. S. Letelier, Phys. Lett. A **285**, 127 (2001)].

[67] U. Leonhardt and T. G. Philbin, New J. Phys. **8**, 247 (2006).

[68] S. Bleher, C. Grebogi, and E. Ott, Physica D **45**, 87 (1990).

[69] Y.-T. Lau, J. M. Finn, and E. Ott, Phys. Rev. Lett. **66**, 978 (1991).

[70] Y.-C. Lai, R. Blümel, E. Ott, and C. Grebogi, Phys. Rev. Lett. **68**, 3491 (1992), Y.-C. Lai, M. Ding, C. Grebogi and R. Blümel, Phys. Rev. A **46**, 4661 (1992); Y.-C. Lai, Phys. Rev. E **60**, R6283 (1999); Y.-C. Lai, A. P. S. de Moura, and C. Grebogi, Phys. Rev. E **62**, 6421 (2000); J. Seoane, J. Aguirre, M. A. F. Sanjuan, and Y.-C. Lai, Chaos **16**, 023101 (2006).

[71] V. Rom-Kedar and D. Turaev, Physica D **130**, 187 (1999).

[72] V. J. Donnay, J. Stat. Phys. **96**, 1021 (1999).

[73] P. R. Baldwin, Physica D **29**, 321 (1988).

[74] D. Turaev and V. Rom-Kedar, Nonlinearity **11**, 575 (1998).

[75] D. Turaev and V. Rom-Kedar, J. Stat. Phys. **112**, 765 (2003).

[76] C. Grebogi, E. Ott, and J. A. Yorke, Physica D **7**, 181 (1983).

[77] B. S. White, J. Fluid Mech. **355**, 113 (1998); M. Onorato, A. R. Osborne and M. Serio, Phys. Rev. Lett. **96**, 014503 (2006); N. Akhmediev, J. M. Soto-Crespo and A. Ankiewicz, Phys. Lett. A **373**, 2137 (2009); B. Eliasson and P. K. Shukla, Phys. Rev. Lett. **105**, 014501 (2010); K. Hammani, B. Kibler, C. Finot and A. Picozzi, Phys. Lett. A **374**, 3585 (2010).

[78] M. A. Wolfson and S. Tomsovic, The J. Acou. Soci. Amer. **109**, 2693 (2001); F. J. Beron-Vera, M. G. Brown, J. A. Colosi, S. Tomsovic, A. L. Virovlyansky, M. A. Wolfson and G. M. Zaslavsky, The J. Acou. Soci. Amer. **114**, 1226 (2003); M. G. Brown, J. A. Colosi, S. Tomsovic, A. L. Virovlyansky, M. A. Wolfson and G. M. Zaslavsky, The J. Acou. Soci. Amer. **113**, 2533 (2003); M. Onorato, T. Waseda, A. Toffoli, L. Cavaleri, O. Gramstad, P. A. E. M. Janssen, T. Kinoshita, J. Monbaliu, N. Mori, A. R. Osborne, M. Serio, C. T. Stansberg, H. Tamura, and K. Trulsen, Phys. Rev. Lett. **102**, 114502 (2009).

[79] M. Onorato, T. Waseda, A. Toffoli, L. Cavaleri, O. Gramstad, P. A. E. M. Janssen, T. Kinoshita, J. Monbaliu, N. Mori, A. R. Osborne, M. Serio, C. T. Stansberg, H. Tamura and K. Trulsen, Phys. Rev. Lett. **102**, 114502 (2009).

[80] D. R. Solli, P. Ropers, C. Koonath and B. Jalali, Nature (London) **450**, 1054 (2007).

[81] J. M. Dudley, G. Genty and B. Eggleton, Opt. Express **16**, 3644 (2008).

[82] A. N. Ganshin, V. B. Efimov, G. V. Kolmakov, L. P. Mezhov-Deglin, and P. V. E. McClintock, Phys. Rev. Lett. **101**, 065303 (2008).

[83] A. Montina, U. Bortolozzo, S. Residori, and F. T. Arecchi, Phys. Rev. Lett. **103**, 173901 (2009).

[84] F. T. Arecchi, U. Bortolozzo, A. MOntina, and S. Residori, Phys. Rev. Lett. **106**, 153901 (2011).

[85] M. A. Topinka, B. J. LeRoy, R. M. Westervelt, S. E. J. Shaw, R. Fleischmann, E. J. Heller, K. D. Maranowski and A. C. Gossard, Nature **410**, 183–18 (2001).

[86] L. Kaplan, Phys. Rev. Lett. **89**, 18410 (2002).

[87] N. Akhmediev and E. Pelinovsky, Eur. Phys. J. Special Topics **185**, 1 (2010) , and articles therein.

[88] R. Höhmann, U. Kuhl, H.-J. Stöckmann, L. Kaplan and E. J. Heller, Phys. Rev. Lett. **104**, 093901 (2010).

[89] R. C. Rumpf, *Design and optimization of nano-optical elements by coupling fabrication to optical behavior.* Ph.D. diss. (University of Central Florida, 2006).

[90] C.-P. Yu and H.-C. Chang, Opti. Expr. **12**, 1397 (2004).

[91] S.-D. Wu and E. N. Glytsis, J. the Opti. Soci. Amer. A **19**, 2018 (2002).

[92] Briefly, this method uses Yee's grid, which is a leap-frog discretization scheme for electric and magnetic field components. Instead of solving the Maxwell curl equations directly with time iterations as in the classical FDTD (Finite Difference Time Domain) scheme, FDFD considers a snapshot of the steady state and uses matrix formulation to solve the whole material system at once. See, for example, Ref. [90] and [91].

[93] B. Shapiro, Phys. Rev. Lett. **57**, 216 (1986).

[94] T. M. Nieuwenhuizen and M. C. W. V. Rossum, Phys. Rev. Lett. **74**, 267 (1995).

[95] A. D. Mirlin, R. Pnini and B. Shapiro, Phys. Rev. E **57**, R628 (1998).

[96] M. Störzer, P. Gross, C. M. Aegerter and G. Maret, Phys. Rev. Lett. **96**, 06390 (2006).

[97] X. Ni, W.-X. Wang and Y.-C. Lai, Europhys. Lett. **96**, 44002 (2011).

[98] E. Akkermans, P. E. Wolf and R. Maynard, Phys. Rev. Lett. **56**, 147 (1986).

[99] S. John, Phys. Rev. Lett. **53**, 216 (1984).

[100] S. John, Phys. Rev. B **31**, 30 (1985).

[101] P.-E. Wolf and G. Maret, Phys. Rev. Lett. **55**, 269 (1985).

[102] D. S. Wiersma, M. P. V. Albada, B. A. V. Tiggelen and A. Lagendijk, Phys. Rev. Lett. **74**, 419 (1995).

[103] E. Abrahams, P. W. Anderson, D. C. Licciardello and T. V. Ramakrishnan, Phys. Rev. Lett. **42**, 67 (1979).

[104] P. W. Anderson, Phys. Rev. **109**, 1492 (1958).

[105] D. S. Wiersma, P. Bartolini, A. Lagendijk and R. Righini, Nature **390**, 671 (1997).

[106] A. A. Chabanov, M. Stoytchev and A. Z. Genack, Nature **404**, 850 (2000).

[107] T. Schwartz, G. Bartal, S. Fishman and M. Segev, Nature **446**, 52 (2007).

[108] Y. Lahini, A. Avidan, F. Pozzi, M. Sorel, R. Morandotti, D. N. Christodoulides and Y. Silberberg, Phys. Rev. Lett. **100**, 01390 (2008).

[109] S. Hughes, L. Ramunno, J. F. Young and J. E. Sipe, Phys. Rev. Lett. **94**, 03390 (2005).

[110] M. Patterson, S. Hughes, S. Combrié, N.-V.-Q. Tran, A. D. Rossi, R. Gabet and Y. Jaouën, Phys. Rev. Lett. **102**, 25390 (2009).

[111] N. Engheta, R. W. Ziolkowski, I. O. Electrical and E. Engineers, *Metamaterials: physics and engineering explorations* (John Wiley and Sons, 2006).

[112] D. Morits and C. Simovski, Phys. Rev. B **82**, 16511 (2010).

[113] R. M. May, Science **186**, 645 (1974); R. M. May and W. J. Leonard, SIAM J. Appl. Math. **29**, 243 (1975).

[114] R. M. May, *Stability and Complexity in Model Ecosystems* (Princeton University Press, Princeton, N.J., 1973).

[115] J. Hofbauer and K. Sigmund, *Evolutionary Games and Population Dynamics* (Cambridge University Press, Cambridge, England, 1998).

[116] P. Chesson, Annu. Rev. Ecol. Syst. **31**, 343 (2000).

[117] G. Szabó and G. Fath, Phys. Rep. **446**, 97 (2007).

[118] B. Kerr, M. A. Riley, M. W. Feldman and B. J. M. Bohannan, Nature (London) **418**, 171 (2002).

[119] B. C. Kirkup and M. A. Riley, Nature (London) **428**, 412 (2004).

[120] T. L. Czárán, R. F. Hoekstra, and L. Pagie, Proc. Natl. Acad. Sci. U.S.A. **99**, 786 (2002).

[121] Y. Iwasa, M. Nakamaru, S. A. Levin, Evol. Ecol. **12**, 785 (1998).

[122] D. W. Yu, H. B. Wilson, N. E. Pierce, Ecology **82**(6) 1761 (2001).

[123] D. W. Yu, H. B. Wilson, M. Frederickson, W. Palomino, R. de la Colina, D. P. Edwards, A. A. Balareso, Anim. Ecol. **73**, 1102 (2004).

[124] M. P. Hassell, H. N. Comins, R. M. May, Nature **370**, 290 (1994).

[125] M. C. Boerlijst and P. Hogeweg, Physica D **48**, 17 (1991).

[126] J. A. Sherratt, M. A. Lewis, and A. C. Fowler, Proc. Natl. Acad. Sci. U. S. A. **92**, 2524 (1995).

[127] P. Amarasekare, Ecol. Lett. **6** 1109 (2003).

[128] R. Durrett and S. Levin, Theor. Pop. Biol. **46**, 363 (1994).

[129] K. Mágori, P. Szabó, F. Mizera, G. Meszeńa, Evol. Ecol. Res. **7**, 1 (2005).

[130] G. Szabó, J. Phys. A: Math. Gen. **38**, 6689 (2005); G. Szabó and G. A. Sznaider, Phys. Rev. E **69**, 031911 (2004); G. Szabó, A. Szolnoki, and G. A. Sznaider, Phys. Rev. E **76**, 051921 (2007); G. Szabó, A. Szolnoki, and I. Borsos, Phys. Rev. E **77**, 041919 (2008).

[131] A. Traulsen, J. C. Claussen and C. Hauert, Phys. Rev. Lett. **95**, 238701 (2005); *ibid*, Phys. Rev. E **74**, 011901 (2006); J. C. Claussen and A. Traulsen, Phys. Rev. Lett. **100**, 058104 (2008).

[132] T. Reichenbach, M. Mobilia and E. Frey, Nature (London) **448**, 1046 (2007); Phys. Rev. Lett. **99**, 238105 (2007).

[133] T. Reichenbach, M. Mobilia and E. Frey, J. Theor. Biol. **254**, 368 (2008).

[134] T. Reichenbach and E. Frey, Phys. Rev. Lett. **101**, 058102 (2008).

[135] A. Szolnoki, M. Perc, and G. Szabó, Phys. Rev. E **80**, 056104 (2009).

[136] H. Shi, W.-X. Wang, R. Yang, and Y.-C. Lai, Phys. Rev. E **81**, 030901 (2010).

[137] J. B. C. Jackson and L. Buss, Proc. Natl. Acad. Sci. U.S.A. **72**, 5160 (1975).

[138] C. E. Paquin and J. Adams, Nature (London) **306**, 368 (1983).

[139] B. Sinervo and C. M. Lively, Nature (London) **380**, 240 (1996).

[140] G. Szabó, A. Szolnoki, and R. Izsák, J. Phys. A: Math. Gen. **37**, 2599 (2004).

[141] G.-Y. Zhang, Y. Chen, W.-K. Qi, and S.-M. Qing, Phys. Rev. E **79**, 062901 (2009).

[142] A. N. Zaikin and A. M. Zhabotinsky, Nature (London) **225**, 535 (1970).

[143] A. T. Winfree, Science **175**, 634 (1972).

[144] J. M. Davidenko, A. V. Pertsov, R. Salomonsz, W, Baxter, and J. Jalife, Nature **355**, 349 (1992).

[145] M. P. Hassell, H. N. Comins, and R. M. May, Nature **353**, 255 (1991).

[146] M. C. Boerlijst and P. Hogeweg, Physica D **88**, 29 (1995); J. Theor. Biol. **176**, 199 (1995).

[147] J. A. Sherratt and M. J Smith, J. R. Soc. Interface **5**, 483 (2008).

[148] Note that plane waves have never been observed on discrete lattices for mobile species. If we regard the plane wave as a special kind of spiral waves with infinite wavelength, the effects of interaction range can be distinguished from those due to individual mobility, i.e., spiral waves whose wavelength exceeds the lattice size cannot occur.

[149] R. M. May, Science **186**, 645 (1974).

[150] R. M. May and W. J. Leonard, SIAM J. Appl. Math. **29**, 243 (1975).

[151] M. C. Boerlijst and P. Hogeweg, Physica D **48**, 17 (1991); **88**, 29 (1995).

[152] M. C. Boerlijst and P. Hogeweg, J. Theor. Biol. **176**, 199 (1995).

[153] M. Perc, and A. Szolnoki, New J. Phys. **9** 267 (2007).

[154] S. A. Levin, Am. Nat. **108**, 207 (1974).

[155] Y.-C. Lai and Y.-R. Liu, Phys. Rev. Lett. **94**, 038102 (2005).

[156] L. A. Dugatkin, *Cooperation among animals* (Oxford University Press, Oxford, UK, 1997).

[157] E. Fehr and U. Fischbacher, Nature (London) **425**, 785 (2003).

[158] T. Reichenbach, M. Mobilia and E. Frey, Nature (London) **448**, 1046 (2007).

[159] T. Reichenbach, M. Mobilia and E. Frey, J. Theor. Biol. **254**, 368 (2008).

[160] M. Peltomäki and M. Alava, Phys. Rev. E **78**,031906 (2008).

[161] M. Frean and E. R. Abraham, Proc. R. Soc. London, Ser. B **268**, 1323 (2001); M. Berr, T. Reichenbach, M. Schottenloher, and E. Frey, Phys. Rev. Lett. **102**, 048102 (2009).

[162] J. C. Claussen and A. Traulsen, Phys. Rev. Lett. **100**, 058104 (2008).

[163] P. M. Altrock and A. Traulsen, Phys. Rev. E **80**, 011909 (2009).

[164] W.-X. Wang, Y.-C. Lai, and C. Grebogi, Phys. Rev. E **81**, 046113 (2010).

[165] R. Yang, W.-X. Wang, Y.-C. Lai, and C. Grebogi, Chaos **20**, 023113 (2010).

[166] G. Szabó, Attila Szolnoki, and I. Borsos, Phys. Rev. E **77**, 041919 (2008).

[167] Benjamin Andrae, Jonas Cremer, Tobias Reichenbach, and Erwin Frey Phys. Rev. Lett. 104, 218102 (2010).

[168] See, for example, S. W. McDonald, C. Grebogi, E. Ott, and J. A. Yorke, Physica D **17**, 125 (1985).

[169] S. Redner, *A Guide to First-Passage Processes* (Cambridge Univ. Press, Cambridge, 2001).

[170] L. Van Valen, J. Theor. Biol. **44**, 19 (1974).

[171] B. J. Rathcke, Ecology **57**, 76 (1976).

[172] M. D. Bertness, Ecology **70**, 257 (1989)

[173] Y. Yom-Tov, S. Yom-Tov and H. Moller, J. Biogeography **26**, 947 (1999).

[174] D. Tilman and S. Pacala, *in Species Diversity in Ecological Communities* (eds R. E. Ricklefs and D. Schluter) 13-25 (Univ. Chicago Press, Chicago, 1993).

[175] J. Hofbauer and K. Sigmund, *Evolutionary Games and Population Dynamics* (Cambridge University Press, Cambridge, England, 1998).

[176] J. Maynard Smith, *Evolution and the Theory of Games* (Cambridge Univ. Press, Cambridge, 1982).

[177] K. Sigmund, *Games of Life* (Oxford Univ. Press, Oxford, 1993).

[178] A. M. Colman, *Game Theory and its Applications in the Social and Biological Sciences* (Butterworth-Heinemann, Oxford, 1995).

[179] M. A. Nowak, *Evolutionary Dynamics* (Belknap Press, Cambridge, Massachusetts, 2006).

[180] J. B. C. Jackson and L. Buss, Proc. Natl. Acad. Sci. U.S.A. **72**, 5160 (1975).

[181] C. E. Paquin and J. Adams, Nature (London) **306**, 368 (1983).

[182] B. Sinervo and C. M. Lively, Nature (London) **380**, 240 (1996).

[183] G. Szabó, A. Szolnoki, and G. A. Sznaider, Phys. Rev. E **76**, 051921 (2007).

[184] T. Reichenbach, M. Mobilia and E. Frey, Nature (London) **448**, 1046 (2007); Phys. Rev. Lett. **99**, 238105 (2007); J. Theor. Biol. **254**, 368 (2008).

[185] D. Helbing, W. Yu, Proc. Natl Acad. Sci. USA **106**, 3680 (2009).

[186] S. A. Levin, Am. Nat. **108**, 207 (1974).

[187] Target wave patterns were previously found in excitable systems. See, for example, E. Pálsson and E. C. Cox, Proc. Natl Acad. Sci. USA **93**, 1151 (1996) and K, J. Lee, Phys. Rev. Lett. **79**, 2907 (1997).

[188] G. Szabó, A. Szolnoki, and R. Izsák, J. Phys. A: Math. Gen. **37**, 2599 (2004); A. Szolnoki and G. Szabó, Phys. Rev. E **70**, 037102 (2004); C.-Y. Ying, D.-Y. Hua, and L.-Y Wang, J. Phys. A: Math. Theor. **40**, 4477 (2007).

[189] T. Reichenbach, M. Mobilia, and E. Frey, Nature **448**, 1046 (2007).

[190] R. A. Gray, A. M. Pertsov, and J. Jalife, Nature (London) **392**, 75 (1998).

[191] H. Zhang, Z. Cao, N. J. Wu, H. P. Ying, and G. Hu, Phys. Rev. Lett. **94**, 188301 (2005);

[192] T. Reichenbach, M. Mobilia, and E. Frey, J. Theor. Biol. **254**, 368 (2008).

[193] K. I. Agladze and V. I. Krinsky, Nature (London) **296**, 424 (1982).

[194] B. Vasiev, F. Siegert, and C. Weijer, Phys. Rev. Lett. **78**, 2489 (1997).

[195] V. K. Vanag and I. R. Epstein, Science **294**, 835 (2001).

[196] N. Bursac, F. Aguel, and L. Tung, Proc. Natl. Acad. Sci. U.S.A. **101**, 15530 (2004)

[197] C. Zemlin, K. Mukund, M. Wellner, R. Zaritsky, and A. Pertsov, Phys. Rev. Lett. **95**, 098302 (2005).

[198] L.-Y. Deng, H. Zhang, and Y.-Q. Li, Phys. Rev. E **81**, 016204 (2010).

[199] B. Kerr, M. A. Riley, M. W. Feldman, and B. J. M. Bohannan, Nature **418**, 171 (2002).

[200] Y.-C. Lai and Y.-R. Liu, Phys. Rev. Lett. **94**, 038102 (2005).

[201] L.-L. Jiang, T. Zhou, M. Perc, X. Huang, and B.-H. Wang, New J. Phys. **11**, 103001 (2009).

[202] G.-Y. Zhang, Y. Chen,W.-K. Qi, and S.-M. Qing, Phys. Rev. E **79**, 062901 (2009).

[203] H.-J. Shi, W-X Wang, R. Yang, and Y.-C. Lai, Phys. Rev. E **81**, 030901(R) (2010).

[204] W-X Wang, Y.-C. Lai, and C. Grebogi, Phys. Rev. E **81**, 046113 (2010).

[205] L.-L. Jiang, T. Zhou, M. Perc, and B.-H. Wang, Phys. Rev. E **84**, 021912 (2011).

[206] S. Redner, A Guide to First-Passage Processes (Cambridge University Press, Cambridge, 2001).

[207] D. T. Gillespie, J. Comput. Phys. **22**, 403 (1976).

[208] C. E. Shannon, Bell Syst. Tech. J. **27**, 379 (1948).

[209] A. S. Mikhailov and K. Showalter, Phys. Rep. **425**, 79 (2006).

[210] L. Huang, Y.-C. Lai, D. K. Ferry, R. Akis, and S. M. Goodnick, J. of Physics: Condensed Matter **21**, 344203 (2009).

[211] D. K. Ferry, L. Huang, R. Yang, Y.-C. Lai, R. Akis, J. of Physics: Conference Series **220**, 012015 (2010).

[212] R. Yang, L. Huang, Y.-C. Lai and C. Grebogi, Europhysics Letters **94**, 40004 (2011).

APPENDIX A

CALCULATION OF ONE- AND TWO-DIMENSIONAL RELATIVISTIC TUNNELING RATES

To understand the quantum tunneling in the relativistic limit and the tunneling behavior for our double-well system, we develop a theory based on the self energy concept already employed by the electron transport theory [210–212]. Noting that the coupling strength between the two wells is rather weak, we consider an equivalent system where the tunneling between left and right wells can be treated as the escaping rate of Dirac fermions between two closed but weakly coupled wells. Let the left well be denoted by superscript (1), and the barrier together with the right well denoted by superscript (2). The Dirac equations for the whole double-well system can be written in terms of the Hamiltonians for the separated closed wells,

$$\begin{bmatrix} H_1 & V_{12} \\ V_{21} & H_2 \end{bmatrix} \begin{bmatrix} \psi^{(1)} \\ \psi^{(2)} \end{bmatrix} = E \begin{bmatrix} \psi^{(1)} \\ \psi^{(2)} \end{bmatrix}, \tag{A.1}$$

where V_{ij} are the coupling matrices. If the left well were itself closed, the equation should be

$$H_1 \psi^{(1)} = E_1 \psi^{(1)}. \tag{A.2}$$

However, due to the weakly coupled right part to the left well, now the equation becomes

$$(H_1 + \Sigma^R)\psi^{(1)} = E\psi^{(1)}, \tag{A.3}$$

where $\Sigma^R = V_{12} G^R V_{21}$ is the self energy for the barrier and the right well, with $G^R = (E + i\eta - H_2)^{-1}$ denoting the retarded Green's function. For each eigenstate of the left well, the energy shift can be obtained through the first order perturbation theory as

$$\langle \Sigma^R \rangle = \langle \psi^{(1)} | \Sigma^R | \psi^{(1)} \rangle. \tag{A.4}$$

This energy shift is typically complex. The real part of this shift changes the oscillating frequency of the corresponding eigenstate, while the imaginary part, denoted by $-\gamma$, introduces a decay factor $\exp(-C\gamma t/\hbar)$ in the time evolution of Dirac fermion probability, which describes the escaping rate of the Dirac fermions from the left well to the right part. Note that since the whole system is still closed, γ only describes the a transient event that the particle tunnels from left to right, while ignores the recurring of the state from right to left. If we let the right well be infinite long in which case

no reflective wave is detected, the situation becomes a single left well coupled with an semi-infinite lead by a potential barrier, and γ will then be the tunneling rate for the single left well system.

A.1. One-dimensional solution

Let us first consider the simplest case, a one-dimensional Dirac equation. Not only for its simplicity, but the one-dimensional Dirac equation also preserves some of the important properties in the tunneling rate, e.g., the large tunneling rates for small energies. We start by solving one dimensional Dirac equation

$$(-i\hbar v\sigma_x\partial_x)\psi = (E-V)\psi \tag{A.5}$$

separately for the two closed systems. For the left well of width L_x, $V=0$, so the solution is

$$\psi_n^{(1)}(x) = \frac{1}{\sqrt{L_x}}\exp(i\frac{\pi}{4})\begin{bmatrix} \cos(k_n x - \frac{\pi}{4}) \\ i\sin(k_n x - \frac{\pi}{4}) \end{bmatrix} \tag{A.6}$$

where $k_n = (n+1/2)\pi/L_x$. For the right part, the barrier has width W and $V=V_0$, and the right well has width L and $V=0$. We obtain the solution

$$\psi_n^{(2)}(x) = \begin{cases} A_1 e^{i\kappa_n x}u_+ \quad + \quad A_2 e^{-i\kappa_n x}u_- \\ A_3 e^{ik_n x}u_+ \quad + \quad A_4 e^{-ik_n x}u_- \end{cases}, \tag{A.7}$$

where $k_n = E/(\hbar v) = [V_0 W/(\hbar v) + (m+1/2)\pi]/(L+W)$, $\kappa_n = k_n - V_0/(\hbar v)$, $u_+ = (1,1)^T$ and $u_- = (1,-1)^T$ are bases for the spinor, and the coefficients A_i are determined by the boundary conditions. Note that this is a combined solution for $E < V_0$ and $E > V_0$. We are only interested in the junction between the left well and the right part where the coupling locates, and so far we have assumed x-coordinate to be continuous. What we need is the Green's function on a discrete lattice, having lattice points spaced by a, between two points along x-axis. We express the energy shift using the discrete lattice,

$$\langle\Sigma^R\rangle = \psi_n^{(1)\dagger}(L_x-a)V_{12}G^R(L_x+a,L_x+a)V_{21}\psi_n^{(1)}(L_x-a), \tag{A.8}$$

where $x=L_x$ is the junction between the left well and the barrier, and the coupling $V_{12} = V_{21}^\dagger = -i\hbar v\sigma_x$. Let us compute the Green's function

$$G^R(L_x+a,L_x+a) = \sum_n \frac{\psi_n^{(2)}(L_x+a)\psi_n^{(2)\dagger}(L_x+a)}{E+i\eta-\hbar v k_n}. \tag{A.9}$$

To eliminate reflection back to the left well, we let the right well be infinite long, i.e., $L \to \infty$ so that the summation changes to integration

$$\sum_k \to \frac{L+W}{\pi} \int dk. \tag{A.10}$$

Note that $|A_1|^2 = 1/[4(L+W)]$, which cancels the $L+W$ factor in Eq. (A.10). The Green's function value at $x = L_x + a$ becomes

$$G^R \to \frac{1}{2\pi} \int_0^\infty \frac{I_2 + M_k}{E + i\eta - \hbar v k}, \tag{A.11}$$

where I_2 is a 2×2 identity matrix and

$$M_k = \begin{bmatrix} \sin(2\kappa a) & i\cos(2\kappa a) \\ -i\cos(2\kappa a) & -\sin(2\kappa a) \end{bmatrix}. \tag{A.12}$$

The integral over I_2 diverges, but the imaginary part of the integral is finite, which eventually contributes to γ. This imaginary contribution turns out to be $-\hbar v\eta/(2\pi L_x E)$. To calculate the integral for the components of M_k, we define

$$\begin{aligned} S &= \int_0^\infty dk \frac{\sin(2\kappa a)}{E + i\eta - \hbar v k} \\ C &= \int_0^\infty dk \frac{\cos(2\kappa a)}{E + i\eta - \hbar v k} \end{aligned} \tag{A.13}$$

The rate γ can be expressed by these integrals

$$\gamma = -\frac{(\hbar v)^2}{2\pi L_x} \left[\cos(2ka)\mathrm{Im}(C) - \sin(2ka)\mathrm{Im}(S)\right] - \frac{\hbar v \eta}{2\pi L_x E} \tag{A.14}$$

We calculate the integrals S and C, and use $E \approx E_1 = \hbar v k_n$, we obtain

$$\begin{aligned} \gamma_n &= -\frac{\hbar v}{4\pi L_x} \mathrm{Im}\left[2\mathrm{Ci}(-2k_n a - i\delta)\cos\left(4k_n a - \frac{2aV_0}{\hbar v} + i\delta\right)\right. \\ &\quad \left. + \left[\pi + 2\mathrm{Si}(2k_n a + i\delta)\right]\sin\left(4k_n a - \frac{2aV_0}{\hbar v} + i\delta\right)\right] \\ &\quad -\frac{\hbar v \delta}{4\pi a L_x k_n}, \end{aligned} \tag{A.15}$$

where $\delta = 2a\eta/(\hbar v)$, and $\mathrm{Ci}(x)$ and $\mathrm{Si}(x)$ are cosine and sine integrals defined as follows.

$$\begin{aligned} \mathrm{Ci}(x) &= \gamma_0 + \ln(x) + \int_0^x \frac{cos(t) - 1}{t} dt \\ \mathrm{Si}(x) &= \int_0^x \frac{sin(t)}{t} dt, \end{aligned}$$

where γ_0 is Euler-Mascheroni constant. When a and η are small, Im[Ci$(-2k_n a - i\delta)$] $\approx -\pi/2[1 + u(\hbar v k - \eta)]$, where $u(\cdot)$ is a step function. So for $k > \eta/(\hbar v)$, we obtain a constant expression for γ,

$$\gamma = \frac{\hbar v}{2L_x} \tag{A.16}$$

We can also find the constant C by comparing the result with that from solving the whole double-well system directly.

Considering the symmetry of the double-well system, the solution $\psi = (\phi, \chi)^T$ must be divided into two types, symmetric and antisymmetric. We set the origin at the the center of the double-well, so that for the first component ϕ, symmetric and antisymmetric solutions require $\phi'(0) = 0$ and $\phi(0) = 0$, respectively. Interestingly, the second component is symmetric when the first is antisymmetric, and vice versa. We name the symmetry type according to the first component, and compute the energy levels for $E < V_0$. For symmetric and antisymmetric states, the energy levels are

$$\begin{aligned} E_S &= \frac{WV_0/2 + (n_S + 1/4)\hbar v\pi}{L_x + W/2} \\ E_A &= \frac{WV_0/2 + (n_A - 1/4)\hbar v\pi}{L_x + W/2}, \end{aligned}$$

where $n_S, n_A \in \mathbb{Z}$. Because these energy levels are equally spaced, the energy spacing between symmetric and antisymmetric states is

$$\Delta E = \frac{\hbar v\pi}{2L_x + W}. \tag{A.17}$$

Comparing the ΔE with γ, and noting that $L_x \gg W$, we have the coefficient $C = \pi$. Figure 61 shows both ΔE and $\pi\gamma$ with the numerical simulation. The simulation and the ΔE actually describe exactly the same system. We can see that $\pi\gamma$ calculated from the equivalent system using the self-energy method agrees with ΔE quite well, which demonstrates that the tunneling rate is almost constant for all energies in one dimension.

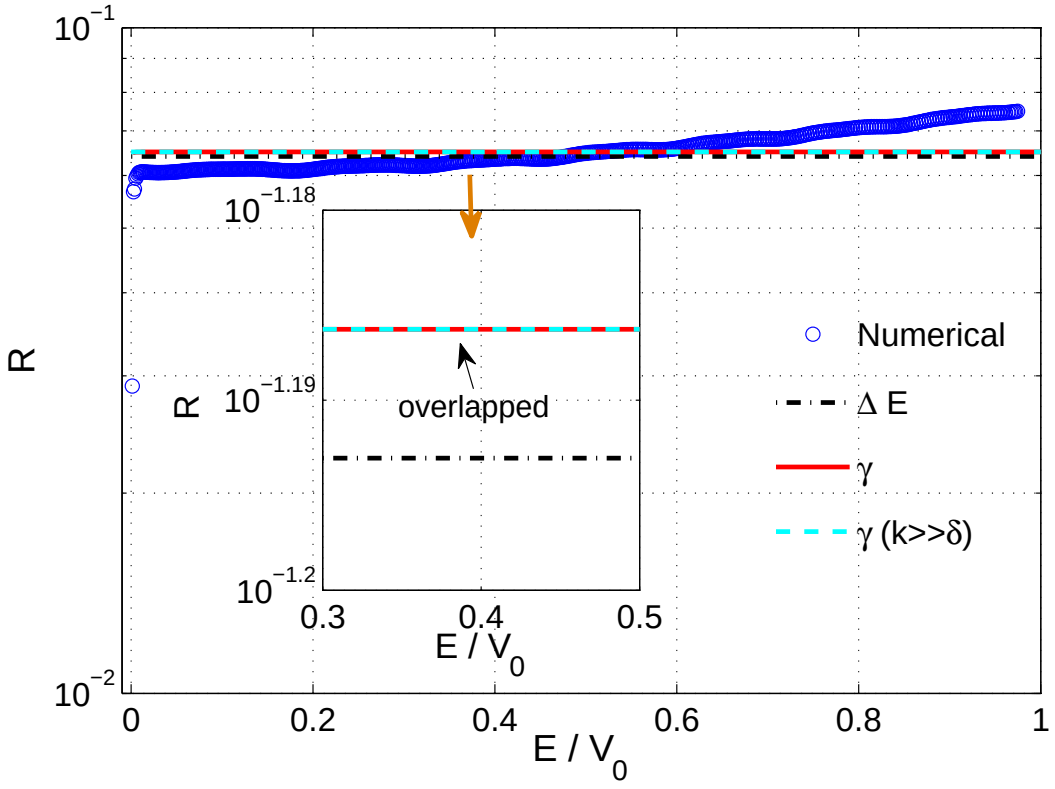

Fig. 61. (Color online.) Theoretical tunneling rates compared with numerics for one-dimensional massless Dirac fermion. Two theoretical curves are plotted: ΔE from computing the energy spacings between symmetric/antisymmetric eigenstate pairs for the whole double-well system, and $\pi\gamma$ from the self-energy method. Inset shows zoom-in view for $E/V_0 \in [0.3, 0.5]$ where the γ curve overlaps with $\gamma(k \gg \delta)$ curve.

A.2. Two-dimensional solution

To validate our proposed theory analytically in two dimensions is a rather hard problem. This is largely due to the entanglement of the two Cartesian coordinates in the first order Dirac equation. The problem is solvable only for certain types of boundary conditions via separation of variables. One particular case is the circular boundary condition. Imagine a ring with a thin concentric ring-shaped barrier in it, which makes it a ring double-well. When all four radii are large, this ring double-well is equivalent topologically to a rectangular double-well with periodic boundary condition in one direction. To solve the two-dimensional Dirac equation

$$(-i\hbar v\boldsymbol{\sigma}\cdot\nabla)\psi = (E-V)\psi, \tag{A.18}$$

we need to use polar coordinates (r,θ). Use $\partial_x \pm i\partial_y = \exp(\pm i\theta)(\partial_r \pm i\partial_\theta/r)$, the general solutions are of the following form

$$\psi_n = e^{in\theta}\begin{bmatrix} Z_n(\lambda r) \\ \text{sgn}(E-V)ie^{i\theta}Z_{n+1}(\lambda r)\end{bmatrix},\ n=\pm1,\pm2,\ldots \tag{A.19}$$

where $Z_n(x) = AJ_n(x) + BY_n(x)$ is the linear combination of the first and second kind Bessel functions, and $\lambda = |E-V|/(\hbar v)$.

Using the same strategy, we separate the ring double-well into two parts, the inner ring (denoted by superscript (1)) and the outer part (denoted by superscript (2)) consisting of the barrier ring and the outer ring. To be able to obtain an analytical expression for the energy levels, we use the asymptotic form of the Bessel functions for $x \gg |n^2-1/4|$,

$$J_n(x) \sim \sqrt{\frac{2}{\pi x}}\cos(x-\frac{n\pi}{2}-\frac{\pi}{4}) \tag{A.20}$$

$$Y_n(x) \sim \sqrt{\frac{2}{\pi x}}\sin(x-\frac{n\pi}{2}-\frac{\pi}{4}). \tag{A.21}$$

Applying two boundary conditions at $r=R_1,R_2$ and the normalization, we have for large radii, the solution for the inner ring is

$$\psi^{(1)}_{m,n} = N\frac{1}{\sqrt{r}}e^{in\theta}\begin{bmatrix} \sin(k_m(r-R_2)+3\pi/4) \\ -ie^{i\theta}\cos(k_m(r-R_2)+3\pi/4)\end{bmatrix}, \tag{A.22}$$

where $k_m = (m + 1/2)\pi/(R_2 - R_1)$, $m = 0, 1, 2, \ldots$, and $N = (2\pi(R_2 - R_1))^{-1/2}$. Note that the eigen-energy $\hbar v k_m$ doesn't depend on the angular quantum number n, meaning that all different angular modes are degenerate for a single energy level. This happens when we let the ring be infinite large, the radial functions take the trigonometric form, and the variation of the functions become periodic so that the energy levels are equally spaced. However, if we were to use the original radial solution, the energy levels are found through the zeros of integer order Bessel functions, and thus are spaced with a decreasing spacing. In that case, because different integer order Bessel functions differ in zeros, the eigen-energies are non-degenerate. For the outer part, the solutions combining $E < V_0$ and $E > V_0$ is

$$\psi^{(2)}_{\ell,n} = \begin{cases} N\frac{1}{\sqrt{r}}e^{in\theta} \begin{bmatrix} \sin(\kappa_\ell(r - R_2) + \pi/4) \\ -ie^{i\theta}\cos(\kappa_\ell(r - R_2) + \pi/4) \end{bmatrix} \\ N\frac{1}{\sqrt{r}}e^{in\theta} \begin{bmatrix} \sin(k_\ell(r - R_4) + 3\pi/4) \\ -ie^{i\theta}\cos(k_\ell(r - R_4) + 3\pi/4) \end{bmatrix} \end{cases}, \tag{A.23}$$

where $k_\ell = [(R_3 - R_2)V_0/(\hbar v) + (\ell + 1/2)\pi]/(R_4 - R_2)$, and $\kappa_\ell = k_\ell - V_0/(\hbar v)$. Similar to one dimension, the Green's function at the coupling boundary $R_2 + a$ is

$$G^R(r, \theta; r, \theta')\Big|_{r=R_2+a} = \sum_n \sum_\ell \frac{\psi^{(2)}_{\ell,n}(r, \theta)\psi^{(2)\dagger}_{\ell,n}(r, \theta')}{E + i\eta - \hbar v k_\ell}. \tag{A.24}$$

Let the outer boundary be infinite, the summation over k_ℓ turns into integration, we have

$$G^R \to \sum_n \frac{e^{in(\theta-\theta')}}{(2\pi)^2 R_2} \int_0^\infty dk \frac{M'_k}{E + i\eta - \hbar v k}, \tag{A.25}$$

where

$$M'_k = \begin{bmatrix} 1 + \sin(2\kappa a) & ie^{-i\theta'}\cos(2\kappa a) \\ -ie^{i\theta}\cos(2\kappa a) & e^{i(\theta-\theta')}[1 - \sin(2\kappa a)] \end{bmatrix}. \tag{A.26}$$

The energy shift is given by

$$\langle \Sigma^R \rangle_m = \int d\theta \int d\theta' \psi^{(1)\dagger}_{m,j}(\theta) V_{12} G^R(\theta; \theta') V_{21} \psi^{(1)}_{m,j}(\theta'), \tag{A.27}$$

where $\psi^{(1)}_{m,j}(\theta')$ is computed at $r = R_2 - a$, and the coupling matrix for two dimensions is obtained as follows. We know

$$\boldsymbol{\sigma} \cdot \nabla = \begin{bmatrix} 0 & e^{-i\theta} \\ e^{i\theta} & 0 \end{bmatrix} \partial_r + \begin{bmatrix} 0 & -ie^{-i\theta} \\ ie^{i\theta} & 0 \end{bmatrix} \frac{\partial_\theta}{r}, \tag{A.28}$$

so the coupling matrix should be for r. We take out the integration over the coordinates θ and θ',

$$\int_0^{2\pi} d\theta \int_0^{2\pi} d\theta' e^{i(j-n)(\theta-\theta')} = (2\pi)^2 \delta_{jn}. \tag{A.29}$$

This Kronecker delta cancels the summation over n. The final expression for rate γ is exactly the same as in one dimension, i.e., Eq. (A.14) and (A.16). The reason for the same rate γ as in one dimension largely owes to the degeneracy of the angular modes. Because all tangent modes are degenerate for one specific energy level that depends on the radial function only, one cannot separate this system from a true one-dimensional system. Therefore the rate γ must be the same as that in one dimension.

While the two-dimensional solution we have presented here is a special case where we have used the large r asymptotic form of radial functions, the general solution for circular boundaries is not the like. As we have discussed earlier that for a certain energy level, the degenerate angular modes require infinite R_i condition, however, for finite rings, different angular modes associate with different energy levels. Therefore, the tunneling rates for finite rings have a wide spread instead of a single straight line. In order to obtain rate γ for finite size rings, we must solve for the eigenstates numerically. Using the general solution for finite inner ring, Eq. (A.19), the normalization of the eigenstates, and the boundary conditions $Z_{n+1}(k_m R_i)/Z_n(k_m R_i) = \pm 1$ at $r = R_i$, $i = 1, 2$, we can find the roots k_m for each angular mode n numerically. For the outer part, however, things get more complicated by considering the ring with potential and the outer ring, and most importantly, to eliminate reflection, we need to set R_4 to infinite. This means we need to sum over infinite terms of k_ℓ in Eq. (A.24). A workaround for the infinity is to set a threshold k_{max} for the summation, and the criteria for choosing such k_{max} is the quality of the orthogonality,

$$\sum_{\{\ell : k_\ell < k_{max}\}, n} \psi^{(2)}_{\ell,n}(\mathbf{r}) \psi^{(2)\dagger}_{\ell,n}(\mathbf{r}') \approx I_2 \delta^2(\mathbf{r} - \mathbf{r}'). \tag{A.30}$$

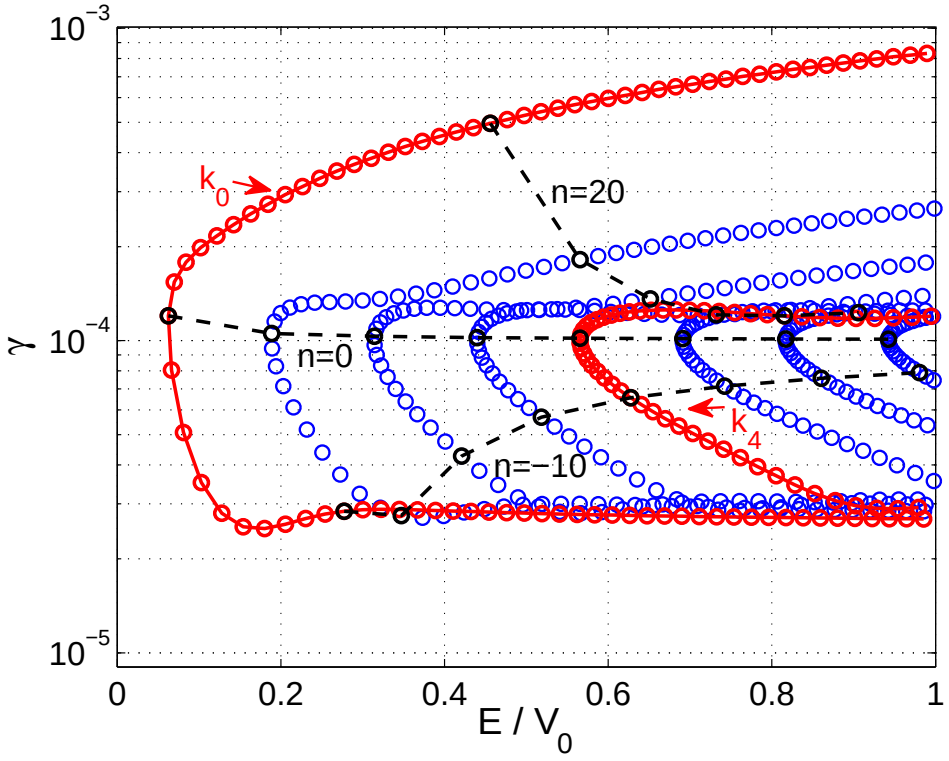

Fig. 62. (Color online.) Theoretical rate γ for two-dimensional rings. n denotes the angular quantum number, and k_i are the i^{th} energy level for all n. The eigenstates of the inner ring are found numerically, while the Green's function values for the outer part are calculated analytically using Eq. (A.25). The radii and potential are $R_1 = 5$, $R_2 = 10$, and $V_0 = 5$.

However, as number of eigenstates ℓ below k_{max} increases, the computation burden increases as ℓ^2. For fast computations, we consider two approximated results for the outer part: one uses the analytical solution of Green's function in Eq. (A.25), and the other uses a relatively larger outer ring to numerically calculate the rates. The γ values are shown in Fig. 62 and Fig. 15 for the above two schemes, respectively.

In Fig. 62, one can see that the tunneling rates of angular modes for the same energy level (e.g. k_0 and k_4 in Fig. 62) separate and scatter into a wide range, instead of clustering together as a single point, which is the case in one dimension and two-dimensional rings with all infinite radii. Figure 15

shows a complete numerically solution to the rate γ for rings with finite radii. A true γ should be calculated by setting the outermost boundary R_4 to infinity, however, a finite R_4 is computationally much easier to handle, and is enough to show qualitatively that there exist some points with very low tunneling rates, which are the survival states from the opening process of the originally closed left well (inner ring). One might notice that many points are concentrating at the high energy, low tunneling rate region. This is actually an artificial effect introduced by finite R_4. With a finite R_4, some fast tunneling states may appear to be slow ones due to the reflected waves. Also, the threshold k_{max} introduced for fast computation may break the orthogonality condition Eq. (A.30), which will affect high energy states even severely.

A.3. Non-relativistic quantum tunneling

For non-relativistic integrable systems (Fig.63), one can see that different energy states may have the same tunneling rate. This is because the particle momentum can be separated into p_x and p_y. While tunneling rates only relate to p_x, those modes with different p_y but having the same p_x contribute a horizontal line in the figure. When the shape becomes chaotic, these orbits are broken and mixed together, giving rise to a uniform rate of tunneling.

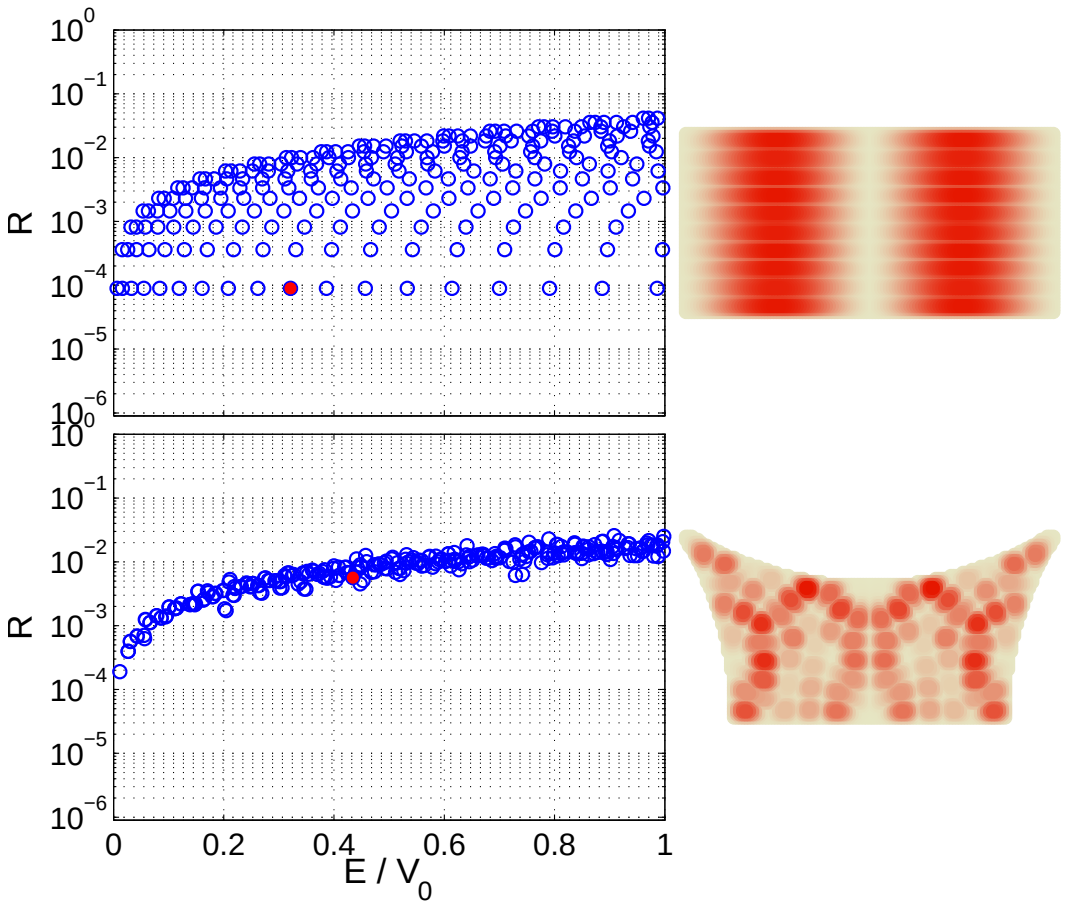

Fig. 63. (Color online.) Tunneling rates and LDSs for classical systems.

APPENDIX B

ACHIEVEMENTS DURING PHD STUDIES

Following are the relevant publications on the topics presented in this dissertation.

1. X. Ni, L. Huang, Y.-C. Lai, and C. Grebogi, "Scarring of Dirac fermions in chaotic billiards", Phys. Rev. E **86**, 016702 (2012). (Chapter 2)

2. X. Ni, L. Huang, Y.-C. Lai, and L. M. Pecora, "Effect of chaos on relativistic quantum tunneling", Europhysics Letters **98**, 50007 (2012). (Chapter 3)

3. X. Ni, and Y.-C. Lai, "Transient chaos in optical metamaterials", Chaos **21**, 033116 (2011). (Chapter 4)

4. X. Ni, W.-X. Wang, and Y.-C. Lai, "Origin of branched wave structures in optical media and long-tail algebraic intensity distribution", Europhysics Letters **96**, 44002 (2011). (Chapter 5)

5. X. Ni, W.-X. Wang, Y.-C. Lai, and C. Grebogi, "Cyclic competition of mobile species on continuous space: Pattern formation and coexistence", Phys. Rev. E **82**, 066211 (2010). (Chapter 6)

6. X. Ni, R. Yang, W.-X. Wang, Y.-C. Lai, and C. Grebogi, "Basins of coexistence and extinction in spatially extended ecosystems of cyclically competing species", Chaos **20**, 045116 (2010). (Chapter 7)

7. W.-X. Wang, X. Ni, Y.-C. Lai, and C. Grebogi, "Pattern formation, synchronization, and outbreak of biodiversity in cyclically competing games", Phys. Rev. E **83**, 011917 (2011). (Chapter 8)

8. L.-L. Jiang, W.-X. Wang, Y.-C. Lai, X. Ni, "Multi-armed spirals and multi-pairs antispirals in spatial rockpaperscissors games", Phys. Lett. A **376**, 2292 (2012). (Chapter 9)

Other works that have not been included in this dissertation are listed below.

9. W.-X. Wang, X. Ni, Y.-C. Lai, and C. Grebogi, "Optimizing controllability of complex networks by minimum structural perturbations", Phys. Rev. E **85**, 026115 (2012).

10. R.-Q. Su, X. Ni, W.-X. Wang, and Y.-C. Lai, "Forecasting synchronizability of complex networks from data", Phys. Rev. E **85**, 056220 (2012).